

# **Autonomous Formation Flying in Low Earth Orbit**



# **Autonomous Formation Flying in Low Earth Orbit**

## **Proefschrift**

ter verkrijging van de graad van doctor  
aan de Technische Universiteit Delft,  
op gezag van de Rector Magnificus prof.ir. K.C.A.M. Luyben,  
voorzitter van het College voor Promoties,  
in het openbaar te verdedigen

op maandag 1 maart 2010 om 15:00 uur

door

Simone D'AMICO

Laurea in Ingegneria Aerospaziale, Indirizzo Spazio  
Politecnico di Milano, Italy

Dit proefschrift is goedgekeurd door de promotoren:

Prof.ir. B.A.C. Ambrosius

Prof.dr. E.K.A. Gill

Copromotor:

Dr.ir. P.N.A.M. Visser

Samenstelling promotiecommissie:

Rector Magnificus,

Prof.ir. B.A.C. Ambrosius,

Prof.dr. E.K.A. Gill,

Dr.ir. P.N.A.M. Visser,

Prof.dr.ir. J.A. Mulder,

Prof.em.dr.dr.E.h.C. Reigber,

Prof.Dr.-Ing. B. Dachwald,

Dr. O. Montenbruck,

Prof.dr.ir. M. Mulder,

voorzitter

Technische Universiteit Delft, promotor

Technische Universiteit Delft, promotor

Technische Universiteit Delft, copromotor

Technische Universiteit Delft

GeoForschungsZentrum Potsdam, Germany

Aachen University of Applied Sciences (FH),  
Germany

Deutsches Zentrum für Luft- und Raumfahrt,  
Germany

Technische Universiteit Delft, reservelid

*Pushed by:* Ridderprint BV

ISBN 978-90-5335-253-3

Publishing of this thesis was partly funded by the Deutsches Zentrum für  
Luft- und Raumfahrt

Cover image courtesy of the Swedish Space Corporation, Stockholm, Sweden

©2010 by S. D'Amico

All rights reserved. No part of the material protected by this copyright may be reproduced, or utilized in any other form or by any means, electronic or mechanical, including photocopying, recording or by any other information storage and retrieval system, without prior permission of the author.



# Contents

<b>Acknowledgments</b>	<b>IX</b>
<b>List of symbols</b>	<b>XI</b>
<b>Acronyms</b>	<b>XV</b>
<b>Summary</b>	<b>XIX</b>
<b>Samenvatting (Summary in Dutch)</b>	<b>XXIII</b>
<b>1 Introduction</b>	<b>1</b>
1.1 Why Autonomous Formation Flying?	1
1.2 Applications and Development Lines	2
1.3 Research Objectives	4
1.4 State of the Art	6
1.4.1 Formation Flying Guidance	6
1.4.2 GPS-based Relative Navigation	8
1.4.3 Impulsive Relative Orbit Control	10
1.5 Contributions of This Research	11
1.5.1 Formation Flying Guidance and Control	11
1.5.2 GPS-based Relative Navigation	12
1.5.3 GNC System Integration and Validation	14
1.6 The PRISMA and TerraSAR-X/TanDEM-X Missions	14
1.6.1 PRISMA	15
1.6.2 TerraSAR-X/TanDEM-X	16
1.7 Thesis Outline	18
<b>2 Formation Flying Guidance and Control</b>	<b>21</b>
2.1 Unperturbed Relative Motion	21
2.1.1 Orbital Elements Parameterization	21
2.1.2 Cartesian Coordinates Parameterization	23
2.1.3 Relative Orbital Elements as C-W Integration Constants	25
2.2 Eccentricity/Inclination Vector Separation	26
2.2.1 Relative Eccentricity and Inclination Vectors	26
2.2.2 Collision Avoidance	27
2.2.3 Collision-free Formation-flying Configurations	29
2.3 Perturbed Relative Motion	32
2.3.1 Earth Oblateness $J_2$ Perturbation	32
2.3.2 Passively Stable Formation-Flying Configurations	35
2.3.3 Differential Drag	37

2.3.4	Numerical Validation of Analytical Relative Motion Model	38
2.4	Relative Orbit Control	41
2.4.1	Gauss' Variational Equations	41
2.4.2	In-plane Relative Orbit Control	42
2.4.3	Out-of-plane Relative Orbit Control	46
2.4.4	Formation Maintenance	46
2.4.5	Control Windows and Maneuver Budget	52
2.4.6	Formation Reconfiguration	54
2.4.7	Numerical Validation of Control Schemes	55
<b>3</b>	<b>GPS-based Relative Navigation</b>	<b>61</b>
3.1	Design of the Optimal Real-Time Estimator	61
3.1.1	Top-level Functional View	61
3.1.2	Key Objectives and Requirements	62
3.2	Estimation Concept	64
3.2.1	GPS Measurements	65
3.2.2	Selection of Measurements and State Parameters	68
3.2.3	Kalman Filter Modeling	72
3.2.4	Extended Kalman Filter Algorithm	77
3.3	Orbit Dynamics Modeling	80
3.3.1	Force Model Selection	81
3.3.2	Numerical Integration and Orbit Prediction	84
3.3.3	Maneuver Handling	85
3.4	Numerical Validation of Navigation Process	88
3.4.1	Simulation Environment	88
3.4.2	Numerical Tests and Results	90
3.4.3	Validation using GRACE Flight Data	106
<b>4</b>	<b>GNC System Architecture</b>	<b>111</b>
4.1	Model-Based Software Design	111
4.1.1	General Concept	111
4.1.2	System Structure	111
4.1.3	Specific Application Cores	112
4.2	Architectural Design	113
4.2.1	Physical System	113
4.2.2	Software Architecture	114
4.3	Software Modules	117
4.3.1	GPS Interface	117
4.3.2	GPS-based Orbit Determination	120
4.3.3	GPS-based Orbit Prediction	123
4.3.4	Autonomous Formation Control	125
4.3.5	Error Diagnostics within the Flight Software	128
4.4	Maneuver Handling within the Navigation System	130
4.4.1	Maneuver Related Interfaces	130
4.4.2	GPS-based Orbit Prediction	132
4.4.3	GPS-based Orbit Determination	132

4.5	Max-Path Unit Tests of GPS-based Flight Software . . . . .	134
4.5.1	Software Development and Testing Environment . . . . .	135
4.5.2	Max-Path Tests Definition . . . . .	137
4.5.3	Results from Max-Path Tests . . . . .	140
<b>5</b>	<b>Formation Flying Testbed . . . . .</b>	<b>143</b>
5.1	System Testing and Validation Concept . . . . .	143
5.2	Formation Control Experiment Rehearsal . . . . .	144
5.2.1	Test Specification . . . . .	145
5.2.2	Flight Software Settings . . . . .	147
5.2.3	True Motion from Real-time Simulator . . . . .	150
5.2.4	Flight Software Status . . . . .	152
5.2.5	Guidance and Control Results . . . . .	153
5.2.6	Navigation Results . . . . .	157
5.2.7	Flight Software Timeliness . . . . .	160
5.3	Integrated Tests with GPS Hardware in the Loop . . . . .	162
5.3.1	GPS Signal Simulator Scenario Definition . . . . .	164
5.3.2	Short-term GPS-based Closed-Loop Test . . . . .	166
5.3.3	PRISMA Spacecraft Separation Sequence . . . . .	177
<b>6</b>	<b>Conclusions . . . . .</b>	<b>185</b>
6.1	Summary . . . . .	185
6.2	Navigation and Control Accuracy . . . . .	188
6.3	Outlook . . . . .	190
<b>Appendix</b>	<b>. . . . .</b>	<b>195</b>
A.1	Reference Frame Transformations . . . . .	195
A.1.1	Standard Epochs and Time System . . . . .	195
A.1.2	Earth-Centered Reference Frames . . . . .	196
A.1.2.1	Earth Mean Equator and Equinox of Date . . . . .	196
A.1.2.2	World Geodetic System 1984 . . . . .	197
A.1.3	Reference Frames in this Research . . . . .	198
A.1.3.1	Co-moving Orbital Reference Frame . . . . .	198
A.1.3.2	Star Camera and GNC system in PRISMA . . . . .	198
A.1.3.3	GPS-Based Navigation . . . . .	198
<b>Bibliography</b>	<b>. . . . .</b>	<b>200</b>



# Acknowledgments

It is difficult to fairly acknowledge all those who helped me throughout this research and finally made this work possible. This thesis has its roots on decades of research conducted at the German Space Operations Center (GSOC) of the German Aerospace Center (DLR). The work presented here has been mainly conceived in the frame of the DLR's contributions to PRISMA, a technology demonstration mission of the Swedish Space Corporation (SSC) and the Swedish National Space Board (SNSB). Last but not least, Delft University of Technology (TU Delft) has given me the guidance and trust to build a PhD project out of it. Therefore, my deepest acknowledgments, as presented in the sequel, go to a number of people from these organizations.

First and foremost I would like to express my gratitude to my mentors E. Gill (former DLR/GSOC, presently TU Delft) and O. Montenbruck (DLR/GSOC), not only for their ideas and visions, and the daily technical supervision, but also for being a source of constant inspiration. Their criticisms and suggestions have greatly enhanced the quality, clarity and scope of this work. At TU Delft, I would like to thank P. Visser and B. Ambrosius, for guiding me through the PhD process and for their review of the manuscript.

In addition, I would like to thank my colleagues in DLR/GSOC's Space Flight Technology Department, many of whom contributed and/or motivated part of the material in this thesis. Special credits are due, in chronological order, to M. Markgraf for the GPS hardware support, to M. G. Fernandez for the software development support, to J.-S. Ardaens and S. De Florio for the software testing support.

I have really enjoyed to work together with the PRISMA team at SSC in a young, versatile and highly professional environment. Especially, I would like to thank the PRISMA project manager S. Persson, for the close and fruitful cooperation, and the colleagues P. Bodin, R. Noteborn, R. Larsson and C. Chasset, for the many technical discussions and the joint testing of the PRISMA system. I am also obliged to acknowledge M. Nylund from SSC and T. Yamamoto from JAXA who made key contributions to the full integration of the DLR's GPS signal simulator into the SATellite LABoratory (SATLAB) facility at SSC.

Besides those who have directly helped me with the technical side of this work, I would like to thank my lovely wife Silvia. The completion of this dissertation would have not been possible without her faithful support and patience with my late nights and long weekends spent in front of my laptop.

Munich, Germany, June 2009  
Simone D'Amico



## List of symbols

$A$	Cross-section area for drag computation
$a$	Semi-major axis
$\mathbf{a}$	Integration constants of C-W equations
$\mathbf{a}_{\text{emp}}$	Empirical accelerations
$b$	Tracking loop bandwidth
$B$	Ballistic coefficient
$c$	Speed of light ( $c = 299792458$ m/s)
$C_D$	Aerodynamic drag coefficient
$C/N_0$	Carrier to noise density ratio
$d$	Subscript indicating deputy spacecraft
$e$	Eccentricity
$\mathbf{e}$	Eccentricity vector
$E$	GPS satellite elevation
$E()$	Expected value
$\mathbf{G}$	Partials of estimator state with respect to process noise
$\mathbf{H}$	Partials of estimator measurements with respect to state
$i$	Inclination
$I$	Ionospheric path delay
$I_0$	Vertical ionospheric path delay
$J_2$	Geopotential second-order zonal coefficient ( $J_2 = 0.00108263$ )
$\mathbf{K}$	Kalman filter gain
$L$	Lear mapping function
$L1$	First L-band transmission frequency of GPS satellites ( $L1 = 1575.42$ MHz)
$M$	Mean anomaly
$m$	Spacecraft mass or number of EKF measurements
$n$	Mean motion or EKF state dimension
$N$	Float GRAPHIC bias in unit of meters
$N_C$	Integer number of carrier phase cycles
$N_{\text{CP}}$	Float carrier phase bias in unit of cycles
$\mathbf{o}_s$	Line of sight unit vector
$\mathbf{o}_n$	Cross-track unit vector
$\mathbf{o}_r$	Radial unit vector
$\mathbf{o}_t$	Along-track unit vector
$\mathbf{p}$	Estimator force model parameters
$\mathbf{P}$	State error covariance matrix
$q$	Process noise variance
$\mathbf{Q}$	Process noise matrix
$\mathbf{r}$	Spacecraft orbit position in ECI frame
$\mathbf{r}^{\text{ant}}$	Antenna phase center position of user satellite in ECEF frame

$\mathbf{r}^{\text{gps}}$	Antenna phase center position of GPS spacecraft in ECEF frame
$R_E$	Earth's equatorial radius
$R^{\text{ecf}}$	Rotation matrix from ECEF to ECI frame
$R^{\text{eci}}$	Rotation matrix from ECI to ECEF frame
$R^{\text{rtn}}$	Rotation matrix from Hill orbital frame to ECI frame
$\mathbf{R}_z$	Rotation matrix around z-axis
$S$	GPS systematic errors or biases
$t$	Time
$u$	Mean argument of latitude
$u_M$	Maneuver's mean argument of latitude
$\mathbf{v}$	Orbit velocity
$\mathbf{w}$	Estimator process noise
$\mathbf{x}$	Orbit state vector
$\mathbf{y}$	Estimator state vector
$\mathbf{z}$	Estimator measurements
$\boldsymbol{\alpha}$	Orbital elements vector
$\gamma$	$J_2$ dependent factor
$\Delta$	Arithmetic difference operator
$\delta_j^i$	Kronecker delta or Dirac delta function
$\delta a$	Relative semi-major axis
$\delta B$	Differential ballistic coefficient
$\delta \mathbf{e}$	Relative eccentricity vector
$\delta \mathbf{i}$	Relative inclination vector
$\delta e$	Modulus of the relative eccentricity vector
$\delta i$	Modulus of the relative inclination vector
$\delta r$	Position difference in Hill's orbital frame
$\delta r_{nr}$	Position difference in cross-track/radial plane
$\delta t$	GPS clock offset
$\delta u$	Relative mean argument of latitude
$\delta v$	Velocity difference in Hill's orbital frame
$\delta \phi$	Maximum allowed deviation of the relative perigee
$\delta \mathbf{v}$	Instantaneous maneuver velocity increment
$\delta \mathbf{x}$	Relative orbit state vector
$\delta \boldsymbol{\alpha}$	Relative orbital elements vector
$\delta \lambda$	Relative mean longitude
$\Delta t$	Maneuver cycle
$\Delta u_M$	Angular separation between maneuver location
$\epsilon$	GPS thermal noise or random errors
$\boldsymbol{\epsilon}$	Estimator measurement errors
$\eta$	Eccentricity dependent factor
$\theta$	Fractional stepsize of Hermite interpolation
$\vartheta$	Relative ascending node
$\lambda$	Mean longitude
$\lambda_1$	Wavelength of GPS L1 signal ( $\lambda_1 \approx 19.0$ cm)
$\mu$	Earth's gravitational coefficient ( $\mu = 398600.4415 \text{ km}^3/\text{s}^2$ )



$\nu$	True anomaly
$\xi$	Orientation of relative eccentricity vector correction
$\rho$	Atmospheric density or GPS geometric range
$\rho_{\text{PR}}$	GPS pseudorange measurement
$\rho_{\text{CP}}$	GPS carrier phase measurement
$\sigma$	Standard deviation
$\tau$	Process noise correlation time constant
$\tau_{\text{c}}$	True light travel time
$\varphi$	Relative perigee
$\Phi$	State transition matrix
$\chi$	Auxiliary parameter for maneuver computation
$\omega$	Argument of perigee
$\omega_{\text{E}}$	Earth's rotation rate ( $\omega_{\text{E}} = 7.2921158553 \cdot 10^{-5} \text{ rad/s}$ )
$\Omega$	Right ascension of the ascending node



# Acronyms

ACC	Accelerometer
AFC	Autonomous Formation Control (software module)
AMS	Asynchronous Monotonic Scheduler
AOCS	Attitude and Orbit Control System
ARV	Automated Transfer Vehicle Rendezvous Pre-development Program
ASW	Application Software level
ATV	Automated Transfer Vehicle
BSW	Basic Software level
CDGNSS	Carrier Phase Differential Global Navigation Satellite System
CHAMP	Challenging Mini Satellite Payload
CNES	French Space Agency
CP	Carrier phase
CPU	Core Processing Unit
C-W	Clohessy-Wiltshire equations
DART	Demonstration of Autonomous Rendezvous Technology
DEM	Digital Elevation Model
DD	Double difference
DGPS	Differential Global Positioning System
DLL	Delay Lock Loop
DLR	Deutsches Zentrum für Luft- und Raumfahrt
DOY	Day of Year
DTU	Danish Technical University
ECI	Earth-Centered Inertial reference frame
ECEF	Earth-Centered Earth-Fixed reference frame
EGSE	Electrical Ground Support Equipment
EM	Engineering Model
EKF	Extended Kalman Filter
FDIR	Fault Detection Isolation and Recovery
FFRF	Formation Flying Radio Frequency Sensor
FM	Flight Model
FPGA	Field Programmable Gate Array
FPU	Floating Point Unit
FT	Fault Tolerant
GIF	GPS Interface (software module)
GNC	Guidance, Navigation and Control
GNSS	Global Navigation Satellite System
GOD	GPS-based Orbit Determination (software module)
GOP	GPS-based Orbit Prediction (software module)
GEO	Geostationary Orbit

GOCE	Gravity Field and Steady-State Ocean Circulation Explorer
GPS	Global Positioning System
GR	GRAPHIC
GSOC	German Space Operations Center
GRACE	Gravity Recovery And Climate Experiment
GRAPHIC	GRoup And Phase Ionosphere Correction
GSS	GPS Signal Simulator
GYR	Angular-rate sensor
HEO	High Elliptical Orbit
HIL	Hardware-in-the-loop
HP	Hydrazine Propulsion
I/O	Input/Output
ISL	Inter Satellite Link
KBR	Ka-Band Ranging System
KF	Kalman Filter
LEO	Low Earth Orbit
LEOP	Launch and Early Operations Phase
LNA	Low Noise Amplifier
LTAN	Local Time at the Ascending Node
M	<i>Main</i> spacecraft
MOS	Mission Operations Segment
MM	Magnetometers
MT	Magnetic torque rods
NASA	National Aeronautics and Space Administration
OBS	On-board Software
PC	Personal Computer
FC	Fuel Consumption
PDOP	Position Dilution Of Precision
PEM	Phoenix Emulation software
PLL	Phase Lock Loop
PPP	Public-Private Partnership
PPS	Pulse Per Second
PR	Pseudorange
RAM	Random Access Memory
RCC	RTEMS Cross-Compilation system
RD	Rendezvous and Docking
RF	Radio Frequency
RK4R	4-th order Runge-Kutta augmented with Richardson extrapolation
RMS	Root-Mean-Square
RTEMS	Real-Time Executive for Multiprocessor Systems
RTU	Remote Terminal Unit
RTW	Real-Time Workshop (from Mathworks)
RW	Reaction wheels
SAR	Synthetic Aperture Radar
SATLAB	Satellite Laboratory

SCA	Star-tracker Camera
SCET	Spacecraft Elapsed Time (on-board time)
SD	Single difference
SISRE	Signal in Space Range Error
SNR	Signal to noise ratio
SRP	Solar radiation pressure
SS	Sun Sensors
SSC	Swedish Space Corporation
S/C	Spacecraft
T	<i>Target</i> spacecraft
TAFF	TanDEM-X Autonomous Formation Flying
TC	Telecommand
TEC	Total Electron Content
TDX	TanDEM-X
THR	Hydrazine Mono-Propellant Thruster System
TM	Telemetry
TPF	Terrestrial Planet Finder
TSX	TerraSAR-X
TU Delft	Delft University of Technology
TTL	TransistorTransistor Logic
UHF	Ultra High Frequency
UKF	Unscented Kalman Filter
VBS	Vision Based Sensor
XEUS	X-Ray Evolving Universe Spectroscopy
XRO	X-Ray Observatory
3D	Three Dimensions



## Summary

Formation flying is commonly identified as the collective usage of two or more cooperative spacecraft to exercise the function of a single monolithic virtual instrument. The distribution of tasks and payloads among fleets of coordinated smaller satellites offers the possibility to overcome the classical limitations of traditional single-satellite systems. The science return is enhanced through observations made with larger, configurable baselines and an improved degree of redundancy can be achieved in the event of failures. Different classes of formation flying missions are currently under discussion within the engineering and science community: technology demonstration missions (e.g., PRISMA, PROBA-3), synthetic aperture interferometers and gravimeters for Earth observation (e.g., TanDEM-X, postGOCE), dual spacecraft telescopes which aim at the detailed spectral investigation of astronomical sources (e.g., XEUS, SIMBOL-X), multi-spacecraft interferometers in the infrared and visible wavelength regions as a key to new astrophysics discoveries and to the direct search for terrestrial exoplanets (e.g., DARWIN, PEGASE). These missions are characterized by different levels of complexity, mainly dictated by the payload metrology and actuation needs, and require a high level of on-board autonomy to satisfy the continuously increasing demand of relative navigation and control accuracy.

Despite the promising theoretical studies of the last decades, the requirements posed by future autonomous multi-satellite systems indicate clearly the necessity of precursor technology demonstration missions. The research in the area of formation flying has been characterized by a high level of multidisciplinary. Many authors have worked independently on different disciplines like Guidance, Navigation and Control (GNC) of multiple satellites but little effort has been put into the design of a complete functional subsystem to be embedded in a spacecraft platform. This research work is motivated by the conviction that only the development, deployment and on-orbit validation of innovative GNC techniques can bring formation flying to the forefront and enable the definitive transfer of this revolutionary technology to space. Therefore the choice has been made to devote this study not only to the design, development and extensive validation of a suitable GNC system for Low Earth Orbit (LEO) formations, but also to its implementation into real upcoming space missions like PRISMA and TanDEM-X.

This dissertation presents the first realistic demonstration of a complete GNC system for formation flying spacecraft in LEO. Numerous technical contributions have been made during the course of this research in the areas of formation flying guidance, GPS-based relative navigation, and impulsive relative orbit control, but the primary contribution of this thesis does not lie in one or more of these disciplines. The innovation and originality of this work stems from the design and implementation of a comprehensive formation flying sys-

tem through the successful integration of various techniques. This research has led to the full development, testing and validation of the GNC flight code to be embedded in the on-board computer of the active spacecraft of the PRISMA technology demonstration. Furthermore key guidance and control algorithms presented here are going to be demonstrated for the first time in the TanDEM-X formation flying mission. Overall this thesis focuses on realistic application cases closely related to upcoming formation flying missions. The intention is to realize a practical and reliable way to formation flying: a technology that is discussed and studied since decades but is still confined in research laboratories. Hardware-in-the-loop real-time simulations including a representative flight computer and the GPS hardware architecture show that simple techniques, which exploit the natural orbit motion to full extent, can meet the demanding requirements of long-term close formation-flying.

In this dissertation a description of the satellites relative motion in terms of relative orbital elements has been preferred to the canonical Cartesian parameterization. In contrast to the fast varying position and velocity variables, the use of orbital element differences simplifies the formation-flying description and the satellite relative state computation. Various sets of relative orbital elements have been proposed in the past decades in the frame of formation-flying dynamics and control, but actually the most intuitive, straightforward representation in terms of relative eccentricity and inclination vectors has never been investigated for formation-flying design in LEO. This research generalizes the method of eccentricity/inclination vector separation, first developed for the safe collocation of geostationary satellites, and extends its application to proximity operations of formation-flying spacecraft. The spontaneous geometrical representation offers a direct correlation between the relevant characteristics of the bounded relative motion in near circular orbit and the magnitude/phase of the relative eccentricity/inclination vectors. This aspect extremely simplifies the design of safe, passively stable formation-flying configurations. In particular minimum collision risk conditions can be guaranteed by imposing the (anti)parallelism of the eccentricity and inclination vectors of the respective satellites, while  $J_2$ -stable relative orbits are obtained by setting a specific nominal phase for the configuration. The new approach is shown to be suitable either for the realization of synthetic aperture radar interferometers with baselines below 1 km or the application in longitude swap operations with along-track separations above 200 km.

The results obtained so far by various authors demonstrate that carrier phase differential GPS is an invaluable source of relative navigation in LEO. The use of space-borne GPS receivers hardware and true GPS signals in their hardware simulations marks a major progress on the way to acquire flight experiments. Nevertheless some limitations characterize the previous studies and, as a consequence, are addressed in this research. First of all the presented prototype navigation systems do not incorporate maneuvers, which will be crucial for use in orbital control and formation-keeping. Secondly the handling of the spacecraft attitude and the robustness of the filter to non-ideal non-zenith



orientations of the GPS antennas are neglected. Last but not least contingency scenarios or delicate formation-flying operations phases like the Launch and Early Operations Phase (LEOP) or the safe separation of the spacecraft from a common combined configuration are typically not addressed. The weakness of previously designed filters makes the strength of this development. One of the main challenges of real formation flying is the realization of an on-board navigation system for all mission phases which is robust and accurate even for various spacecraft orientations and frequent thruster firing for orbit control. In contrast to earlier approaches that separate the GPS-based navigation into the independent reconstruction of absolute and relative states, a single reduced-dynamic Kalman filter for the absolute states of both spacecraft has been adopted in this thesis. The inherent robustness of the symmetric filter design originates from the fact that common GPS satellites visibility is not a prerequisite to reconstruct the relative state. Even in the case of spacecraft with completely different attitude, the relative state can be determined by simply subtracting absolute estimates exclusively based on pseudorange measurements. As shown in this dissertation, the unified filter design simplifies the initialization and the maneuver handling procedures, and, consequently, improves the flexibility of the navigation system and its reliability during formation flying experiments.

This dissertation addresses the testing and validation of the GPS-based flight software throughout the complete development process. The GNC system is first tested as a standalone unit in a dedicated software development environment at DLR and later validated after its full integration into the PRISMA spacecraft on-board computer. Thanks to a novel model-based software design, the GNC software can be implemented and executed on different platforms in a fully consistent manner. This allows a seamless transition between off-line, real-time and hardware-in-the-loop tests during the validation phase. In particular off-line simulations are first conducted in a Matlab/Simulink environment on a standard host PC. Here, the flight software is stimulated through different sources of GPS data with an increasing level of realism. Apart from the classical pure software simulations which make use of emulated GPS measurements, this research presents numerical results obtained from the use of real GPS flight data from the Gravity Recovery and Climate Experiment (GRACE) during the closest encounter of the twin satellites. As a next step, real-time hardware-in-the-loop system tests are conducted on the integrated spacecraft flight models, comprising the Phoenix-S GPS receivers and a dual-spacecraft GPS Signal Simulator. Overall the test and validation process shows the compliance of the navigation and control software to the challenging requirements of PRISMA in terms of functionality, data interface, GNC accuracy, on-board memory and CPU load and paves the way for the successful launch and experiment operations of the PRISMA technology demonstration mission.



## Samenvatting

Formatievliegen wordt in het algemeen gezien als het gemeenschappelijke gebruik van twee of meer satellieten, die als zodanig tezamen één virtueel instrument vormen. De verdeling van taken en instrumenten over formaties van kleinere satellieten biedt de mogelijkheid de klassieke beperkingen van enkelvoudige satellietsystemen teniet te doen. De wetenschappelijke opbrengst wordt versterkt door de mogelijkheid waar te nemen met satellieten met configureerbare onderlinge afstanden, en bovendien kan een hogere graad van redundantie worden behaald. Vandaag de dag worden binnen de technische en wetenschappelijke wereld verschillende klassen van formatievliegende satellietmissies beschouwd: missies met als doel het demonstreren van nieuwe technologie (bijv. PRISMA, PROBA-3), aardobservatiemissies met SAR ("Synthetic Aperture Radar") antennes en gravimeters (bijv. TanDEM-X, opvolgers van GOCE), astronomische missies met samenwerkende telescopen (bijv. XEUS, SIMBOL-X), missies met diverse interferometers in het infrarode and zichtbare licht om nieuwe astrofysische ontdekkingen te doen en om terrestrische exoplaneten te vinden (bijv. DARWIN, PEGASE). Deze missies worden gekarakteriseerd door een verschillend niveau van complexiteit, voornamelijk bepaald door de omvang van de instrumenten en door de eisen op het gebied van aansluiting. Bovendien is een hoge mate van autonomie nodig om te voldoen aan steeds stringenter wordende nauwkeurigheidseisen voor de relatieve navigatie en baancontrole.

Ondanks veelbelovende theoretische studies van de afgelopen tientallen jaren, zijn demonstratiemissies nodig om de haalbaarheid van toekomstige concepten en doelstellingen van autonome satellietformaties aan te tonen. Het onderzoek op het gebied van formatievliegen van satellieten is sterk multidisciplinair. Vele wetenschappers hebben onafhankelijk van elkaar gewerkt aan verschillende relevante disciplines, zoals Geleiding, Navigatie en Controle (GNC) van constellaties van satellieten, maar slechts weinig inspanning is gestoken in het ontwerp van een compleet GNC subsysteem voor implementatie aan boord van de betreffende satellieten. De motivatie voor dit onderzoek ligt in de overtuiging dat de ontwikkeling, het gebruik en het daadwerkelijk testen van GNC technieken een vereiste is om tot een optimaal gebruik van formatievliegen van satellieten te komen. Daarom is de keuze gemaakt om deze studie niet alleen te wijden aan het ontwerpen, ontwikkelen en uitgebreid valideren van een bruikbaar GNC systeem voor laagvliegende aardsatellieten ofwel "Low-flying Earth Orbiting (LEO) satellites", maar ook aan het daadwerkelijk implementeren aan boord van aanstaande ruimtemissies zoals PRISMA en TanDEM-X.

Dit proefschrift bevat de resultaten van de eerste realistische demonstratie van een compleet GNC systeem voor formatievliegende satellieten in een lage aardbaan. Tijdens dit onderzoek zijn verschillende technische bijdragen gele-

verd op het gebied van geleiding van satellietformaties, relatieve plaatsbepaling met behulp van GPS, en relatieve positiecontrole door middel van kortstondige manoeuvres, maar de primaire bijdrage ligt elders. De innovatie en originaliteit van dit onderzoek ligt met name in de integrale benadering van ontwerp en implementatie van een compleet systeem voor formatievliegen van satellieten, waarbij gebruik is gemaakt van diverse technieken. Dit onderzoek heeft geleid tot de volledige ontwikkeling, en tot het volledig testen en valideren van de GNC software code in een boordcomputer van de satellieten van de PRISMA technologie demonstratiemissie. Bovendien worden in dit proefschrift belangrijke algoritmes beschreven voor geleiding en controle, die voor het eerst gedemonstreerd zullen worden tijdens de TanDEM-X missie. In het algemeen is bij dit onderzoek rekening gehouden met een zo realistisch mogelijke toepassing voor aanstaande formaties van satellieten. De doelstelling is een praktische en betrouwbare methode om formatievliegen te realiseren: een technologie die sinds tientallen jaren is bestudeerd maar tot recent niet verder is gekomen dan de tekentafel en laboratoriumonderzoek. Simulaties waarbij daadwerkelijk instrumenten en een representatieve boordcomputer aan elkaar werden gekoppeld in een laboratoriumomgeving laten zien dat met eenvoudige technieken, waarbij optimaal gebruik wordt gemaakt van de natuurlijke evolutie van de beweging van satellieten, kan worden voldaan aan de stringente eisen voor het voor lange(re) tijd in stand houden van satellietformaties.

In dit proefschrift is de voorkeur gegeven aan het gebruik van relatieve baanelementen om de relatieve beweging van satellieten te beschrijven boven canonieke Cartesiaanse parameters. Het gebruik van baanelementen vereenvoudigt de beschrijving van de relatieve beweging van formatievliegende satellieten, dit in tegenstelling tot de snel veranderende positie- en snelheidsvariabelen. In de afgelopen tientallen jaren zijn verschillende sets van relatieve baanelementen voorgesteld om de relatieve dynamica en controle van satellietformaties te beschrijven en modelleren, maar eigenlijk is de meest voor de hand liggende set, namelijk bestaande uit de relatieve excentriciteit- en inclinatievectoren, nooit gebruikt voor formatievliegen en het gerelateerde ontwerpproces. Dit onderzoek veralgemeniseert de methode van scheiding van excentriciteit- en inclinatievectoren, die oorspronkelijk was ontwikkeld voor het veilig naast elkaar plaatsen van geostationaire satellieten, en breidt haar toepassingsgebied uit naar GNC van dicht bij elkaar vliegende LEO satellieten. De gerelateerde geometrische beschrijving geeft een directe correlatie tussen de relevante eigenschappen van de gecontroleerde relatieve beweging in cirkelvormige banen en de grootte/fase van de relatieve excentriciteit- en inclinatievectoren. Dit aspect leidt tot een aanzienlijke vereenvoudiging van het ontwerp van veilige, passief stabiele formatievliegende satellietconfiguraties. Met name kan het vermijden van botsingen worden gegarandeerd door te eisen dat de excentriciteit- en inclinatievectoren evenwijdig zijn, terwijl tevens  $J_2$ -stabiele relatieve banen worden verkregen door de juiste nominale waarde van de fase van deze vectoren te kiezen. Het wordt aangetoond dat de nieuwe aanpak geschikt is voor zowel het realiseren van SAR interferometriemissies met onderlinge satellietaf-

standen van rond de 1 km als voor missies waarbij het nodig is om satellieten binnen een formatie van plaats te verwisselen waarbij de onderlinge afstand in de vliegrichting 200 kilometer of meer bedraagt.

Onderzoek door verschillende wetenschappers heeft tot nu toe laten zien dat differentiële GPS fasemetingen van onschatbare waarde zijn voor relatieve navigatie van LEO satellieten. Gedurende het betreffende onderzoek is veel vooruitgang geboekt in voorbereiding op daadwerkelijke vluchtexperimenten door gebruik te maken van voor satellieten geschikte GPS ontvangers en echte GPS signalen in simulaties op de grond. Het betreffende onderzoek kenmerkt zich echter door een aantal beperkingen. De eerste beperking betreft het niet meenemen van manoeuvres, die cruciaal zijn voor het in stand houden van satellietformaties. Een tweede beperking betreft het niet rekening houden met afwijkingen van de stand van de satelliet ten opzichte van de nominale situatie waarin de GPS antenne altijd precies omhoog wijst. Ten slotte, en minstens zo belangrijk, werd nauwelijks gekeken naar GNC scenario's voor speciale periodes tijdens de levensduur van satellietformaties, zoals de fase vlak na de lancering ("Launch and Early Operations Phase" ofwel LEOP) of periodes gedurende welke satellieten binnen de formatie veilig naar een andere plaats moeten worden gemanoeuvreed. Het onderzoek beschreven in dit proefschrift kent deze beperkingen niet en heeft daarmee een duidelijk toegevoegde waarde. Eén van de grootste uitdagingen van formatievliegen betreft het realiseren van een navigatiesysteem aan boord van de satellieten dat gedurende alle fasen van de levensduur robuust en nauwkeurig werkt, zelfs indien sprake is van verschillende standbewegingen van de betreffende satellieten en wanneer sprake is van regelmatig manoeuvreren. In tegenstelling tot eerder onderzoek waarbij de bepaling van de absolute en relatieve positie en snelheid met behulp van GPS gescheiden wordt gedaan, is voor het onderzoek, dat beschreven is in dit proefschrift, een Kalman filter ontworpen dat gelijktijdig de absolute en relatieve positie en snelheid bepaalt. Gebruik wordt gemaakt van een gereduceerd-dynamische methode, waarbij een optimale afweging kan worden gemaakt tussen de kwaliteit van krachtenmodellen en GPS metingen. Het betreffende symmetrische filter heeft een inherente robuustheid, omdat het niet nodig is voor de relatieve plaatsbepaling dat GPS satellieten tegelijkertijd zichtbaar zijn voor alle satellieten in de formatie. De relatieve positie kan zelfs worden bepaald wanneer satellieten in een formatie een totaal verschillende stand hebben, namelijk door simpelweg de absolute posities van elkaar af te trekken. Deze absolute posities zijn dan bepaald uit de zogenaamde GPS pseudo-afstandsmetingen. Zoals wordt aangetoond in dit proefschrift, worden de procedures voor opstarten en voor het uitvoeren van manoeuvres met dit gecombineerde filter vereenvoudigd. Dit leidt tevens tot een grotere flexibiliteit van het navigatiesysteem en zijn betrouwbaarheid tijdens experimenten van formatievliegen.

In dit proefschrift wordt het testen en valideren van software beschreven, dat daadwerkelijk aan boord van satellieten zal worden gebruikt voor GNC aan de hand van GPS metingen. Het betreffende GNC systeem wordt eerst als een zelfstandige eenheid getest in een speciale software omgeving van het

Duitse ruimtevaartagentschap DLR, en vervolgens gevalideerd nadat deze eenheid volledig is geïntegreerd in de boordcomputer van de PRISMA satelliet. Dankzij een nieuw software ontwerp kan de GNC software op een vergelijkbare manier op verschillende platformen worden geïmplementeerd en draaien. Hierdoor kan naadloos worden overgegaan op de verschillende manieren van testen van de GNC software, of dit nu als zelfstandige eenheid, of als onderdeel van de boordcomputer, of als onderdeel van de gehele satelliet is. In het bijzonder zijn allereerst simulaties uitgevoerd in een Matlab/Simulink omgeving op een standaard PC, waarbij de betreffende software wordt gevoed met verschillende typen, steeds realistischer wordende, GPS metingen. Naast de pure simulaties waarin gebruikt wordt gemaakt van kunstmatige metingen, zijn tevens berekeningen en testen uitgevoerd aan de hand van echte metingen van de Gravity Recovery and Climate Experiment (GRACE) missie. Een periode is geselecteerd, gedurende welke de GRACE satellieten elkaar dicht naderden. De GNC software is vervolgens geïmplementeerd en uitvoerig getest in geïntegreerde vluchtmodellen van satellieten, bestaande uit Phoenix-S GPS ontvangers en een simulator voor het genereren van GPS signalen voor twee satellieten. De test- en validatieprocedures tonen in het algemeen aan dat de ontwikkelde software voldoet aan de uitdagende eisen voor de PRISMA missie in termen van functionaliteit, gegevensuitwisseling, GNC nauwkeurigheid, geheugenbeperkingen van de boordcomputers en de belasting van de centrale verwerkingseenheid (CPU). Bovendien wordt hiermee verder de weg geplaveid voor een succesvolle lancering en uitvoering van experimenten die zijn gedefinieerd voor de PRISMA technologie demonstratiemissie.

# 1. Introduction

## 1.1 Why Autonomous Formation Flying?

Spacecraft formation flying is a revolutionary technology for scientific and commercial applications in space. The distribution of functions and payloads among fleets of coordinated small satellites offers the possibility to overcome the classical limitations of a monolithic system. The science return can be enhanced through observations made with larger, configurable baselines and a high degree of redundancy is guaranteed in the event of failures.

Satellites can be flown in a formation either by ground control or in autonomous mode. In the first case, guidance, navigation and control tasks are primarily performed on-ground with tight constraints in terms of ground station visibility. This introduces severe limitations on the achievable control accuracies, and may not lead to an optimum use of on-board resources. On the contrary on-board autonomy guarantees superior performance and prompt response to contingencies. The continuously increasing demand of spatial and temporal resolution for aperture synthesis and the required imaging performances for novel missions can only be satisfied by spaceborne autonomous formation flying systems. Furthermore the cost of mission operations can be drastically reduced by a harmonic coordination of on-board and on-ground resources.

Despite evident technology needs and promising theoretical studies, nowadays autonomous formation flying is mostly confined to laboratory research. The reason for such a gap is that the benefits of satellites flying in formation come at a cost. The new system architecture poses challenges in the areas of on-board sensing and actuation, high-level mission management and planning, as well as distributed fault detection, isolation and recovery.

Mission failures and terminations, furthermore, decrease the level of confidence in multi-satellite systems. Examples include the NASA Demonstration of Autonomous Rendezvous Technology (DART) in 2005, which ended in an unintentional collision with the target satellite [NASA, Last accessed: 2006], and the U.S. Air Force TechSat-21 formation flying experiment in 2005, which was terminated due to technical issues "far more challenging than originally thought" [Krebs, Last accessed: 2006]. These experiences indicate clearly the necessity of precursor technology demonstration missions for autonomous proximity operations and formation flying.

This research work is motivated by the conviction that only the development, deployment and on-orbit validation of innovative Guidance, Navigation

and Control (GNC) techniques can bring formation flying to the forefront and enable the definitive transfer of this revolutionary technology to space. Therefore the choice has been made to devote this study not only to the design, development and extensive validation of a suitable GNC system for Low Earth Orbit (LEO) formations, but also to its implementation into real upcoming space missions like PRISMA [Persson et al., 2006] and TerraSAR-X/TanDEM-X [Moreira et al., 2004].

## 1.2 Applications and Development Lines

Three main development lines can be identified in the frame of spacecraft formation flying. As shown in Table 1.1 the mission concepts are characterized by an increasing level of complexity, mainly dictated by the payload metrology and actuation needs. Synthetic Aperture Radar (SAR) interferometers and gravimeters are placed at the beginning of the time scale and are natural precursors of the more advanced virtual telescopes. The objective of these LEO instruments is to respond to the demand of highly accurate Digital Elevation Models (DEM) [Moreira et al., 2004] and Earth's gravity models on a global scale [Aguirre-Martinez and Sneeuw, 2003]. Two or more satellites of identical type and build are flown at typical separations of a few kilometers to synthesize three-dimensional baselines that can be reconfigured during the mission lifetime. The relative orbit control accuracy required for such formations is relatively coarse ( $> 10$  m) and drives the need for real-time on-board relative navigation accuracies at the meter level ( $> 1$  m). A specific challenge for these kinds of missions is the need of high precision (sub-)millimeter post-facto reconstruction of the three-dimensional relative motion. A key example of a dual spacecraft SAR interferometer with such formation metrology requirements is given by the TanDEM-X mission. Two identical spacecraft, namely TerraSAR-X (launched in summer 2007) and TanDEM-X (launch expected three years later in 2010) will fly in a precisely controlled formation to form a radar interferometer with typical baselines of ca. 1 km. This allows a much higher resolution than achievable in the X-SAR/SRTM Shuttle Topography mission and thus the generation of DEMs with unrivaled accuracy [Moreira et al., 2004].

At the same time, future gravity field satellite missions are being discussed to overcome the intrinsic limitations of gravimeters like the Challenging Mini Satellite Payload (CHAMP) [Reigber et al., 2002], the Gravity Recovery And Climate Experiment (GRACE) [Tapley et al., 2004], or the Gravity Field and Steady-State Ocean Circulation Explorer (GOCE) [Johannessen et al., 2003]. The GRACE geodetic observables, for example, are inherently non-isotropic, due to the permanent along-track orientation of the microwave radar link and to its scalar character. In order to enhance the spectral content, future geodetic satellite missions would like to make use of autonomous formation flying with multiple baselines (i.e., Cartwheel concepts) [Sneeuw and Schaub, 2005].

For LEO formation flying applications, the usage of the Global Navigation Satellite System (GNSS) poses an attractive alternative to other relative naviga-



tion sensors (e.g., optical metrology or radar) in terms of accuracy, robustness, flexibility, and acquisition cost. With the continuous advancement in microelectronic engineering, the size and power consumption of GNSS receivers will further reduce, which make them a perfect candidate for operation in microsatellite and nanosatellite buses.

**Table 1.1:** Development lines for satellite formation flying missions over the next decades.

Applications	SAR Interferometer and Gravimeter	Dual Spacecraft Telescope	Multi Spacecraft Telescope
Time line	2010	2017	2020
Orbit	Low Earth Orbit	High Earth Orbit (or Lagrange Point)	Lagrange Point (or High Earth Orbit)
Number of satellites	2–4	2	3+
Typical separation	50–1000 m	30–100 m	50–500 m
Orbit control accuracy	10–100 m	$0.1\text{--}10\text{ m}^{-2}$	$1\text{ m}^{-3}$
Navigation accuracy	1–10 m ( $1\text{ m}^{-3}$ post-facto)	$0.01\text{--}1\text{ m}^{-2}$	$1\text{--}100\text{ m}^{-6}$
Example missions	TanDEM-X, Cartwheel	XRO, SIMBOL-X	DARWIN, PEGASE, TPF

Dual spacecraft telescopes represent the second relevant class of future formation flying applications. These instruments aim at the detailed spectral investigation of sources which are too faint for study with the current generation of observatories like for example the Chandra X-ray Observatory [SMO, Last accessed: 2007] and the XMM-Newton [ESA, Last accessed: 2007]. The typical mission profile seeks orbits characterized by a low level of perturbations, stable thermal environment, lack of eclipses, and wide sky visibility. In contrast to the unfavorable LEO environment, in this context optimum conditions are offered by geostationary orbits (GEO), highly elliptical orbits (HEO) and Halo orbits around the Libration points of the Sun-Earth system. Distributed telescopes are composite spacecraft composed of a detector and a mirror unit flying as a formation during science operations. Typical separations aim at focal lengths of the order of 30–100 m. Autonomous formation flying capabilities are driven by the telescope optical design and should allow un-interrupted science observations. This translates into combined attitude/orbit control systems with required relative navigation accuracies at (sub-)centimeter level. The technological gap that exists between remote sensing LEO formations and outer space distributed telescopes is evident. It is not only given by the envisaged three-order-of-magnitude improvement of the required metrology and actuation needs, but is mainly caused by the necessity of implementing a navigation system at altitudes above the GNSS constellations. Provided that the GNSS receivers can acquire and track the very weak side lobes of the broadcast signals,

real-world simulations have demonstrated centimeter level relative navigation accuracies in GEO (ca. 5 cm) and HEO (ca. 30 cm) at radial distances up to 17 Earth radii [Mohiuddin and Psiaki, 2006]. Only self-contained relative (inter-satellite) navigation sensors (i.e., radio frequency and optical) can fulfill the requirements of autonomous formation flying at even higher altitudes.

**Table 1.2:** Formation flying metrology technologies.

Metrology technology	Navigation Accuracy	Comments
GNSS	m-cm	Limited to orbit altitude < GEO Primarily suited for LEO
Radio frequency (ranging, radar, wireless)	m-cm	Same measurement and technology principles as GNSS
Optical metrology	mm- $\mu$ m	-
Laser interferometry	nm	Fringe sensors and optical delay lines

The X-Ray Observatory (XRO), also known as XEUS (X-Ray Evolving Universe Spectroscopy), is a relevant example of a dual spacecraft telescope. One of the main science goals of XRO is to investigate the high-redshift Universe. The current mission scenario is based on a Halo orbit around Earth-Sun L2 and a composite spacecraft with a focal length of 35 m. The detector satellite is designed to support the payload units and track the focus point of the mirror satellite as to maintain it at the instrument focal plane. The launch of both units as a single stack is planned at the end of 2017, with nominal operations extending until the end of 2022 [XEUS, 2006].

The ultimate accuracy in terms of formation flying metrology and actuation is required for the successful deployment and operations of the third set of applications listed in Table 1.1. Interferometry in the infrared and visible wavelength regions has been identified as the key technology to new astrophysics discoveries and to the direct search for terrestrial exoplanets. To that purpose, clusters of three or more units need to fly in millimeter precision close formations with inter-satellite navigation accuracies at the sub-millimeter level. As shown in Table 1.2, only optical sensors and laser interferometers can provide the required formation flying metrology performances. Examples of these types of missions are given in Europe by the infrared space interferometers DARWIN and PEGASE and in USA by the NASA's Terrestrial Planet Finder (TPF) [Ollivier et al., 2005].

### 1.3 Research Objectives

Although characterized by short duration, heavy involvement of the ground control and blank checks, the first formation flying experiments bring us back to the rendezvous and docking (RD) of manned and unmanned capsules 30–40 years ago [Carpenter and Schieeser, 2001]. The famous Clohessy-Wiltshire

(C-W) equations [Clohessy and Wiltshire, 1960], used to simulate the terminal rendezvous between the Gemini chase vehicle and the Agena target vehicle [Bainum, 2002], first appeared in the 1960 paper by Clohessy and Wiltshire. These equations find nowadays applications in orbit perturbation analysis, station keeping of satellites in close formation and constitute the theoretical basis of the work conducted in this research.

Despite its relatively remote history, formation flying is considered today as a revolutionary technology that poses numerous challenges in the areas of guidance, navigation and control (GNC), on-board sensing and actuation, high-level mission management, planning and operations, as well as distributed fault detection isolation and recovery and inter-spacecraft communication. The attempt of this thesis is to bring together and build upon the work done by many others, in various areas of formation flying.

First of all the author investigates a formation-flying concept in LEO able to realize the demanding baselines for aperture synthesis, while minimizing the collision hazard associated with proximity operations. The focus is to meet the mission objectives while reducing the system complexity. Because following arbitrary trajectories generally requires prohibitive amounts of fuel, the aim is to define fuel-efficient relative spacecraft trajectories that are useful for synthesizing scientific instruments.

Having identified the appropriate guidance strategy, the main objective of this research is to design, develop and validate a GNC subsystem for a representative two-satellite formation in LEO. After its testing and validation, the system will be flown on the PRISMA technology demonstration mission with an expected launch date in 2010. The developed GNC modules will be integrated, as part of the flight software, into the on-board computer of the formation flying spacecraft. The primary objectives of the GNC subsystem are to

1. provide a guidance law implementing a safe collision-free separation strategy,
2. provide real-time continuous absolute orbit information with an accuracy better than 3 m and 1 cm/s (3D, RMS) for the position and velocity of both spacecraft respectively,
3. provide real-time continuous relative orbit information with an accuracy better than 0.2 m and 0.2 mm/s (3D, RMS) for the relative position and velocity of the active spacecraft with respect to the co-orbiting one, and to
4. provide a robust control algorithm for formation keeping with an accuracy better than 30 m (3D, RMS) for typical formation separations below 1 km.

As explained in the previous section, these requirements are very well applicable to a wide variety of close formations in LEO with relevant applications in the frame of Earth's gravimetry and SAR interferometry. The goals of this research are to further enhance the state of the art with a focus on the real-time

performance of the system on a platform representative of the spacecraft on-board computer. Because of its emphasis on a real upcoming mission, drivers of cost, and implementation constraints have largely influenced the GNC design. As detailed in the following sections, these aspects have turned out to represent the main contributions of this research to the body of knowledge.

## 1.4 State of the Art

In general the research in the area of formation flying is characterized by a high level of multidisciplinary. As illustrated in Fig. 1.1, many authors have worked independently on different disciplines like guidance, navigation and control of multiple satellites but little effort has been put into the design of a complete functional subsystem to be embedded in a spacecraft platform.

This section is devoted to the presentation of the body of knowledge and experience gained in the past years in three distinctive areas, namely formation flying guidance, GPS-based relative navigation and impulsive relative orbit control. The selection of specific methods like GPS and impulsive control reflects the real applications under examination in this work and hides some relevant design choices that are strictly related to the kind of problem we want to solve.

As mentioned in Section 1.2, GPS is the primary source of relative navigation in LEO. GPS provides highly accurate timing information for on-board time synchronization, enables simultaneous measurements from the spacecraft within the formation and offers the required level of accuracy in the context of carrier-phase differential GNSS (CDGNSS) techniques [Leung and Montenbruck, 2005], [Ebinuma, 2001], [Hartrampf et al., 2002].

Impulsive orbit control is nowadays the only feasible option considering the limitations imposed by the current propulsion technologies and by the sensitivity of scientific instruments to external accelerations. In general thruster activities have to be minimized to maximize the available time for data collection, thus orbit maintenance maneuvers are realized in short time intervals so to maximize the thrust-free portion of the spacecraft trajectories [Scharf et al., 2002].

### 1.4.1 Formation Flying Guidance

Various parameterization methods have been used in the past to describe the relative motion between co-orbiting spacecraft in a formation. The aforementioned C-W equations utilized a Hill-like [Hill, 1878] rotating Cartesian coordinate frame with origin on the chief satellite to express the relative position and velocity vectors of a deputy satellite. Hence the other name of Hill's equations often used together with C-W. Curvilinear coordinates in the same Hill frame have also been adopted to derive more accurate expressions of the relative motion. The linear formulation provided by the C-W equations assumes small deviations from a circular reference orbit about a spherical Earth. Consid-

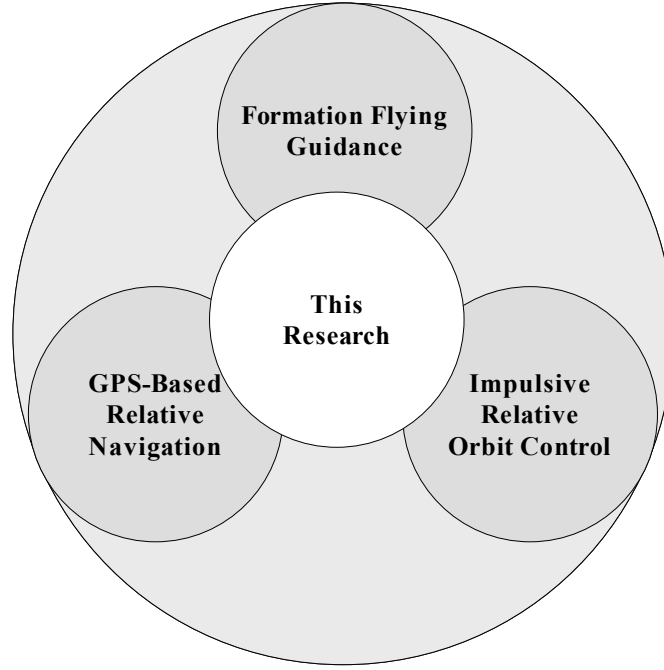


**Fig. 1.1:** This research brings together and build upon the work done by many others in the areas of formation flying guidance [Clohessy and Wiltshire, 1960; Eckstein et al., 1989; Sabol et al., 2001; Schaub, 2004; D’Amico and Montenbruck, 2006], GPS-based relative navigation [Kawano et al., 1999; Ebinuma, 2001; Busse, 2003; Leung, 2003; D’Amico et al., 2006a] and impulsive relative orbit control [Micheau, 1995; Schaub and Alfriend, 2001; Vaddi et al., 2005; D’Amico et al., 2006b].

erable effort has been put into the generalization of these equations to include disturbance forces [Sabol et al., 2001], [Schweighart and Sedwick, 2004], and eccentric reference orbits [Inalhan et al., 2002], [Gim and Alfriend, 2001].

The six Cartesian initial conditions are the invariant parameters of the relative motion described by the C-W equations. As originally suggested by Hill in his development of the lunar theory [Hill, 1878], an alternate set of six invariant parameters can be used to conveniently express the motion relative to the reference orbit (i.e., relative to the chief spacecraft). For a Keplerian motion, as assumed by the C-W equations, the chief and deputy satellite trajectories are conics conveniently defined by a Lagrange set of orbital elements:  $a$ ,  $e$ ,  $i$ ,  $\omega$ ,  $\Omega$ , and  $M_0$  which correspond to semi-major axis, eccentricity, inclination, argument of perigee, right ascension of the ascending node and the mean anomaly at the initial time  $t_0$ . The existence of invariant parameters of the absolute motion (the Lagrange orbital elements) and the well known non-linear one-to-one mapping between these parameters and the Cartesian position and velocity at the same instant of time  $t_0$  pushed several authors to search combinations of orbital elements as constants of the relative motion [Eckstein et al., 1989], [Kasdin and Gurfil, 2003], [Schaub, 2004]. In the following these invariant parameters are referred to as *relative* orbital elements to distinguish them from the classical Keplerian (or *absolute*) orbital elements.

The relative orbital elements found their first definitions and applications in the years 1980–1990 when the full potential of the Geostationary Orbit (GEO) as provider of facilities for communications and Earth observation was recognized on a global scale. The growth trend in telecommunications and thus the huge demand for orbital positions in GEO induced the development of the concept of satellite colocation. Several satellites had to be positioned in so-called GEO windows usually reserved for one satellite only. The interference between satellites due to the high probability of close approaches and collision risks had to be mitigated through coordinated orbit control strategies in order to separate the satellites physically in space whilst still maintaining them within the nominal window. Various approaches to the separation of colocated satellites have been developed, such as introducing a time interval between the application of station keeping maneuvers for each satellite or operating each satellite in a slightly non-GEO orbit by selecting appropriate differences in the orbital elements (e.g., using a slightly different eccentricity or inclination), or a combination of the two [Eckstein et al., 1989], [Harting et al., 1988].

More recently the clear advantage of the parameterization of the relative motion in terms of relative orbital elements has been recognized by various authors. This approach provides direct insight into the shape, size and location of the formation geometry and allows the straightforward adoption of variational equations such as Lagrange’s planetary equations or Gauss’s variational equations to study the effects of orbital perturbations on the relative motion. Kasdin and Gurfil have tried to unify the merits of the C-W and orbital elements-based approaches by developing a Hamiltonian methodology that models the relative motion dynamics using canonical coordinates, termed “epicyclic” elements [Kasdin and Gurfil, 2003]. A lower level of abstraction is finally presented by Schaub who has extensively examined the relative orbit geometry through classical orbital element differences [Schaub, 2004]. Here direct linearized relationships between classical orbital elements differences and the resulting relative orbit geometry are presented for both circular and eccentric (chief) orbits with the incorporation of the gravitational perturbation resulting from the Earth’s flattening.

#### 1.4.2 GPS-based Relative Navigation

A fundamental need of spacecraft autonomous formation flying is the determination of the relative motion (i.e., position and velocity) between individual satellites in near real-time. For formation flying in LEO, differential GPS (DGPS) represents an ideal sensor which can be used to directly measure the relative positions and velocities to a high level of accuracy with low costs. In particular raw measurements of carrier phase and pseudo-range from two or more user spacecraft made to common GPS satellites in the constellation can be subtracted from each other to reduce systematic errors. Compared to typical raw measurements, differenced GPS observation data have a high level of common error cancellation and, as a consequence, are less sensitive to GPS satellite clock offsets, GPS broadcast ephemeris errors, ionospheric refraction, and biases due

to hardware delays.

Many authors have recognized these advantages and worked on GPS-based relative navigation of space vehicles since the late 1990s. Relative navigation accuracies at the meter level have first been demonstrated in earlier missions like the Automated Transfer Vehicle (ATV) Rendezvous Predevelopment Program (ARP) [Carpenter, 2001], and the ETS-VII mission [Kawano et al., 1999] by making use of differenced pseudo-range measurements only. Recent hardware-in-the-loop simulations using GPS signal simulators have performed much better, mainly because more sophisticated carrier phase differential techniques have been used. Studies performed by Ebinuma [2001], Busse [2003], Hartrampf et al. [2002], Leung and Montenbruck [2005] have all demonstrated real-time relative navigation at the (sub-)centimeter level using single frequency GPS receivers.

While achieving these results, each of the aforementioned authors has addressed different facets of the navigation problem. Ebinuma has demonstrated precise closed-loop rendezvous of two spacecraft and achieved a relative position accuracy of 5 cm (3D, RMS) for baselines up to 10 km [Ebinuma, 2001]. His navigation filter processes double-difference carrier phase data and the relative state is computed from the difference between the two absolute state estimates. No ambiguity fixing to integer values is performed. A high-performance desktop computer is used for real-time simulations. Busse [2003] has also achieved similar accuracies through a filter which directly estimates the relative states from single-difference carrier phase measurements and a known local absolute state. The prototype code is tested through off-line analysis of raw GPS measurements recorded in a signal simulator testbed. Hartrampf has demonstrated relative navigation with an accuracy of about 1 cm (3D, RMS) in an ionosphere-free simulation scenario for a 1-km baseline [Hartrampf et al., 2002]. The relative navigation filter makes use of double-difference carrier phase data types in a purely kinematic manner by fixing the integer ambiguities. Real-time simulations are implemented on a standard desktop computer.

The best results to date have been achieved by Leung and Montenbruck who demonstrated GPS-based real-time relative navigation accuracies at the sub-centimeter level for formations with 1–10 km baselines [Leung, 2003]–[Leung and Montenbruck, 2005]. At the basis of this improved performance is the adoption of a more rigorous relative motion model, the resolution of double-difference integer ambiguities and the use of a GPS receiver optimized for low-noise carrier phase tracking under space dynamics. Furthermore the authors used a convenient linear combination of pseudo-range and carrier phase termed GRoup And Phase Ionosphere Correction (GRAPHIC) for absolute navigation [Yunck, 1993]. This ionosphere-free GRAPHIC measurement is characterized by a lower noise compared to pseudorange measurements and removes an otherwise significant source of error for single frequency GPS users. In contrast to previous studies, Leung and Montenbruck have developed a real-time navigation system embedded in a realistic flight computer with its inherent limitations in memory and computing performance. The navigation accuracies have been evaluated in hardware-in-the-loop simulations comprising GPS signal simula-

tors, GPS receivers, the navigation computer and radio modems.

### 1.4.3 Impulsive Relative Orbit Control

The control of satellite formations is efficiently performed by the activation of on-board thrusters. Typically, short burn durations applied at dedicated sparse locations along the orbit (i.e., impulsive control), is preferred to low thrust applications for an extended period of time (i.e., continuous control). This approach is not only justified because of the current limitations in propulsion technologies but also because of the typical payload requirements [Gill and Runge, 2004]. Indeed impulsive-feedback-control laws can be designed analytically, give the possibility to exploit the natural orbital dynamics to its full extent and can be easily adopted for a ground-in-the-loop scheme or for an autonomous implementation.

The Gauss' variational equations of motion offer the ideal mathematical framework for designing impulsive control laws [Battin, 1987], [Micheau, 1995]. These equations have been extensively used in the last decades for absolute orbit keeping of single spacecraft, but only recently are being exploited for formation flying control in LEO [Schaub and Alfried, 2001], [Vaddi et al., 2005]. The reason for such an evident delay is that the Gauss' variational equations provide relationships between the control acceleration and the time derivative of the orbital elements which were normally used to parameterize the motion of an individual satellite but not the relative motion of a formation. After the advent of the first characterizations of the relative motion in terms of relative orbital elements (cf. Section 1.4.1), many authors realized how natural and convenient was the adoption of the Gauss' variational equations for formation flying applications.

Mainly Alfried [Alfried et al., 2003], Schaub [Schaub and Alfried, 2001], Vadali [Vadali et al., 1999] and Vaddi [Vaddi et al., 2005] have addressed the problem of impulsive relative orbit control for formation establishment and reconfiguration, in presence of  $J_2$  Earth's oblateness effects and for  $J_2$  invariant formations. The works mentioned clearly demonstrate the high potential of impulsive orbit control for formation-flying applications but do not provide a realistic validation of the fundamental algorithms in terms of accuracy and robustness. The authors make use of pure software simulations in an ideal perturbation environment (e.g., neglecting differential drag). Issues like sensors, actuators and on-board implementation of the algorithms in real-time are ignored.

A few studies exist on formation keeping using impulsive orbit control which make use of Cartesian coordinates feedback laws instead of relative orbital elements [Middour, 1991], [Wiesel, 2003]. The control laws developed by Middour acquire and maintain the desired along-track separation through impulsive maneuvers in the along-track direction only [Middour, 1991]. Wiesel addressed the theory of optimal impulse control of relative satellite motion and solved numerically the resulting optimization problem [Wiesel, 2003]. In general the element feedback based control is typically applied in a pulse like man-



ner, the Cartesian coordinate feedback normally demands a continuous thrust. The reason for this is that the orbital elements errors are very slowly varying quantities if compared with the position and velocity vector errors. This is also the reason why it is more difficult to bring the thrust magnitudes within practical constraints when dealing with Cartesian position and velocity.

## 1.5 Contributions of This Research

This research presents the first realistic demonstration of a complete GNC system for formation flying spacecraft in LEO. Numerous technical contributions have been made during the course of this research in the areas of formation flying guidance [D'Amico and Montenbruck, 2006], [D'Amico et al., 2005], GPS-based relative navigation [D'Amico et al., 2006a], and impulsive relative orbit control [D'Amico et al., 2006b], but the primary contribution of this thesis does not lie in one or more of these disciplines. The innovation and originality of this work stems from the design and implementation of a comprehensive formation flying system through the successful integration of various techniques [Gill et al., 2007]. This research has led to the full development, testing and validation of the GNC flight code to be embedded in the on-board computer of the active spacecraft of the PRISMA technology demonstration [D'Amico et al., 2008]. Furthermore key guidance and control algorithms presented here are going to be demonstrated for the first time in the TerraSAR-X/TanDEM-X formation flying mission [Ardaens et al., 2007].

Overall this thesis focuses on realistic application cases closely related to upcoming formation flying missions. The intention is to realize a practical and reliable way to formation flying: a technology that is discussed and studied since decades but is still confined in research laboratories. Hardware-in-the-loop real-time simulations including a representative flight computer and the GPS hardware architecture show that simple techniques, which exploit the natural orbit motion to full extent, can meet the demanding requirements of long-term close formation flying. For completeness the following sections give a detailed summary of the relevant contributions of this research to the body of knowledge.

### 1.5.1 Formation Flying Guidance and Control

Although using the Hill frame coordinates is a common method to describe the satellites relative motion, they have the distinct disadvantage that for a general orbit the differential equations of motions must be solved to obtain the precise instantaneous geometry of the formation. Because of this fact, in this dissertation a description in terms of relative orbital elements has been preferred to the canonical Cartesian parameterization. In contrast to the fast varying position and velocity variables, the use of orbital element differences simplifies the formation-flying description and the satellite relative position computation.

Various sets of relative orbital elements have been proposed in the past decades in the frame of formation-flying dynamics and control, but actually the most intuitive, straightforward representation in terms of relative eccentricity and inclination vectors has never been investigated for formation-flying design in LEO. This research generalizes the method of eccentricity/inclination vector separation, first developed for the safe collocation of geostationary satellites, and extends its application to proximity operations of formation-flying spacecraft.

The spontaneous geometrical representation offers a direct correlation between the relevant characteristics of the bounded relative motion in near circular orbit and the magnitude/phase of the relative eccentricity/inclination vectors. This aspect extremely simplifies the design of safe, passively stable formation-flying configurations. In particular minimum collision risk conditions can be guaranteed by imposing the (anti-)parallelism of the eccentricity and inclination vectors of the respective satellites, while  $J_2$ -stable relative orbits are obtained by setting a specific nominal phase for the configuration.

The new approach is shown to be suitable either for the realization of SAR interferometers with baselines below 1 km or the application in longitude swap operations with along-track separations above 200 km [D'Amico and Montenbruck, 2006], [Montenbruck et al., 2006]. This dissertation addresses the first case where an active relative orbit control strategy is necessary, in order to compensate for the main disturbance forces represented by Earth's oblateness perturbations and differential aerodynamic drag. The proposed strategy is based on the eccentricity/inclination vectors control and makes use of pairs of pulses separated by half a revolution in velocity and anti-velocity directions. The method is very simple and can be used for a ground-in-the-loop control system as well as for an autonomous on-board implementation. The required velocity budget for formation-keeping can be expressed in terms of relative orbital elements and is directly proportional to the relative eccentricity offset. Furthermore the proposed two-impulse analytical solution is adopted to reconfigure the formation in a safe and fuel-efficient way.

### 1.5.2 GPS-based Relative Navigation

The results obtained so far by various authors demonstrate that CDGPS is an invaluable source of relative navigation in LEO. The use of space-borne GPS receivers hardware and true GPS signals in their hardware simulations marks a major progress on the way to acquire flight experiments. Nevertheless some limitations characterize the previous studies and, as a consequence, are addressed in this research. First of all the presented prototype navigation systems do not incorporate maneuvers, which will be crucial for use in orbital control and formation-keeping. Secondly the handling of the spacecraft attitude and the robustness of the filter to non-ideal non-zenith orientations of the GPS antennas are neglected. Last but not least contingency scenarios or delicate formation-flying operations phases like the Launch and Early Operations Phase (LEOP) or the safe separation of the spacecraft from a common combined con-

figuration are typically not addressed. The weakness of previously designed filters makes the strength of this development.

One of the main challenges of real formation flying is the realization of an on-board navigation system for all mission phases which is robust and accurate even for various spacecraft orientations and frequent thruster firing for orbit control. In contrast to earlier approaches that separate the GPS-based navigation into the independent reconstruction of absolute and relative states, a single reduced-dynamic Kalman filter for the absolute states of both spacecraft has been adopted in this thesis. Two different types of measurements are processed by the filter: undifferenced GRAPHIC measurements of the individual spacecraft as well as single-difference carrier-phase measurements.

GRAPHIC denotes an ionosphere-free linear combination of pseudo-range and carrier phase data. It enables an absolute orbit determination of each individual spacecraft with a representative accuracy of about 1–2 m, whenever a sufficient number of GPS satellites is tracked. The single-difference carrier phase measurements in contrast can only be formed for commonly observed GPS satellites but exhibit a much lower noise level of ca. 1–2 mm and thus provide the relative orbit with much higher accuracy. Both data types are subject to ambiguities related to the nature of carrier phase measurements. Channel specific ambiguities must therefore be estimated as part of the navigation filter. However, no effort is made to fix double-difference ambiguities to integer values. In view of residual modeling uncertainties (caused, for example, by the limited knowledge of the spacecraft attitude and antenna position) the benefits of ambiguity fixing cannot be materialized in a practical real-time navigation filter.

Overall, a total of 49 parameters are estimated in the navigation filter. These comprise the position/velocity vector, empirical accelerations, drag coefficient and clock offset as well as a total of 12 GRAPHIC bias parameters for each of the two spacecraft. In addition, the filter state is augmented by a 3-parameter delta-v vector to enable the estimation of impulsive velocity increments after maneuvers. The inherent robustness of the symmetric filter design originates from the fact that common GPS satellites visibility is not a prerequisite to reconstruct the relative state. Even in the case of spacecraft with completely different attitude, the relative state can be determined by simply differencing absolute estimates exclusively based on GRAPHIC data types [Gill et al., 2007].

As shown in this dissertation, the unified filter design simplifies the initialization and the maneuver handling procedures, and, consequently, improves the flexibility of the navigation system and its reliability during formation flying experiments. A Runge-Kutta fourth order integrator with Richardson extrapolation and Hermite interpolation allows the provision of continuous position and velocity data at a 1 Hz rate and gives the possibility to efficiently cover the GPS data gaps caused by the tumbling of the chief spacecraft during the early separation phase. Moreover the developed GPS system is able to incorporate orbit control maneuvers in the navigation process. This feature enables not only the absorption of the velocity variations imparted to the two spacecraft by

the separation mechanism but also their estimation via the Kalman filter state.

### 1.5.3 GNC System Integration and Validation

This dissertation addresses the testing and validation of the GPS-based flight software throughout the complete development process. The GNC system is first tested as a standalone unit in a dedicated software development environment at DLR and later validated after its full integration into the PRISMA spacecraft on-board computer. Thanks to a novel model-based software design, the GNC software can be implemented and executed on different platforms in a fully consistent manner. As explained later, this allows a seamless transition between off-line, real-time and hardware-in-the-loop tests during the validation phase.

In particular off-line simulations are first conducted in a Matlab/Simulink environment on a standard host PC. Here, the flight software is stimulated through different sources of GPS data with an increasing level of realism. Apart from the classical pure software simulations which make use of emulated GPS measurements, this research presents numerical results obtained from the use of real GPS flight data from the Gravity Recovery and Climate Experiment (GRACE) during the closest encounter of the twin satellites. As a next step, real-time hardware-in-the-loop integrated tests are conducted on the spacecraft flight models, comprising the Phoenix-S GPS receivers [Montenbruck and Markgraf, 2006] and a 2x12 channels Spirent GSS7700 GPS Signal Simulator (GSS) [SPIRENT, 2006]. In particular the complete application is ported to a Real-Time Executive for Multiprocessor Systems (RTEMS) environment in the LEON3-based PRISMA on-board computer [Gaisler, 2001] by means of Matlab/Simulink Real-Time-Workshop.

Overall the test and validation process shows the compliance of the navigation and control software to the challenging requirements of the PRISMA mission in terms of functionality, data interface, GNC accuracy, on-board memory and CPU load and paves the way for the successful launch and experiment operations of the PRISMA technology demonstration mission.

## 1.6 The PRISMA and TerraSAR-X/TanDEM-X Missions

A dedicated research and development program on autonomous spacecraft navigation and formation flying was initiated at the German Space Operations Center (GSOC) of DLR (German Aerospace Center) in 1998. Numerous contributions in the area of space-borne GPS receiver technology, precision relative navigation and autonomous orbit control of satellite formations as a prerequisite for spacecraft autonomy have been made. Practical experience in the operations of a two-satellite formation has been gained by the GRACE mission [Kirschner, 2003].

Next, GSOC is supporting the Swedish Space Cooperation (SSC) in the implementation of the PRISMA formation flying demonstration mission, where

a fully autonomous, robust and accurate formation flying of spacecraft will be conducted by several experiments [Persson et al., 2006]. Finally, the TerraSAR-X/TanDEM-X radar satellites will be Europe's first space mission equipped and operated routinely with an autonomous formation flying system [Ardaens et al., 2007].

Most of the work conducted in this research is motivated by and find practical application in the aforementioned projects. Therefore an overview of the PRISMA and TerraSAR-X/TanDEM-X missions is provided in the following.

### 1.6.1 PRISMA

The mission objectives of PRISMA may be divided into the validation of sensor and actuator technologies related to formation flying and the demonstration of experiments for formation flying and rendezvous. Key sensor and actuator components [Persson et al., 2005] comprise a GPS receiver system, two vision-based sensors (VBS), two formation flying radio frequency sensors (FFRF), and a hydrazine mono-propellant thruster system (THR). These will support and enable the demonstration of autonomous spacecraft formation flying, homing, and rendezvous scenarios, as well as close-range proximity operations.

The mission schedule foresees a launch of the two spacecraft in the first half of 2010. The spacecraft are named *Main* and *Target* and will be injected by a DNEPR-1 launcher into a sun-synchronous orbit at 700-km altitude and  $98.2^\circ$  inclination. A dusk-dawn orbit with a 6 or 18 h nominal local time at the ascending node (LTAN) is targeted. Maximum eclipse times of 23 minutes may occur for injections within  $\pm 1$  h off the nominal LTAN, depending on the sun's declination. Following a separation from the launcher, the two spacecraft will stay in a clamped configuration for initial system checkout and preliminary verification (cf. Fig. 1.2). Once the spacecraft are separated from each other, various experiment sets for formation flying and in-orbit servicing will be conducted within a minimum targeted mission lifetime of eight months.

Spacecraft operations will be performed remotely from Solna, near Stockholm, making use of the European Space and Sounding Rocket Range (Esrange) ground station in northern Sweden. The S-band groundspace link to *Main* supports commanding with a bit rate of 4 kbps and telemetry with up to 1 Mbps. In contrast, communication with the *Target* spacecraft is only provided through *Main* acting as a relay and making use of a *Main-Target* intersatellite link (ISL) in the ultrahigh-frequency (UHF) band with a data rate of 19.2 kbps.

The *Main* spacecraft has a wet mass of 150 kg and a size of  $80 \times 83 \times 130$  cm in launch configuration. In contrast to the highly maneuverable *Main* spacecraft, *Target* is a passive and much simpler spacecraft, with a mass of 40 kg at a size of  $80 \times 80 \times 31$  cm (cf. Fig. 1.2). Electrical power for the operation of the *Main* spacecraft bus and payload is provided by two deployable solar panels delivering a maximum of 300 W, whereas *Target* relies on one body-mounted solar panel providing a maximum of 90 W.

The *Main* spacecraft implements a three-axis, reaction-wheel based attitude control and three-axis delta-v capability. To this end, the *Main* GNC sensors

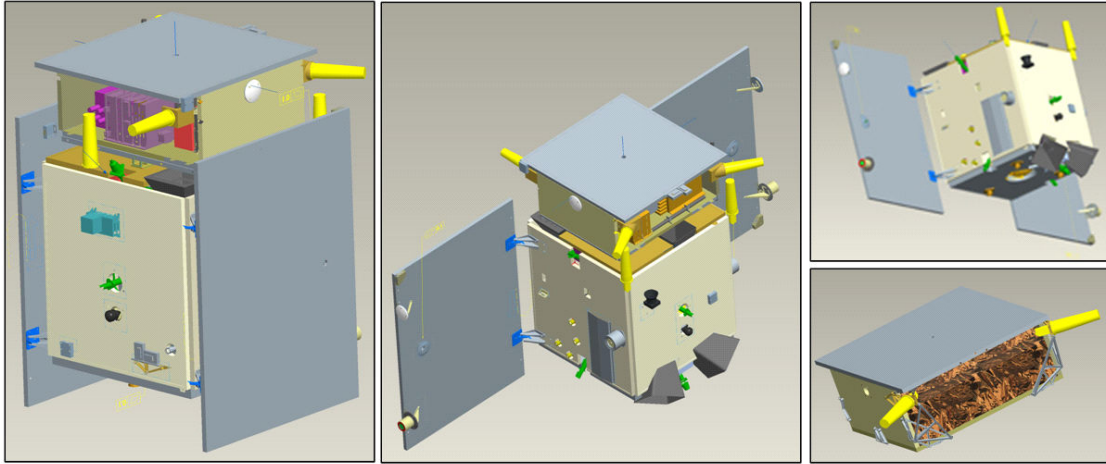


**Fig. 1.2:** Artist's impression of the PRISMA clamped configuration after launch (left), with the *Main* solar panels deployed (center), and the individual *Main* (right-top) and *Target* (right-bottom) spacecraft when separated. Courtesy of Swedish Space Corporation (SSC).

comprise two three-axis magnetometers (MM), one pyramid sun acquisition sensors and five sun-presence sensors (SS), five single-axis angular-rate sensors (GYR), five single-axis accelerometers (ACC), two star-tracker camera (SCA) heads for inertial pointing, two GPS receivers, two vision-based sensors (VBS) and two formation flying radio frequency sensors (FFRF). As actuators, three magnetic torque rods (MT), four reaction wheels (RW), and six thrusters are employed (THR).

The *Target* spacecraft applies a coarse three-axis attitude control based on magnetometers, sun sensors, and GPS receivers (similar to *Main*), with three magnetic torque rods as actuators. The nominal attitude profile for *Target* will be sun or zenith pointing.

For completeness the overall GNC sensors and actuators used for attitude and orbit control on *Main* and *Target* are listed in Table 1.3.

**Table 1.3:** *Main* and *Target* key sensors and actuators for attitude and orbit control.

PRISMA	GNC	<i>Main</i>	<i>Target</i>
Attitude	Sensors	MM,SS,GYR,ACC,SCA,GPS	MM,SS,GPS
	Actuators	MT,RW	MT
Orbit	Sensors	GPS,VBS,FFRF,ACC	-
	Actuators	THR	-

### 1.6.2 TerraSAR-X/TanDEM-X

TerraSAR-X (TSX) is an advanced SAR-satellite system for scientific and commercial applications, which is realized in a Public-Private Partnership (PPP)

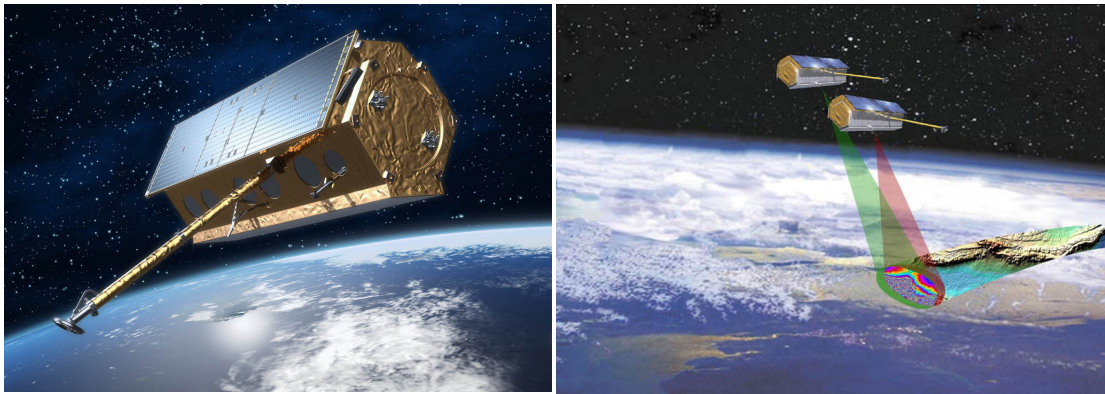


**Fig. 1.3:** Artist's impression of the TerraSAR-X spacecraft (left) and the TerraSAR-X/TanDEM-X formation (right). Courtesy of EADS Astrium GmbH.

between DLR and EADS Astrium GmbH. The satellite has a size of 5 m x 2.4 m, a mass of 1341 kg and carries a high-resolution SAR operating in the X-band (9.65 GHz). A Russian DNEPR-1 rocket launched from Baikonur, Kazakhstan, in mid 2007 has injected TerraSAR-X into a 514 km sun synchronous dusk-dawn orbit with  $97^\circ$  inclination and an 11 day repeat period. TerraSAR-X is planned to be operated for a period of 5 years and will therefore provide SAR-data on a long-term, operational basis. DLR/GSOC will provide the Mission Operations Segment (MOS) using ground stations at Weilheim and Neustrelitz. As a complement to TSX, the TanDEM-X (TDX) mission is under development in the frame of new Earth observation missions within the German national space program (cf. Fig. 1.3). It involves a second spacecraft, which is almost identical to TerraSAR-X and shall likewise be operated for 5 years with an expected launch date in the first half of 2010. The two spacecraft will fly in a precisely controlled formation to form a radar interferometer with typical baselines of 1 km.

TanDEM-X will be equipped with an Autonomous Formation Flying (TAFF) system developed at DLR/GSOC concurrent with this dissertation. This offers a unique chance to both enhance and intensify the knowledge and experience in the area of formation flying. Furthermore, the implementation of autonomous formation flying functionalities on the TDX spacecraft is considered to be a key driver for a more efficient use of the available on-board resources. The objective of TAFF is to enable a simple and robust formation control in order to ease on-ground operations. To achieve this goal dedicated functions for formation guidance, navigation and control will be implemented on-board TanDEM-X. Navigation will employ GPS data from the Mosaic GNSS receivers on-board TanDEM-X and TerraSAR-X. TSX GPS data will be provided through a dedicated S-Band ISL. Instead of raw code and phase measurements, TAFF will make use of the dynamically filtered GPS navigation solutions. These are differenced and then processed in a Kalman Filter employing a C-W dynamical model of the relative motion. The robustness of the formation control will be achieved by guidance and control functions which are based on the separation

of relative eccentricity and inclination vectors. This allows a robust formation configuration with minimum collision risk.

TerraSAR-X/TanDEM-X will furthermore be the first operational mission requiring a post-facto baseline reconstruction with an accuracy of 1 mm. The feasibility of achieving this goal using GPS dual-frequency measurements of the IGOR GPS receiver has earlier been demonstrated by the GRACE mission [Kroes et al., 2005]. The respective algorithms will further be refined and adapted to benefit from the small separation of the two spacecraft, which would even allow a single-frequency integer ambiguity resolution. Furthermore, the impact of phase pattern variations will be addressed through dedicated calibration campaigns of the antenna system.

## 1.7 Thesis Outline

This dissertation is structured in six chapters and its aim is to accompany the reader step by step through the ideation, design, implementation and validation of an innovative GNC system for formation flying spacecraft in LEO. After this introduction, the second chapter focuses on the relative orbit dynamics of spacecraft formations in near-circular low Earth orbits. In particular a novel linear relative motion model is derived based on the parameterization of the spacecraft motion in terms of relative eccentricity and inclination vectors. The linearized equations of motion are adopted to design a safe and fuel-efficient guidance and control strategy for formation flying spacecraft. Chapter 2 includes a preliminary numerical validation of the developed linear model and control schemes in the presence of second-order Earth's oblateness perturbations only.

The treatment in the second chapter assumes an ideal knowledge of the absolute and relative orbit available on-board in the computation of the feedback control law. The assumption of ideal navigation sensors is abandoned in the third chapter which is devoted to the problem of real-time autonomous GPS-based relative navigation of co-orbiting satellites. In particular Chapter 3 presents the design of a robust and accurate reduced-dynamic Kalman Filter for real-time absolute and relative navigation intended to serve the needs of the guidance and control functionalities. Several aspects of the navigation filter design are addressed, including the selection of the state parameters, the choice of the GPS observation types, the description of the applied dynamics and measurements models. Special attention is given to the incorporation of the maneuvers in the navigation process and to the robustness of the filter in presence of GPS data gaps and formation flying contingency scenarios. Finally the third chapter includes a numerical validation of the navigation process based on the adoption of a software based emulation of GPS receivers in LEO.

The guidance, navigation and control functions that have been addressed independently in Chapter 2 and 3 are implemented and integrated into a self-contained GNC system in the fourth chapter. After an overview of the software development environment based on Matlab/Simulink high level components



and C/C++ lower level modules, the overall GNC architecture is described, including data interfaces, data flows and processing schemes. In addition Chapter 4 discusses the embedding of the GNC software into a representative spacecraft on-board computer. The prototype flight software application is ported to a Real-Time Executive for Multiprocessor Systems (RTEMS) environment in a LEON3 microprocessor by means of Matlab/Simulink Real-Time-Workshop. Details are then provided on the usage of on-board resources in terms of computational load through dedicated max-path tests.

Chapter 5 is devoted to the so-called formation flying testbed adopted to ultimately verify the overall GNC system behavior and performances in typical scenarios characteristic of the PRISMA formation flying mission. The testbed consists of a 2x12 channels Spirent GSS7700 GPS Signal Simulator (GSS) which generates L1 GPS signals for two independent Phoenix-S GPS receivers to be flown on the PRISMA mission. Real-time hardware-in-the-loop simulations in open- and close-loop are presented together with a real-world assessment of the expected navigation and control performance.

Finally Chapter 6 provides a summary of the achieved results and concludes the dissertation with recommendations and open issues for future study.



## 2. Formation Flying Guidance and Control

### 2.1 Unperturbed Relative Motion

In this section a description of the relative motion of close spacecraft in near-circular orbits is obtained from an analytical treatment of the Keplerian equations of motion. The goal of the following development is to describe the relative motion in terms of orbital element differences and introduce the definitions of relative eccentricity and inclination vectors as a straightforward way to express the solution of the linearized equations of motion.

#### 2.1.1 Orbital Elements Parameterization

The formation under investigation is composed of a chief and a deputy satellite. The chief satellite is taken as the reference of the formation and is the spacecraft about which the deputy satellite is orbiting. Here the adopted denomination is completely arbitrary and does not imply any privileged or specific responsibility to the chief satellite with respect to the deputy. The parameterization of the absolute orbit of the spacecraft in the Earth-Centered-Inertial (ECI) reference frame is based on the following vector of orbital elements

$$\boldsymbol{\alpha} = \begin{pmatrix} a \\ u \\ e_x \\ e_y \\ i \\ \Omega \end{pmatrix} = \begin{pmatrix} a \\ \omega + M \\ e \cos \omega \\ e \sin \omega \\ i \\ \Omega \end{pmatrix}, \quad (2.1)$$

where the classical representation in Keplerian elements is modified by adopting the eccentricity vector  $\mathbf{e} = (e_x, e_y)^T$  and the mean argument of latitude  $u$  which are particularly suited to avoid singularities for near-circular orbits.

The relative motion of the deputy with respect to the chief satellite can be parameterized through an appropriate set of relative orbital elements which are obtained by the following non-linear combination of the absolute orbital elements defined in Eq. (2.1)

$$\delta\boldsymbol{\alpha} = \begin{pmatrix} \delta a \\ \delta\lambda \\ \delta e_x \\ \delta e_y \\ \delta i_x \\ \delta i_y \end{pmatrix} = \begin{pmatrix} (a_d - a)/a \\ (u_d - u) + (\Omega_d - \Omega) \cos i \\ e_{x_d} - e_x \\ e_{y_d} - e_y \\ i_d - i \\ (\Omega_d - \Omega) \sin i \end{pmatrix}. \quad (2.2)$$

Here the subscript  $d$  is introduced to denote quantities related to the deputy satellite and to distinguish them from the orbital elements of the chief spacecraft. The semi-major axis difference has been normalized through the chief semi-major axis to have dimensionless quantities.  $\delta\lambda$  denotes the relative mean longitude between the spacecraft. Apart from  $\delta a$  and  $\delta\lambda$ , the relative orbit representation defined by Eq. (2.2) is based on the relative eccentricity and inclination vectors for which the following Cartesian and polar notations are applied

$$\delta \mathbf{e} = \begin{pmatrix} \delta e_x \\ \delta e_y \end{pmatrix} = \delta e \begin{pmatrix} \cos \varphi \\ \sin \varphi \end{pmatrix} \quad , \quad (2.3)$$

$$\delta \mathbf{i} = \begin{pmatrix} \delta i_x \\ \delta i_y \end{pmatrix} = \delta i \begin{pmatrix} \cos \vartheta \\ \sin \vartheta \end{pmatrix} \quad . \quad (2.4)$$

The amplitudes (or lengths) of the relative e/i-vectors are denoted by  $\delta e$  and  $\delta i$  respectively and should not be confused with the arithmetic differences of eccentricity and inclination for which the  $\Delta(\cdot)$  operator is used. The phases of the relative e/i-vectors are termed relative perigee  $\varphi$  and relative ascending node  $\vartheta$  because they characterize the geometry of the relative orbit as seen by the chief spacecraft. In particular, as will be shown later,  $\varphi$  and  $\vartheta$  determine the angular locations of the perigee and ascending node of the relative orbit.

For a Keplerian two-body problem the absolute orbital elements defined in Eq. (2.1) are all invariants with the exception of the mean argument of latitude  $u$ , which increases at a constant rate given by

$$\dot{u} = \frac{du}{dt} = \sqrt{\frac{\mu}{a^3}} \quad , \quad (2.5)$$

where  $\mu$  denotes the Earth's gravitational parameter. Equivalently the relative orbital elements obtained in Eq. (2.2) are constants with the exception of the relative mean longitude  $\delta\lambda$ . When the chief and deputy orbits have unequal semi-major axes the drift of the relative mean argument of latitude can be derived to first-order by differencing Eq. (2.5) through

$$\Delta \dot{u} = \frac{d(\Delta u)}{dt} = -\frac{3}{2} \sqrt{\frac{\mu}{a^5}} \Delta a = -\frac{3}{2} n \frac{\Delta a}{a} \quad , \quad (2.6)$$

where  $n$  denotes the mean orbit motion. The only linearizing assumption made to derive Eq. (2.6) is that  $\Delta u$  and  $\Delta a$  are small quantities compared to the inertial chief orbit radius. No small eccentricity assumptions have been made. Under these circumstances the general linearized relative motion of the deputy satellite relative to the chief for arbitrary eccentricities in a Keplerian two-body problem is provided in terms of relative orbital elements by

$$\delta \alpha_j(t) = \delta \alpha_{j0} - \frac{3}{2} (u(t) - u_0) \delta \alpha_{10} \delta_j^2 \quad , \quad (2.7)$$

where  $j$  denotes the vector index ( $j = 1, \dots, 6$ ), the subscript 0 indicates quantities at the initial time  $t_0$  and  $\delta_j^i$  is the Kronecker delta.

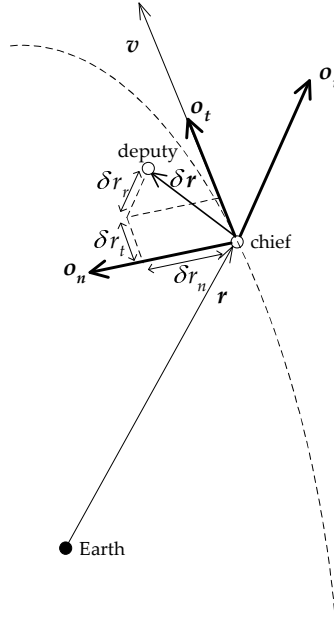


**Fig.2.1:** Relative state vector mapped into the orbital frame of the chief spacecraft

### 2.1.2 Cartesian Coordinates Parameterization

A common way to parameterize the absolute orbit motion of a spacecraft about a central body is to adopt the Cartesian coordinates state vector

$$\mathbf{x} = \begin{pmatrix} r_x \\ r_y \\ r_z \\ v_x \\ v_y \\ v_z \end{pmatrix}, \quad (2.8)$$

being  $\mathbf{r} = (r_x, r_y, r_z)^T$  the orbit position vector and  $\mathbf{v} = (v_x, v_y, v_z)^T$  the orbit velocity vector in the ECI frame. Similar to the orbital elements representation, the relative motion of two co-orbiting satellites can be described by a set of relative Cartesian coordinates obtained by the combination of the individual state vectors. To this end we introduce the Hill orbital frame [Hill, 1878] as a natural basis of measurements and scientific observations. Its origin is at the chief position and its orientation is given by the vector triad  $(\mathbf{o}_r, \mathbf{o}_t, \mathbf{o}_n)$  shown in Fig. 2.1. The unit vector  $\mathbf{o}_r$  is aligned with the radial direction (positive outwards), while  $\mathbf{o}_n$  is parallel to the chief angular momentum vector (positive in the orbit normal direction). The vector  $\mathbf{o}_t$  completes the right-handed coordinate system (positive in chief velocity direction). The relative motion of the deputy with

respect to the chief spacecraft can be expressed through Hill coordinates as

$$\delta \mathbf{x} = \begin{pmatrix} \delta r_r \\ \delta r_t \\ \delta r_n \\ \delta v_r \\ \delta v_t \\ \delta v_n \end{pmatrix} = \begin{pmatrix} \Delta \mathbf{r} \cdot \mathbf{o}_r \\ \Delta \mathbf{r} \cdot \mathbf{o}_t \\ \Delta \mathbf{r} \cdot \mathbf{o}_n \\ \Delta \mathbf{v} \cdot \mathbf{o}_r + \Delta \mathbf{r} \cdot \dot{\mathbf{o}}_r \\ \Delta \mathbf{v} \cdot \mathbf{o}_t + \Delta \mathbf{r} \cdot \dot{\mathbf{o}}_t \\ \Delta \mathbf{v} \cdot \mathbf{o}_n + \Delta \mathbf{r} \cdot \dot{\mathbf{o}}_n \end{pmatrix}. \quad (2.9)$$

In parallel with Section 2.1.1 the  $\Delta(\cdot)$  operator indicates arithmetic differences between absolute Cartesian parameters, while  $\delta(\cdot)$  refers to a non-linear combination of the formers. Under the assumptions of a Keplerian two-body motion, a circular chief orbit, and spacecraft separations which are small as compared to the chief orbit radius, the fundamental equations of dynamics can be linearized to obtain the familiar Clohessy-Wiltshire equations of relative motion [Clohessy and Wiltshire, 1960]. These equations have the following convenient homogeneous analytical solution for the relative position and velocity

$$\begin{aligned} \delta r_r &= a_1 & -a_3 \cos(nt) & -a_4 \sin(nt) \\ \delta r_t &= -\frac{3}{2}na_1t & a_2 & +2a_3 \sin(nt) & -2a_4 \cos(nt) \\ \delta r_n &= & +a_5 \sin(nt) & -a_6 \cos(nt) \\ \delta v_r &= & +na_3 \sin(nt) & -na_4 \cos(nt) \\ \delta v_t &= -\frac{3}{2}na_1 & +2na_3 \cos(nt) & +2na_4 \sin(nt) \\ \delta v_n &= & +na_5 \cos(nt) & +na_6 \sin(nt) \end{aligned} \quad (2.10)$$

For convenience the initial time has been chosen as the origin of the time scale, i.e.  $t_0 = 0$ . The integration constants  $a_j$  with  $j = 1, \dots, 6$ , are related to the components of the relative state vector at a generic time  $t$  by

$$\begin{aligned} a_1 &= 4\delta r_r & +2\delta v_t/n \\ a_2 &= 6nt\delta r_r + \delta r_t & -2\delta v_r/n + 3t\delta v_t \\ a_3 &= 3\delta r_r \cos(nt) & +\delta v_r \sin(nt)/n + 2\delta v_t \cos(nt)/n \\ a_4 &= 3\delta r_r \sin(nt) & -\delta v_r \cos(nt)/n + 2\delta v_t \sin(nt)/n \\ a_5 &= \delta r_n \sin(nt) & +\delta v_n \cos(nt)/n \\ a_6 &= -\delta r_n \cos(nt) & +\delta v_n \sin(nt)/n \end{aligned} \quad (2.11)$$

The advantage of expressing the integration constants at a generic time will be appreciated in the next sections. Note that if  $\delta r_r$  and  $\delta r_t$  are interpreted as curvilinear coordinates (instead of rectilinear), no changes of Eq. (2.10) are required and the linearization results can be applied to near-circular chief orbits with no loss of accuracy [Schaub and Junkins, 2003]. The general homogeneous analytical solution of the C-W equations can be written in phase/amplitude form using the trigonometric identities

$$A \sin t + B \cos t = \sqrt{A^2 + B^2} \cos(t - \arctan(A/B)) \quad , \quad (2.12)$$

this allows to rewrite Eq. (2.10) as

$$\begin{aligned}
 \delta r_r &= a_1 & -a_{34} \cos(nt - \phi) \\
 \delta r_t &= a_2 & -\frac{3}{2}na_1t & +2a_{34} \sin(nt - \phi) \\
 \delta r_n &= & +a_{56} \sin(nt - \theta) \\
 \delta v_r &= & +na_{34} \sin(nt - \phi) \\
 \delta v_t &= & -\frac{3}{2}na_1 & +2na_{34} \cos(nt - \phi) \\
 \delta v_n &= & +na_{56} \cos(nt - \theta) .
 \end{aligned} \tag{2.13}$$

The amplitudes of the in-plane and out-of-plane relative motion oscillations are  $a_{34} = \sqrt{a_3^2 + a_4^2}$  and  $a_{56} = \sqrt{a_5^2 + a_6^2}$  respectively. The phases of the harmonic in-plane and out-of-plane oscillations are  $\phi = \arctan(a_4/a_3)$  and  $\theta = \arctan(a_6/a_5)$  respectively.

### 2.1.3 Relative Orbital Elements as C-W Integration Constants

This section is intended to demonstrate that the relative orbital elements  $\delta\alpha = (\delta\alpha_j)$  with  $j = 1, \dots, 6$ , defined by Eq. (2.2) match the integration constants of the C-W equations  $\mathbf{a} = (a_j)$ , defined by Eq. (2.13) under the assumption of near-circular chief orbits and relative orbit radius small compared to the inertial orbit radius (i.e., all  $\delta\alpha$  components are small,  $\delta\alpha \ll 1$ , or  $\delta r/r \ll 1$ ). It is important to make two remarks on this assumption before continuing with the demonstration. First of all the assumption of small relative orbit radius with respect to the inertial orbit radius does not imply that  $\Delta M \ll 1$  or  $\Delta\omega \ll 1$ , but only that their sum  $\delta u \equiv \Delta u = \Delta M + \Delta\omega \ll 1$ . On the contrary all other classical orbit elements differences are small. Secondly the relative orbital elements have been introduced as dimensionless or angular quantities, while all C-W integration constants have the dimension of a length for rectilinear coordinates. Here the correspondence between these vectors refers to normalized quantities with respect to the semi-major axis of the chief orbit.

The direct mapping between Hill frame position coordinates and classical orbital element differences yields to first-order [DeVries, 1963], [Alfriend et al., 2000]

$$\begin{aligned}
 \delta r_r &\approx (r/a)\Delta a + (ae \sin \nu/\eta)\Delta M - a \cos \nu \Delta e \\
 \delta r_t &\approx (r/\eta^3)(1 + e \cos \nu)^2 \Delta M + r \Delta\omega + (r \sin \nu/\eta^2)(2 + e \cos \nu) \Delta e + r \Delta\Omega \cos i \\
 \delta r_n &\approx r(\sin(\nu + \omega) \Delta i - \cos(\nu + \omega) \Delta\Omega \sin i)
 \end{aligned} \tag{2.14}$$

with  $\Delta(\cdot)$  being the arithmetic difference operator,  $\nu$  the true anomaly and  $\eta = \sqrt{1 - e^2}$  an eccentricity factor. These equations are valid for arbitrary eccentricities and can be reduced to a convenient form under the additional assumption of near-circular chief orbits. In this special case, apart from  $\Delta M$  and  $\Delta\omega$ , both  $\Delta(\cdot)$ , and  $e$  are small quantities and terms obtained by the product or powers of these terms can be dropped. If we substitute  $\eta \approx 1$  and  $r \approx a(1 - e \cos \nu)$  in Eq. (2.14) and drop second-order terms, the following relations are obtained

$$\begin{aligned}
 \delta r_r &\approx \Delta a & -a \Delta e \cos \nu & +ae \Delta M \sin \nu \\
 \delta r_t &\approx a \Delta u + a \Delta\Omega \cos i & +2a \Delta e \sin \nu & +2ae \Delta M \cos \nu \\
 \delta r_n &\approx & +a \sin(\nu + \omega) \Delta i & -a \cos(\nu + \omega) \Delta\Omega \sin i
 \end{aligned} . \tag{2.15}$$

In order to conclude our demonstration we have to introduce the parameterization of the relative motion as described in Section 2.1.1. Under our assumptions the relative eccentricity vector can be expanded as follows

$$\begin{aligned}\delta e_x &= (\Delta e + e) \sin(\Delta\omega + \omega) - e \sin \omega \approx \Delta e \cos \omega - e \Delta\omega \sin \omega \\ \delta e_y &= (\Delta e + e) \cos(\Delta\omega + \omega) - e \cos \omega \approx \Delta e \sin \omega + e \Delta\omega \cos \omega\end{aligned}\quad , \quad (2.16)$$

furthermore it can be recognized from the harmonic expansion of the Kepler problem [Brouwer and Clemence, 1961], [Jarnagin, 1965] that the difference between true anomaly  $\nu$  and mean anomaly  $M$  is given by  $\nu - M \approx 2e \sin M$  for near-circular orbits. Based on these considerations, we can rearrange Eq. (2.15) to show explicitly the dependency of  $\delta r_r$  and  $\delta r_t$  on the relative eccentricity vector components as expressed by Eq. (2.16). Finally after substituting Eq. (2.16) in Eq. (2.15) we obtain

$$\begin{aligned}\delta r_r/a &\approx \delta a & -\delta e_x \cos u & -\delta e_y \sin u \\ \delta r_t/a &\approx -\frac{3}{2}\delta a u + \delta\lambda & +2\delta e_x \sin u & -2\delta e_y \cos u \\ \delta r_n/a &\approx & +\delta i_x \sin u & -\delta i_y \cos u\end{aligned}\quad . \quad (2.17)$$

It is important to note that use of Eq. (2.7) has been made to compute the relative along-track position  $\delta r_t$  in Eq. (2.17). In such a way we have been able to express the Hill frame coordinates as a linear function of the constant relative orbital elements at  $nt_0 = u_0 = 0$  with the mean argument of latitude as independent variable. The comparison between the general solution of the C-W equations in Eq. (2.10) and the first-order near-circular mapping between Hill coordinates and relative orbital elements in Eq. (2.17) demonstrates the equivalence between the C-W integration constants and the relative orbital elements as defined in Eq. (2.2). As shown in the next sections this correspondence paves the way to the design of straightforward guidance and control algorithms for formation-flying satellites in near-circular orbits. The interpretation of Eq. (2.11) in terms of relative orbital elements gives a useful tool to calculate the effects of impulsive velocity increments on the relative orbit. Furthermore the usage of relative orbital elements instead of position and velocity increases the accuracy of the C-W general solution. Indeed the relative eccentricity vector retains second-order terms in the eccentricity which are normally dropped using Hill coordinates as shown by Eq. (2.16).

## 2.2 Eccentricity/Inclination Vector Separation

### 2.2.1 Relative Eccentricity and Inclination Vectors

The general linear solution given by Eq. (2.17) provides the relative Cartesian state vector  $\delta \mathbf{x}$  at any mean argument of latitude  $u$  (i.e.,  $u$  is the independent variable) as a function of the relative orbital elements  $\delta \boldsymbol{\alpha}$  at epoch  $t_0$ . Although  $\delta a$  and  $\delta \lambda$  represent classical normalized Keplerian elements differences,  $\delta e$  and  $\delta i$  deserve further reflections. Making use of the polar representation of the



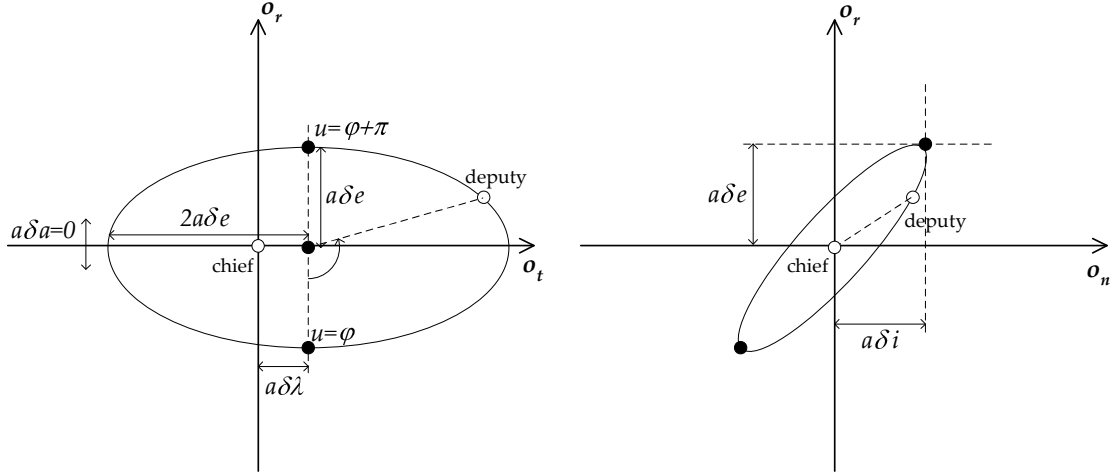


**Fig. 2.2:** Projections of relative motion in the along-track/radial (left) and cross-track/radial (right) directions for arbitrary relative orbital elements with  $a\delta a = 0$ .

relative e/i-vectors, Eq. (2.13) becomes

$$\begin{aligned}
 \delta r_r/a &= \delta a & -\delta e \cos(u - \varphi) \\
 \delta r_t/a &= \delta \lambda - \frac{3}{2}\delta a u & + 2\delta e \sin(u - \varphi) \\
 \delta r_n/a &= & + \delta i \sin(u - \vartheta) \\
 \delta v_r/v &= & + \delta e \sin(u - \varphi) \\
 \delta v_t/v &= -\frac{3}{2}\delta a & + 2\delta e \cos(u - \varphi) \\
 \delta v_n/v &= & + \delta i \cos(u - \vartheta) .
 \end{aligned} \tag{2.18}$$

Obviously the necessary conditions for bounded, centered relative motion of a deputy with respect to the chief spacecraft are given by

$$\begin{aligned}
 \delta a &= 0 \\
 \delta \lambda &= 0 \Leftrightarrow \Delta u = -\Delta \Omega \cos i .
 \end{aligned} \tag{2.19}$$

When these conditions apply, the relative orbit of the deputy with respect to chief spacecraft is an ellipse of semi-major axis  $2a\delta e$  in along-track direction and semi-minor axis  $a\delta e$  in radial direction (cf. Fig. 2.2). While  $\delta e$  measures the size of the relative trajectory, the angle  $\varphi$  defines the relative pericenter. Whenever the argument of latitude  $u$  equals  $\varphi$ , the deputy is located right below the center. As soon as  $u = \varphi + \pi/2$ , the deputy takes over and is just ahead of the chief satellite. In analogy with the preceding concepts, the relative inclination vector is used to describe the relative motion perpendicular to the orbital plane. The cross-track relative motion is described by a harmonic oscillation of amplitude  $a\delta i$  and phase angle  $u - \vartheta$ .

### 2.2.2 Collision Avoidance

The concept of e/i-vector separation has originally been developed for the safe collocation of geostationary satellites [Eckstein et al., 1989], but can likewise

be applied for proximity operations in LEO formations. It is based on the consideration that the uncertainty in predicting the along-track separation of two spacecraft is generally much higher than for the radial and cross-track component. Because of the coupling between semi-major axis and orbital period, small uncertainties in the initial position and velocity result in a corresponding drift error and thus a secularly growing along-track error. Predictions of the relative motion over extended periods of time are therefore particularly sensitive to both orbit determination errors and maneuver execution errors.

To avoid a collision hazard in the presence of along-track position uncertainties, care must be taken to properly separate the two spacecraft in radial and cross-track direction. As shown for GEO satellites, this can be achieved by a parallel (or anti-parallel) alignment of the relative eccentricity and inclination vectors. Even though these vectors are differently defined for near-equatorial, geostationary satellites, the convention adopted here ensures consistency with [Eckstein et al., 1989] and the same considerations are therefore applicable.

The relative distance between deputy and chief spacecraft, projected onto the cross-track/radial plane, is

$$\delta r_{nr} = (\delta r_n^2 + \delta r_r^2)^{1/2} \quad . \quad (2.20)$$

We can express this equation in terms of relative orbital elements by using Eq. (2.18)

$$\delta r_{nr}^2 = a^2(\delta a^2 + \delta e^2 \cos^2(u - \varphi) - 2\delta a\delta e \cos(u - \varphi) + \delta i^2 \sin^2(u - \vartheta)) \quad . \quad (2.21)$$

Offsets in semi-major axis of the individual satellites are impractical because they introduce divergent drifts in along-track direction. In the case of bounded relative motion (i.e.,  $\delta a = 0$ ), the minimum distance between deputy and chief spacecraft can be obtained from Eq. (2.21) as

$$\delta r_{nr}^{\min} = \frac{\sqrt{2}a |\delta e \cdot \delta i|}{(\delta e^2 + \delta i^2 + |\delta e + \delta i| \cdot |\delta e - \delta i|)^{1/2}} \quad . \quad (2.22)$$

This expression for the minimum distance shows that vector offsets in eccentricity and inclination between any co-orbiting spacecraft should be as large as possible and parallel (or anti-parallel) to each other. In particular parallel vectors  $\delta e$  and  $\delta i$  imply equality of the respective phase angles  $\varphi$  and  $\vartheta$ . As shown in Fig. 2.3,  $u = \varphi + k\pi$  with  $k$  integer (i.e.,  $k = 1, 2, \dots$ ) mark the positions at which the two spacecraft exhibit their maximum radial separation. Instead,  $u = \varphi + (k + \frac{1}{2})\pi$  are the points of vanishing radial separation. Considering that  $\varphi = \vartheta$  identifies the line of intersection of both orbital planes at which the cross-track separation vanishes, then  $\delta e \parallel \delta i$  ensures maximum  $\delta r_r$  when  $\delta r_n = 0$  and vice versa, maximum  $\delta r_n$  when  $\delta r_r = 0$ .

In contrast to this, the radial and cross-track separation can jointly vanish (i.e.,  $\delta r_r = \delta r_n = 0$ ) for orthogonal vectors  $\delta e \perp \delta i$ , which is risky in the presence of along-track position uncertainties (cf. Fig. 2.3). For (anti-)parallel

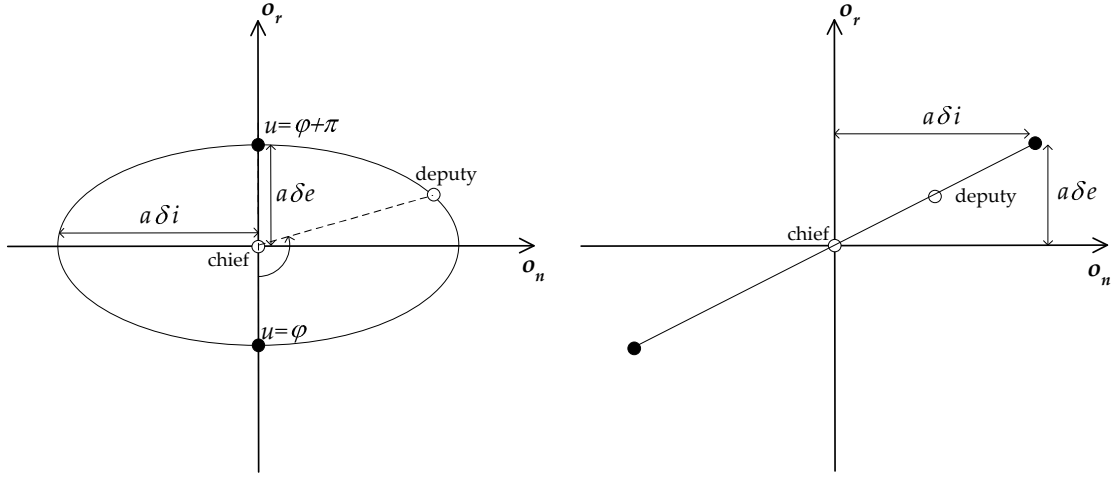


**Fig. 2.3:** Projection of relative motion in the cross-track/radial plane for parallel (left) and orthogonal (right) e/i-vectors.

relative e/i-vectors the inter-satellite distance is always ensured to be larger than

$$\delta r_{nr}^{\min}(u = \varphi, \varphi + k\pi) = a \min \{\delta e, \delta i\} \quad , \quad (2.23)$$

even in the case of a vanishing along-track separation. In the case of drifting satellites (i.e.,  $\delta a \neq 0$ ), the radial offset has to be accounted as well. In general, this can be compensated by a suitably increased eccentricity vector separation.

### 2.2.3 Collision-free Formation-flying Configurations

As outlined in the previous chapter typical payload requirements (e.g., SAR interferometry or gravimetry) of formation flying missions in LEO demand baselines as flexible as possible in terms of size and variability with time. As a consequence different formation-flying configurations (or constellations) have to be exploited during the mission lifetime to achieve the mission goals. A formation flying configuration is univocally identified by a specific set of relative orbital elements. Excluding temporarily  $\delta\lambda$  and  $\delta a$ , a formation-flying configuration is given by values for  $(\delta e_x, \delta e_y)$  and  $(\delta i_x, \delta i_y)$ , or in polar notation for  $(\delta e, \varphi)$  and  $(\delta i, \vartheta)$ . Ideally, scientific objectives would require no limitations on the size and phase of the relative e/i-vectors. Practically, collision avoidance issues and operational constraints impose restrictions on the domain of all possible formation-flying configurations. This section is intended to explore the formation-flying configurations space to identify safe and unsafe regions in terms of collision risk.

The risk of a collision between deputy and chief spacecraft has to be minimized. From an operational perspective, in case of small along-track separations (i.e., typically below 10 km), it is appropriate to adopt the distance between the two satellites projected onto the radial/cross-track plane (cf. Eq.

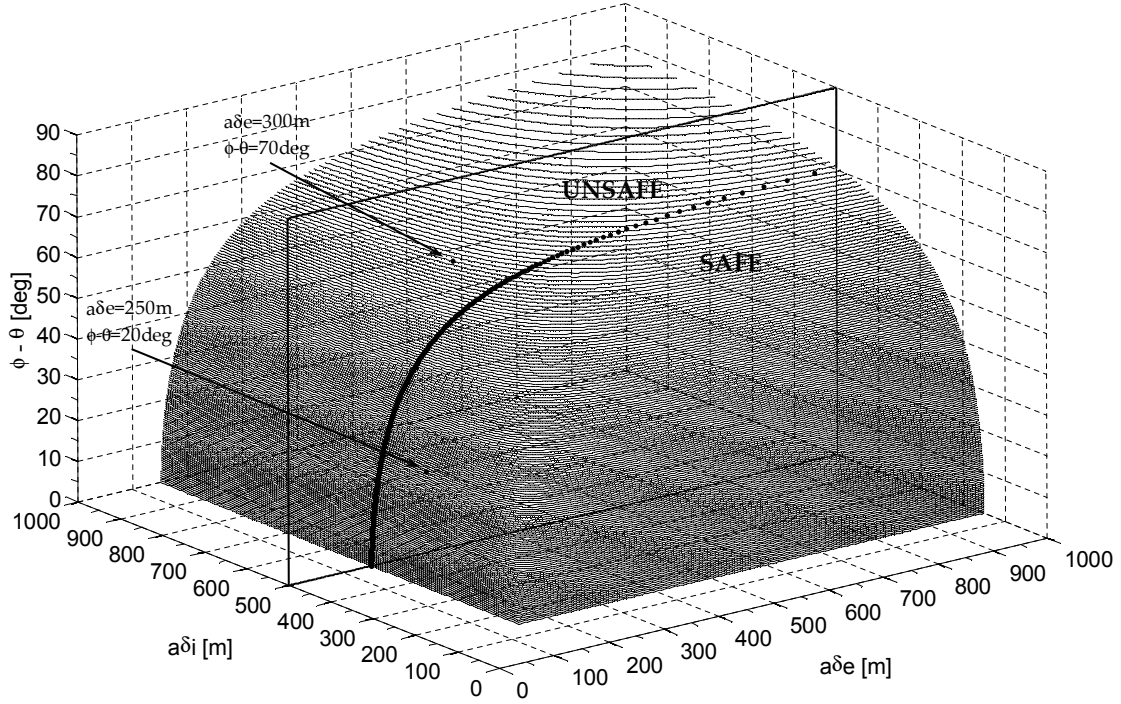


**Fig.2.4:** Safe and unsafe regions of the formation-flying configurations space. The shown 3D surface is formed by the triplets  $(a\delta e, a\delta i, \phi - \vartheta)$  that satisfy the equality  $\delta r_{nr}^{\min} = 150$  m. Constellation geometries that correspond to triplets on the surface and below the surface are collision-free. Geometries that correspond to triplets above the surface have a high collision risk. The condition  $a\delta i = 500$  m is visualized as the intersection of a plane with the boundary surface. The indicated triplet  $(300, 500, 70)$  is considered unsafe (cf. Eq. (2.24)). The triplet  $(250, 500, 20)$  is considered safe even if the average inter-spacecraft separation is smaller.

(2.20)) to define a measure of the collision risk level. This is mainly due to two interplaying aspects. First of all the relative motion in along-track direction is affected by the largest navigation errors, if compared with radial and cross-track, due to the uncertainties associated with the characteristics of the upper atmosphere (e.g., atmospheric density, solar activity, etc.). Second of all the spacecraft orbit dynamics in along-track direction are highly coupled due to the Kepler equations. Any orbit determination and prediction uncertainty, any attitude non-nominal motion like e.g. during safe modes as well as any maneuver execution errors and cross-coupling will cause a rapidly varying along-track motion with an offset which accumulates over time.

The impact hazard can be minimized if the minimum separation perpendicular to the flight direction is larger than a predefined minimum threshold  $d_{\min}$ . The safety limit  $d_{\min}$  is driven by practical considerations related to contingency scenarios and to uncertainties in the knowledge of the relative motion. For a SAR interferometry mission like e.g. TanDEM-X the minimum threshold is set to about 150 m, but it can be modified depending on the specific operational scenario. In this specific mission worst case conditions are given by the occurrence of long attitude safe mode phases or equivalently by the execution

of large tangential absolute orbit keeping maneuvers ( $\approx 6$  cm/s) involving only one of the co-orbiting spacecraft. Such events cause a differential variation of the semi-major axis ( $\approx 110$  m) and a pronounced drift of the relative mean argument of latitude ( $\approx 1040$  m per orbital revolution). In other terms the relative orbit ellipse in the plane perpendicular to the flight direction (cf. Fig. 2.2) is shifted by a constant offset in radial direction, while the relative along-track motion is affected by an accumulated offset growing with time. Especially during the first orbital revolution immediately after the contingency, the minimum separation perpendicular to the flight direction can be heavily reduced. These effects drive the selection of  $d_{\min}$  to guarantee safe conditions at all times. Alternatively one can consider mission phases where the along-track separation is very large ( $> 10$  km), then the minimum satellite distance perpendicular to the flight direction may be decreased to zero without risk.

By analyzing the minimum separation between two co-orbiting spacecraft as a function of the relative e/i-vectors, i.e. Eq. (2.22), it is possible to define rigorous limits for the domain of all the possible formation-flying configurations. The permitted and prohibited constellations can be defined by the following inequalities

$$\begin{aligned} \delta r_{nr}^{\min} &\geq d_{\min} &\Leftrightarrow &\text{SAFE} \\ \delta r_{nr}^{\min} &< d_{\min} &\Leftrightarrow &\text{UNSAFE} \end{aligned} \quad (2.24)$$

Using these relations in combination with Eq. (2.22), one can identify acceptable and unacceptable regions in the formation configurations space (i.e., the relative e/i-vector plane). An example of such a methodology is given by Fig. 2.4. If we analyze Eq. (2.22) more closely, one can deduce that the minimum separation perpendicular to the flight direction is in general a function of three parameters only: the e-vector magnitude  $\delta e$ , the i-vector magnitude  $\delta i$ , and the angle enclosed by the e/i-vectors  $\varphi - \vartheta$ . The minimum separation threshold  $d_{\min}$  can be set to a trade-off constant value (e.g.,  $d_{\min} = 150$  m in our case). As a consequence the function  $\delta r_{nr}^{\min}(\delta e, \delta i, \varphi - \vartheta) = d_{\min}$  can be easily visualized through contour 3D-lines of triplets  $(\delta e, \delta i, \varphi - \vartheta)$  which satisfy the equality in Eq. (2.24). The resulting 3D surface is visualized in Fig. 2.4 for  $d_{\min} = 150$  m and  $a = 6892945$  m which corresponds to the TerraSAR-X and TanDEM-X mean altitude of 514 km. This surface divides the formation-flying configurations space in two regions characterized by low and high collision risk with respect to the fixed  $d_{\min}$  threshold. Depending on the specific mission under consideration other constraints may come into play and restrict the domain of acceptable nominal relative motion geometries. Again Fig. 2.4 shows a typical case where the magnitude of the relative inclination vector is set to a constant value (e.g., 500 m in our case) due to baseline requirements in cross-track direction. The intersection between the plane defined by  $\delta i = 500$  m and the  $\delta r_{nr}^{\min} = d_{\min}$  surface is a 2D curve which discriminates safe from unsafe couples  $(\delta e, \varphi - \vartheta)$ . The example illustrated in Fig. 2.4 shows how shorter inter-spacecraft separations can be achieved with full safety by a proper angular separation of the relative e/i-vectors. In the specific case a relative e-vector magnitude of 300 m, which is unsafe with  $\varphi - \vartheta = 70^\circ$ , can be even reduced to 250 m if the angular separation

between the relative  $e/i$ -vectors drops to  $20^\circ$ .

## 2.3 Perturbed Relative Motion

The actual relative motion differs from the presented solution of the C-W equations for various reasons. While the relative acceleration due to a spherical Earth under the C-W assumptions is a linear function of the relative separation of the formation, the second-order terms neglected in C-W cause an acceleration which is quadratic in the spacecraft separation. This acceleration generates osculating deviations from the C-W solution that are cyclic in nature and do not cause unbounded relative orbit growth.

The deviation of the Earth's gravity field from radial symmetry causes additional perturbations which are of more interest for LEO formations. The most prominent contributions stem from the  $J_2$  gravity term which results from the Earth's flattening. This causes periodic and secular variations of the Keplerian orbital elements. For formation-flying satellites operating in close proximity, the short-periodic perturbations are essentially canceled, leaving long-periodic and secular changes of the relative orbital elements.

Finally, a satellite formation in LEO will be subject to differential forces caused mainly by aerodynamic drag. The resulting differential accelerations are predominantly due to differences in the ballistic coefficients and attitude motion of the spacecraft and may cause significant secular along-track deviations for high relative ballistic coefficients.

An overview of the mentioned dynamical contributions to the relative motion is provided in Fig. 2.5. Here, the relative acceleration is expressed as a function of representative spacecraft separations for formation flying missions in LEO. It is obvious that the C-W relative accelerations are by far dominating the relative motion. The perturbation by  $J_2$  is dominating higher order contributions to C-W up to separations of about 10 km. For LEO formations, the differential drag is typically two orders of magnitude smaller than contributions from  $J_2$ . The differential solar radiation pressure is in general negligible.

In general differential accelerations which cause long-periodic and secular drifts of the relative orbit need to be analyzed to evaluate the stability of the relative motion and investigate the necessity of an orbit control strategy. The following sections present an approximate solution of the equations of relative motion under the influence of  $J_2$  perturbations and differential drag. The straightforward development is made possible by the parameterization of the relative motion in terms of relative orbital elements.

### 2.3.1 Earth Oblateness $J_2$ Perturbation

The satellite orbits examined here are characterized by altitudes below 1500 km and are therefore particularly sensitive to perturbations because of the geopotential. In general these perturbations are related to the zonal, tesseral and

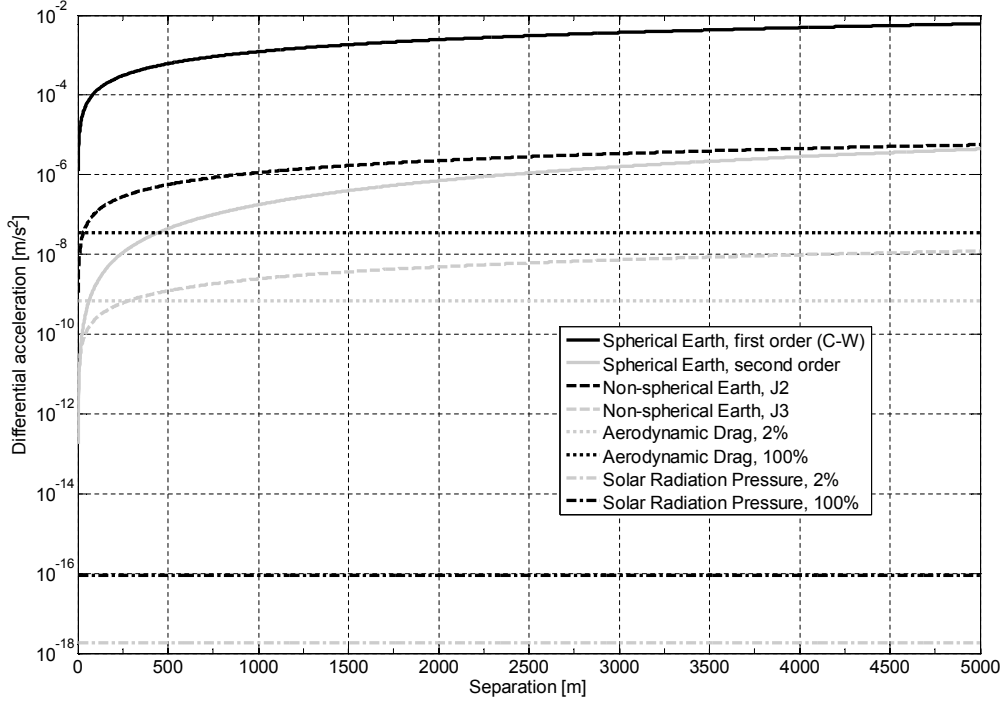


**Fig.2.5:** Magnitude of relative accelerations for close near-circular formations as a function of the spacecraft separation.

sectorial terms of the geo-potential, but the main effect is caused by the second-order zonal coefficient  $J_2$ . The Earth's equatorial bulge causes a regression of the line of nodes, a rotation of the line of apsides along with a change of the mean anomaly. In general the relative motion of formation-flying spacecraft is affected by short-periodic, long-periodic and secular perturbations of the relative orbital elements. This section extends the relative motion model described in the previous sections by considering  $J_2$  perturbations of the orbital elements differences. The analytical treatment is based on the theory developed by Brouwer [Brouwer, 1959] and Lyddane [Lyddane, 1963]. The modifications suggested by Lyddane provide a more robust algorithm for near-zero eccentricities and inclinations. Only first-order terms in  $J_2$  are retained throughout the discussion. Thus, small errors of the order of  $J_2^2$  and  $e \cdot J_2$  are to be expected on top of the quadratic terms related to spacecraft separation and eccentricity discussed in the previous section.

The secular variations of the relative orbital elements are easily obtained from the differentiation of the secular variations of the Keplerian orbital elements for each formation-flying satellite (i.e., chief and deputy spacecraft). In particular if  $R_E$  is the Earth's equatorial radius and

$$\gamma = \frac{J_2}{2} \left( \frac{R_E}{a} \right)^2 \frac{1}{\eta^4} \quad , \quad (2.25)$$

then the expression for the secular variations of the Keplerian elements is given

by [Brouwer, 1959]

$$\frac{d}{dt} \begin{pmatrix} a \\ e \\ i \\ \Omega \\ \omega \\ M \end{pmatrix} = \begin{pmatrix} 0 \\ 0 \\ 0 \\ -3\gamma n \cos i \\ \frac{3}{2}\gamma n(5 \cos^2 i - 1) \\ \frac{3}{2}\gamma n(3 \cos^2 i - 1) \end{pmatrix}. \quad (2.26)$$

We can substitute Eq. (2.26) into the definition of the relative orbital elements given by Eq. (2.2), set  $\eta \approx 1$ ,  $\eta_d \approx \eta$  and  $n_d \approx n$  for close near-circular orbits to obtain

$$\delta \dot{\alpha} = \begin{pmatrix} 0 \\ 12\gamma n(\cos^2 i_d - \cos^2 i - \frac{1}{4}(\cos i_d - \cos i) \cos i) \\ -\frac{3}{2}e\gamma n((5 \cos^2 i_d - 1) \sin \omega_d - (5 \cos^2 i - 1) \sin \omega) \\ \frac{3}{2}e\gamma n((5 \cos^2 i_d - 1) \cos \omega_d - (5 \cos^2 i - 1) \cos \omega) \\ 0 \\ -3\gamma n(\cos i_d - \cos i) \sin i \end{pmatrix}. \quad (2.27)$$

Finally, if we neglect second-order terms in the orbital element differences in line with the assumption of close spacecraft adopted so far, after some manipulations one obtains

$$\delta \dot{\alpha} = \begin{pmatrix} 0 \\ -\frac{21}{2}\gamma n \sin(2i) \delta i_x \\ -\frac{3}{2}\gamma n(5 \cos^2 i - 1) \delta e_y \\ \frac{3}{2}\gamma n(5 \cos^2 i - 1) \delta e_x \\ 0 \\ 3\gamma n \sin^2 i \delta i_x \end{pmatrix}, \quad (2.28)$$

which represents the secular variation of the relative orbital elements induced by  $J_2$  for close near-circular orbits. In order to extend the validity of our first-order relative motion model in the presence of  $J_2$  perturbations, we can integrate Eq. (2.28) over time. Using the mean argument of latitude as independent variable we obtain the following extension of Eq. (2.7) in the presence of  $J_2$

$$\delta \alpha(t) = \begin{pmatrix} \delta a \\ \delta \lambda - \frac{21}{2}(\gamma \sin(2i) \delta i_x + \frac{1}{7} \delta a)(u(t) - u_0) \\ \delta e \cos(\varphi + \varphi'(u(t) - u_0)) \\ \delta e \sin(\varphi + \varphi'(u(t) - u_0)) \\ \delta i_x \\ \delta i_y + 3\gamma \sin^2 i \delta i_x(u(t) - u_0) \end{pmatrix}, \quad (2.29)$$

where

$$\varphi' = \frac{d\varphi}{du} = \frac{3}{2}\gamma(5 \cos^2 i - 1) \quad (2.30)$$

is the derivative of the relative argument of perigee with respect to the mean argument of latitude.



The substitution of Eq. (2.29) into Eq. (2.18) provides a relative motion model which constitutes a first order approximation of the solution of the equations of relative motion in the presence of  $J_2$  perturbations. This is made possible by the fact that the short-period variations of the orbital elements are only a function of the mean argument of latitude and cancel out completely when computing the orbital elements differences for close formation flying satellites [Montenbruck et al., 2006].

These considerations will be verified at the end of this chapter by numerical integration. At this stage, it is interesting to notice that the relative orbital elements are no longer integration constants of the equations of motion. Apart from the semi-major axis difference and the inclination difference, all the relative orbital elements show a secular trend that is directly proportional to  $J_2$  and the elapsed time (i.e.,  $u(t) - u_0$ ).

### 2.3.2 Passively Stable Formation-Flying Configurations

Following the treatment of the previous section, the first-order solution of the equations of relative motion for close formation-flying spacecraft in near-circular chief orbits in the presence of  $J_2$  perturbations can be parameterized as

$$\begin{aligned} \delta r_r/a &= \delta a - \delta e \cos(u - \varphi - \varphi'(u - u_0)) \\ \delta r_t/a &= \delta \lambda - \frac{21}{2}(\gamma \sin(2i)\delta i_x + \frac{1}{7}\delta a)(u - u_0) + 2\delta e \sin(u - \varphi - \varphi'(u - u_0)) \\ \delta r_n/a &= \delta i_x(\sin u - 3\gamma \sin^2 i(u - u_0) \cos u) - \delta i_y \cos u \end{aligned} \quad (2.31)$$

The relative position is expressed as a function of the relative orbital elements at the initial time and the independent variable  $u$ . Due to the nature of the  $J_2$  effects on the relative e/i-vectors, we have retained in Eq. (2.31) a polar notation for  $\delta e$  but a Cartesian notation for  $\delta i$ .

In fact the relative eccentricity vector evolves along a circle of radius  $\delta e$  that is centered in the origin of the e-vector plane, with an angular velocity  $\varphi'$ . The period of the relative e-vector motion is roughly 1000 times larger than the orbital period. For sun-synchronous formations with orbital inclinations of 97–102° and associated altitudes of 500-1500 km, Eq. (2.30) yields a clockwise motion of  $\delta e$  with a period of roughly 100-200 days.

The relative inclination vector is likewise affected by  $J_2$  perturbations causing a secular shift of the orbital planes and thus a linear drift of  $\delta i_y$ . The secular motion of the relative e/i-vectors caused by the Earth oblateness is illustrated in Fig. 2.6. An initial configuration will ultimately be destroyed unless correction maneuvers are performed to compensate for the natural drift of both vectors.

It can be recognized from Eqs. (2.29)–(2.31) that the absolute inclination of the formation-flying spacecraft should be identical (i.e.,  $\Delta i = 0$ ) to avoid a secular motion of the relative inclination vector. In this case, a separation of the two orbital planes by an angle  $\delta i$  is achieved through a small offset in the right ascensions of their ascending nodes  $\Delta \Omega = \pm \delta i / \sin i$ . The resulting relative inclination vector has a phase angle  $\vartheta = \pm \pi/2$ , and the same (or opposite phase) must be selected for the relative eccentricity vector to obtain a safe formation.

Adding the necessary conditions for bounded, centered relative motion of the deputy with respect to the chief spacecraft (cf. Eq 2.19) one obtains the following convenient nominal configuration

$$\delta\alpha_{\text{nom}} = \begin{pmatrix} \delta a \\ \delta\lambda \\ \delta e_x \\ \delta e_y \\ \delta i_x \\ \delta i_y \end{pmatrix} = \begin{pmatrix} 0 \\ 0 \\ 0 \\ \pm\delta e_{\text{nom}} \\ 0 \\ \pm\delta i_{\text{nom}} \end{pmatrix} . \quad (2.32)$$

Such a choice for the nominal configuration provides a sort of passive stability to the formation because the secular Earth oblateness perturbations have minimum impact on the relative motion. The two orbital planes intersect near the poles (i.e.,  $u = \pm\pi/2$ ), and the spacecraft achieve the largest cross-track separation at the equator, and vice versa the radial separation vanishes at the equator crossing and is maximized near the poles. This provides the typical helix-shaped formation-flying configuration introduced by Moreira et al. [2004] for advanced SAR applications.

Note that the absence of an inclination difference between the spacecraft orbits eliminates the secular variation of  $\delta\lambda$  and  $\delta i_y$ , leaving only a perturbation of the relative eccentricity vector. No secular effects induced by  $J_2$  would be present in case of co-orbiting formation flying satellites in polar orbits (i.e.,  $i_d = i = 90^\circ$ ).

Considering both safety and imaging constraints, the typical requirements for a SAR interferometry mission can be fulfilled by a formation with parallel relative e/i-vectors (cf. Eq. (2.32)) or in general by small angles enclosed by the e/i-vectors. The interferometric technique is based on the stereoscopic effect that is induced by matching two SAR images obtained from two slightly different orbital positions. Whereas a differencing of SAR images obtained from two antennas separated in cross-track direction basically yields measurements of terrain elevations and therefore permits the derivation of digital elevation models (DEM), an adequate along-track separation provides measurements of the velocity of on-ground objects (e.g., for traffic monitoring, ocean currents, and glacier monitoring).

Apart from the trivial initial conditions given by Eq. (2.19), closed relative orbits around an oblate Earth are given to first-order by

$$\gamma \sin(2i) \overbrace{\Delta i}^{\delta i_x} + \frac{1}{7} \overbrace{\Delta a/a}^{\delta a} = 0 . \quad (2.33)$$

This equation can be solved for combinations of  $\gamma$  (or  $a$ ) and  $i$  (i.e., chief orbit selection) given the desired difference in inclination and semi-major axis or vice versa for combinations of  $\delta i_x$  and  $\delta a$  (i.e., relative orbit selection) given the chief orbit. For near-circular sun-synchronous formations with orbital inclinations of  $97\text{--}102^\circ$  and associated altitudes of 500-1500 km, Eq. (2.33) yields  $\Delta a \approx 1000\Delta i$ . In general, in the presence of  $J_2$ , closed and centered relative orbits are only

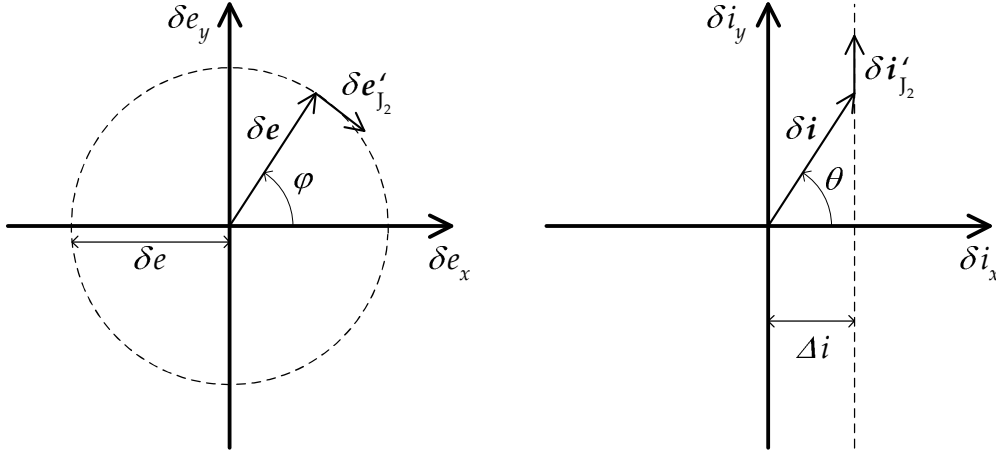


**Fig. 2.6:** Secular evolution of the relative eccentricity (left) and inclination vectors (right).

achievable via relative orbit control in the case of  $i_d \neq i \neq k\pi/2$ , with  $k = 0, 1, 2$  for near-circular chief orbits.

### 2.3.3 Differential Drag

The interaction of the upper atmosphere with the satellite's surface produces the dominant disturbance for LEO spacecraft after differential gravity. The main force caused by the impact of atmospheric molecules on the spacecraft surface is predominantly anti-parallel to the velocity of the spacecraft relative to the incident stream and is named aerodynamic drag. The along-track satellite acceleration

$$|\ddot{r}_t| = \frac{1}{2} \rho v^2 C_D \frac{A}{m} \quad (2.34)$$

caused by drag is determined by the atmospheric density  $\rho$ , the spacecraft velocity with respect to the atmosphere  $v$ , and the ballistic coefficient (i.e., the effective area-to-mass ratio)

$$B = C_D \frac{A}{m} \quad (2.35)$$

Here,  $A$  is the satellite cross-section area,  $m$  is the satellite mass, and  $C_D$  is the aerodynamic drag coefficient. As a preliminary approximation, density variations over distances of less than a few kilometers can be neglected. Thus, the relative along-track acceleration for two formation-flying spacecraft is driven by the differences in their ballistic coefficients  $\Delta B = (B_d - B)$ . This causes an accumulated along-track offset

$$\delta r_t = \frac{1}{2} a \Delta \ddot{u} (t - t_0)^2 = \frac{3}{4n^2} \Delta B \rho v^2 (u(t) - u_0)^2 \quad (2.36)$$

over a time interval  $(t - t_0)$ , which has to be compensated to maintain the nominal formation-flying configuration. Our first-order relative motion model can be extended to incorporate differential drag by adding Eq. (2.36) to the along-track component of Eq. (2.31). The relative semi-major axis is linked to the

derivative of the relative mean argument of latitude through Eq. (2.6). Thus in addition to the quadratic trend of the along-track separation, one has to take into account a linear drift of the radial separation given by

$$\delta r_r = \Delta \dot{a}(t - t_0) = -\frac{2}{3n} a \Delta \ddot{u}(t - t_0) = -\frac{1}{n^2} \Delta B \rho v^2 (u(t) - u_0) \quad . \quad (2.37)$$

The impact of differential drag may be minimized using identical design for the participating satellites. In such a way the ballistic coefficients can be matched to roughly 1% at launch [Kirschner, 2003]. Assuming that mass variations during the mission lifetime can contribute an additional estimated difference of 1%, a differential ballistic coefficient  $\delta B = \Delta B/B = 2\%$  can be adopted for a realistic operational scenario. According to the Harris Priester model [Montenbruck and Gill, 2001a] the atmospheric density at a representative altitude of 500 km amounts to  $1 \text{ g/km}^3$  for mean solar flux conditions. At a ballistic coefficient  $B = 0.006 \text{ m}^2/\text{kg}$  and an orbital velocity  $v = 7.6 \text{ km/s}$ , Eq. (2.34) yields a differential acceleration of about  $3.5 \text{ nm/s}^2$  while Eq. (2.36) yields an along-track offset of 16 cm within one orbital revolution and a 38-m offset after one day. The required maneuver delta-v to compensate these effects is of the order of  $3.5 \text{ mm/s}$  in  $10^6 \text{ s}$  or 11.5 days. Even though these values might increase by a factor of 10 during high solar activities and geomagnetic storms, differential drag has evidently modest impact on the formation control during nominal operations even for LEO orbits.

On the other hand, this conclusion is no longer valid if one of the spacecraft enters a safe mode with uncontrolled yaw angle or the co-orbiting spacecraft are of different type and build. Depending on the specific geometry, the effective cross-section might increase and thus cause large differential drag accelerations of several hundred  $\text{nm/s}^2$ . When lasting over extended periods of time, a safe mode can thus cause notable change in along-track separation [Feucht et al., 2003]. However, given the fact that no science data can be collected in safe mode and considering the collision protection provided by the e/i-vector separation, the undesired changes of the relative orbit is considered non-critical from a mission operations point of view. The nominal formation configuration can be restored by a series of corrective maneuvers performed either autonomously or with ground intervention after the end of the safe mode.

### 2.3.4 Numerical Validation of Analytical Relative Motion Model

In this section the proposed first-order analytical solution is compared with a numerical integration of the nonlinear differential equations of motion including only  $J_2$  effects. The following simulations verify that the relative motion approximation in Eq. (2.31) do predict the spacecraft formation geometry to the specified accuracy. The numerical integration is performed using the variable-order, multi-step method of Shampine and Gordon [Shampine and Gordon, 1975], and spans one day at an orbital altitude of approximately 700 km.

The initial orbital elements of the chief satellite have been chosen to provide a representative reference for formation flying missions in LEO. A dusk-dawn

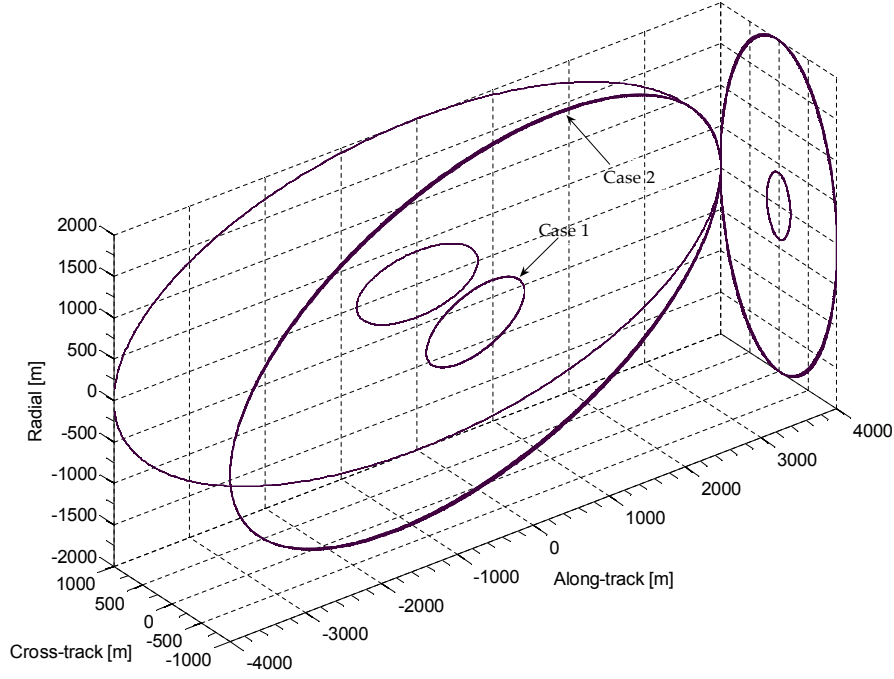


**Fig.2.7:** Relative motion of the deputy spacecraft mapped in the Hill's orbital frame centered on the chief spacecraft. The relative orbit is projected onto the radial/along-track and radial/cross-track planes. The two test cases are indicated in the figure.

sun-synchronous orbit with about  $98.2^\circ$  inclination, 18 h nominal local time at the ascending node (LTAN) and 0.001 eccentricity is considered in the scenario. The initial conditions for the deputy spacecraft are derived from the chief orbit by adding the desired set of relative orbital elements. The selected nominal configuration corresponds to a bounded, centered geometry with parallel  $e/i$ -vectors, as prescribed by Eq. (2.32). For completeness the initial chief orbital elements and the initial relative orbital elements are listed in Table 2.1.

**Table 2.1:** Initial chief orbital elements and initial relative orbital elements for two test cases (cf. superscripts 1 and 2 for first and second case).

Orbit elements	Value	Relative orbit elements	Value
$a$ [m]	7078135.0	$a\delta a$ [m]	0
$u$ [ $^\circ$ ]	0.0	$a\delta\lambda$ [m]	0
$e_x$ [-]	0.001	$a\delta e_x$ [m]	0
$e_y$ [-]	0.0	$a\delta e_y$ [m]	$400^1$ or $2000^2$
$i$ [ $^\circ$ ]	98.19	$a\delta i_x$ [m]	0
$\Omega$ [ $^\circ$ ]	189.89086	$a\delta i_y$ [m]	$200^1$ or $1000^2$

In order to appreciate the dependency of the model's accuracy on the spacecraft separation, two different cases are considered. Fig. 2.7 depicts the 3D relative motion geometry in the Hill frame centered on the chief spacecraft for the two test cases. The length of the relative eccentricity and inclination vectors

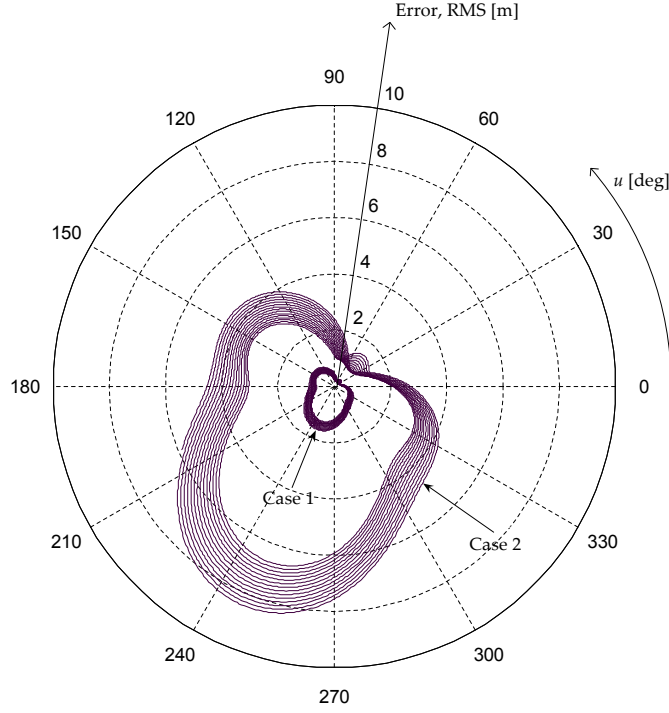


**Fig. 2.8:** RMS relative position error as a function of the mean argument of latitude for two test cases.

in the second case are five times larger than in the first case. Note that the selected relative orbit is characterized by a ratio  $\delta r/r$  below 0.0003. The chosen eccentricity and the value of  $J_2$  itself are one order of magnitude larger. As a consequence the adopted validation scenario can be considered fairly conservative with respect to the range of validity of our relative motion model which assumes  $e$  and  $J_2$  small and of the same order of  $\delta r/r$ .

The relative motion model accuracy is computed by subtracting the approximate relative position provided by Eq. (2.31) from the true relative position computed through the numerical integration at 10 second intervals. The Root-Mean-Square (RMS) of the error is plotted in Fig. 2.8 versus the mean argument of latitude using polar coordinates. The modeling error has a periodic pattern that matches the orbital period. As expected the relative position error increases with the separation between the spacecraft. In particular the maximum RMS error increases by roughly the same factor as the spacecraft separation. As expected the error budget is dominated by quadratic terms in  $e$ ,  $J_2$  and their products with  $\delta r/r$  which are larger than the dropped second-order terms in the spacecraft separation for these two test cases. In general the order of magnitude of the resulting orbit errors indicates that an analytical orbit control law based on this linear solution can not be more accurate than a few meters.

## 2.4 Relative Orbit Control

A relative orbit control system is necessary either to maintain the nominal formation geometry over the mission lifetime (i.e., station-keeping or maintenance) or to acquire new formation geometries to realize certain specific objectives (i.e., acquisition or reconfiguration). The control of satellite formations is efficiently performed by the activation of appropriate on-board thrusters. Continuous firing is often not desirable for space missions in LEO because it collides with the science objectives and has to be coupled with attitude maneuvering. Furthermore the required continuous thrust levels are too low for their efficient implementation with current propulsion system technologies. In this section an impulsive control scheme is proposed based on the aforementioned first-order relative motion model. The analytical treatment seeks for a minimum number of thruster activations along the orbit and for a minimum expenditure of propellant consumption (measured through a delta-v budget). The resulting feedback control law is simple and fully deterministic. These characteristics, in combination with its inherent optimality, renders the proposed scheme especially suitable for an embedded on-board implementation. Furthermore traditional tasks like mission planning and operations, challenged by a formation flying scenario, can take advantage of the reliable a-priori knowledge of maneuver location and size offered by the proposed control strategy.

### 2.4.1 Gauss' Variational Equations

We consider an operational scenario with two formation-flying spacecraft in near-circular low Earth orbits. While the chief satellite is passive from a relative orbit control point of view, the deputy is performing orbit correction maneuvers. The proposed linearized relative motion model offers an ideal mathematical tool to process orbit maneuvers. In particular we make use of the inverse solution of the C-W equations expressed in terms of relative orbital elements as given by Eq. (2.11). If we set  $\delta r_r = \delta r_t = \delta r_n = 0$  in Eq. (2.11), then the solution of the C-W equations describes the relative motion of a deputy spacecraft which is initially located at the same position of the chief spacecraft but with a different velocity. In other words the inversion of our linear relative motion model provides the direct relation between an instantaneous velocity increment in the Hill's orbital frame and the consequent change of the orbital elements as the following system of equations

$$\begin{aligned}
 a\delta a &\approx & +2\delta v_t/n \\
 a\delta \lambda &\approx & -2\delta v_r/n & -3(u - u_M)\delta v_t/n \\
 a\delta e_x &\approx & +\delta v_r \sin u_M/n & +2\delta v_t \cos u_M/n \\
 a\delta e_y &\approx & -\delta v_r \cos u_M/n & +2\delta v_t \sin u_M/n \\
 a\delta i_x &\approx & & +\delta v_n \cos u_M/n \\
 a\delta i_y &\approx & & +\delta v_n \sin u_M/n \quad ,
 \end{aligned} \tag{2.38}$$

commonly known as the Gauss' variational equations [Micheau, 1995] adapted to near-circular non-equatorial orbits. Here the parameterization in terms of rel-

ative orbital elements introduced in the previous section has been adopted. The left hand terms  $\delta\alpha_i$  ( $i = 1, \dots, 6$ ) correspond to the variations of the relative orbital elements induced by the instantaneous velocity changes  $\delta v_r$ ,  $\delta v_t$  and  $\delta v_n$ , respectively in radial, along-track and cross-track directions (i.e., in the Hill's orbital frame). It is noted that the term  $3(u - u_M)\delta v_t/n$  appears in Eqs. (2.38) and Eqs. (2.11) with the same magnitude but opposite sign. This is due to the fact that the provided solution of the C-W equations describe the relationship between Cartesian relative coordinates at time  $t$  and relative orbital elements at the initial time  $t_0$  (i.e., integration constant  $a_2 = a\delta\lambda(t_0)$ ), while the Gauss' variational equations provide the mapping between a velocity increment at time  $t_0$  and the relative orbital elements at a later time  $t$  (i.e.,  $a\delta\lambda(t)$ ). Eqs. (2.38) show that for a given thrust, located at a specific mean argument of latitude  $u_M$ , instantaneous variations of the actual relative orbital elements are generated, as well as a net change of mean longitude  $a\delta\lambda$  within the time interval between the maneuver execution and the epoch of the relative orbital elements. As expected the control problem is fully decoupled with respect to in-plane and out-of-plane. Whereas a thrust in cross-track direction affects only the relative inclination vector, a thrust in the orbital plane (i.e., along-track and radial directions) influences the relative eccentricity vector, the relative semi-major axis and the relative longitude. Note that this result is made possible by the specific choice of  $\delta\lambda = \Delta u + \Delta\Omega \cos i$  as relative orbital element. In fact a thrust in cross-track direction generates a variation of the mean argument of latitude given by  $-\Delta\Omega \cos i$  which balances the equal and opposite term contained in the definition of the relative longitude.

In the following development we assume that the deputy spacecraft has 3D maneuvering capability, like e.g. in the PRISMA mission. One of the available thrusters can always be aligned with the desired  $\delta v$  direction. The Fuel Consumption (FC) is then proportional to the magnitude of the impulsive velocity variation (i.e.,  $FC \propto \|\delta v\| = \delta v$ ). Anyhow particular solutions are provided in the typical case where maneuvers are constrained to certain directions because of spacecraft bus limitations (e.g., thrusters accommodation, attitude constraints, etc. like in the TanDEM-X mission).

As a first step we will address the problem of how to achieve predefined instantaneous variations of the relative orbital elements (i.e., the strict control problem) using a minimum number of pulses. As a second step the problem of how to select the desired variations of the relative orbital elements is addressed (i.e., the guidance problem) for formation maintenance and reconfiguration. In contrast to similar developments available in literature, the following treatment is general, includes disturbance forces like  $J_2$  and differential drag, includes considerations on operational constraints and provides an estimate of the delta-v budget as a function of the required control accuracy.

### 2.4.2 In-plane Relative Orbit Control

#### Single-impulse solution

In this case we have a total of three unknowns  $\delta v_t$ ,  $\delta v_r$  and  $u_M$  for the single



pulse and four equations (cf. (2.38)) which govern the in-plane control problem. For the moment we decide to use only the three relationships for  $\delta a$  and  $\delta e$ , and consequently let  $\delta \lambda$  free to evolve under the influence of the orbit dynamics and the single computed maneuver. In practice  $\delta a$  and  $\delta \lambda$  are tightly linked through the Kepler equations when a differential mean motion exists. Thus we can always control  $\delta \lambda$  over a desired orbital period by a proper selection of  $\delta a$ .

Provided that only  $\delta a$  and  $\delta e$  are prescribed and  $|\delta a| \leq \delta e$ , the in-plane Gauss' variational equations can be solved to obtain the following single maneuver solution

$$\begin{aligned} \delta v_t &= \frac{n}{2} a \delta a \\ \delta v_r &= n a \sqrt{\delta e^2 - \delta a^2} \\ u_M &= \arctan(\delta v_r / 2 \delta v_t) - \xi \end{aligned} \quad , \quad (2.39)$$

with

$$\xi = \arctan(\delta e_y / \delta e_x) \quad . \quad (2.40)$$

Here the solution is conveniently expressed as a function of the known desired variations of the relative orbital elements. In the special case where no variation of semi-major axis is desired (i.e.,  $\delta a = 0$ ) the solution reduces to the simple expression

$$\begin{aligned} \delta v_t &= 0 \\ \delta v_r &= n a \delta e \\ u_M &= -\arctan(\delta e_x / \delta e_y) \end{aligned} \quad . \quad (2.41)$$

The single impulse solution given by Eq. (2.39) is of particular relevance in scenarios where a complete reconfiguration of the formation has to be performed in a short time interval. A typical application could be for example the case where two spacecraft initially clamped in a single combined unit (e.g., after separation from the launcher) need to be separated and achieve a first collision-free constellation in a timely manner. The one-impulse control scheme is able to establish a parallel relative e/i-vector configuration, to guarantee minimum collision risk and avoid the evaporation of the formation. Still the formation needs to be located at a mean argument of latitude  $u_M$  along the orbit which depends on the desired correction of the relative orbital elements. The single-impulse control scheme has the side effect of generating a variation of the mean longitude  $\delta \lambda$ . In general this effect should be taken into account when selecting the desired  $\delta a$  in the computation of the maneuver.

#### Double-impulse solution

In this case we have a total of six unknowns  $\delta v_{t_i}$ ,  $\delta v_{r_i}$  and  $u_{M_i}$  ( $i = 1, 2$ ), for the first ( $i = 1$ ) and second ( $i = 2$ ) pulse, and the four equations (cf. (2.38)) which govern the in-plane control problem. Being only four equations available, we decide to compute the four unknowns  $\delta v_{t_i}$  and  $\delta v_{r_i}$  as a function of the desired orbit element variations and the remaining unknowns  $u_{M_i}$ . After some algebraic and trigonometric manipulation of Eq. (2.38), the general double maneuver solution can be expressed as a function of the mean argument of latitude of the first pulse  $u_{M_1}$  and the angular shift between the second and the

first pulse locations  $\Delta u_M = u_{M_2} - u_{M_1}$  as follows

$$\begin{aligned} \delta v_{t_1} &= \frac{na}{4} [\delta a + \delta e \cos(u_{M_1} - \xi)] & -\frac{na}{4} \chi \left[ \frac{\delta \lambda}{2} + \delta e \sin(u_{M_1} - \xi) \right] \\ \delta v_{r_1} &= \frac{na}{2} \left[ -\frac{\delta \lambda}{2} + \delta e \sin(u_{M_1} - \xi) \right] & -\frac{na}{2} \chi [\delta a - \delta e \cos(u_{M_1} - \xi)] \\ \delta v_{t_2} &= \frac{na}{4} [\delta a - \delta e \cos(u_{M_1} - \xi)] & +\frac{na}{4} \chi \left[ \frac{\delta \lambda}{2} + \delta e \sin(u_{M_1} - \xi) \right] \\ \delta v_{r_2} &= \frac{na}{2} \left[ -\frac{\delta \lambda}{2} - \delta e \sin(u_{M_1} - \xi) \right] & +\frac{na}{2} \chi [\delta a - \delta e \cos(u_{M_1} - \xi)] \end{aligned} \quad (2.42)$$

with

$$\chi = \frac{\sin(\Delta u_M)}{\cos(\Delta u_M) - 1} \quad (2.43)$$

The proposed solution is only valid for  $u_{M_2} - u_{M_1} \in ]0, 2\pi[$  and has an interesting structure. In fact the size of the individual velocity variations in along-track and radial directions is given by a left term which is only a function of the first maneuver location  $u_{M_1}$ , plus a right term that depends on both the location of the first and second maneuvers  $u_{M_1}$  and  $\Delta u_M$ . Convenient maneuver locations can be found through the minimization of the fuel consumption (i.e., the total delta-v cost). It should be noted that this control scheme does not take into account the drift of the relative orbital elements which occurs in the time frame between the two maneuvers due to the orbit dynamics. In particular the individual pulses in along-track direction will cause a variation of semi-major axis  $\delta a$  and thus a drift of  $\delta \lambda$ . These effects must be taken into account when selecting the desired  $\delta a$ ,  $\delta \lambda$  and  $\delta e$  in the computation of the maneuvers.

#### In-plane Maneuver Cost

The cost of the single-impulse solution given by Eq. (2.39) can be expressed as

$$\delta v_I = \|\delta \mathbf{v}\| = \sqrt{\delta v_t^2 + \delta v_r^2} = na \sqrt{\delta e^2 - \frac{3}{4} \delta a^2} \quad (2.44)$$

and is only a function of the desired relative orbit elements corrections. Note that Eq. (2.39) requires  $|\delta a| \leq \delta e$ , thus the in-plane maneuver cost is always larger than  $\delta v_t$ .

The cost of the double-impulse solution can be expressed as

$$\delta v_{II} = \|\delta \mathbf{v}_1\| + \|\delta \mathbf{v}_2\| = \|\delta \mathbf{v}_1(u_{M_1}) - \delta \mathbf{v}(u_{M_1}, \chi)\| + \|\delta \mathbf{v}_2(u_{M_1}) + \delta \mathbf{v}(u_{M_1}, \chi)\| \quad (2.45)$$

where we have separated the delta-v contribution that is only a function of the first maneuver location  $\delta \mathbf{v}_i(u_{M_1})$  ( $i = 1, 2$ ), from the delta-v contribution which also depends on the location of the second maneuver  $\delta \mathbf{v}(u_{M_1}, \chi)$ . The propellant consumption is thus a function of the location of the maneuvers along the orbit (i.e.,  $u_{M_1}$  and  $u_{M_2}$  or equivalently  $u_{M_1}$  and  $\chi$ ) which are still unknowns of our problem.

In the typical case of bounded relative motion, where no variations of semi-major axis (i.e.,  $\delta a = 0$ ) and relative longitude (i.e.,  $\delta \lambda = 0$ ) are desired, the in-plane maneuver cost can be further reduced to the form

$$\delta v_{II}^2 = 4\delta v_1(u_{M_1})^2 + 4\delta v(u_{M_1}, \chi)^2 - 8\delta \mathbf{v}_1(u_{M_1}) \cdot \delta \mathbf{v}(u_{M_1}, \chi) \quad (2.46)$$

We can search for convenient fuel-efficient maneuver locations by minimizing Eq. (2.46) with respect to  $u_{M_1}$  and  $\chi$ . In particular the selected maneuver locations have to satisfy the following conditions

$$\min_{\chi, u_{M_1}} \delta v_{II} \Leftrightarrow \begin{cases} \frac{\partial \delta v_{II}^2}{\partial \chi} = 0, & \frac{\partial^2 \delta v_{II}^2}{\partial \chi^2} > 0 \\ \frac{\partial \delta v_{II}^2}{\partial u_{M_1}} = 0, & \frac{\partial^2 \delta v_{II}^2}{\partial u_{M_1}^2} > 0 \end{cases} \quad (2.47)$$

The conditions on the first and second derivatives of the cost function with respect to the location of the second maneuver are identically satisfied by

$$\chi = \bar{\chi} = \frac{\sin[2(u_{M_1} - \xi)]}{2[\sin(u_{M_1} - \xi)^2 - \frac{4}{3}]} \quad (2.48)$$

$\chi$  is now only a function of the location of the first maneuver and can be substituted in Eq. (2.47) to compute the following expression for the cost function's first derivative with respect to  $u_{M_1}$

$$\left[ \frac{\partial \delta v_{II}^2}{\partial u_{M_1}} \right]_{\chi=\bar{\chi}} = \frac{4}{3} n^2 a^2 \delta e^2 \frac{\sin[2(u_{M_1} - \xi)]}{4[\sin(u_{M_1} - \xi)^2 - \frac{4}{3}]^2} = \frac{\frac{2}{3} n^2 a^2 \delta e^2 \bar{\chi}}{\sin(u_{M_1} - \xi)^2 - \frac{4}{3}} \quad (2.49)$$

Obviously the maneuver cost function's minima belong to the solutions of the following system of equations

$$\chi = \bar{\chi} = 0 \Leftrightarrow \begin{cases} \Delta u_M = \pi & \text{cf. Eq. (2.43)} \\ u_{M_1} - \xi = 0, \frac{\pi}{2}, \pi, \frac{3}{2}\pi, 2\pi & \text{cf. Eq. (2.48)} \end{cases} \quad (2.50)$$

The second derivative of the cost function is always positive when evaluated at these maneuver locations. In order to find the absolute minimum among the local minima we substitute directly Eq. (2.50) into our double-impulse solution given by Eq. (2.42). The minimum delta-v solutions are given by

$$\begin{aligned} \delta v_{t_1} &= -\delta v_{t_2} = \frac{na}{4} \delta e, & -\frac{na}{4} \delta e \\ \delta v_{r_1} &= -\delta v_{r_2} = 0, & 0 \\ u_{M_1} &= u_{M_2} - \pi = \xi, & \xi + \pi \end{aligned} \quad (2.51)$$

which represent couples of along-track maneuvers separated by half an orbital revolution in flight and anti-flight direction. The two maneuvers have the same magnitude, opposite versus and guarantee a homogeneous distribution of the control action along the orbit and among different spacecraft at the following total delta-v cost

$$\delta v_{II} = |\delta v_1| + |\delta v_2| = na\delta e/2 \quad (2.52)$$

Note that due to the double efficiency of pulses in along-track direction, the delta-v cost induced by the double-impulse scheme is half the cost of the single-impulse scheme (i.e.,  $\delta v_{II} = 0.5\delta v_I$ ) which adopts maneuvers in radial direction.

### 2.4.3 Out-of-plane Relative Orbit Control

#### Single-impulse solution

In this case we have a total of two unknowns  $\delta v_n$  and  $u_M$  and the two equations (cf. (2.38)) governing the out-of-plane control problem. The straightforward solution is given by

$$\begin{aligned} \delta v_n &= na\delta i \\ u_M &= \arctan(\delta i_y / \delta i_x) \end{aligned} \quad , \quad (2.53)$$

or equivalently

$$\begin{aligned} \delta v_n &= -na\delta i \\ u_M &= \arctan(\delta i_y / \delta i_x) + \pi \end{aligned} \quad . \quad (2.54)$$

#### Double-impulse solution

Even if one pulse is sufficient to control the relative inclination vector, operational constraints may induce the splitting of the out-of-plane maneuver in two components. In this case the two pulses are located at  $u_M$  and  $u_M + \pi$  and are given by

$$\begin{aligned} \delta v_{n_1} &= pna\delta i \\ \delta v_{n_2} &= (1 - p)na\delta i \end{aligned} \quad , \quad (2.55)$$

where  $p \in [0, 1]$ .

#### Out-of-plane Maneuver Cost

The choice of  $p$  does not influence the total propellant consumption in the addressed scenario because  $FC \propto |\delta v_{n_1}| + |\delta v_{n_2}| = |\delta v_n|$  for all choices of  $p$ . Anyhow  $p = 0.5$  provides a homogeneous distribution of maneuvers along the orbit and/or among different spacecraft and can ultimately decrease the total propellant consumption of the formation. The cost of the out-of-plane solution can be expressed as

$$\delta v = |\delta v_n| = na\delta i \quad . \quad (2.56)$$

### 2.4.4 Formation Maintenance

#### Relative Eccentricity and Inclination Vectors

At this stage we know how to obtain predefined corrections of the relative orbital elements through dedicated impulsive maneuvers. This section addresses the problem of how to efficiently compute the desired variations of the orbital elements for formation maintenance. The goal of the relative orbit control system is to plan and execute correction maneuvers to ensure conformance with predefined nominal relative orbital elements  $\delta \alpha_i^{\text{nom}}, i = 1, \dots, 6$  (cf. Section 2.3.2). The aim is to maintain the actual orbital differences  $\delta \alpha_i$  confined within symmetric control windows centered on the nominal values

$$|\delta \alpha_i - \delta \alpha_i^{\text{nom}}| \leq \delta \alpha_i^{\text{max}} \quad . \quad (2.57)$$

As explained in Section 2.3 the relative eccentricity and inclination vectors are mainly affected by the Earth's oblateness perturbations. The former is characterized by a circular motion in the e-vector plane, the latter by a linear drift

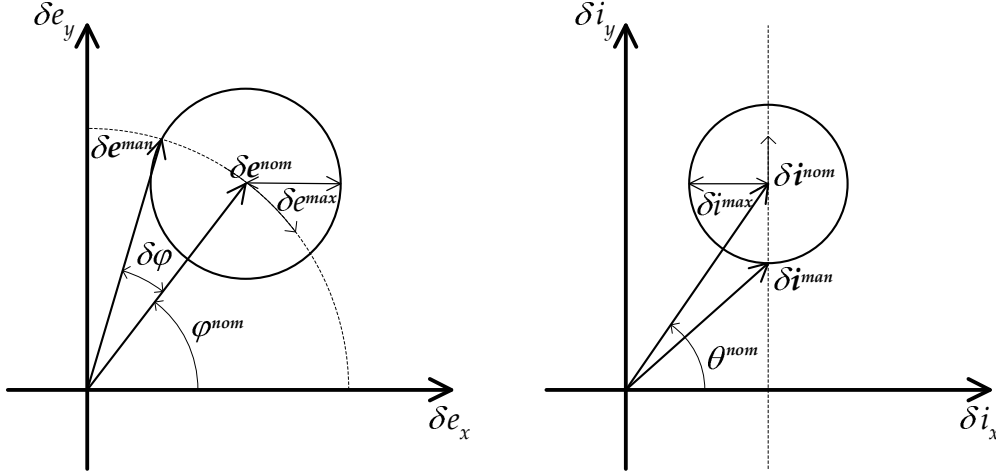


**Fig. 2.9:** Graphical representation of the control windows for the relative eccentricity vector (left) and the relative inclination vector (right). Refer to Fig. 2.6 for the visualization of the secular evolution of the two vectors subject to orbital perturbations. The superscript *nom* stands for nominal configuration, *max* for maximum allowed deviation from nominal, and *man* for quantities to be achieved after the execution of maneuvers.

proportional to the inclination difference. We can take advantage of this natural secular motion and define convenient control windows for the relative *e/i*-vectors as depicted in Fig. 2.9.

When the magnitudes of the relative *e/i*-vector tracking errors,  $\|\delta e - \delta e^{\text{nom}}\|$  and  $\|\delta i - \delta i^{\text{nom}}\|$ , exceed the respective maximum allowed deviations,  $\delta e^{\text{max}}$  and  $\delta i^{\text{max}}$ , the control scheme solves the Gauss' variational equations for the velocity increments and the location of the maneuvers along the orbit. The computed velocity increments will transfer the relative orbital elements to the opposite limit of the circular control window. The relative eccentricity vector desired after the execution of the in-plane maneuver(s) is given by

$$\delta e^{\text{man}} = \mathbf{R}_z(\delta\varphi)\delta e^{\text{nom}} = \begin{pmatrix} \delta e_x^{\text{nom}} \cos(\delta\varphi) - \delta e_y^{\text{nom}} \sin(\delta\varphi) \\ \delta e_x^{\text{nom}} \sin(\delta\varphi) + \delta e_y^{\text{nom}} \cos(\delta\varphi) \end{pmatrix}, \quad (2.58)$$

where  $\delta\varphi$  is the maximum allowed deviation of the relative perigee from its nominal value

$$\delta\varphi \approx \text{sign}(\varphi') \arcsin(\delta e^{\text{max}}/\delta e^{\text{nom}}), \quad (2.59)$$

and  $\mathbf{R}_z(\delta\varphi)$  represents the elementary rotation matrix around the *z*-axis (normal to the *e*-vector plane). Similarly the relative inclination vector desired after the execution of the out-of-plane maneuver(s) is given by

$$\delta i^{\text{man}} = \begin{pmatrix} \delta i_x^{\text{nom}} \\ \delta i_y^{\text{nom}} - \text{sign}(\delta i_x)\delta i^{\text{max}} \end{pmatrix}. \quad (2.60)$$

For a matter of generality we have introduced the signs of  $\varphi'$  and  $\delta i_x = \Delta i$  (cf. Eqs. (2.29) and (2.30)) in the expressions of  $\delta e^{\text{man}}$  and  $\delta i^{\text{man}}$ . This renders the formulas valid in the case of anti-clockwise motion of the relative eccentricity vector as well as negative inclination difference. Note that given the

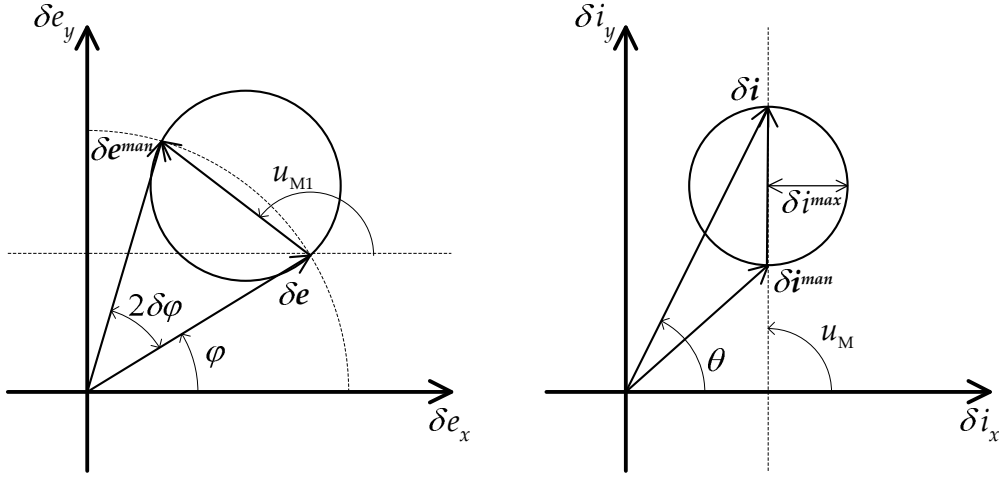


**Fig. 2.10:** Graphical representation of in-plane (left) and out-of-plane (right) maneuver locations and their relationship to the control windows for the relative eccentricity vector (left) and the relative inclination vector (right).

desired amplitude of the control windows and the absolute reference orbit in terms of eccentricity and inclination, Eqs. (2.58) and (2.60) can be used to determine uniquely the desired relative e/i-vectors after each orbit control maneuver. These are constants until a new nominal configuration or new control windows are prescribed.

The relationships given by Eqs. (2.58) and (2.60) are accurate for a one-impulse control scheme. In the case that a two impulse-scheme is adopted to correct the relative e/i-vectors, one may consider to slightly modify these expressions to take into account the drift of  $\delta e$  and  $\delta i$  which occurs in the time frame between the two pulses. The idea is to define the desired  $\delta e^{man}$  and  $\delta i^{man}$  after the pair of maneuvers so that they are shifted with respect to the border of the control window by the expected drift caused by  $J_2$  between the maneuvers. This is easily obtained through the substitution in Eqs. (2.58) and (2.60) of the following adapted expression for the maximum allowed deviation of the relative perigee

$$\delta\varphi \approx \text{sign}(\varphi') \arcsin(\delta e^{\max}/\delta e^{\text{nom}}) + \varphi' \Delta u_M \quad , \quad (2.61)$$

and for the size of the relative inclination vector control window

$$\delta i^{\max} = \delta i^{\max} + |3\gamma\delta i_x \Delta u_M \sin^2 i| \quad . \quad (2.62)$$

The guidance strategy given by Eqs. (2.58)–(2.62) ensures that the time between consecutive corrections of the relative e/i-vectors (i.e., the maneuver cycle) is maximized and represents as a consequence a fuel-efficient approach for formation maintenance. Depending on the desired control window, or equivalently on the required orbit control accuracy, along-track and cross-track maneuvers (in the form of single or double-pulses) are executed at regular time intervals in a deterministic fashion. As shown in the previous section the minimum delta-v cost is given by pairs of along-track maneuvers separated by half

an orbital revolution (i.e.,  $\Delta u_M = \pi$ ) and executed in (anti-)flight direction at the locations  $u_{M_1} = \xi$  and  $u_{M_2} = \xi + \pi$ . By substituting these values in Eq. (2.42), the size and location of the individual maneuvers can be expressed as follows

$$\begin{aligned}\delta v_{t_1} &= \frac{na}{4} [(\delta a^{\text{man}} - \delta a) + \|\delta \mathbf{e}^{\text{man}} - \delta \mathbf{e}\|] \\ \delta v_{t_2} &= \frac{na}{4} [(\delta a^{\text{man}} - \delta a) - \|\delta \mathbf{e}^{\text{man}} - \delta \mathbf{e}\|] \\ u_{M_1} &= \arctan [(\delta e_y^{\text{man}} - \delta e_y)/(\delta e_x^{\text{man}} - \delta e_x)]\end{aligned}\quad (2.63)$$

Here the corrections of the relative eccentricity vector and semi-major axis have been expressed as the difference between their desired values after the two maneuvers,  $\delta e^{\text{man}}$  and  $\delta a^{\text{man}}$ , and their actual values right before the execution of the first maneuver,  $\delta e$  and  $\delta a$ .  $\delta e^{\text{man}}$  can be computed using Eqs. (2.58)–(2.62),  $\delta a^{\text{man}}$  is discussed in the following section.

One cross-track maneuver is necessary and sufficient to control the out-of-plane relative motion and is given by

$$\begin{aligned}\delta v_n &= na \|\delta \mathbf{i}^{\text{man}} - \delta \mathbf{i}\| \\ u_M &= \arctan [(\delta i_y^{\text{man}} - \delta i_y)/(\delta i_x^{\text{man}} - \delta i_x)]\end{aligned}\quad (2.64)$$

Note that once the nominal formation configuration and the size of the desired control window are fixed by design, the locations of the along-track and cross-track maneuvers are also known and constant during the mission. As shown in Fig. 2.10 the first along-track maneuver and the cross-track maneuver are located at a mean argument of latitude that matches the phase of the relative e/i-vector corrections. This characteristic of the control law is of extreme relevance when designing a formation of spacecraft with the aim of minimum complexity and operational effort.

#### Relative Semi-major Axis and Mean Argument of Latitude

The relative semi-major axis  $\delta a$  and the relative mean argument of latitude  $\delta u$  have not been discussed so far in the guidance strategy. These parameters govern the relative motion in along-track direction and are influenced by differential gravity and differential drag. As discussed in the previous section the semi-major axis is only affected by drag and is characterized by a linear drift proportional to the differential ballistic coefficient under the assumption of constant atmospheric density, cf. Eq. (2.37). The relative mean argument of latitude shows instead a linear drift proportional to  $J_2$ , in the presence of inclination differences (cf. (2.29)) and a quadratic accumulated offset proportional to the differential ballistic coefficient, cf. Eq. (2.36).

The compensation of these effects can be conveniently coupled with the correction of the relative eccentricity vector using the double-impulse solution presented in the previous section, cf. Eq. (2.63). We can take advantage of the tight link between  $\delta a$  and  $\delta u$  given by the Kepler equation (2.6) and determine a desired relative semi-major axis to be established after the along-track maneuvers

$$\delta a^{\text{man}} = -\frac{2}{3} \frac{\delta u^{\text{tot}}}{n \Delta t - \pi} \quad (2.65)$$

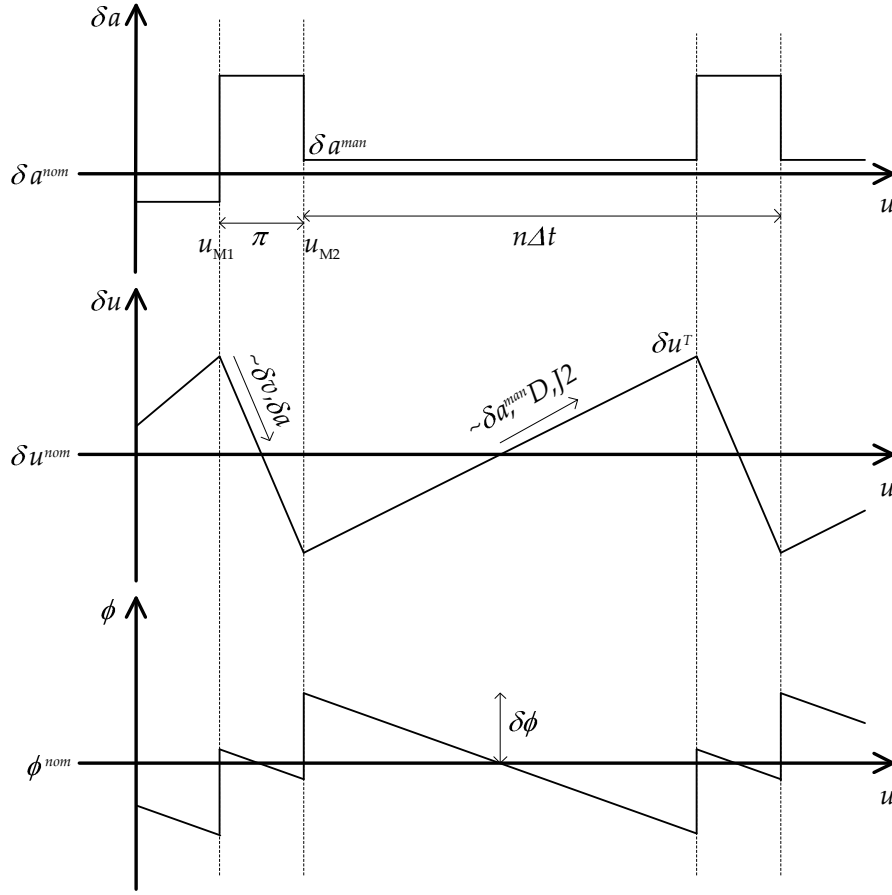


**Fig. 2.11:** Schematic view of along-track control process via simultaneous correction of relative eccentricity vector and semi-major axis. The relative semi-major axis (top) is corrected by each maneuver pair, so that the desired variation of the relative mean argument of latitude (middle) is achieved during the maneuver cycle up to the next maneuver pair. The maximum excursion of the relative mean argument of latitude is driven by the prescribed control window for the relative perigee (bottom).

Here  $\delta u^{\text{tot}}$  represents the total variation of the mean argument of latitude to be achieved during the maneuver cycle in the time frame  $\Delta t - n\pi$  comprised between the second maneuver and the first maneuver of the next maneuver pair.  $\Delta t$  is the maneuver cycle and is defined as the time interval comprised between the first pulses of two consecutive maneuver pairs. In general the desired total variation  $\delta u^{\text{tot}}$  has to take into account

1. the target relative mean argument of latitude to be reached at the end of the maneuver cycle,  $\delta u_T$
2. the current relative mean argument of latitude right before the execution of the first maneuver,  $\delta u$
3. the variation of the relative mean argument of latitude caused by the first maneuver during the time interval that precedes the execution of the second maneuver,  $\delta u_{\delta v}$



4. the variation of the relative mean argument of latitude caused by the current relative semi-major axis,  $\delta a$  during the time interval that precedes the execution of the second maneuver,  $\delta u_{\delta a}$
5. the variation of the relative mean argument of latitude caused by differential gravity and drag during the complete maneuver cycle,  $\delta u_{J_2}$  and  $\delta u_D$  respectively.

The total desired variation of the relative mean argument of latitude can be expressed as

$$\delta u^{\text{tot}} = \delta u_T - \delta u - \delta u_{\delta v} - \delta u_{\delta a} - \delta u_{J_2} - \delta u_D \quad . \quad (2.66)$$

$\delta u_{\delta v}$  can be derived from the combination of Eq. (2.6) and Eq. (2.63) as follows

$$\delta u_{\delta v} = -\frac{3}{na} \delta v_{t_1} \Delta u_M = -\frac{3\pi}{4} (\delta a^{\text{man}} - \delta a + \|\delta e^{\text{man}} - \delta e\|) \quad . \quad (2.67)$$

Similarly  $\delta u_{\delta a}$  is given by

$$\delta u_{\delta a} = -\frac{3\pi}{2} \delta a \quad . \quad (2.68)$$

As derived in Section 2.3,  $\delta u_{J_2}$  and  $\delta u_D$  can be expressed as a function of the maneuver cycle  $\Delta t$  as

$$\delta u_{J_2} + \delta u_D = -12\gamma \sin(2i) \delta i_x n \Delta t + \frac{3}{4} \delta B |\ddot{r}_t| \Delta t^2 / a \quad . \quad (2.69)$$

The target relative mean argument of latitude at the end of the maneuver cycle can be computed in order to obtain a control window that is centered on the nominal value  $\delta u^{\text{nom}}$ . This approach guarantees that the relative along-track motion is symmetric with respect to its nominal prescribed value. As shown in Fig. 2.11 the maximum desired excursion of the relative mean argument of latitude over the maneuver cycle has to match the total variation of  $\delta u$  which occurs between the execution of the first and second maneuvers of a maneuver pair. Nominally we can express  $\delta u_T$  as a function of the relative e-vector control window as follows

$$\delta u_T = \frac{3\pi}{8} \|\delta e^{\text{man}} - \delta e\| + \delta u^{\text{nom}} \approx \frac{3\pi}{4} \delta e^{\text{max}} + \delta u^{\text{nom}} \quad . \quad (2.70)$$

We can now substitute Eqs. (2.66)–(2.70) into Eq. (2.65) and solve for  $\delta a^{\text{man}}$  as follows

$$\delta a^{\text{man}} \approx -\frac{\pi}{2n\Delta t - \pi} \left[ 3\delta e^{\text{max}} + \delta a - \frac{4}{3\pi} (\delta u - \delta u^{\text{nom}} + \delta u_{J_2} + \delta u_D) \right] \quad . \quad (2.71)$$

This expression is only a function of known quantities like the maneuver cycle, the relative e-vector control window, the nominal configuration and the current relative orbital elements. The approximations introduced here to compute the desired relative semi-major axis  $\delta a^{\text{man}}$  after each pair of maneuvers are due to the adopted relative motion model and to the assumption of constant relative semi-major axis during the maneuver cycle.

### 2.4.5 Control Windows and Maneuver Budget

The characterization of the relative orbit control strategy in terms of maneuver frequencies and magnitude depends on the predefined nominal relative e/i-vectors,  $\delta e^{\text{nom}}$  and  $\delta i^{\text{nom}}$ , and the maximum allowed deviations  $\delta e^{\text{max}}$  and  $\delta i^{\text{max}}$  of the actual relative e/i-vectors from the nominal values. A proper choice of the nominal relative orbital elements has to account for collision avoidance, propellant consumption and science requirements. The minimum collision hazard is provided by (anti-)parallel relative e/i-vectors, while a perpendicular orientation gives the maximum collision risk. In general, the angle enclosed by  $\delta e^{\text{nom}}$  and  $\delta i^{\text{nom}}$  (i.e.,  $\varphi - \vartheta$ ) should guarantee a minimum safe spacecraft separation perpendicular to the flight direction at all times. The propellant consumption can be easily reduced by studying the  $J_2$  perturbations via Eq. (2.31). It is quite clear that a convenient orientation of  $\delta i^{\text{nom}}$  is given by  $\vartheta = \pi/2$ , and is equivalent to the choice of identical inclinations for the two spacecraft. A zero x-component of the relative inclination vector would cancel out the secular drift of the relative right ascension of the ascending node, and consequently eliminate the necessity of out-of-plane maneuvers.

Even if  $\varphi = \vartheta = \pi/2$  represents an optimum constellation geometry from an engineering point of view (i.e., it minimizes collision risk and propellant consumption), it does not always satisfy the science requirements, especially with Synthetic Aperture Radar (SAR) interferometric missions. In order to preserve the generality of the problem, different orientations and magnitudes have been selected for the nominal relative e/i-vectors in this section. In particular, we adopt the formation flying configuration specified in Table 2.2 as a test bed to assess the relationship between control windows and maneuver budget [D'Amico et al., 2006b]. The relative inclination vector has a non-zero x-component which corresponds to an inclination difference  $\Delta i = \delta i_x^{\text{nom}} = 0.0016^\circ$ . Magnitude and orientation of the relative inclination vector are  $a\delta i^{\text{nom}} = 300$  m and  $\vartheta^{\text{nom}} = 50^\circ$  respectively. Magnitude and orientation of the relative eccentricity vector are  $a\delta e^{\text{nom}} = 500$  m and  $\varphi^{\text{nom}} = 80^\circ$  respectively. The nominal relative mean argument of latitude results from  $a\delta u^{\text{nom}} = -a\delta i_y^{\text{nom}} / \tan i = 33.1$  m, providing close relative trajectories centered on the chief spacecraft.

**Table 2.2:** Chief orbital elements and nominal relative orbital elements for maneuver budget evaluation.

Orbit elements	Value	Relative orbit elements	Value
$a$ [m]	7078135.0	$a\delta a^{\text{nom}}$ [m]	0
$u$ [°]	0.0	$a\delta \lambda^{\text{nom}}$ [m]	0
$e_x$ [-]	0.001	$a\delta e_x^{\text{nom}}$ [m]	86.8241
$e_y$ [-]	0.0	$a\delta e_y^{\text{nom}}$ [m]	492.4039
$i$ [°]	98.19	$a\delta i_x^{\text{nom}}$ [m]	192.8363
$\Omega$ [°]	189.89086	$a\delta i_y^{\text{nom}}$ [m]	229.8133

The maximum prescribed deviation of the relative e/i-vectors from the nominal values depends on the specific formation flying application and the ap-

plied orbit control system. The impulsive feedback control scheme is limited to a minimum possible maneuver cycle of one orbital revolution for either the in-plane double burns or the out-of-plane single pulses (i.e., the total maneuver sequence has to take place within one orbital revolution). If a safe coordinated along-track/cross-track maneuver strategy is required, the minimum maneuver cycle can easily be two or three orbital revolutions. A second important aspect to be considered is the fact that the magnitude of the impulsive maneuvers should be fairly larger than the minimum impulse bit permitted by the applied propulsion system. This consideration drives the selection of control windows (or equivalently maneuver cycles) so that the performance of the relative orbit control is not spoiled by specific propulsion system characteristics.

Let us first consider the out-of-plane maneuver planning problem. The maximum allowed deviation of the relative inclination vector  $\delta i^{\max}$  can be expressed as a function of the maneuver cycle  $\Delta t$  for out-of-plane control through Eq. (2.29)

$$a\delta i^{\max} = \left| \frac{3}{2} n \gamma a \delta i_x^{\text{nom}} \Delta t \sin^2 i \right| \approx (0.7826 \cdot N) \text{ m} \quad , \quad (2.72)$$

where  $N$  represents the number of orbital revolutions between consecutive pulses (i.e., out-of-plane maneuver cycle in units of orbital revolutions). The size of the individual cross-track maneuvers required to maintain the relative inclination vector is given by

$$\delta v_n = 2na\delta i^{\max} \approx (1.7 \cdot N) \text{ mm/s} \quad . \quad (2.73)$$

Eqs. (2.72) and (2.73) provide the relationship between relative orbit control accuracy  $a\delta i^{\max}$  and maneuver cost  $\delta v_n$  as a function of the maneuver cycle  $N$ . Similar considerations apply for the relative eccentricity vector control. The maximum allowed deviation of the relative eccentricity vector  $\delta e^{\max}$  can be expressed as a function of the maneuver cycle  $\Delta t$  for in-plane control through Eq. (2.29)

$$a\delta e^{\max} \approx a\delta e^{\text{nom}} \sin \delta \varphi \approx \left| \frac{3}{4} n \gamma a \delta e^{\text{nom}} \Delta t (5 \cos^2 i - 1) \right| \approx (0.9306 \cdot N) \text{ m} \quad , \quad (2.74)$$

while the size of the individual along-track maneuvers required to maintain the relative eccentricity vector only is given by

$$\delta v_{t_1} = -\delta v_{t_2} = na\delta e^{\max}/2 \approx (0.49 \cdot N) \text{ mm/s} \quad . \quad (2.75)$$

Finally, we consider the relative mean argument of latitude control. As explained in the previous section, no additional thrusts are necessary if the size of the relative eccentricity vector maneuvers (cf. Eq. (2.63)) is properly adjusted. The maximum deviation of the relative mean argument of latitude  $\delta u^{\max}$  can be expressed as a function of the maneuver cycle  $\Delta t$  for in-plane control through Eq. (2.70) and Eq. (2.74)

$$a\delta u^{\max} = a\delta u_T - a\delta u^{\text{nom}} \approx \frac{3\pi}{4} a\delta e^{\max} = (2.1926 \cdot N) \text{ m} \quad . \quad (2.76)$$

**Table 2.3:** Control windows and maneuver budget for mean along-track separation control.

$a\delta u^{\max}$ [m]	$N$ [rev]	$\delta v_{t_1} + \delta v_{t_2}$ [mm/s]	$a\delta u_{J_2}$ [m]	$a\delta u_D$ [m]
2.1926	1	-0.0209	1.8022	2.3037
4.3852	2	0.1301	3.6045	9.2148
6.5778	3	0.2656	5.4067	20.7332
8.7703	4	0.3979	7.2089	36.8591
10.9629	5	0.5290	9.0111	57.5923
13.1555	6	0.6596	10.8134	82.9329

Table 2.3 lists the size of the control window for the relative mean argument of latitude  $a\delta u^{\max}$ , the required differential corrections of the tangential maneuver sizes in terms of  $\delta v_{t_1} + \delta v_{t_2}$ , cf. Eq. (2.63), and the accumulated along-track offsets  $a\delta u_{J_2}$  and  $a\delta u_D$  caused by differential gravity and drag during the maneuver cycle. The accumulated offset induced by differential drag has been computed via Eq. (2.69) assuming an atmospheric density  $\rho = 0.11946 \text{ g/km}^3$ , and ballistic coefficients  $B_d = 0.045 \text{ m}^2/\text{kg}$  and  $B = 0.019 \text{ m}^2/\text{kg}$  for the deputy and chief spacecraft respectively.

Obviously when the accumulated along-track offset induced by differential gravity and drag exceeds the length of the nominal control window (i.e.,  $a\delta u_{J_2} + a\delta u_D > 2a\delta u^{\max}$ ), then the asymmetric pair of along-track maneuvers has to establish a positive relative semi-major axis in order to reduce the drift of the relative mean argument of latitude during the maneuver cycle. Vice versa when the accumulated along-track offset induced by differential forces is smaller than the overall extension of the control window, then a negative relative semi-major axis has to be created after the pair of maneuvers to increase the drift of  $\delta u$ . In our specific scenario the latter case occurs only for the shortest maneuver cycle (i.e.,  $N = 1$ ), cf. Table 2.3.

#### 2.4.6 Formation Reconfiguration

The formation maintenance strategy described in the previous section can be used as well for formation reconfiguration. One has to prescribe the desired nominal relative orbital elements and apply Eq. (2.63) and (2.64) to compute size and locations of the necessary orbit control maneuvers in along-track and cross-track direction respectively. The drawback of this control scheme is given by the undesired variation of the mean argument of latitude that is always induced by the first tangential pulse. In the case of large formation reconfigurations or acquisitions this effect can become unacceptably large.

An alternative approach for formation reconfiguration is presented in this section. The goal is to achieve a more accurate formation reconfiguration, avoiding large drifts of the mean along-track separation, by the use of maneuvers in radial direction. Although the radial pulses are two times less fuel-efficient than the tangential maneuvers (cf. Section 2.4.2), they do not produce any variation of the semi-major axis, and as a consequence are inherently more accurate with respect to along-track control.

The discussion on the propellant consumption in Section 2.4.2 has shown how minimum delta-v cost solutions of the Gauss' variational equations are provided by  $u_{M_1} - \xi = 0$ ,  $\frac{\pi}{2}$  and  $\Delta u_M = \pi$ . If  $\delta a = \delta \lambda = 0$  the absolute minimum is given by  $u_{M_1} - \xi = 0$  and consists of along-track maneuvers in (anti-)flight directions separated by half an orbital revolution (cf. Eq. (2.42)). The alternative control scheme is based on the choice of  $u_{M_1} - \xi = \frac{\pi}{2}$ . In this case Eq. (2.42) reduces to the following expression

$$\begin{aligned} \delta v_{r_1} &= \frac{na}{2} [-(\delta \lambda^{\text{man}} - \delta \lambda)/2 + \|\delta \mathbf{e}^{\text{man}} - \delta \mathbf{e}\|] \\ \delta v_{r_2} &= \frac{na}{2} [-(\delta \lambda^{\text{man}} - \delta \lambda)/2 - \|\delta \mathbf{e}^{\text{man}} - \delta \mathbf{e}\|] \\ u_{M_1} &= \arctan [(\delta e_x^{\text{man}} - \delta e_x)/(\delta e_y^{\text{man}} - \delta e_y)] \end{aligned} \quad (2.77)$$

The computation of  $\delta \mathbf{e}^{\text{man}}$  is identical to the previous control scheme and can be performed through Eq. (2.58) and (2.61). In parallel with the previous section, the computation of  $\delta \lambda^{\text{man}}$  has to take into account the variation of relative mean argument of latitude which occurs between two maneuvers of a single pair  $\delta a_{\delta a}$  and during the maneuver cycle due to external perturbations like  $J_2$  and differential drag. Starting from Eq. (2.66), the total desired variation of mean argument of latitude will be

$$\delta u^{\text{tot}} = \delta u^{\text{nom}} - \delta u - \delta u_{\delta a} - \delta u_{J_2} - \delta u_D \quad (2.78)$$

Due to the cancellation of the mean argument of latitude drift caused by the variation of semi-major axis (i.e.,  $\delta u_{\delta v} = 0$ ), the reconfiguration approach does not specify any control window for  $\delta \lambda$  (i.e.,  $\delta u_T = \delta u^{\text{nom}}$ ). The computation of  $\delta u_{\delta a}$  is done through Eq. (2.68), while  $\delta u_{J_2} + \delta u_D$  is given by Eq. (2.69). The remaining quantities are prescribed by the user, like  $\delta u^{\text{nom}}$ , or estimated by a navigation process like  $\delta u$  and  $\delta a$ .

Obviously the presented reconfiguration algorithm can not compensate for the drift of the relative semi-major axis caused by differential drag. Radial maneuvers cannot correct the semi-major axis, thus a net difference between chief and deputy semi-major axis will accumulate over time and induce a gradually increasing variation rate of the mean along-track separation. This side effect has to be taken into account only if the presented control scheme (cf. Eqs. (2.77)-(2.78)) is applied to achieve a more accurate, but more expensive, formation maintenance. In this case we can simply introduce aside Eq. (2.77), at the same maneuver locations, the following small tangential maneuvers

$$\begin{aligned} \delta v_{t_1} &= \frac{na}{4} (\delta a^{\text{man}} - \delta a) \\ \delta v_{t_2} &= \frac{na}{4} (\delta a^{\text{man}} - \delta a) \end{aligned} \quad (2.79)$$

to compensate for semi-major axis changes only.

## 2.4.7 Numerical Validation of Control Schemes

The aim of this section is to validate the proposed control schemes through a numerical integration of the nonlinear differential equations of motion including only  $J_2$  effects. The idea is to make use of the feedback control law to

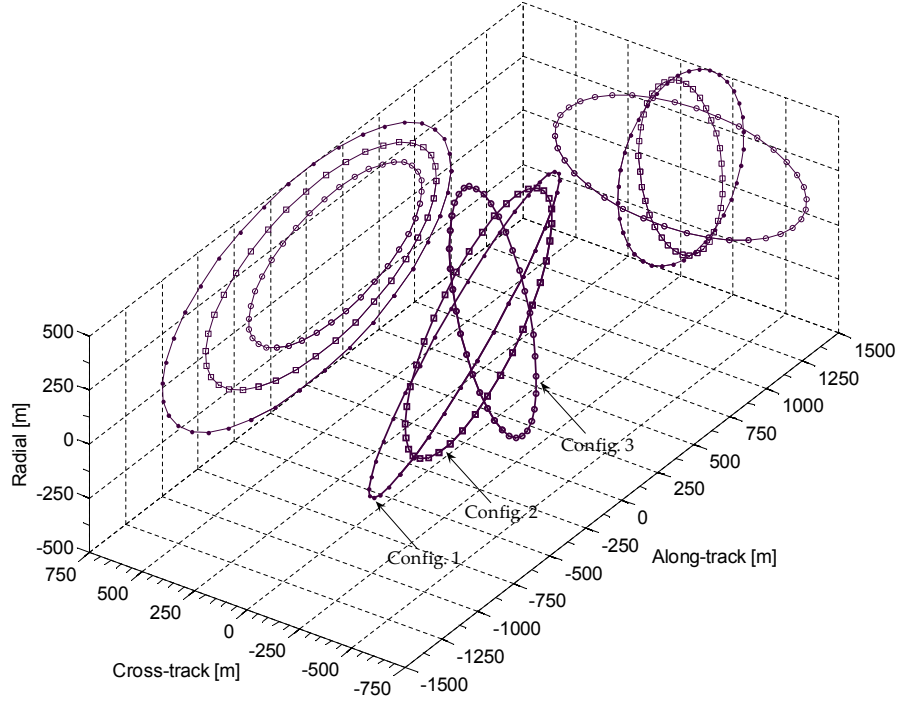
maintain and reconfigure various formation flying configurations in an ideal scenario where no sensors and actuators errors are present, as well as no orbit perturbations apart from  $J_2$  are considered. More realistic simulations are deferred to the next chapters of the thesis. The numerical integration method and the reference orbit of the chief spacecraft have already been described in Section 2.3.4. Orbit control maneuvers are included in the numerical propagation as instantaneous variations of the deputy orbit velocity (i.e., an impulsive maneuver model is applied).

Table 2.4 lists three formation flying configurations that we want to consecutively maintain and acquire over a total time interval of three days (i.e., going from constellation 1 to 2 and finally to 3). The formation maintenance control law (based on along-track pulses only, cf. Section 2.4.4) will be applied to each constellation for about one day. At the end of each day the reconfiguration control scheme (based on radial and along-track pulses, cf. Section 2.4.6) will be used to establish the new desired nominal relative orbital elements. The initial formation configuration matches the one analyzed in the previous sections through the correlation of control windows, maneuver size and frequency. The second formation is characterized by parallel relative e/i-vectors aligned with the y-axis of the e-vector plane (i.e.,  $\varphi = \vartheta = 90^\circ$ ). At each formation reconfiguration a mean along-track offset of 100 m is introduced. Finally the third and last formation is characterized by a relative ascending node  $\vartheta = 90^\circ$  and by a relative perigee  $\varphi = 100^\circ$ . For a matter of clarity the 3D nominal relative motion associated with the three formation flying configurations is depicted in Fig. 2.12.

The control windows for the relative eccentricity and inclination vectors are kept constant during the complete simulation and are given by  $a\delta e^{\max} = a\delta i^{\max} = 2$  m. As a consequence we expect a maximum excursion of the relative mean argument of latitude from its nominal value given by  $a\delta u^{\max} \approx 5$  m during formation maintenance phases (cf. Eq. (2.70)). Considering as an example the first formation flying configuration, Eqs. (2.72)–(2.75) provide an estimated maneuver cycle for formation maintenance given by  $N \approx 2.5$  rev with correspondent individual cross-track maneuvers  $\delta v_n \approx 4$  mm/s and along-track ma-

**Table 2.4:** Nominal relative orbital elements of three formation flying configurations to be maintained and acquired autonomously.

Nominal elements	Config. 1	Config. 2	Config. 3
$a\delta a^{\text{nom}}$ [m]	0	0	0
$a\delta \lambda^{\text{nom}}$ [m]	0	100	200
$a\delta e_x^{\text{nom}}$ [m]	86.8241	0	-52.0944
$a\delta e_y^{\text{nom}}$ [m]	492.4039	400	295.4423
$\varphi^{\text{nom}}$ [°]	80	90	100
$a\delta i_x^{\text{nom}}$ [m]	192.8363	0	0
$a\delta i_y^{\text{nom}}$ [m]	229.8133	200	600
$\vartheta^{\text{nom}}$ [°]	50	90	90



**Fig. 2.12:** Nominal relative motion associated with the three formation flying configurations to be maintained and acquired. The relative motion of the deputy spacecraft is mapped in the Hill's orbital frame centered on the chief spacecraft. The relative orbit is projected onto the radial/along-track and radial/cross-track planes. The three formation flying configurations are identified in the figure by dot (first config.), square (second config.) and circle (third config.) markers.

neuvers  $\delta v_t \approx 1.2 \text{ mm/s}$ . These orders of magnitude are fairly matched by our numerical simulations as depicted in Figs. 2.13–2.18.

More specifically Fig. 2.13 shows the global evolution of the relative eccentricity vector during the three days simulation. The relative e-vector is kept close to its nominal value during the daily formation maintenance phases and it is changed at the occurrence of formation reconfigurations by the double-impulse scheme. Fig. 2.14 offers some zoomed details on the motion of the relative e-vector with respect to the prescribed control window during formation maintenance phases. Some excursions out of the control window are due to the applied maneuver triggering logic, in particular the guidance algorithm waits for the violation of the prescribed limits before planning a new maneuver with associated size and location along the orbit. Depending on the orbit mean argument of latitude at the time of the dead-band violation, the first correction maneuver could occur up to one orbital revolution later, thus causing an overshooting of the limits. This side effect can be easily removed by scaling the control window applied in the guidance algorithm to satisfy the orbit control accuracy requirements in a conservative scenario.

In parallel with the relative e-vector discussion, Fig. 2.15 shows the relative inclination vector behavior during the simulation. In this case the relative i-vector is corrected at once by single out-of-plane maneuvers. As shown by the

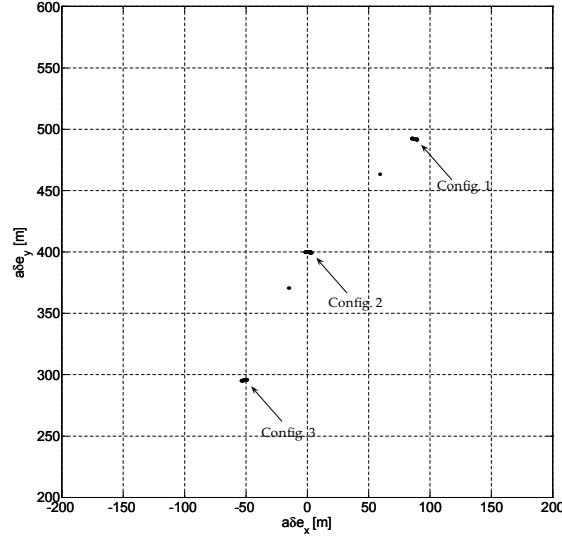


**Fig. 2.13:** Relative eccentricity vector during the three days simulation. The relative eccentricity vector is kept within a predefined control window centered on the nominal value for each formation flying configuration. Furthermore the relative eccentricity vector is changed at the end of each day to acquire a newly desired configuration. According to the proposed control scheme, the formation reconfigurations are realized through pairs of maneuvers, thus the relative eccentricity vector occupies intermediate positions between the individual configurations.

zoomed view in Fig. 2.16 the relative  $i$ -vector needs to be corrected only during the first formation configuration. In fact the identical inclination of the chief and deputy spacecraft orbits cancels the relative  $i$ -vector drift due to  $J_2$  for the rest of the simulation. The relative orbital elements governing the mean along-track separation between the spacecraft are illustrated in Fig. 2.17. As explained in Section 2.4.4, the semi-major axis is changed at the instance of each along-track maneuver in order to establish the desired drift of the relative mean argument of latitude. Due to the absence of differential drag, the relative semi-major axis is always negative after each maneuver pair. In fact the accumulated  $a\delta u_{J_2}$  offset

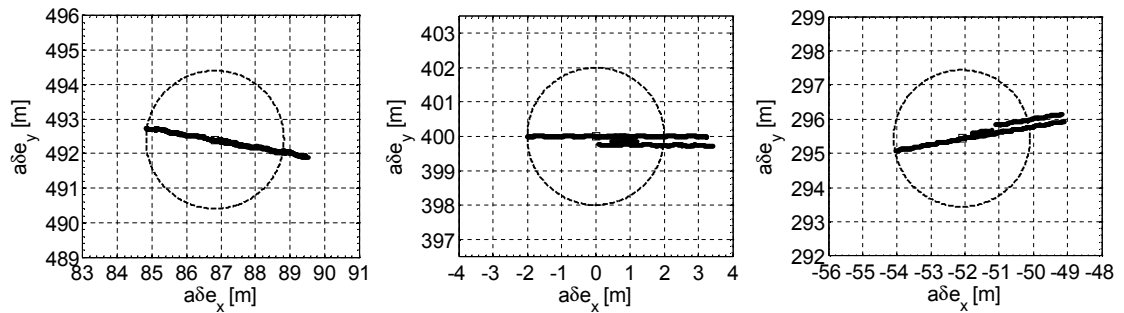


**Fig. 2.14:** Actual relative eccentricity vector (straight line) and control window (dashed line) during the orbit keeping phase for the first (left), second (middle) and third (right) formation flying configurations.



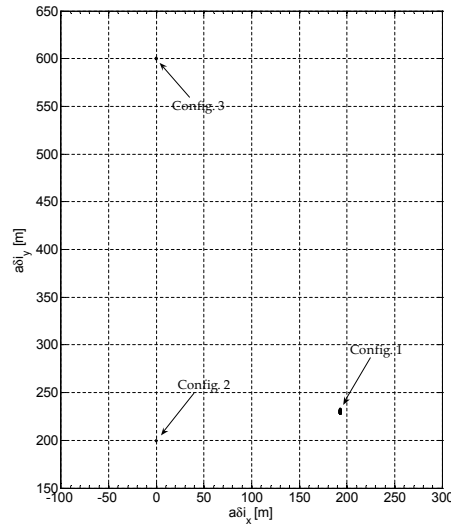


**Fig.2.15:** Relative inclination vector during the three days simulation. The relative inclination vector is kept within a predefined control window centered on the nominal value for each formation flying configuration. Furthermore the relative inclination vector is changed at the end of each day to acquire a newly desired configuration.

during the maneuver cycle is always smaller than the along-track offset caused by the first pulse of each maneuver pair, cf. Table 2.3. Note that during the formation reconfigurations, where mainly radial maneuvers are used, nearly no change of semi-major axis is generated. The full set of relative orbit control maneuvers planned and executed during the simulation is shown in Fig. 2.18. Radial pulses are only used during the formation reconfigurations at about 24 and 48 hours since start. In correspondence with the radial maneuvers, small  $\delta v$ 's of about 0.1 mm/s are executed to compensate for residual semi-major axis offsets. During formation maintenance individual along-track maneuvers of about 1.5 mm/s and cross-track maneuvers of about 3.5 mm/s are executed with a frequency of about 2.5 orbital revolutions.

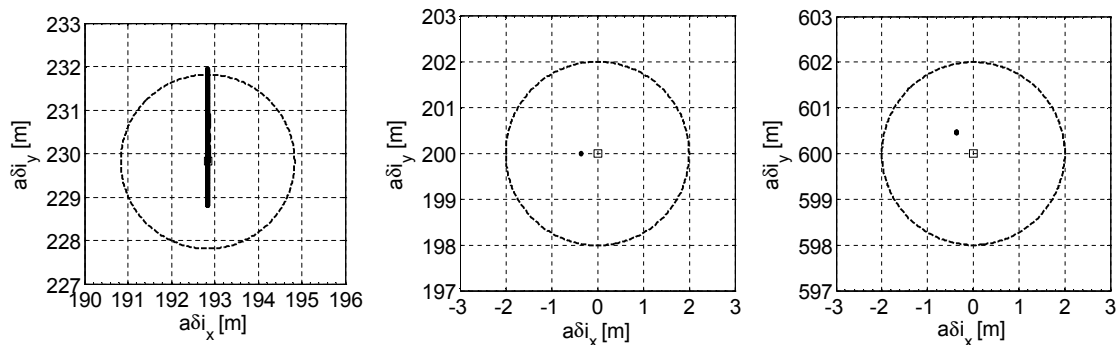


**Fig.2.16:** Actual relative inclination vector (straight line) and control window (dashed line) during the orbit keeping phase for the first (left), second (middle) and third (right) formation flying configurations.

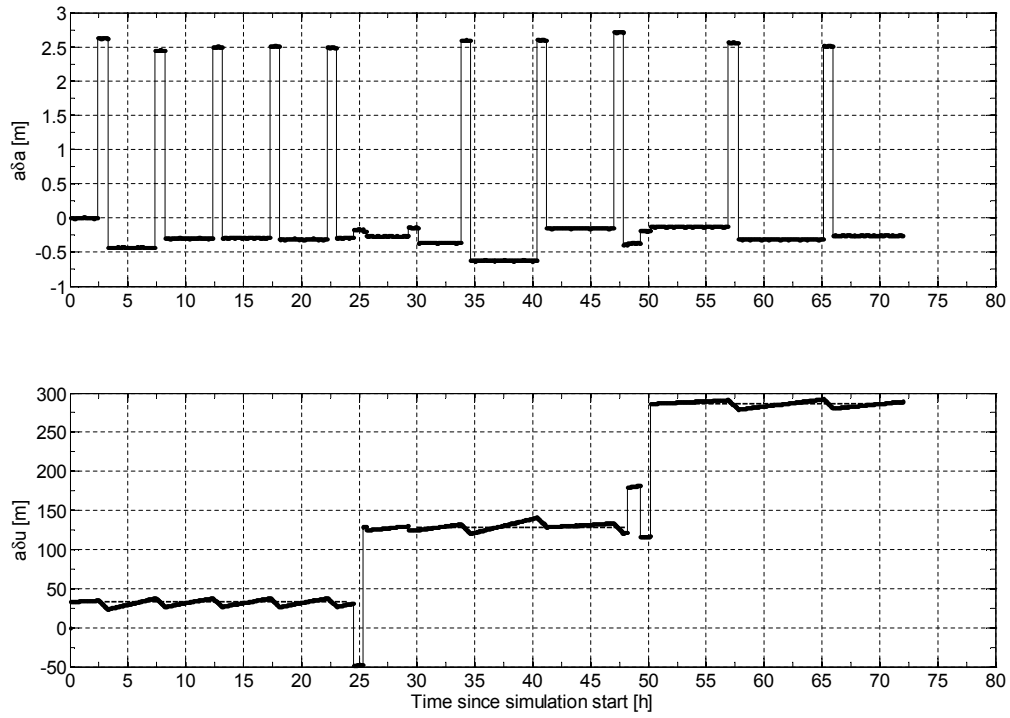


**Fig. 2.17:** Actual relative semi-major axis (top) and relative mean argument of latitude (bottom) during the three days simulation. The nominal relative mean argument of latitude for each phase is also depicted (dashed line).

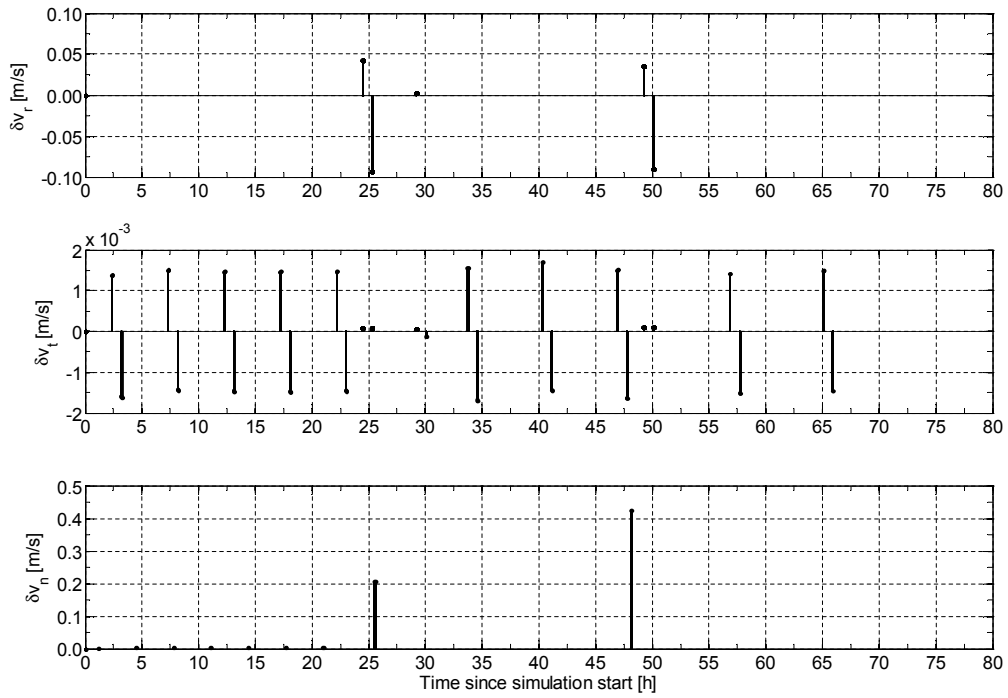


**Fig. 2.18:** Radial (top), along-track (middle) and cross-track (bottom) relative orbit control maneuvers for formation maintenance and reconfiguration.

## 3. GPS-based Relative Navigation

### 3.1 Design of the Optimal Real-Time Estimator

Chapter 2 presented a safe and fuel-efficient guidance and control strategy for formation flying spacecraft. The treatment assumed an ideal knowledge of the absolute and relative orbit available on-board in the computation of the analytical closed-form feedback control law. The assumption of ideal navigation sensors is abandoned in this chapter which is devoted to the problem of real-time GPS-based absolute and relative positioning of co-orbiting satellites. We address the preliminary design, implementation and validation of an on-board navigation system aiming at the provision of absolute and relative position and velocity for the PRISMA space-segment which consists of two satellites flying in formation in Low Earth Orbit. The key drivers and constraints for the design of the navigation system are first identified and discussed. The navigation software has to be integrated and executed on a spacecraft on-board computer with limited memory and computational capacity. The available GPS receivers offer raw measurements of C/A-code pseudorange and L1 integrated carrier phase which have to be processed as soon as they are received in a reduced-dynamic sequential estimation algorithm. The absolute and relative orbit determination and prediction accuracy requirements drive the selection of the applied force model and measurement concept. Furthermore, the widely varying formation flying scenarios necessitate a high level of robustness and flexibility of the navigation system which shall handle thruster pulses of the propulsion system and operate properly in the presence of GPS data gaps caused for example by power constraints or spacecraft reorientation phases.

#### 3.1.1 Top-level Functional View

A top-level functional view of the GPS-based guidance, navigation and control system developed for PRISMA is presented in Fig. 3.1. The GPS receivers will provide raw single-frequency data to the navigation subsystem and deliver a Pulse Per Second (PPS) for the synchronization of the on-board clock. The use of GPS data from both spacecraft implies an inter-satellite link (ISL) between *Main* and *Target*. The navigation filter will only be implemented on *Main* and provide the desired absolute and relative orbit information in real-time to the various PRISMA experiment users. Among them Fig. 3.1 shows the Autonomous Formation Control experiment (AFC) which makes use of the algorithms defined in the previous chapter to compute output control requests to the *Main* propulsion system.

The GPS-based navigation system is naturally split into three modules devoted to the input/output interfacing of the GPS receivers (GIF), to the GPS-

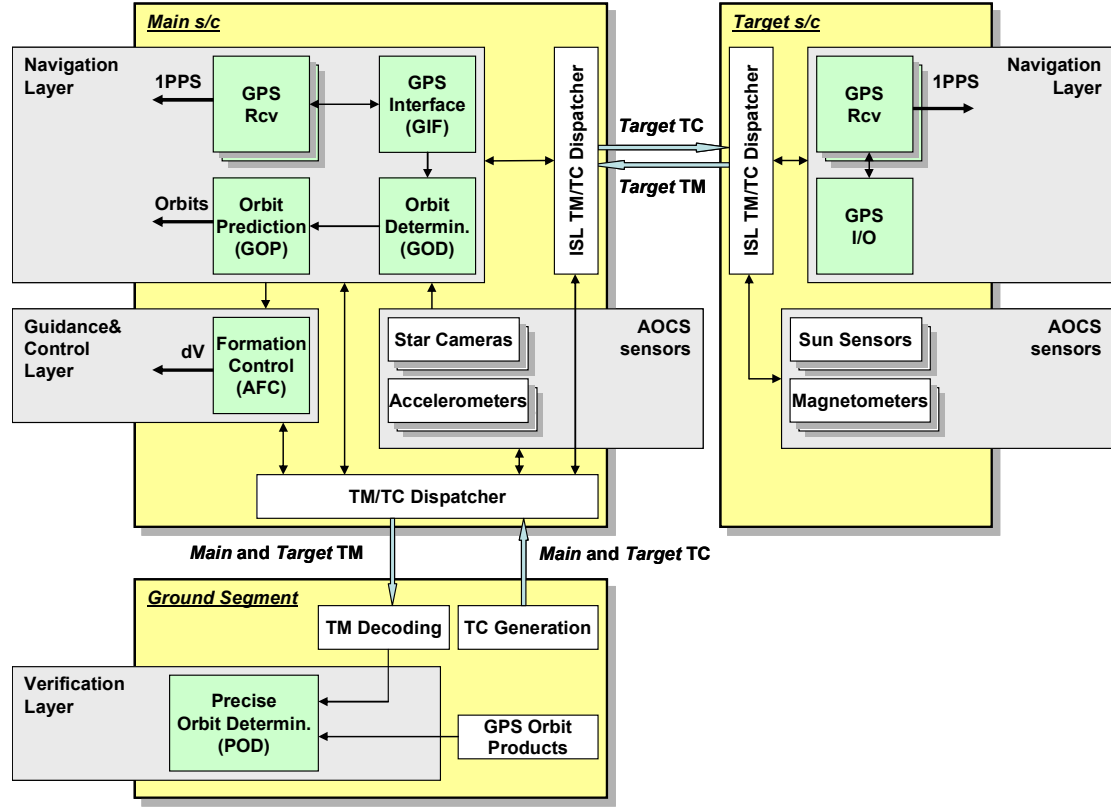


**Fig. 3.1:** Top-level functional view of the GPS-based guidance, navigation and control system developed for PRISMA. The *Main* and *Target* spacecraft as well as the ground-segment are enclosed in yellow rectangles. Hardware and software elements strictly related to GPS are green. Interfaces to other subsystems of the space-segment are gray. The provided architecture is simplified and focuses on GPS related functions. On-board signal conditioning and filtering related to AOCS sensors measurements are not shown.

based Orbit Determination (GOD) and to the GPS-based Orbit Prediction (GOP). Additional interfaces with attitude sensors and accelerometers are foreseen to handle the offsets of the GPS antennas with respect to the spacecraft center of mass and the orbit control maneuvers, respectively.

GPS data as well as auxiliary attitude and maneuver info will be downloaded during ground-station contacts and provided to the Precise Orbit Determination (POD) function which is used for the on-ground post-facto highly precise reconstruction of the formation absolute and relative orbits. The POD products will be required for the a posteriori evaluation of sensor data and the validation of the formation flying experiments.

### 3.1.2 Key Objectives and Requirements

This section is intended to identify the key drivers of the navigation system design. Based on typical formation flying mission needs in LEO and more specifically on the PRISMA case, the following specifications cover the most relevant aspects of what the GPS-based navigation subsystem should do (i.e., functions)

and how well it should be done (i.e., performance).

From a functional perspective the primary objective of the GPS-based navigation system addressed in this thesis is to perform a real-time reduced-dynamic orbit determination based on raw GPS C/A code and L1 carrier phase measurements. Considering that ionospheric errors dominate the GPS measurements error budget, a suitable combination of raw code and carrier phase shall be exploited to remove those errors. As a minimum the orbit determination is asked to adjust the spacecraft position, velocity, clock error and carrier phase biases. In order to simplify operations, it shall be possible to start and initialize the autonomous estimation process from GPS data available on-board. Furthermore the orbit determination shall be able to detect and reject bad GPS data and be robust against erroneous measurements. The orbit determination shall continue to operate properly after GPS data gaps of up to one orbital revolution and shall be able to handle thruster pulses of the PRISMA propulsion system applied as part of the formation keeping and reconfiguration activities.

Continuous orbit information is important for autonomous on-board GNC applications. As a consequence, orbit prediction is a mandatory function of the navigation system and shall provide continuous absolute and relative position and velocity information of the co-orbiting satellites. Furthermore the navigation system shall provide an accuracy measure indicating the expected quality of the orbit results.

From a performance point of view the navigation function shall provide position and velocity data of the participating spacecraft at a 1 Hz rate for guidance and control purposes as well as for the PRISMA payload. Under the provision of continuous and sufficient GPS data, the estimated absolute position and velocity shall be better than 3 m and 1 cm/s (3D, RMS). The estimated relative position and velocity of *Main* with respect to *Target* shall be better than 0.2 m and 0.2 mm/s (3D, RMS). These accuracy requirements are expressed in the Earth-Centered Earth-Fixed (ECEF) reference frame to ensure consistency with the coordinate system where the GPS measurements are naturally modelled. In general data gaps, a limited number of tracked GPS satellites and deficiencies in the dynamic model cause a degradation of the achievable orbit prediction accuracy. In our representative case the predicted absolute position shall be better than 10/100/5 m (R/T/N, RMS) and the predicted relative position shall be better than 0.5/10/0.5 m (R/T/N, RMS) within a 50 minutes prediction interval. For convenience the position errors have been expressed in the orbital frame defined by the vector triad ( $\mathbf{o}_r$ ,  $\mathbf{o}_t$ ,  $\mathbf{o}_n$ ) illustrated in Fig. 2.1 with origin at the *Target* spacecraft center of mass. Generally a dynamical orbit determination requires an adequate data arc to obtain reliable velocity estimates from pseudorange and carrier phase measurements, here the orbit determination process shall require less than one orbit of GPS measurements to achieve its steady state performance in the absence of thruster activity.

From a system perspective the navigation software will be installed on the *Main* spacecraft on-board computer which is based on a LEON-3 FPGA microprocessor clocked at 24 MHz with Floating Point Unit (FPU). For sake of

robust operations a heuristic safety margin shall be considered and the navigation software shall employ less than 30% of the total processor memory and capacity under normal operations. In addition, when *Target* is clamped to *Main* after separation from the launcher (cf. Fig. 1.2), PRISMA will allow for verification of the relative navigation function in space. In fact the clamped spacecraft configuration after separation offers the unique chance to verify and calibrate the relative navigation function. Thus the system will support the provision of GPS data collected onboard *Target* to *Main* using the ISL in the combined configuration.

As shown in the next sections, the design of the real-time GPS-based navigation system is the product of a progressive and iterative trade-off. On top of the succinct but well-defined requirements, more qualitative aspects have to be considered like e.g. simplicity, scalability, and re-usage of existing algorithms, especially if characterized by high maturity and flight heritage.

### 3.2 Estimation Concept

The most suitable approach to the real-time reduced-dynamic orbit determination is based on the sequential estimation filter of Swerling [1958] and Kalman [1960]. A Kalman filter (KF) design provides an optimal state estimate in the sense of minimum variance, supports (near-)real-time solutions through sequential processing and consequently avoids the on-board storage of GPS measurements. In order to reduce the effects of errors due to the neglect of higher order terms in the linearization procedure leading to the conventional KF, the so-called extended form of the sequential estimation algorithm is chosen here. Instead of linearizing about the nominal trajectory, the Extended Kalman Filter (EKF) [Jazwinski, 1970] linearizes about the estimated trajectory. This approach can better retain linearity of the approximation, because the estimated state is on the average closer to the actual state. The more rapid convergence of the EKF to the best state estimate comes at a higher computational cost due to the necessity of re-initializing the differential equations for the reference trajectory after each set of GPS observations is processed. In addition, the EKF covariance differs from the KF in that it depends on the estimate and thus cannot be evaluated off-line.

Recently, there has been an increasing interest in the development of techniques for nonlinear estimation [Bierman, 2006], [Simon, 2006]. Alternatives to the EKF can be employed, like the Unscented Kalman Filter (UKF) which uses a finite number of sigma points to propagate the probability of state distribution as accurately as possible. This approach exhibits higher performance since the EKF first order approximations can lead to poor representations of the nonlinear dynamics and statistics of the process. Furthermore the overall computational complexity of the UKF is comparable with the EKF [Bierman, 2006]. Anyhow, considering the problem under study, the advantages of an UKF over an EKF become more evident when dealing with dynamics characterized by higher nonlinearities and intense maneuvering. As discussed in the previous

section, high technological readiness level and flight heritage are important drivers in the selection of on-board software algorithms, thus we have decided to adopt a filter design based on an EKF in this thesis.

In order to design an EKF the nonlinear differential equations governing the orbit dynamics and the adopted measurements are first linearized about a nominal reference motion through a Taylor's series expansion. The well-known linearization procedure of the orbit determination process [Montenbruck and Gill, 2001a], [Schaub and Junkins, 2003] leads to a system of linear differential equations with time dependent coefficients. In the presence of model and measurement uncertainties, the general solution for this linear system can be expressed as

$$\begin{aligned} \mathbf{y}(t) &= \boldsymbol{\Phi}(t, t_0)_{n \times n} \mathbf{y}(t_0) + \mathbf{G}(t, t_0)_{n \times n_w} \mathbf{w}(t_0) \\ \mathbf{z}(t) &= \mathbf{H}(t)_{m \times n} \mathbf{y}(t) + \boldsymbol{\epsilon}(t) \quad , \end{aligned} \quad (3.1)$$

where  $\boldsymbol{\Phi}(t, t_0)$  is the nonsingular transition matrix relating the  $n$ -dimensional state vector  $\mathbf{y}(t_0)$  at time  $t_0$  to the state  $\mathbf{y}(t)$  at time  $t$ .  $\mathbf{w}$  is the  $n_w$ -dimensional vector of process noise parameters,  $\mathbf{z}$  is the  $m$ -dimensional measurement vector and  $\boldsymbol{\epsilon}$  is the  $m$ -dimensional vector of measurement errors. The design of the real-time estimator will go first through the characterization of this linear system by identifying and selecting the GPS measurements (with their associated errors) and the formation state estimation parameters (with their associated process noise). Next the partial derivatives  $\mathbf{H}$  of the selected measurements (with respect to the state) and the partial derivatives  $\boldsymbol{\Phi}$  and  $\mathbf{G}$  of the selected state (with respect to the state itself and the process noise) will be computed.

### 3.2.1 GPS Measurements

#### Elementary GPS observables

Three types of GPS observations are supported by the single-frequency L1 DLR's Phoenix-S GPS receiver used throughout this research, the code or pseudorange observation, the carrier phase or integrated Doppler observation, and the range-rate or instantaneous Doppler observation. The pseudorange observations  $\rho_{\text{PR}}$  are a coarse measure of the actual geometric range  $\rho$  between the antenna phase centers of the GPS transmitting satellite and the GPS user receiver. The main difference between  $\rho_{\text{PR}}$  and  $\rho$  is due to the clock offsets  $\delta t$  and  $\delta t_{\text{GPS}}$  of the user GPS receiver and the GPS satellite (subscript GPS) relative to the GPS system time. Furthermore the collected observations are affected by the ionospheric path delay  $I$  which is the only atmospheric effect present between 50 and 1000 km altitude, by systematic errors or biases on the receiver tracking channels  $S_{\text{PR}}$  (e.g., instrumental delays, signal multipath) and measurement noise  $\epsilon_{\text{PR}}$  (caused e.g. by thermal effects on the decimeter level). These independent error contributions can be summed up to provide the observation equation for a pseudorange measurement on the L1 transmitting frequency

$$\rho_{\text{PR}} = \rho + c(\delta t - \delta t_{\text{GPS}}) + I + S_{\text{PR}} + \epsilon_{\text{PR}} \quad , \quad (3.2)$$

where  $c$  represents the speed of light and all the individual terms are a function of the GPS time which has been omitted for simplicity.

The GPS receiver can track the carrier onto which the code was modulated, thus producing the carrier phase observable  $\rho_{CP}$

$$\rho_{CP} = \rho + c(\delta t - \delta t_{GPS}) - I + \lambda_1 N_{CP} + S_{CP} + \epsilon_{CP} \quad , \quad (3.3)$$

where  $\lambda_1$  is the L1 signal wavelength and  $N_{CP}$  represents a float bias, constant over a continuous tracking arc, which results from an unknown integer number of carrier cycles  $N_C$  and hardware dependent line biases. Similar to the pseudorange observation, the carrier phase is a measure of the geometric range and is affected by systematic  $S_{CP}$  and random errors  $\epsilon_{CP}$ . In contrast to the pseudorange, the carrier phase measurements are ambiguous (cf.  $\lambda_1 N_{CP}$ ), are more accurate having a thermal noise on the mm level (i.e.,  $\epsilon_{CP} \approx \epsilon_{PR}/1000$ ), and are affected by ionospheric path delays of equal size but opposite sign (cf.  $I$  in Eqs. (3.2) and (3.3)). For a receiver in low Earth orbit, these ionospheric effects can to first order be modeled as a function of the elevation  $E$  of the observed GPS satellite [Lear, 1989]

$$I = I_0 L(E) \quad , \quad (3.4)$$

where  $I_0$  represents the vertical path delay and  $L$  is the Lear mapping function

$$L(E) = \frac{2.037}{\sqrt{\sin^2 E + 0.076 + \sin E}} \quad . \quad (3.5)$$

#### Linear data combinations for positioning

More powerful data types can be obtained out of the elementary GPS observables through dedicated linear combinations of pseudorange (PR) and carrier phase (CP) measurements. These measurements could be taken by the same GPS receiver for the purpose of absolute positioning or by different GPS receivers on-board different formation flying spacecraft for relative positioning. Here we consider four fundamental combinations, the Group and Phase Ionospheric Correction (GRAPHIC), the Single Difference Pseudorange (SDPR), the Single Difference Carrier Phase (SDCP) and the Double Difference Carrier Phase (DDCP) measurements.

The GRAPHIC data type introduced by Yunck [1993] is simply the arithmetic average of pseudorange and carrier phase taken by the same receiver at the same instant and originating from the same GPS satellite

$$\begin{aligned} \rho_{GR} &= (\rho_{PR} + \rho_{CP})/2 = \\ &= \rho + c(\delta t - \delta t_{GPS}) + N + S_{GR} + \epsilon_{GR} \quad , \end{aligned} \quad (3.6)$$

where  $N = \lambda_1 N_{CP}/2$  is the unknown GRAPHIC bias,  $S_{GR}$  and  $\epsilon_{GR}$  are the arithmetic average of the respective PR and CP values. Besides being independent of ionospheric path delays,  $\rho_{GR}$  exhibits a two times smaller noise level (i.e.,  $\epsilon_{GR} \approx \epsilon_{PR}/2$ ) than the pseudorange.



The SDCP observation is obtained by subtracting two carrier phase measurements taken by two GPS receivers at the same instant and originating from a commonly tracked GPS satellite

$$\begin{aligned}\rho_{\text{SDCP}} = \Delta\rho_{\text{CP}} &= \rho_{\text{CP}}^{\text{M}} - \rho_{\text{CP}}^{\text{T}} = \\ &= \Delta\rho + c\Delta\delta t + 2\Delta N - I_0\Delta L + \Delta S_{\text{CP}} + \Delta\epsilon_{\text{CP}} \quad .\end{aligned}\quad (3.7)$$

In line with the convention adopted so far  $\Delta$  denotes arithmetic differences between corresponding parameters relative to the *Main* (superscript M) and *Target* (superscript T) spacecraft (i.e.,  $\Delta(\cdot) = (\cdot)^{\text{M}} - (\cdot)^{\text{T}}$ ). If compared with the elementary carrier phase observation, the GPS satellite clock offset is eliminated in the SDCP data type (i.e.,  $\Delta\delta t_{\text{GPS}} = 0$ ) which could also profit from the cancellation of common hardware dependent errors (i.e.,  $\Delta|S_{\text{CP}}| < |S_{\text{CP}}|$ ). Furthermore for small inter-satellite separations ( $< 5$  km) the single difference ionospheric path delay might become smaller than the signal noise (i.e.,  $I_0\Delta L$  is on sub-centimeter level) like demonstrated using flight data from the GRACE mission [van Barneveld et al., 2008].

An unbiased but less accurate single difference data type can be formed by subtracting code measurements taken by two GPS receivers at the same instant and originating from a commonly tracked GPS satellite

$$\begin{aligned}\rho_{\text{SDPR}} = \Delta\rho_{\text{PR}} &= \rho_{\text{PR}}^{\text{M}} - \rho_{\text{PR}}^{\text{T}} = \\ &= \Delta\rho + c\Delta\delta t + I_0\Delta L + \Delta S_{\text{PR}} + \Delta\epsilon_{\text{PR}} \quad .\end{aligned}\quad (3.8)$$

Finally the DDCP measurement is obtained by subtracting two SDCP observables taken by the same two GPS receivers at the same instant but each relating to a different GPS satellite

$$\begin{aligned}\rho_{\text{DDCP}} = \Delta_j^k \rho_{\text{SDCP}} &= \rho_{\text{SDCP}}^k - \rho_{\text{SDCP}}^j = \\ &= \Delta_j^k \Delta\rho + \Delta_j^k \Delta N_{\text{C}} - I_0 \Delta_j^k \Delta L + \Delta_j^k \Delta S_{\text{CP}} + \Delta_j^k \Delta\epsilon_{\text{CP}}\end{aligned}\quad (3.9)$$

where the operator  $\Delta_j^k$  denotes arithmetic differences between corresponding parameters relative to the  $k$ th (superscript k) and  $j$ th (superscript j) GPS satellite (i.e.,  $\Delta_j^k(\cdot) = (\cdot)^k - (\cdot)^j$ ). The resulting double difference operator  $\Delta_j^k \Delta(\cdot)$  is usually denoted in literature by the symbol  $\nabla \Delta_j^k(\cdot)$ . This combination removes completely the GPS receiver clock offset (i.e.,  $\Delta_j^k \Delta\delta t = 0$ ) as well as common systematic errors (i.e.,  $\Delta_j^k \Delta|S_{\text{CP}}| < \Delta|S_{\text{CP}}|$ ). In particular hardware dependent line biases present in the SDCP ambiguities  $2\Delta N$ —which are still float values—are canceled out in the DDCP ambiguities  $2\Delta_j^k \Delta N$ —which are now of integer nature (i.e.,  $2\Delta_j^k \Delta N = \Delta_j^k \Delta N_{\text{C}}$ ).

In the sequel the Kalman filter formulation assumes that all the systematic errors and biases (captured in the terms  $S_{\text{PR}}$ ,  $S_{\text{CP}}$  and their combinations) are zero. Furthermore the thermal noise for each observation (captured in the terms  $\epsilon_{\text{PR}}$ ,  $\epsilon_{\text{CP}}$  and their combinations) is assumed to be purely random with a zero mean. As a consequence, according to Eqs. (3.2-3.9), the considered GPS data types can be easily modeled in a form compatible with the second part of Eqs. (3.1), provided that geometric ranges, clock offsets, ionospheric path delays and carrier phase ambiguities can be related to the EKF state vector.

### 3.2.2 Selection of Measurements and State Parameters

#### Proposed state and measurements concepts

The objective is to find the most efficient filter design that meets the functional and performance requirements as specified in Section 3.2. According to the discussion above the most accurate GPS measurements available which bring along absolute orbit information are the GRAPHIC data types  $\rho_{GR}$ , while the most accurate relative navigation observables are the DDCP data types  $\rho_{DDCP}$ . Both data combinations involve the usage of carrier phase measurements and thus require the laborious handling of carrier phase biases, float or integer valued. On the other hand, the easiest and least computational intensive approach is to use pseudorange measurements  $\rho_{PR}$  only for absolute navigation and implicitly derive the relative navigation information by subtracting two absolute filter states. In between these two extremes, ultimate accuracy using  $\rho_{GR}$  and  $\rho_{DDCP}$  or ultimate simplicity using  $\rho_{PR}$ , the optimal design solution is somewhat in the middle.

Table 3.1 identifies possible estimation concepts which could be applied for real-time GPS-based navigation. This is done through the detailed listing of state vector parameters  $\mathbf{y}$  and measurements  $\mathbf{z}$  of the proposed EKF variants. Furthermore the number of state parameters  $n$  (i.e., the dimension of the filter) and the maximum number of processed measurements  $m$  is indicated for each filter design. The first row of the table lists the four proposed sets of GPS observables to be used, namely –from left to right– GRAPHIC and DDCP, GRAPHIC and SDCP, PR and SDPR, PR only. Each set of observations can be adopted in a single EKF for combined absolute and relative navigation (cf. upper part of table 3.1), or in two different EKFs dedicated to absolute and relative navigation separately (cf. lower part of table 3.1). In the first case the state vector always comprises absolute position and velocity  $\mathbf{x}^{M,T}$ , GPS receiver clock offset  $c\delta t^{M,T}$  and  $n_p$  force model parameters  $\mathbf{p}^{M,T}$  of the *Main* and *Target* spacecraft (superscripts M and T). In the latter case the EKF's state vector for absolute navigation includes the same parameters for *Main*, while the EKF's state vector for relative navigation includes the relative position and velocity  $\Delta\mathbf{x}$  and the relative force model parameters  $\Delta\mathbf{p}$  of *Main* with respect to *Target*.

Depending on the specific selection of measurement sets (i.e., column in table 3.1), additional state parameters have to be included in the state vector for estimation (cf.  $\mathbf{y}$  row in table 3.1). Combined filter concepts based on PR only or PR and SDPR require the estimation of the vertical path delay  $I_0$ , the ones based on CP measurements must estimate, in addition, the carrier phase ambiguities (float GRAPHIC biases  $N^{M,T}$  and/or integer number of cycles  $N_C$ ). Number of measurements  $m$  and number of estimation states  $n$  vary depending on the adopted filter concept, thus driving the overall EKF dimension and the number of necessary operations. The Phoenix-S GPS receiver offers 12 single-frequency channels, and thus allows the collection of a maximum of 12 simultaneous and independent pseudorange and carrier phase measurements. Out of these, a maximum total of 12 SD or 11 DD independent carrier phase data types can be formed.

**Table 3.1:** Possible state and measurements vector for real-time GPS-based navigation.

		GRAPHIC DDCP	GRAPHIC SDCP	PR SDPR	PR
<u>Combined EKF</u>					
$\mathbf{z} =$		$\rho_{GR}^{M,T}, \rho_{DDCP}$	$\rho_{GR}^{M,T}, \rho_{SDCP}$	$\rho_{PR}^M, \rho_{SDPR}$	$\rho_{PR}^{M,T}$
$m =$		35	36	24	24
$\mathbf{y} =$	$(\mathbf{x}, \mathbf{p}, c\delta t)^{M,T}$	$I_0, \mathbf{N}^{M,T}, \mathbf{N}_C$	$I_0, \mathbf{N}^{M,T}$	$I_0$	$I_0$
$n =$	$14 + n_p +$	36	25	1	1
<u>Split EKF</u>					
Absolute navigation					
$\mathbf{z} =$		$\rho_{GR}^M$	$\rho_{GR}^M$	$\rho_{PR}^M$	-
$m =$		12	12	12	-
$\mathbf{y} =$	$(\mathbf{x}, \mathbf{p}, c\delta t)^M$	$\mathbf{N}^M$	$\mathbf{N}^M$	$I_0$	-
$n =$	$7 + n_p +$	24	24	1	-
Relative navigation					
$\mathbf{z} =$		$\rho_{DDCP}$	$\rho_{SDCP}$	$\rho_{SDPR}$	-
$m =$		11	12	12	-
$\mathbf{y} =$	$\Delta \mathbf{x}, \Delta \mathbf{p}$	$I_0, \mathbf{N}_C$	$c\Delta \delta t, I_0, \Delta \mathbf{N}$	$c\Delta \delta t, I_0$	-
$n =$	$6 + n_p +$	12	13	2	-

Here the number of force model parameters of a combined filter design is  $n_p = 11$ , including empirical accelerations for *Main* and *Target* (i.e., 3x2 coeff.), drag coefficients for *Main* and *Target* (i.e., 1x2 coeff.) and control maneuvers for *Main* only (i.e., 3 coeff.). For a split EKF design  $n_p = 7$  for both absolute and relative navigation. The resulting maximum dimension of the combined filter design is  $n = 14 + n_p + 36 = 61$  with  $m = 12 + 12 + 11 = 35$  when using GRAPHIC and DDCP, or  $n = 14 + n_p + 25 = 50$  with  $m = 36$  when using GRAPHIC and SDP (cf. table 3.1). The pseudorange-based EKFs are much smaller and can reach a dimension of  $n = 7 + n_p + 1 = 15$  with  $m = 12$  when using PR and SDPR data types.

#### Concept selection through decision-matrix

The selection of the trade-off concept which best meets the key requirements is here based on a Pugh decision-matrix method. Table 3.2 shows the scoring matrix of evaluation criteria versus alternative filter estimation concepts. The key engineering requirements and goals form the basis for the definition of the selection criteria listed in the first column of the Pugh matrix (e.g., Absolute and relative navigation accuracy, computational load, maneuver handling, etc.). On the other hand, the alternatives listed in the first row are the different filter implementations identified in the previous section. The scorings of table 3.2 are based on a seven level scale from -3 to +3 which indicates how well the concept might meet the requirement criteria (i.e.,  $< 0$  concept does not fulfill criterion,  $> 0$  concept does meet criterion, -3 extremely bad, +3 extremely well). The scoring results are summed up for each alternative to obtain a measure (i.e., Total row in table 3.2) of how well the concept could potentially meet the specified requirements.

All the selected filter concepts are able to achieve the desired absolute navigation accuracy of 3 m and 1 cm/s (3D, RMS) [Kroes, 2006], [Leung, 2003]. Thus all the correspondent entries of table 3.2 are positive. The worst performance is known to be given by the combined PR and by the split PR, SDPR

**Table 3.2:** Pugh decision matrix for real-time GPS-based estimation concept.

Selection Criteria	Split GR,DDCP	Combined GR,DDCP	Split GR,SDCP	Combined GR,SDCP	Split PR,SDPR	Combined PR,SDPR	Combined PR
Absolute nav. acc.	2	3	1	2	0	1	0
Relative nav. acc.	3	3	2	2	-1	-1	-3
Exploit. of dynamics	0	2	0	2	0	2	0
Exploit. of measures	1	3	0	2	-2	-2	-1
Robust to attitude	-2	1	-1	2	-1	-1	3
Robust to data gaps	-1	0	-1	0	-1	1	2
Initialization	-2	1	-1	2	0	3	3
Maneuver handling	-1	2	-1	2	-2	1	1
Computational load	1	-1	1	0	3	2	2
Overall complexity	-2	-1	0	1	2	3	3
+	7	15	4	15	5	13	14
-	8	2	4	0	7	4	4
Total	-1	13	0	15	-2	9	10

filters (i.e., score 0). Slightly better absolute navigation accuracy is expected to be given by the combined PR, SDPR due to the usage of single differences in a combined absolute/relative navigation filter (i.e., score 1). The best accuracy is provided by the filters which make use of GRAPHIC data types with the consequent elimination of ionospheric path delays (i.e., scores between 1 and 3). Slight variations of the scoring are due to the adoption of a combined filter, where SDCP and DDCP may contribute to the absolute navigation, or a split filter structure.

The relative navigation accuracy requirement of 0.2 m and 0.2 mm/s (3D, RMS) can be hardly fulfilled by the pseudorange based filters (i.e., negative scores for PR and SDPR). Better chances are offered by SDPR data types which can take advantage of common systematic error cancellations. The utmost relative navigation accuracy is obviously provided by the SDCP and DDCP filters (centimeter to millimeter level depending on integer ambiguity fixing).

The combined EKFs fully exploit the interdependency of absolute and relative dynamics in a common filter (i.e., score 2), while the split EKFs treat the absolute and relative motion separately (i.e., score 0). Furthermore the full information content of the available GPS measurements is only used by the proposed combined GR, CP based filters (i.e., score 2 and 3 for SDCP and DDCP, respectively). Separate absolute and relative navigation filters do not make use of GRAPHIC data types of the *Target* spacecraft (i.e., score 1 and 0 for SDCP and DDCP, respectively), while PR based concepts get negative scores only. Similar considerations apply to the robustness of the filters to different spacecraft attitude and GPS data gaps. Combined filters provide robustness in the case that *Main* and *Target* do not have common GPS satellites in view, while separate absolute/relative filters reconstruct the *Target* orbit using only SD and DD measurements. In general initialization and maneuver handling procedures within the navigation process are simplified with combined filters where only absolute estimates are performed.

Key criteria of the selection process are computational load and overall filter complexity. The computational load of the proposed concepts is driven by the number of operations required by the EKF, and in particular by the mea-

surement update. For large filter sizes, the weighted operations count<sup>1</sup> of a conventional measurement update is of the order  $3n^2m$  after  $m$  observations [Bierman, 2006]. Applied to our filter concepts, this gives best performance for the split PR, SDPR filter with  $3n^2m \approx 15000$  operations. Three times slower are the combined PR and PR, SDPR filters with about 48000 operations. The split filters based on GR and CP require about 74000 operations. The most computationally intensive solutions are the combined GR, SDCP which employs circa 260000 operations and the combined GR, DDCP concept with about 380000 weighted operations. The navigation filter complexity increases gradually from right to left in table 3.2 (cf. Overall complexity selection criteria). The combined PR and PR, SDPR filters are of simple implementation and validation, while the split and combined GR, DDCP are the most complex to handle due to the processing of integer ambiguities.

#### Details on selected estimation concept

According to the Pugh decision-matrix in table 3.2 the concept that is most likely to satisfy our goals and requirements is the combined EKF processing of GRAPHIC and SDCP data types (i.e., total score 15). Compared to the other alternatives this concept suffers from a relatively high computational load and complexity, but guarantees good navigation accuracy, robustness to attitude uncertainty and different GPS antenna orientations, simplicity in filter initialization and maneuver handling. A similar filter concept adopting DDCP measurements obtains a high scoring (i.e., total score 13), but is abandoned mainly because of the extreme computational load and the higher complexity due to the handling of integer carrier phase ambiguities. Good results are obtained by the combined PR, SDPR and PR only filters (i.e., total scores 9 and 10, respectively), which are anyway penalized by the expected poor navigation accuracy and measurements exploitation. Finally the independent absolute and relative navigation filters are judged as not sufficient to meet the specified requirements especially because of the lack of robustness and architecture simplicity (i.e., negative total scores). Please note that these results are only intended as guidelines for the choice of a preliminary design concept. Only the careful subsequent testing and validation can ultimately conclude on the suitability of the navigation system.

The selected filter estimation parameters

$$\mathbf{y} = \left( (\mathbf{x}; \mathbf{p}; c\delta t; \mathbf{N})^M; (\mathbf{x}; \mathbf{p}; c\delta t; \mathbf{N})^T; \delta \mathbf{v} \right), \quad (3.10)$$

comprise the 6-dimensional spacecraft state in the ECI frame  $\mathbf{x} = (\mathbf{r}; \mathbf{v})$ , the scalar GPS receiver clock offset  $c\delta t$ , a fixed number of force model parameters  $\mathbf{p} = (C_D; \mathbf{a}_{\text{emp}})$ , including the aerodynamic drag coefficient  $C_D$  and 3 empirical accelerations  $\mathbf{a}_{\text{emp}}$  in the local orbital frame, and the 12 GRAPHIC float

<sup>1</sup>A weighted operations count is defined in Bierman [2006] as the equivalent total number of required arithmetic additions. The relative weights of the other arithmetic operations is defined by the single precision model UNIVAC 1108 where  $\tau_x \approx 1.4\tau_+$  and  $\tau_f \approx 4.5\tau_+$  are the operation times.

biases  $N$  for each GPS receiver channel. Next to these 23 parameters, which are estimated for each of the co-orbiting spacecraft (superscripts M and T for *Main* and *Target*, respectively), we decide to include the 3 *Main* orbit maneuver increments  $\delta v$  expressed again in the local orbital frame for a total  $n = 49$ . This approach gives the possibility to incorporate the orbit control maneuvers within the navigation process through their direct estimation, and to take into account deficiencies of the maneuver model via dedicated white or colored process noise. Note that in accordance with the considerations made on Eqs. (3.6) and (3.7) we have decided to remove the vertical ionospheric path delay  $I_0$  from the estimation state vector. In fact the adopted GPS data types can be considered as ionosphere-free combinations for small inter-satellite separations ( $<5$  km), being  $I_0 \Delta L \approx 0$  [van Barneveld et al., 2008].

The selected GPS measurements vector

$$\mathbf{z} = (\boldsymbol{\rho}_{\text{GR}}^{\text{M}}; \boldsymbol{\rho}_{\text{GR}}^{\text{T}}; \boldsymbol{\rho}_{\text{SDCP}}) \quad , \quad (3.11)$$

comprises a maximum of 12 GRAPHIC data types  $\boldsymbol{\rho}_{\text{GR}}^{\text{M}}$  taken by the *Main* spacecraft receiver, a maximum of 12 GRAPHIC data types  $\boldsymbol{\rho}_{\text{GR}}^{\text{T}}$  taken by the *Target* spacecraft receiver, and a maximum of 12 single difference carrier phase measurements  $\boldsymbol{\rho}_{\text{SDCP}}$  related to the GPS satellites which are commonly visible by the two spacecraft. The maximum number of processed observations is given by  $m = 36$  and provides a high level of redundancy to the filter because GRAPHIC and SDCP observations which involve the same GPS satellite are not independent (cf. Eqs. (3.6) and (3.7)).

### 3.2.3 Kalman Filter Modeling

Having selected the filter state vector estimation parameters  $\mathbf{y}$  and the adopted measurements  $\mathbf{z}$ , we can continue the characterization of the linear system of Eq. (3.1) by addressing the computation of the state transition matrix  $\boldsymbol{\Phi}$ , the measurement coefficients matrix  $\mathbf{H}$ , as well as the associated process noise  $\mathbf{G}\mathbf{w}$  and measurement errors  $\boldsymbol{\epsilon}$ .

#### State transition matrix, $\boldsymbol{\Phi}$

The state transition matrix provides the direct mapping from an initial state at time  $t_0$  to the final state at any particular time  $t$  and can be defined as

$$\boldsymbol{\Phi}(t, t_0) = \left[ \frac{\partial \mathbf{y}(t)}{\partial \mathbf{y}(t_0)} \right]_{49 \times 49} . \quad (3.12)$$

The structure of the transition matrix applied to the selected filter concept is given by

$$\boldsymbol{\Phi}(t, t_0) = \begin{bmatrix} \boldsymbol{\Phi}_{23 \times 23}^{\text{M}} & \mathbf{0} & \boldsymbol{\Phi}_{23 \times 3}^{\delta v} \\ \mathbf{0} & \boldsymbol{\Phi}_{23 \times 23}^{\text{T}} & \mathbf{0} \\ \mathbf{0} & \mathbf{0} & \mathbf{1}_{3 \times 3} \end{bmatrix}_{49 \times 49} , \quad (3.13)$$

being  $\boldsymbol{\Phi}^{\text{M}}$  and  $\boldsymbol{\Phi}^{\text{T}}$  the transition matrices of the uncontrolled orbit motion of *Main* and *Target*, respectively, and  $\boldsymbol{\Phi}^{\delta v}$  the transition matrix mapping an orbit

maneuver increment at time  $t_M \in [t_0, t]$  to the *Main* spacecraft orbit motion at time  $t$ . The only estimation parameters linked to the impulsive maneuver  $\delta v$  via the state transition matrix are the position and velocity of *Main* and the velocity variation itself (cf. identity matrix  $\mathbf{1}_{3 \times 3}$  in Eq. (3.13)). The applied first order approximation of the state partial derivatives is given by

$$\Phi^{\delta v}(t, t_0) = \begin{bmatrix} (t - t_M) \mathbf{R}_{3 \times 3}^{\text{rtn}} \\ \mathbf{R}_{3 \times 3}^{\text{rtn}} \\ \mathbf{0} \end{bmatrix}_{23 \times 3}, \quad (3.14)$$

where  $\mathbf{R}^{\text{rtn}}$  represents the rotation matrix from the local Hill frame (in which the maneuver increments are given, cf. Fig. 2.1) to the ECI reference frame (where position and velocity are expressed).

$\Phi^{\text{M}}$  and  $\Phi^{\text{T}}$  are characterized by the same shape

$$\Phi^{\text{M}}(t, t_0) = \begin{bmatrix} \Phi_{6 \times 6}^x & \Phi_{6 \times 4}^{x,p} & \mathbf{0} & \mathbf{0} \\ \mathbf{0} & \Phi_{4 \times 4}^p & \mathbf{0} & \mathbf{0} \\ \mathbf{0} & \mathbf{0} & \Phi^{c\delta t} & \mathbf{0} \\ \mathbf{0} & \mathbf{0} & \mathbf{0} & \mathbf{1}_{12 \times 12} \end{bmatrix}_{23 \times 23}. \quad (3.15)$$

The GRAPHIC float biases are constant over a continuous tracking arc, thus the respective transition sub-matrix is the identity matrix  $\mathbf{1}_{12 \times 12}$ . The partial derivatives of the spacecraft orbit state with respect to its initial values  $\Phi^x$  and the partials with respect to the force model parameters  $\Phi^{x,p}$  are obtained through the numerical integration of the variational equations [Montenbruck and Gill, 2001a], which are discussed in the next section together with the selection of the dynamic model. The partials of the force model parameters at time  $t$  with respect to the force model values at time  $t_0$  are given by

$$\Phi^p(t, t_0) = \begin{bmatrix} \mathbf{1} & \mathbf{0} \\ \mathbf{0} & \Phi_{3 \times 3}^{a_{\text{emp}}} \end{bmatrix}_{4 \times 4}. \quad (3.16)$$

The aerodynamic drag coefficient is assumed as constant during the time interval  $(t - t_0)$ , thus a unity mapping scalar has been adopted in the transition matrix. As explained in the next subsection the entries of the state transition matrix relative to the GPS receiver clock offset  $\Phi^{c\delta t}$  and to the empirical accelerations  $\Phi^{a_{\text{emp}}}$  are treated as stochastic variables via the application of dedicated process noise models.

#### White and colored process noise, $Gw$

A wide class of random processes can be approximated by first-order exponentially correlated process noise (or colored noise) [Bierman, 2006]. A recursive mathematical description of such a process is

$$y(t) = \phi(t, t_0)y(t_0) + w(t), \quad (3.17)$$

where state parameter  $y$ , state transition function  $\phi$  and process noise  $w$  are denoted using the same variables adopted in Eq. (3.1). In particular the model of the random process is given by

$$\phi = e^{-(t-t_0)/\tau}, \quad (3.18)$$

being  $\tau$  the correlation time constant of the process, and

$$w = w_\delta \sqrt{\frac{\sigma^2 \tau}{2} (1 - \phi^2)} \quad . \quad (3.19)$$

$w$  and  $w_\delta$  are white, zero mean, Gaussian noise characterized by variance

$$E(w^2) = q = \sigma^2(1 - \phi^2) \quad E(w_\delta^2) = \delta(t - t_0) \quad , \quad (3.20)$$

where  $\delta(t)$  is the Dirac delta function.

Vector-valued colored-noise problems are comprised of concatenations of scalar processes. The degree of correlation of the random process  $\phi$  is determined by the choice of  $\sigma$  and  $\tau$  which can be tuned, or even estimated [Cruickshank, 1998], to generate several time correlated random functions. In our context the colored noise is well suited to model the empirical accelerations  $\mathbf{a}_{\text{emp}}$  in the radial, along-track and cross-track direction. These parameters are considered to compensate for any modeling deficiencies in the employed spacecraft dynamics. Furthermore the usage of process noise in an EKF is shown to improve overall accuracy and maintain non-negativity and symmetry of the computed covariance [Bierman, 2006]. Considering typical orbital periods of roughly 5000 s for LEO satellites and representative measurement intervals of 30 s, a correlation time constant of 900 s is found to be well suitable for sequential estimation of the empirical accelerations (cf. [Kroes, 2006]). In the sequel the mapping factor given by Eq. (3.18) is used to compute the individual entries of the empirical accelerations in the state transition matrix of Eq. (3.16)

$$\Phi^{\mathbf{a}_{\text{emp}}}(t, t_0) = \begin{bmatrix} \phi_r & 0 & 0 \\ 0 & \phi_t & 0 \\ 0 & 0 & \phi_n \end{bmatrix}_{3 \times 3} \quad , \quad (3.21)$$

process noise model  $w_{\mathbf{a}_{\text{emp}}}$  and variance  $q_{\mathbf{a}_{\text{emp}}}$  are given by Eqs. (3.19) and (3.20), respectively.

The process noise model described by Eqs. (3.17)-(3.20) reduces to a white noise sequence in the case  $\tau = 0$ , which gives  $y(t) = w(t)$ . On the other extreme, for a finite value of  $\sigma^2$  and  $\tau \rightarrow \infty$ , the model reduces to  $y(t) = y(t_0) + w(t)$ , which describes a random walk process. The latter is here adopted to model the user clock offset, with a resulting scalar mapping factor

$$\Phi^{c\delta t} = 1 \quad , \quad (3.22)$$

and a process noise which can be obtained from Eq. (3.19) with  $\tau \rightarrow \infty$  as

$$w_{c\delta t} = w_\delta \sigma_{c\delta t} \sqrt{t - t_0} \quad . \quad (3.23)$$

The variance of such a random walk process model is given by

$$q_{c\delta t} = \sigma_{c\delta t}^2 (t - t_0) / \tau_{c\delta t} \quad . \quad (3.24)$$

Depending on the adopted model, colored noise for empirical accelerations and random walk for GPS receiver clock offsets, Eqs. (3.20) and (3.24) are used



to update the EKF covariance. No process noise is added to the other filter estimation parameters, thus

$$\mathbf{G}(t, t_0)\mathbf{w} = \begin{bmatrix} \mathbf{0} & 0 & \mathbf{0} & 0 \\ \mathbf{1}_{3 \times 3} & 0 & \mathbf{0} & 0 \\ 0 & 1 & \mathbf{0} & 0 \\ 0 & 0 & \mathbf{0} & 0 \\ 0 & 0 & \mathbf{1}_{3 \times 3} & 0 \\ 0 & 0 & \mathbf{0} & 1 \\ 0 & 0 & \mathbf{0} & 0 \end{bmatrix}_{49 \times 8} \begin{pmatrix} \mathbf{w}_{a_{\text{emp}}}^M \\ w_{c\delta t}^M \\ \mathbf{w}_{a_{\text{emp}}}^T \\ w_{c\delta t}^T \end{pmatrix}. \quad (3.25)$$

#### Measurement coefficients matrix, $\mathbf{H}$

The measurement coefficients matrix provides the direct mapping from the state estimation parameters to the measurements vector at time  $t$  and can be defined as

$$\mathbf{H}(t) = \begin{bmatrix} \frac{\partial \mathbf{z}(t)}{\partial \mathbf{y}(t)} \end{bmatrix}_{36 \times 49}. \quad (3.26)$$

Because the Phoenix-S GPS receiver provides its measurements synchronized to integer GPS seconds, the filter implementation is also simplified, because a common measurement epoch  $t$  can be chosen for which the *Main* and *Target* pseudorange and carrier phases are available. The structure of the measurement coefficients matrix applied to the selected filter concept is

$$\mathbf{H}(t) = \begin{bmatrix} \mathbf{H}_{12 \times 6}^M & \mathbf{0} & \mathbf{1}_{12 \times 1} & \mathbf{1}_{12 \times 12} & \mathbf{0} & \mathbf{0} & \mathbf{0} & \mathbf{0} & \mathbf{0} \\ \mathbf{0} & \mathbf{0} & \mathbf{0} & \mathbf{0} & \mathbf{H}_{12 \times 6}^T & \mathbf{0} & \mathbf{1}_{12 \times 1} & \mathbf{1}_{12 \times 12} & \mathbf{0} \\ \mathbf{H}_{12 \times 6}^M & \mathbf{0} & \mathbf{1}_{12 \times 1} & \mathbf{2}_{12 \times 12} & -\mathbf{H}_{12 \times 6}^T & \mathbf{0} & \mathbf{1}_{12 \times 1} & -\mathbf{2}_{12 \times 12} & \mathbf{0} \end{bmatrix}_{36 \times 49}. \quad (3.27)$$

As given by the GRAPHIC measurement model of Eq. (3.6), the partial derivatives of  $\rho_{\text{GR}}^M$  with respect to the receiver clock offset  $c\delta t$  and to the GRAPHIC ambiguities  $N$  form the identity matrices  $\mathbf{1}_{12 \times 1}$  and  $\mathbf{1}_{12 \times 12}$ , respectively. The same applies for the *Target* GRAPHIC measurements  $\rho_{\text{GR}}^T$ . Similarly the partials of the SDCP data types  $\rho_{\text{SDCP}}$  can be computed from Eq. (3.7) as  $\mathbf{1}_{12 \times 1}$  (with respect to the *Main* and *Target* clock offsets),  $\mathbf{2}_{12 \times 12}$  (with respect to the *Main* GRAPHIC biases) and  $-\mathbf{2}_{12 \times 12}$  (with respect to the *Target* GRAPHIC biases), where  $\mathbf{2}_{12 \times 12} = 2 \cdot \mathbf{1}_{12 \times 12}$ .  $\mathbf{H}^M$  and  $\mathbf{H}^T$  represent the partial derivatives of the GPS measurements with respect to the ECI position and velocity of the *Main* and *Target* spacecraft, respectively. Considering again the measurement model given by Eq. (3.6), no dependency on the spacecraft velocity is observable while the only quantity depending on the position is the geometric range vector  $\boldsymbol{\rho}$ , thus

$$\mathbf{H}^M = \begin{bmatrix} \frac{\partial \rho_{\text{GR}}}{\partial \mathbf{r}^M} & \frac{\partial \rho_{\text{GR}}}{\partial \mathbf{v}^M} \end{bmatrix}_{12 \times 6} = \begin{bmatrix} \frac{\partial \boldsymbol{\rho}}{\partial \mathbf{r}^M} & \mathbf{0} \end{bmatrix}_{12 \times 6}. \quad (3.28)$$

The geometric range is the distance between the antenna phase center position of the user GPS receiver  $\mathbf{r}^{\text{ant}}$  at the time of signal reception  $t$  and the antenna phase center position of the GPS satellite  $\mathbf{r}^{\text{GPS}}$  at the time of signal transmission ( $t - \tau_c$ ), where both positions are expressed in the ECEF frame and  $\tau_c$

represents the true light travel time. To first order the partial derivative of the geometric range with respect to the inertial spacecraft position is then given by the unit vector aligned with the line of sight  $\mathbf{o}_s$ , with opposite sign, and mapped into the ECI reference frame as follows

$$\frac{\partial \rho(t)}{\partial \mathbf{r}} = -\mathbf{R}^{\text{ecef}} \mathbf{o}_s = -\mathbf{R}^{\text{ecef}} \frac{\mathbf{r}^{\text{gps}}(t - \tau_c) - \mathbf{r}^{\text{ant}}(t)}{\|\mathbf{r}^{\text{gps}}(t - \tau_c) - \mathbf{r}^{\text{ant}}(t)\|}, \quad (3.29)$$

where  $\mathbf{R}^{\text{ecef}}$  represents the rotation matrix from the ECEF frame (in which the modeled pseudorange is computed) to the ECI frame (where state position and velocity are expressed).

The resulting expression of the GPS measurement partials in Eq. (3.29) implies the availability on-board of the GPS satellite positions and clock offsets, necessary to compute  $\mathbf{r}^{\text{gps}}(t - \tau_c)$ , and the spacecraft attitude, necessary to take into account the GPS antenna offset with respect to the spacecraft center of mass and consequently compute  $\mathbf{r}^{\text{ant}}(t)$  from the estimated ECI position. In the frame of this real-time navigation system development, the GPS satellite and clock offsets are obtained from the GPS receiver broadcast ephemerides. The satellite attitude is instead provided by the Attitude and Orbit Control System (AOCS) of the co-orbiting spacecraft. Obviously any error in the provided GPS broadcast ephemerides and spacecraft attitude propagates directly into the modeled observations and measurement partials.

#### Measurements random noise, $\epsilon$

The Phoenix-S GPS receiver measurement errors are modeled as random white noise with zero mean and standard deviation  $\sigma$  within the real-time navigation filter (cf. Eqs. (3.17)-(3.20) with  $\tau = 0$ ). As shown in Fig. 3.2, the measurement noise level depends on the observation type and on the carrier to noise density ratio  $C/N_0$  at which the observation was taken. At a representative  $C/N_0$  level of 42 dB-Hz pseudorange and carrier phase measurements with a standard deviation of 0.5 m and 0.7 mm have been obtained in pre-flight qualification tests [Montenbruck and Renaudie, 2007] conducted in a GPS signal simulator testbed.

The results shown in Fig. 3.2 for the pseudorange, carrier phase and Doppler measurements are consistent with the tracking loop characteristics of the Phoenix-S GPS receiver as shown by the following measurement standard deviation model [Ward, 1996]

$$\begin{aligned} \sigma_{\text{PR}} &= \frac{c}{1.023 \cdot 10^6} \sqrt{\frac{b_{\text{dll}}}{\text{SNR}}} \\ \sigma_{\text{CP}} &= \frac{\lambda_1}{2\pi} \sqrt{\frac{b_{\text{pll}}}{\text{SNR}}} \end{aligned}, \quad (3.30)$$

where  $b_{\text{dll}} = 1/12 \text{ Hz}$  and  $b_{\text{pll}} = 8 \text{ Hz}$  are the receiver Delay Lock Loop (DLL) and Phase Lock Loop (PLL) bandwidths, and

$$\text{SNR} = 10^{\frac{C/N_0}{10}} \quad (3.31)$$

is the signal to noise ratio of the observation.

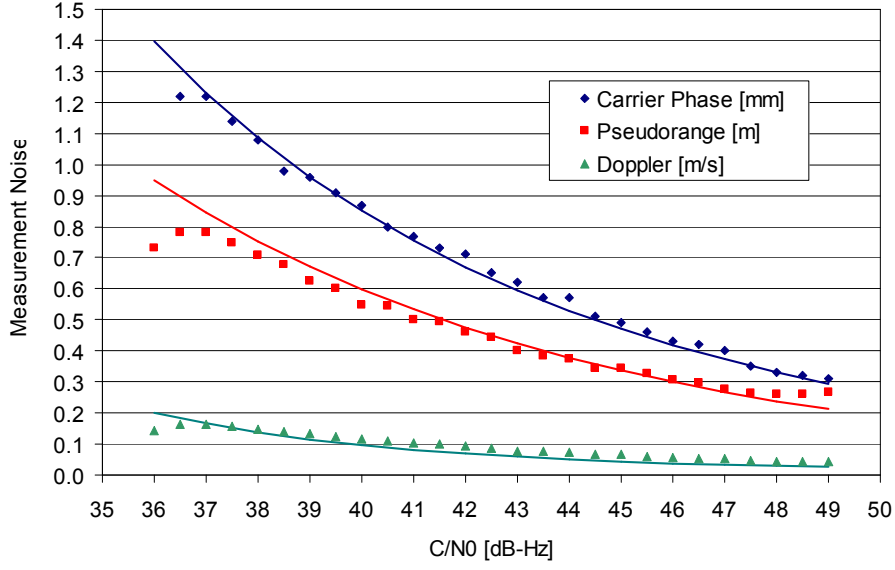


**Fig. 3.2:** Phoenix-S measurement noise standard deviation as a function of the carrier to noise density ratio [Montenbruck and Renaudie, 2007].

Eq. (3.30) will be used in the sequel to emulate the measurements produced by the GPS receiver and perform a realistic numerical validation of the navigation system. The GPS observables which are explicitly processed by the navigation system are the GRAPHIC and SDCP data types. According to the measurement models of Eqs. (3.6) and (3.7), the respective noise standard deviations are approximated by

$$\begin{aligned} \sigma_{GR} &\approx \sigma_{PR}/2 \\ \sigma_{SDCP} &\approx \sqrt{2}\sigma_{CP} \end{aligned} \quad (3.32)$$

The single difference carrier phase noise level is a factor  $\sqrt{2}$  larger than the carrier phase, provided that the individual measurements are independent and have been taken at the same carrier to noise density ratio.

### 3.2.4 Extended Kalman Filter Algorithm

Given the system of state-propagation equations and observation state equations in (3.1), the Kalman filter is able to find the linear, unbiased, minimum variance estimate  $\hat{\mathbf{y}}$  of the state  $\mathbf{y}$  in a sequential two-stages process. The so-called *time update* at step  $i$  comprises the propagation of the filter state  $\hat{\mathbf{y}}^+$  and associated covariance estimate  $\mathbf{P}^+$  from the previous epoch  $t_{i-1}$  to the current epoch  $t_i$  as

$$\begin{aligned} \hat{\mathbf{y}}_i^- &= \mathbf{y}(t_i, \hat{\mathbf{y}}_{i-1}^+) \\ \mathbf{P}_i^- &= \Phi_i \mathbf{P}_{i-1}^+ \Phi_i^t + \mathbf{G}_i \mathbf{Q}_i \mathbf{G}_i^t \end{aligned} \quad (3.33)$$

A process noise matrix is employed to cope with residual modeling deficiencies and to keep the Kalman filter receptive to new measurements

$$\mathbf{Q}(t) = \begin{bmatrix} \mathbf{q}_{\text{aemp}}^M & 0 & \mathbf{0} & 0 \\ \mathbf{0} & q_{\text{c}\delta t}^M & \mathbf{0} & 0 \\ \mathbf{0} & 0 & \mathbf{q}_{\text{aemp}}^T & 0 \\ \mathbf{0} & 0 & \mathbf{0} & q_{\text{c}\delta t}^T \end{bmatrix}_{8 \times 8}, \quad (3.34)$$

where  $\mathbf{q}_{\text{aemp}}$  and  $q_{\text{c}\delta t}$  are computed through Eqs. (3.20) and (3.24), respectively. The propagation of the filter state and the state transition matrix is done through numerical integration of the orbit trajectories and variational equations of *Main* and *Target* separately (cf. next section). Thus the first of eq. (3.1) is not used to update the state, as required by a conventional KF formulation.

Next a so-called *measurement update* is performed at step  $i$  to obtain the updated filter state and covariance at time  $t_i$  including the effects of the GPS measurements  $\hat{\mathbf{z}}(t_i)$ . In order to reduce the number of necessary arithmetic operations, the *measurement update* processes one observation  $\hat{z}_k$  at a time with  $k = 1, \dots, m$ , as follows

$$\begin{aligned} \mathbf{K}_i &= \mathbf{P}_i^- \mathbf{h}_{k_i} (\mathbf{h}_{k_i}^t \mathbf{P}_i^- \mathbf{h}_{k_i} + R_k)^{-1} \\ \mathbf{y}_i^+ &= \mathbf{y}_i^- + \mathbf{K}_i (\hat{z}_{k_i} - z_{k_i}) \\ \mathbf{P}_i^+ &= \mathbf{P}_i^- - \mathbf{K}_i \mathbf{h}_{k_i}^t \mathbf{P}_i^- \end{aligned} \quad (3.35)$$

Here  $\mathbf{h}_{k_i}$  is the  $n$ -dimensional vector of the  $k$ -th measurement partials extracted from row  $k$  of  $\mathbf{H}(t_i)$ .  $R_k$  is the  $k$ -th measurement a-priori covariance (or inverse weight). The  $n$ -dimensional Kalman gain vector  $\mathbf{K}_i$  multiplies the difference between the modeled scalar observation  $\hat{z}_k = \mathbf{h}_{k_i}^t \mathbf{x}^-$  (cf. the second of Eq. (3.1)) and the measurement  $z$  being actually processed.

Various approaches exist to implement and mechanize the measurement update given by Eq. (3.35). The choice of the appropriate method is driven by the necessity to reduce the computational load and guarantee, at the same time, the numerical stability of the filter. In particular various divergence phenomena have been reported in the last decades with Kalman filtering (e.g. due to incorrect a-priori statistics, presence of nonlinearities, computer roundoff errors) [Bierman, 2006]. Among them mainly the divergence due to computer round-off plays a role in the selection of the mechanization method. As shown by the last of Eq. (3.35), numerical errors which affect the arithmetic difference might produce covariance matrices that fail to retain non-negativity and symmetry. These phenomena are more pronounced when the filter is close to steady state and tries to update a covariance matrix whose elements are very small.

Three possible approaches to the Kalman measurement update are examined in Table 3.3 in terms of arithmetic operation counts and mechanization of the data processing algorithm. Let us first concentrate on the conventional Kalman formulation described in the left part of Table 3.3. First the product  $\boldsymbol{\alpha} = \mathbf{P}^- \mathbf{h}$  is computed, which requires  $n^2$  additions (cf. symbol  $+$  in Table 3.3) and  $n^2$  multiplications (cf. symbol  $\times$ ). Following Eq. (3.35), the auxiliary parameter  $\beta = (\mathbf{h}^t \boldsymbol{\alpha} + R)^{-1}$  is computed through  $n + 1$  additions,  $n$  multiplications

**Table 3.3:** Arithmetic operation counts for three possible mechanizations of the Kalman measurement update. The *Standard Kalman* and the *Joseph Stabilized* data processing assume a symmetric covariance matrix. The number of arithmetic operations provided refers to the processing of one scalar measurement.  $\alpha, \beta, \gamma$  are temporary work variables.

Computation	Kalman Standard			Joseph Stabilized			Selected Trade-off		
	+	x	/	+	x	/	+	x	/
$\alpha^t = h^t P^-$							$n^2$	$n^2$	
$\alpha = P^- h$	$n^2$	$n^2$		$n^2$	$n^2$		$n^2$	$n^2$	
$\beta = (h^t \alpha + R)^{-1}$	$n + 1$	$n$	1	$n + 1$	$n$	1	$n + 1$	$n$	1
$K = \alpha \beta$		$n$			$n$			$n$	
$\gamma = \hat{z} - z$	$n$			$n$			$n$		
$y^+ = y^- + K \gamma$	$n$	$n$		$n$	$n$		$n$	$n$	
$P^+ = P^- - K \alpha^t$	$(n^2 + n)/2$	$(n^2 + n)/2$		$(n^2 + n)/2$	$(n^2 + n)/2$		$n^2$	$n^2$	
$\bar{\alpha} = P^+ h$				$n^2$	$n^2$			$n^2$	
$\bar{P}^+ = P^+ - \alpha K^t + K R K^t$				$2n^2 + 3n$	$2n^2 + 3n$				
Total* $m$	$1.5n^2 + 3.5n + 1$	$1.5n^2 + 3.5n$	1	$4.5n^2 + 5.5n + 1$	$4.5n^2 + 5.5n$	1	$3n^2 + 3n + 1$	$3n^2 + 3n$	1

and the only division required by the measurement update. The Kalman gain is finally obtained by  $K = \alpha \beta$  (i.e.,  $n$  multiplications). The filter state is updated through the computation of the measurement residuals  $\gamma = \hat{z} - z$  and  $y^+ = y^- + K \gamma$  for a total of  $2n$  multiplications and  $n$  additions. While the operations counted so far are common to all the considered mechanization methods, the update of the covariance matrix is handled differently. The conventional Kalman formulation (cf. left part of Table 3.3) assumes a perfectly symmetric covariance matrix in the computation of  $P^+ = P^- - K \alpha^t$ . This approach allows the saving of the operations necessary to compute  $h^t P$  which is simply obtained from the transposition of  $\alpha$ , in addition the elements of the updated covariance matrix need only to be computed for the upper or lower triangular part of the matrix requiring only  $(n^2 + n)/2$  additions and multiplications. The drawback of the conventional mechanization is well analyzed in [Verhaegen, 1987] where it is shown how the implementation is especially sensitive to the covariance loss of symmetry. A theoretical error analysis demonstrates that an asymmetric error on the state-error covariance matrix leads to divergence due to the loss of symmetry when the original transition matrix  $\Phi$  is unstable, which is the case for typical orbit determination problems.

The middle part of Table 3.3 presents a formulation of the measurement update based on the Joseph algorithm [Bucy and Joseph, 1968] slightly modified by Bierman [2006]. It differs from the standard formulation by two additional steps in the mechanization process. In particular an updated  $\bar{\alpha} = P^+ h$  and the Kalman gain are used to re-compute the covariance  $\bar{P}^+$  with an additional effort of  $3n^2 + 3n$  multiplications and additions. This formulation ensures that  $P^+$  is always positive definite and can exploit the symmetry of the covariance matrix, irrespective of numerical roundoff errors. Furthermore it has proven to be numerically better conditioned than the usual Joseph stabilized formula due to the averaging of the off-diagonal elements of the covariance matrix. However the computational load is nearly three times higher than the conventional implementation and does not appear suitable for real-time or on-board appli-

cations.

The mechanization selected in this research is presented in the right part of Table 3.3. In order to reduce the sensitivity to numerical roundoff errors, this trade-off formulation does not assume the symmetry of the covariance matrix. This choice has two basic consequences, first of all the term  $\mathbf{h}^t \mathbf{P}^-$ , contained in the last of Eq. (3.35), does not match  $(\mathbf{P}^- \mathbf{h})^t$ , which has already been computed in the first steps. The computation of  $\alpha^t$  can not be done by simply transposing  $\alpha$ , but has to be repeated (cf. first line of Table 3.3) producing  $n^2$  supplementary additions and multiplications. Second of all the update of the covariance matrix has to be done for all its terms, and not only for the upper or lower triangular part, requiring additional  $(n^2 - n)/2$  additions and multiplications compared to the standard formulation.

In contrast to the Joseph stabilized formula, the resulting process requires an arithmetic operation count which is less than two times higher than the unstable Kalman formulation, which makes it the best candidate for implementation into the real-time navigation system.

### 3.3 Orbit Dynamics Modeling

As introduced in the previous section, the time update of the extended Kalman filter requires the numerical propagation of the spacecraft trajectory (cf. first of Eq. (3.33)) and the computation of the partial derivatives of the orbit state with respect to its initial value and with respect to the force model parameters (cf. second of Eq. (3.33)).

The orbit position-velocity vector is obtained through the numerical integration of the following first-order differential equation

$$\dot{\mathbf{x}} = \mathbf{f}(t, \mathbf{x}(t), \mathbf{p}(t)) = \begin{pmatrix} \mathbf{v} \\ \dot{\mathbf{v}}(t, \mathbf{r}, \mathbf{v}, \mathbf{p}) \end{pmatrix} . \quad (3.36)$$

The acceleration acting on the spacecraft  $\dot{\mathbf{v}}$  is caused by gravitational and non-gravitational forces characterized by time-varying parameters  $\mathbf{p}$ , which are also estimated by the reduced-dynamic orbit determination process. Although the force model used to compute these accelerations has little impact on the achievable navigation accuracy, compared to the quality of the GPS measurements, the choice of the dynamic models is the key driver of the orbit prediction accuracy. In fact in the absence of valid GPS observables, the measurement update of the EKF can not be performed and only a time update takes place whose accuracy is mainly driven by the performance of the force model. In addition, the use of accurate dynamics allows the filter to smooth out un-modeled systematic errors over a certain period of time which is governed by the prescribed process noise correlation time scale.

Aside from the numerical integration of the orbit state vector  $\mathbf{x}$ , the partials with respect to the initial values  $\Phi^{\mathbf{x}}(t, t_0)$  and the partials with respect to the force model parameters  $\Phi^{\mathbf{x}, \mathbf{p}}(t)$  are obtained via numerical integration of the

variational equations [Montenbruck and Gill, 2001a]

$$(\dot{\Phi}^x, \dot{\Phi}^{x,p}) = \begin{bmatrix} \mathbf{0}_{3 \times 3} & \mathbf{1}_{3 \times 3} \\ \partial \dot{\mathbf{v}} / \partial \mathbf{r} & \partial \dot{\mathbf{v}} / \partial \mathbf{v} \end{bmatrix}_{6 \times 6} \cdot (\Phi^x, \Phi^{x,p}) + \begin{bmatrix} \mathbf{0}_{3 \times 6} & \mathbf{0}_{3 \times 4} \\ \mathbf{0}_{3 \times 6} & \partial \dot{\mathbf{v}} / \partial \mathbf{p} \end{bmatrix}_{6 \times 10}, \quad (3.37)$$

with  $\Phi^x(t_0, t_0) = \mathbf{1}_{6 \times 6}$  and  $\Phi^{x,p}(t_0) = \mathbf{0}_{6 \times 4}$  as initial values.

All expressions used to compute the accelerations in Eq. (3.36) and the partials in Eq. (3.37) are given in [Montenbruck and Gill, 2001a]. The goal of this section is to select a trade-off force model implemented within the navigation process which is accurate enough to fulfill the orbit prediction requirements and simple enough to reduce system complexity and computational load.

### 3.3.1 Force Model Selection

The main forces acting on a LEO spacecraft depend on the Earth's static gravity field, the aerodynamic drag, the third-body perturbations of the Sun and Moon, the solar radiation pressure (SRP), the effects of tidal displacements due to solid Earth, polar and ocean tides, as well as on general relativity effects. We have to select an appropriate force model that allows for an efficient on-board implementation and fulfill the orbit prediction requirements detailed in Section 3.1.2. In particular the propagated absolute spacecraft position shall be better than 10/100/5 m (R/T/N, RMS) and the propagated relative position shall be better than 0.5/10/0.5 m (R/T/N, RMS) within a 50 minutes prediction interval.

In order to find the most appropriate force model trade-off, a true reference trajectory has been first generated, as representative as possible of the PRISMA formation configuration, and taking into account all the possible orbit perturbations. Table 3.4 provides the selected absolute and relative orbit elements of the formation. The absolute motion corresponds to a dusk-dawn sun-synchronous orbit at 700 km altitude, with about 98.2° inclination, 18 h nominal LTAN and 0.001 eccentricity. The relative motion is characterized by non-parallel relative eccentricity and inclination vectors and a mean along-track separation of 1 km.

**Table 3.4:** Chief orbital elements and relative orbital elements for force model selection.

Orbit elements	Value	Relative orbit elements	Value
$a$ [m]	7078135.0	$a\delta a$ [m]	0
$u$ [°]	0.0	$a\delta\lambda$ [m]	1000
$e_x$ [-]	0.001	$a\delta e_x$ [m]	-34.7296
$e_y$ [-]	0.0	$a\delta e_y$ [m]	196.9616
$i$ [°]	98.19	$a\delta i_x$ [m]	76.6044
$\Omega$ [°]	189.89086	$a\delta i_y$ [m]	64.2788

The spacecraft parameters used for the generation of the true motion are collated in Table 3.5. Here, it is assumed that the solar arrays of *Main* are pointing 20° off from the Sun direction while for *Target* the off pointing amounts to 20–30°. The baseline attitude motion is a default nadir/zenith spacecraft pointing. Drag and solar radiation pressure coefficients differ by about 10% for the two spacecraft. As can be seen from Table 3.5, the ballistic coefficients of *Main*

and *Target* amount to about 0.0210 and 0.0201 m<sup>2</sup>/kg and differ by 4.3%. Furthermore a worst case cross-section area of 2.75 m<sup>2</sup> for drag computation has been considered to provide a conservative assessment of the aerodynamic drag (cf. entry between parenthesis in Table 3.5). In this case the *Main* spacecraft offers the complete frontal solar panel surface to the incident atmosphere stream like e.g. during contingency operations, inducing a ballistic coefficient of about 0.045 m<sup>2</sup>/kg which differs by more than 100% from the *Target* ballistic coefficient.

**Table 3.5:** PRISMA spacecraft parameters for force model evaluation.

Spacecraft Parameters	<i>Main</i>	<i>Target</i>
Cross-section area for drag [m <sup>2</sup> ]	1.3 (or 2.75)	0.38
Cross-section area for SRP [m <sup>2</sup> ]	2.5	0.55
Spacecraft mass [kg]	154.4	42.5
Aerodynamic drag coefficient	2.5	2.25
SRP coefficient	1.32	1.2

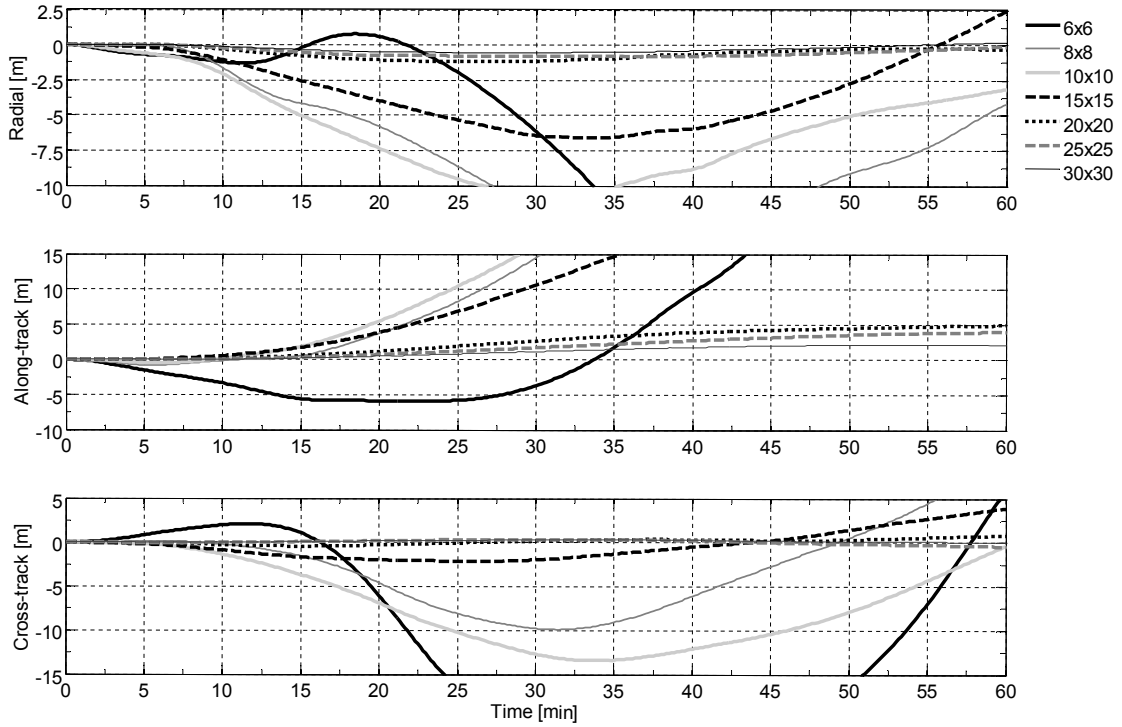


**Fig. 3.3:** Effects of Earth's gravity field model truncation with respect to a precise reference trajectory. The predicted *Main* position error is mapped into the Hill local frame aligned with the radial (top), along-track (middle) and cross-track (bottom) directions.

The absolute and relative prediction errors are computed by subtracting the position propagated through a tailored force model from the true trajectory over 60 minutes at 10 seconds intervals. The tailored force model neglects individual force contributions, one at a time, to evaluate the single effects on the



prediction error budget. The numerical results obtained from this procedure are illustrated in Fig. 3.3 and Fig. 3.4, respectively for the truncation of the Earth's gravity field and the other orbit perturbations. Being the relative position errors at the millimeter level, we have decided to show only the absolute orbit propagation errors which are the drivers of the force model selection.

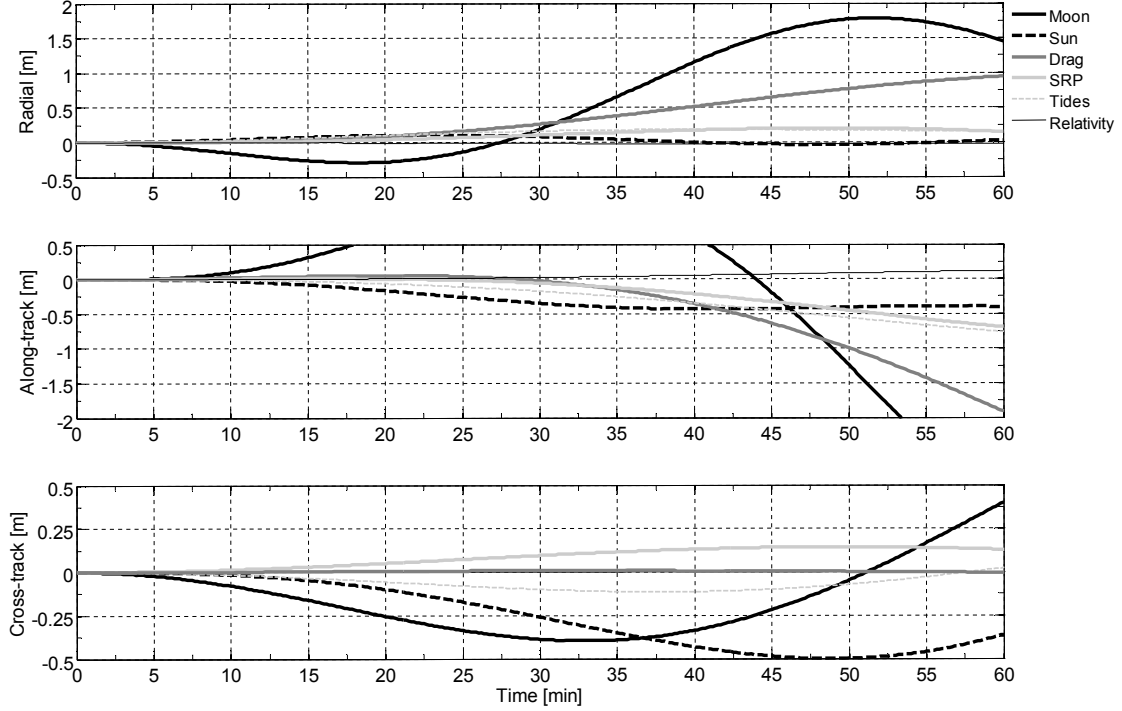


**Fig.3.4:** Effects of force model truncation (excluding Earth's gravity field) with respect to a precise reference trajectory. The predicted *Main* position error is mapped into the Hill local frame aligned with the radial (top), along-track (middle) and cross-track (bottom) directions.

It has to be noted that the prediction error is also influenced by the initial orbit state error, which is a result of the orbit determination process, and by numerical integration and interpolation errors. These effects are taken into account indirectly by introducing a conservative margin on the selection of the individual contributions of the filter force model which shall accumulate a prediction error not larger than the requirement divided by ten, thus 1/10/0.5 m (R/T/N) for the absolute position error and 0.05/1/0.05 m (R/T/N) for the relative position error.

As shown in Fig. 3.3 the truncation of the geopotential harmonics has the major effect on the prediction accuracy. The prediction error after 60 minutes is larger than 5–10 m in all directions for gravity field order and degree 6, 8, 10 and 15. A relatively high performance improvement is observed when switching to a gravity field order and degree 20 and more. Here, the accumulated error stays stably below 1 m in radial direction, 5 m in along-track direction and 0.5 m in cross-track direction. This fact and the minor improvement in accuracy when adopting larger geopotential order and degree, drive the decision to adopt 20 as a trade-off choice.

Similar considerations can be made from Fig. 3.4 on the other force model contributions. The error budget in radial and along-track direction is dominated by the Moon third body force and by aerodynamic drag (here only the worst case scenario is depicted) which accumulate, respectively, to 1.5 and 1 m in radial direction and to 3.5 and 2 m in along-track after 60 minutes. Sun and Moon third body forces drive instead the prediction accuracy in cross-track direction with about 0.5 m error each after 1 hour. On the contrary solar radiation pressure, tides and relativity can be neglected with accumulated errors below 0.5 m and 1 m in radial/cross-track and along-track directions, respectively.

**Table 3.6:** Selected force model for real-time navigation. The first column lists the force model used for the generation of the reference true trajectory. The second and third columns list the force models applied in the real-time navigation filter to propagate orbit state and transition matrix, respectively.

Force model contributions	Modeled truth	Orbit state	Transition matrix
Static gravity field	GGM01S (120x120) [UT/CSR, 2003]	GGM01S (20x20)	up to $C_{2,0}$
Third-body Sun/Moon	Analytical model [Montenbruck and Gill, 2001a]	Analytical model	-
Atmospheric density	Jacchia [Jacchia, 1971]	Harris-Priester [Harris and Priester, 1962]	Harris-Priester
Solar radiation pressure	Cannon-ball Conical Earth's shadow	-	-
Earth tides	Solid, Pole and Ocean UT/CSR 3.0, TEG-2B	-	-
General relativity	First order effect [Montenbruck and Gill, 2001a]	-	-

An overview of the force model selected for the real-time navigation filter is given in Table 3.6. For completeness the model adopted to generate the reference true trajectory is also described. In fact the same dynamics model will be applied later on in this chapter to validate the navigation process via numerical simulations. As shown in the last column of Table 3.6, the applied force model for the computation of the partial derivatives in the state transition matrix is very simplistic. This is due to the fact that we deal with a linear estimation problem where the accuracy requirements on the state transition matrix are much less stringent than for the orbit state. Anyhow in order to improve accuracy and scalability of the navigation system, an analytical formulation of the state transition matrix based on a Keplerian motion model has been ruled out.

### 3.3.2 Numerical Integration and Orbit Prediction

The numerical integration of the orbit state vector and variational equations is performed using the well known fourth-order Runge-Kutta method (RK4) augmented with Richardson extrapolation (also termed RK4R) [Gill and Montenbruck, 2002]. The results  $\eta_{1h}$  and  $\eta_{2h}$  of two consecutive RK4 integration

steps of size  $h$  are combined with the result  $\boldsymbol{\eta}_H$  of a single RK4 macro step of size  $H = 2h$  to obtain fifth-order approximations

$$\hat{\boldsymbol{\eta}}_{1h} = \boldsymbol{\eta}_{1h} + \frac{\boldsymbol{\eta}_{2h} - \boldsymbol{\eta}_H}{2(2^4 - 1)} \quad \text{and} \quad \hat{\boldsymbol{\eta}}_{2h} = \boldsymbol{\eta}_{2h} + \frac{\boldsymbol{\eta}_{2h} - \boldsymbol{\eta}_H}{2^4 - 1} \quad (3.38)$$

of the state vector (or the partials) at times  $t_0 + 1h$  and  $t_0 + 2h$  (see e.g. [Hairer et al., 1987]). By combining the intermediate results, a consistent fifth-order approximation of the state vector over the interval  $[t_0, t_0 + 2h]$  can be obtained as a quintic Hermite polynomial

$$\begin{aligned} \boldsymbol{x}(t_0 + \theta h) = & d_0(\theta)\boldsymbol{x}_0 + d_1(\theta)h\boldsymbol{f}_0 + d_2(\theta)\boldsymbol{x}_1 \\ & + d_3(\theta)h\boldsymbol{f}_1 + d_4(\theta)\boldsymbol{x}_2 + d_5(\theta)h\boldsymbol{f}_2 \quad , \end{aligned} \quad (3.39)$$

with coefficients [Sauer and Szabo, 1968]

$$\begin{aligned} d_0 &= \frac{1}{4}(\theta - 1)^2(\theta - 2)^2(1 + 3\theta) & d_1 &= \frac{1}{4}\theta(\theta - 1)^2(\theta - 2)^2 \\ d_2 &= \theta^2(\theta - 2)^2 & d_3 &= (\theta - 1)\theta^2(\theta - 2)^2 \\ d_4 &= \frac{1}{4}\theta^2(\theta - 1)^2(7 - 3\theta) & d_5 &= \frac{1}{4}(\theta - 2)\theta^2(\theta - 1)^2 \end{aligned} \quad (3.40)$$

where  $\theta$  denotes the time since  $t_0$  in units of  $h$ . The RK4R integrator with Hermite interpolation is an efficient integrator for real-time applications of effectively 5<sup>th</sup> order with 5.5 function calls per micro-step  $h$ , that also supports dense output without need of integrator step-size reduction. In case of LEO satellites the errors achieved by this integration and interpolation scheme are generally one order of magnitude smaller than the trajectory and model errors [Montenbruck and Gill, 2001b]. In view of the timing strategy employed within the navigation system and described in the next chapter, the adopted macro step-size is  $H = 2h = 92$  s. A numerical orbit propagation is invoked by the GPS-based Orbit Determination (GOD) after the EKF processing, each 30 s, which results in a set of orbit coefficients  $\boldsymbol{C} = (\boldsymbol{x}, \dot{\boldsymbol{x}})|_{t_0, t_0+1h, t_0+2h}$ . These coefficients allow for a quintic Hermite interpolation of the spacecraft position and velocity within the interval  $[t_0, t_2 = t_0 + 2h]$ , which is performed by the GOD function to support the EKF time update at the next call (30 s later) and by the GPS-based Orbit Prediction (GOP) function to output the *Main* and *Target* orbit states in the ECI and ECEF frames at a 1 Hz rate.

### 3.3.3 Maneuver Handling

A fundamental task of autonomous navigation for formation flying spacecraft is the incorporation of maneuvers or thrust activities within the filtering scheme. When the orbital uncertainties are small compared to the size of the orbits and the propagation time is relatively short, the orbit determination process can be linearized yielding the formulation of the time and measurement updates of the EKF. If neither the *Main* nor the *Target* spacecraft maneuvers during the time span from  $t_{i-1}$  to  $t_i$ , then Eqs. (3.33) and (3.35) are easy to apply. However, in cases where one or both of the spacecraft maneuvers during the prediction time span, several possible methods can be considered to generalize Eqs. (3.33) and (3.35) [Schiff, 2006].

Provided that full maneuver information is available, the first solution is to adapt  $\Phi_i$  assuming a perfect maneuver model with no uncertainties. This approach is extremely sensitive to the fidelity of the thrust model and fails to produce the final covariance matrix in the presence of uncertainties (e.g., maneuver execution errors). However it can be employed in pre-launch delta-V budget analysis when the maneuver uncertainty is negligible in comparison to other perturbations in the problem.

A second alternative omits the maneuver from the trajectory prediction and schedule  $Q_i$  in such a way that it grows in correspondence of the maneuver execution. This method may be desirable when full information regarding the thrusting is unavailable. As long as the maneuver uncertainty can be properly reflected in the process noise, the measurements should update the state to reflect the unmodeled force. It can be easily shown that this approach yields good accuracy for the covariance computation, but fails to model the orbit state in the time update of the EKF.

A third approach models the maneuver in the process and takes into account its uncertainty by adapting both  $\Phi_i$  and  $Q_i$ . The solution adopted here is a variant of this third approach. The EKF state is enlarged to include the maneuver parameters in the estimation process. As a consequence both state transition and covariance matrix are adapted using the a-priori maneuver information. This method provides a combination of good accuracy in the computation of the covariance matrix, the orbit state and offers at the same time maneuver estimates which may be used for thrust calibration and process monitoring.

Clearly orbit control maneuvers executed by the *Main* spacecraft have to be taken into account in the orbit prediction process. To that end, a history of impulsive maneuver data, comprising time  $t_M$  and size  $\delta v$  in the Hill's frame, is derived on-board from the filtering of accelerometer measurements (cf. next chapter for details) and provided to the real-time navigation system. The maneuver vector has to be first transformed to the ECI and ECEF frames, this is performed through the definition of the Hill's orbital frame (cf. Fig. 2.1)

$$\begin{aligned} \mathbf{o}_r &= \mathbf{r} / \|\mathbf{r}\| \\ \mathbf{o}_n &= (\mathbf{r} \times \mathbf{v}) / \|\mathbf{r} \times \mathbf{v}\| \\ \mathbf{o}_t &= \mathbf{o}_n \times \mathbf{o}_r \end{aligned} \quad (3.41)$$

according to

$$\delta \mathbf{v}_{\text{eci}} = \mathbf{R}^{\text{rtn}} \delta \mathbf{v} = \mathbf{R}(\mathbf{o}_r, \mathbf{o}_t, \mathbf{o}_n) \delta \mathbf{v} \quad , \quad (3.42)$$

and

$$\delta \mathbf{v}_{\text{ecef}} = \mathbf{R}^{\text{eci}} \mathbf{R}^{\text{rtn}} \delta \mathbf{v} = \mathbf{R}(\mathbf{o}_r, \hat{\mathbf{o}}_t, \hat{\mathbf{o}}_n) \delta \mathbf{v} \quad . \quad (3.43)$$

Here  $\mathbf{R}^{\text{rtn}}$  and  $\mathbf{R}^{\text{eci}}$  are the rotation matrices from the Hill local frame to ECI and from the ECI frame to ECEF, respectively.  $\mathbf{R}(\cdot, \cdot, \cdot)$  represents the rotation matrix assembled using the indicated arguments as column vectors. Eq. (3.43) provides a simplified expression for the desired transformation where the unit vectors with a hat are derived from Eq. (3.41) using the velocity

$$\hat{\mathbf{v}} = \mathbf{v}_{\text{ecef}} + \begin{pmatrix} 0 & 0 & \omega_E \end{pmatrix}^t \times \mathbf{r}_{\text{ecef}} \quad , \quad (3.44)$$

which accounts for the effect of the Earth rotation based on the Earth rotation rate  $\omega_E$ . The actual implementation is based on the right side of Eq. (3.43) and (3.44) and thus avoids the computation of the Earth rotation matrix. Position and velocity, in the ECI and ECEF frames, are available as part of the orbit coefficients.

As a second step the orbit coefficients within  $C$  are updated to include the effects of the maneuver. More specifically the orbit state is interpolated at the time of the maneuver using the available orbit polynomials and the input maneuver increment is added to the velocity. Based on a linear interpolation of the acceleration, new position-velocity vectors are computed through an analytical integration of the equations of motion. The time interval of the updated Hermite polynomial is set to  $[t_M, t_2]$  (i.e., the new start time is the time of the maneuver). The update algorithm is based upon the jerk

$$\mathbf{j} = \ddot{\mathbf{v}} = \frac{\dot{\mathbf{v}}_1 - \dot{\mathbf{v}}_0}{h} \quad , \quad (3.45)$$

and is given by

$$\begin{aligned} \dot{\mathbf{v}}_0^* &= \dot{\mathbf{v}}_0 + \mathbf{j}(t_M - t_0) \\ \dot{\mathbf{v}}_1^* &= \dot{\mathbf{v}}_0^* + \mathbf{j}h^* \\ \dot{\mathbf{v}}_2^* &= \dot{\mathbf{v}}_1^* + \mathbf{j}h^* \quad , \end{aligned} \quad (3.46)$$

for the acceleration, by

$$\begin{aligned} \mathbf{v}_0^* &= \mathbf{v}(t_M) + \delta \mathbf{v}_{\text{eci}} \\ \mathbf{v}_1^* &= \mathbf{v}_0^* + \dot{\mathbf{v}}_0^* h^* + \frac{1}{2} \mathbf{j} h^{*2} \\ \mathbf{v}_2^* &= \mathbf{v}_1^* + \dot{\mathbf{v}}_1^* h^* + \frac{1}{2} \mathbf{j} h^{*2} \quad , \end{aligned} \quad (3.47)$$

for the velocity, and by

$$\begin{aligned} \mathbf{r}_0^* &= \mathbf{r}(t_M) \\ \mathbf{r}_1^* &= \mathbf{r}_0^* + \mathbf{v}_0^* h^* + \frac{1}{2} \dot{\mathbf{v}}_0^* h^{*2} + \frac{1}{6} \mathbf{j} h^{*3} \\ \mathbf{r}_2^* &= \mathbf{r}_1^* + \mathbf{v}_1^* h^* + \frac{1}{2} \dot{\mathbf{v}}_1^* h^{*2} + \frac{1}{6} \mathbf{j} h^{*3} \quad , \end{aligned} \quad (3.48)$$

for the position, where  $h^* = (t_2 - t_M)/2$  is the new micro-step size of the orbit coefficients. The computation of the jerk in Eq. (3.45) and the given expressions in Eqs. (3.46)-(3.48) refer to a coefficient update with  $t_0 < t_M < t_0 + h$ . Similar relations hold if the maneuver time lies in the second micro-interval  $t_0 + h < t_M < t_0 + 2h$ . Furthermore the provided expressions refer to the update of the orbit coefficients expressed in the ECI frame. Identical relations hold for an update in the ECEF frame.

Note that even if the *Target* spacecraft does not perform any maneuver, a similar modification of its orbit coefficients is performed in parallel with the update of the *Main* polynomials through the incorporation of a null maneuver increment (i.e., Eqs. (3.46)-(3.48) are used with  $\delta \mathbf{v} = 0$ ). As a result the absolute navigation accuracy is slightly degraded (due to the linear interpolation of the acceleration components), but the relative navigation profits from the cancellation of the common interpolation errors affecting both *Main* and *Target* spacecraft.

### 3.4 Numerical Validation of Navigation Process

#### 3.4.1 Simulation Environment

The goal of this section is to validate the proposed GPS-based absolute and relative navigation filter through purely numerical simulations in a standalone environment. This validation process has to be intended as an intermediate step before the system level hardware-in-the-loop tests which are discussed in the next chapters. Here the aim is to verify the assumptions made during the design process and ensure that the filter design has the potential to meet the assigned requirements (cf. Section 3.1.2). To this end a sophisticated simulation environment has been developed. It includes a rigorous force model (cf. Table 3.6), an efficient variable order variable step-size multi-step numerical integration method DE of Shampine and Gordon [1975], and realistic sensor and actuator models which are discussed in the following subsections.

##### Phoenix-S GPS Receiver

Simulated raw GPS measurements (and navigation solutions) for both spacecraft are generated by a dedicated Phoenix Emulation (PEM) software based on the true orbit and attitude profiles and taking into account the known antenna offsets in the spacecraft body frame. The GPS constellation is modeled based on the YUMA GPS almanac for week 1381 (2 July 2006) which defines a constellation of 29 active GPS satellites.

To study the influence of key error sources, ionospheric path delays and broadcast ephemeris errors are modeled by PEM. The spacecraft ionosphere model implements the Lear mapping function [Lear, 1989] with a constant Total Electron Content (TEC) of  $10 \cdot 10^{16}$  electrons/m<sup>2</sup> (= 10TECU) to simulate ionospheric effects. In an effort to mimic a realistic Signal in Space Range Error (SISRE), broadcast ephemeris are affected by offsets based on uniformly distributed random numbers with zero mean and a standard deviation of 1.5 m. For comparison, the performance of the current GPS constellation and ground segment achieves a representative SISRE of 1.0 to 1.5 m including both ephemeris and clock errors [Warren and Raquet, 2003], [Creel et al., 2006].

A realistic antenna gain profile for the PRISMA GPS antennas (Sensor Systems S67-1575-20) is adopted and measurements are generated for all visible GPS satellites within less than 85° about the boresight direction. Bandwidths of 0.08 Hz and 9 Hz are assumed for the delay locked loop and phase locked loop to replicate the variation of code and carrier phase noise with signal-to-noise ratio in the Phoenix receiver (cf. Eq. (3.30)).

##### Propulsion System

The *Main* spacecraft accommodates a hydrazine-based thruster system which provides delta-V for relative control with respect to *Target*. The system provides thrust in all directions using six thrusters which are characterized by a nominal thrust force of  $1 \pm 0.1$  N and a specific impulse of 2100 Ns/kg at begin of life. The propulsion system is capable of providing impulse bits ranging from 100 ms up to continuous burns of 30 seconds with a maximum burn time resolution

of 10 ms. This translates to a minimum velocity increment of around 0.65 mm/s and to a discretization of ca. 0.065 mm/s which can be applied for formation control. A total of 11 kg propellant provides an overall delta-V of 115 m/s in an accumulated firing time of at least five hours. Thruster-related characteristics relevant to navigation are given in Table 3.7.

**Table 3.7:** Thruster and orbit maneuver characteristics for PRISMA.

Thrusters				
Thrust [N] $T$ 1	Spacecraft mass [kg] $m$ 154.4	Thrust acceleration [mm/s <sup>2</sup> ] $a_T = T/m$ 6.5	Impulse bit [Ns] $m\delta v_{\min}$ 0.1(+0.01)	Vel. increment [mm/s] $\delta v_{\min}$ 0.65(+0.065)
Orbit maneuvers				
Impulsive burn [mm/s] 0.65	Vel. offset (1s) [mm/s] 0.65	Vel. offset (30s) [mm/s] 0.65	Pos. offset (1s) [m] 0.00065	Pos. offset (30s) [m] 0.0195
Continuous burn [mm/s <sup>2</sup> ] 6.5	Vel. offset (1s) [mm/s] 6.5	Vel. offset (30s) [mm/s] 195	Pos. offset (1s) [m] 0.00325	Pos. offset (30s) [m] 2.925

In contrast to the on-board navigation software the orbit control maneuvers are modeled as a continuous acceleration applied throughout the actual thrust burn time (i.e., extended maneuver model) instead of an instantaneous velocity increment (i.e., impulsive maneuver model), cf. Table 3.7 for further details. The propulsion system model includes the limitations given by the minimum burn duration and by the discretization of the burn time as listed in Table 3.7. Furthermore, the performance error of the thruster system is quantified by

$$\eta = \left| \frac{\delta v^P - \delta v^A}{\delta v^A} \right| \cdot 100 \quad , \quad (3.49)$$

where  $\delta v^P$  is the planned velocity increment, computed by the feedback control law, and  $\delta v^A$  is the actual velocity increment realized by the propulsion system. In the sequel the performance error  $\eta$  is treated as Gaussian noise with 1% mean and standard deviation of 2%.

#### Accelerometers

The *Main* Guidance, Navigation and Control (GNC) sensors comprise five single-axis accelerometers to determine the velocity increments imparted to the spacecraft by its thruster system. To this end, the accelerometer Q-Flex model QA3000-020 of Honeywell (Table 3.8) has been selected. The accelerometer units are integrated in a pyramidal geometry and operated in hot redundancy, allowing detection and isolation of one failed sensor.

The thrust imparted to the spacecraft is about  $650 \mu g$  and can, according to the above given figures, be resolved with an intrinsic noise of about 1%. To provide products generated from accelerometer output which are unbiased to better than 10% of the spacecraft thrust (i.e.,  $65 \mu g$ ), the bias has to be resolved

**Table 3.8:** Characteristics of Honeywell's accelerometer model QA3000-020.

Measurement range	Accelerometer bias	Intrinsic noise		
[g]	[g]		$[\mu g - \text{RMS}]$	
		0 – 10 Hz	10 – 500 Hz	500 – 10000 Hz
$\pm 60$	$< 4$	7	70	1500

to better than 0.002% of its absolute value in a filtering scheme. Thus, bias resolution is a key issue in the treatment of accelerometer data.

As emphasized above, the accelerometer data are affected by intrinsic noise and biases and can, thus, not directly be used in the GPS-based navigation system. To this end, a filtering of the accelerometer data is performed on-board which determines the bias, reduces the noise and converts acceleration into velocity increments. Furthermore, the accelerometer output is provided at a rate of 200 Hz by the Remote Terminal Unit (RTU) which implements an analogue low-pass filter. The filter output is then polled at 1 Hz from the RTU. Finally, the filtered acceleration is given in a spacecraft body-fixed frame and requires a transformation to the local Hill's orbital frame. The rotation matrix from the body axes to the ECI frame is provided by the star camera on *Main* while the rotation matrix from ECI to the Hill's co-rotating frame can be derived from the navigation output of the GPS-based orbit prediction function or, alternatively, from the evaluation of orbital elements. The velocity increment  $\delta v$  in each direction is finally obtained as the sum of the correspondent accelerations over time slices  $\Delta t$  according to  $\delta v = \sum_i a_i \Delta t_i$ .

The accelerometer data are corrected for their dependency on temperature based on a polynomial approximation scheme and for spacecraft rates. The bias resolution accuracy depends on the measurement noise, systematic sensor errors, residual dynamic accelerations, e.g. due to atmospheric drag, as well as on the filtering scheme. Since atmospheric drag is expected to be in the range of  $50 - 500 \text{ nm/s}^2$  maximum, the measurement noise is expected to dominate the bias error budget. Since the raw accelerometer measurements are not time tagged, the 1 Hz velocity increments will be delivered at current spacecraft on-board elapsed time minus 0.5 s.

According to the discussion above the accelerometer model generates equivalent delta-V measurements, as filtered by the on-board GNC software, at a 1 Hz rate. In particular the maneuvers actually executed by the thruster system are fed by the propulsion system model to the accelerometer model which adds a Gaussian error characterized by 2% mean and 5% standard deviation. The filtered accelerometer measurements are finally provided to the orbit determination and prediction functions for incorporation into the navigation process.

### 3.4.2 Numerical Tests and Results

Four test cases have been defined to validate the navigation concept and perform a preliminary assessment of the expected navigation accuracy. The aim is to increase the scenario complexity in a stepwise approach and cover the opera-



tional configurations that are most likely to be met during flight. First an open-loop scenario is specified, where no orbit control maneuvers are performed and the spacecraft attitude profile is nominal (i.e., default nadir/zenith pointing of the *Main* and *Target* spacecraft). Second a closed-loop scenario is presented, where the relative motion is controlled routinely using the algorithms defined in the previous chapter. Next operational contingencies are defined, where data gaps have to be autonomously bridged by the navigation software. In particular long GPS measurements outages are introduced in the open-loop and closed-loop simulations to assess the robustness and reliability of the GPS navigation concept.

#### Open-Loop Nominal Operations

The first test case covers a time span of 24 hours starting on 2. July 2006, 00:00:00.0 GPS Time and can be considered the most simple scenario from a GNC point of view. The PRISMA formation is not controlled and the satellites are freely moving under the influence of the natural orbit perturbations (cf. rigorous force model in Table 3.6). The initial absolute and relative orbital elements are listed in Table 3.4, while the spacecraft parameters are given in Table 3.5. The orientation of the *Main* and *Target* spacecraft is such that the spacecraft body-fixed axes are aligned with the co-moving orbital frame defined by the radial, along-track and cross-track directions (i.e., Hill's local frame). This attitude configuration ensures a zenith pointing of the GPS antennas in use on the formation flying spacecraft. In order to reproduce as close as possible the conditions met during flight, attitude determination errors are added to the *Main* and *Target* true attitude profile. The typical attitude error distribution is characterized by roughly  $0.1^\circ$  mean and  $0.3^\circ$  standard deviation on *Target* and about  $0.0^\circ$  mean and  $0.005^\circ$  standard deviation on *Main*. The actually estimated attitude is then fed to the GPS-based relative navigation filter to correct for the GPS antennas offsets with respect to the satellite's center of mass.

**Table 3.9:** Settings of the EKF used during the 24-hours open-loop scenario.

Parameter	Value	Parameter	Value
<i>A-priori standard deviation</i>		<i>Process noise</i>	
$\sigma_r$ [m]	1000.0	$\sigma_{a_r}$ [nm/s <sup>2</sup> ]	15.0
$\sigma_v$ [m/s]	1.0	$\sigma_{a_t}$ [nm/s <sup>2</sup> ]	30.0
$\sigma_{C_D}$	1.0	$\sigma_{a_n}$ [nm/s <sup>2</sup> ]	20.0
$\sigma_{a_r}$ [nm/s <sup>2</sup> ]	150.0	$\sigma_{c\delta t}$ [m]	500.0
$\sigma_{a_t}$ [nm/s <sup>2</sup> ]	300.0	<i>Measurements standard deviation</i>	
$\sigma_{a_n}$ [nm/s <sup>2</sup> ]	200.0	$\sigma_{PR}$ [m]	1.0
$\sigma_{c\delta t}$ [m]	500.0	$\sigma_{CP}$ [mm]	1.0
$\sigma_N$ [m]	0.5		
<i>Auto-correlation time scale</i>			
$\tau_a$ [s]	900.0		
$\tau_{c\delta t}$ [s]	100.0		

The most important settings applied to the EKF for absolute and relative

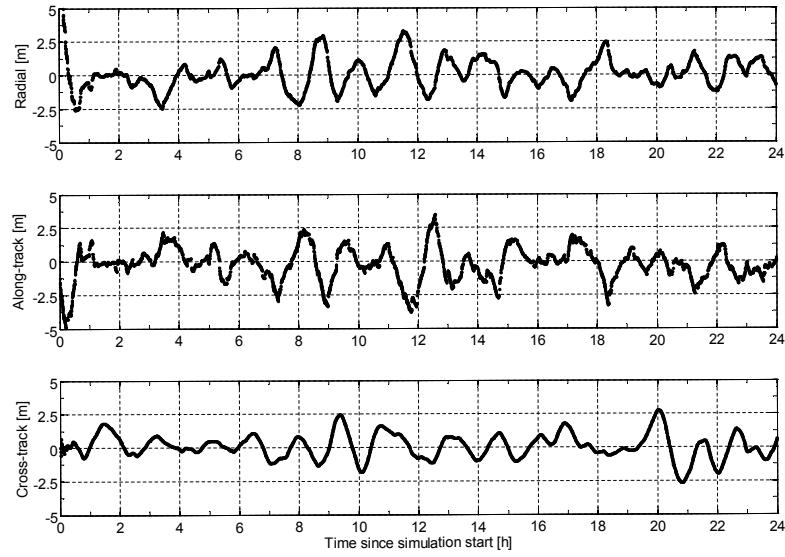


**Fig.3.5:** Absolute *Main* position error mapped into the orbital frame aligned with the radial (top), along-track (middle) and cross-track (bottom) directions. Statistics computed excluding the convergence phase of the EKF provide an absolute navigation accuracy of 1.9 m (3D, RMS).

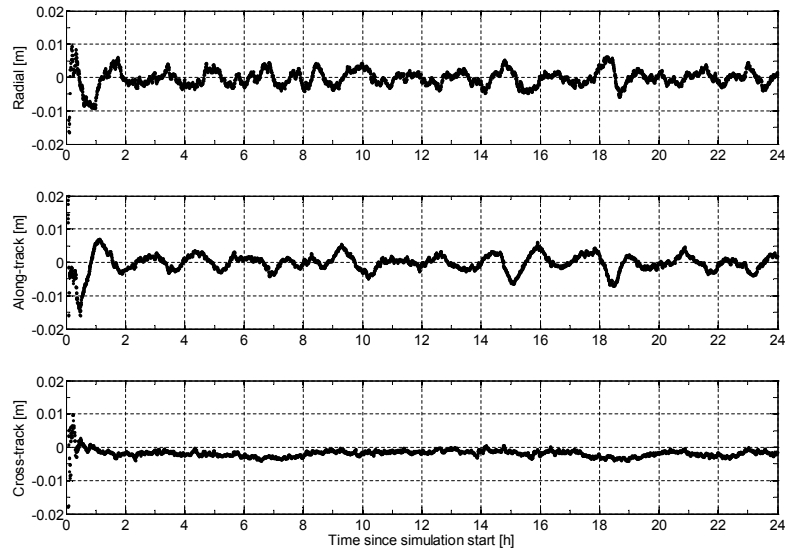


**Fig.3.6:** Relative position error (i.e., *Main* with respect to *Target*) mapped into the orbital frame aligned with the radial (top), along-track (middle) and cross-track (bottom) directions. Statistics computed excluding the convergence phase of the EKF provide a relative navigation accuracy of 3.6 mm (3D, RMS).

navigation during the open-loop simulation are collated in Table 3.9 and are chosen identical for *Main* and *Target* related state variables. The process noise time scales of empirical accelerations and clock offsets have been set to trade-off values of 900 s and 100 s, respectively. The a-priori and steady state variances are chosen in such a way to reflect the uncertainties of the adopted force model, which are driven mainly by the truncated Earth's gravity field, by the solar ra-

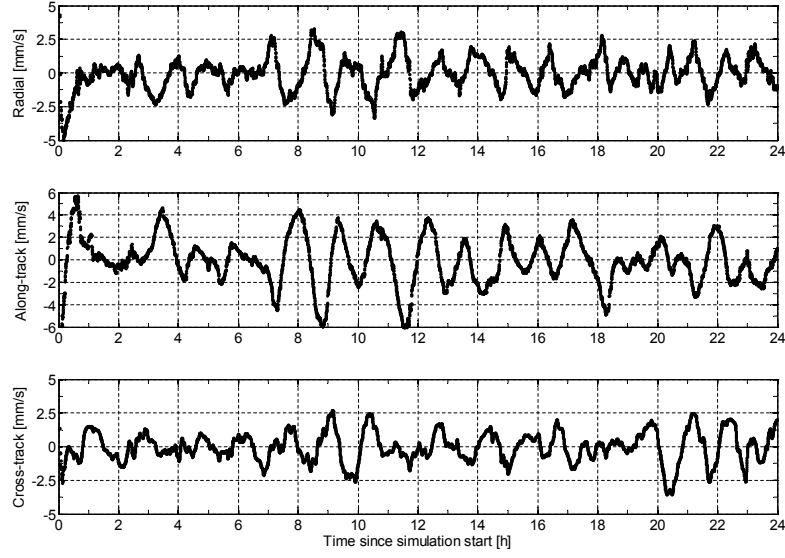


**Fig.3.7:** Absolute *Main* velocity error mapped into the orbital frame aligned with the radial (top), along-track (middle) and cross-track (bottom) directions. Statistics computed excluding the convergence phase of the EKF provide an accuracy of 2.7 mm/s (3D, RMS).

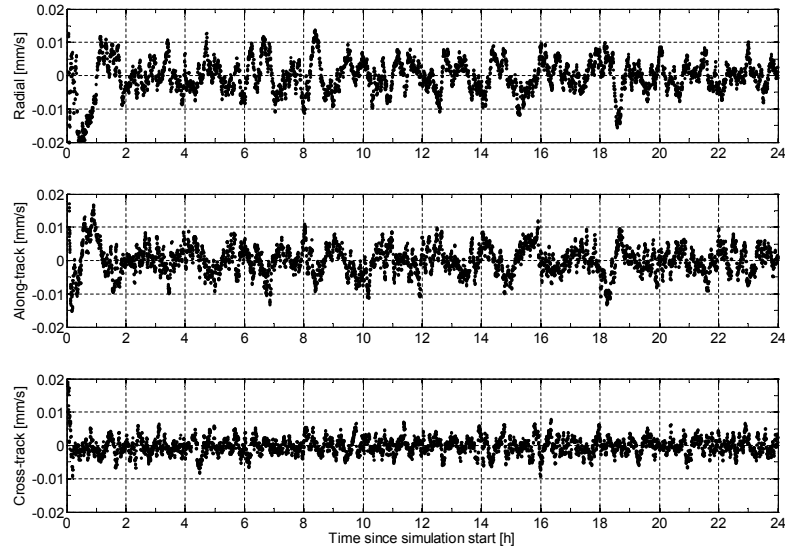


**Fig.3.8:** Relative velocity error (i.e., *Main* with respect to *Target*) mapped into the orbital frame aligned with the radial (top), along-track (middle) and cross-track (bottom) directions. Statistics computed excluding the convergence phase of the EKF provide an accuracy of 0.006 mm/s (3D, RMS).

diation pressure and tidal forces. Tighter a-priori and process noise variances have been selected for the radial component of the empirical acceleration. This is shown to be beneficial due to the heavy dynamic coupling and the lower sensitivity in this direction. The pseudorange and carrier phase measurement noise level is set to 1.0 m and 1.0 mm, respectively, in accordance with the discussion in Section 3.2.3.

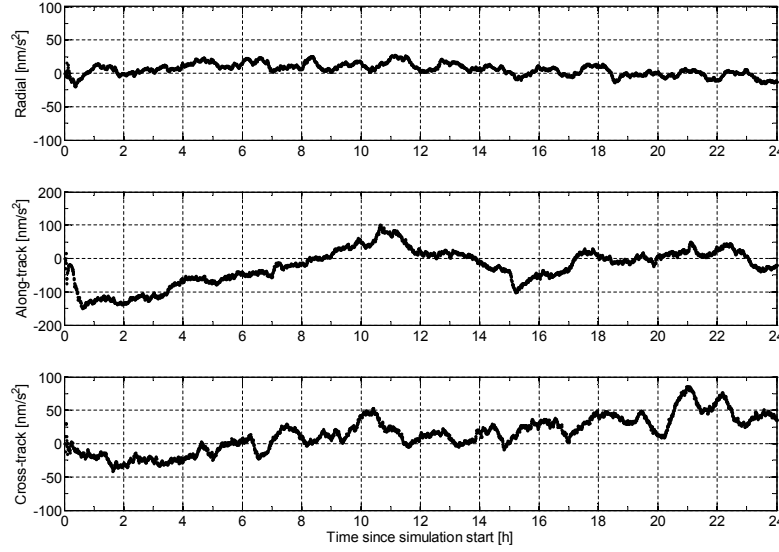


**Fig. 3.9:** Empirical accelerations of *Main* mapped into the orbital frame aligned with the radial (top), along-track (middle) and cross-track (bottom) directions.

The accuracy of the navigation filter is evaluated by subtracting the estimated position and velocity of the *Main* and *Target* spacecraft from the true reference trajectory in the ECEF reference frame at 10 s samples. The absolute and relative navigation errors are then mapped in the orbital frame aligned with the radial, along-track and cross-track directions and finally plotted in Figs. 3.5-3.8. Statistics computed excluding the convergence phase of the EKF provide an absolute and relative navigation accuracy of 1.9 m and 3.6 mm (3D, RMS), respectively (cf. Figs. 3.5 and 3.6). A minor periodic amplitude modulation is visible especially in the absolute position errors with a period of about one orbital revolution. It is interesting to note that the magnitude and pattern of the position residuals in radial and along-track directions are extremely similar and show opposite signs (cf. Fig. 3.5). This is once again an evidence of the high dynamic coupling present in the orbital plane.

Similar considerations can be done for the absolute and relative velocity errors which are affected by errors of 2.7 mm/s and 0.006 mm/s (3D, RMS), respectively (cf. Figs. 3.7 and 3.8). Typical results for the absolute empirical accelerations estimated in open-loop scenarios are depicted in Fig. 3.9. The along-track component is left more free to absorb unmodeled effects of the dynamic model and can reach values larger than  $100 \text{ nm/s}^2$ , the radial and cross-track components are limited to magnitudes of  $50 - 100 \text{ nm/s}^2$ .

These preliminary results give confidence on the capability of the filter design to fulfill the assigned accuracy requirements because orbit position and velocity errors are well within the prescribed limits. Anyhow the presence of orbit control maneuvers, if not properly handled, can cause a drastic degradation of the navigation accuracy. Thus a second test case is addressed in the next subsection to study the behavior of the filter in a closed-loop scenario.

### Closed-Loop Nominal Operations

The second test case covers a time interval of 48 hours and is based on the scenario described for the open-loop simulation with the fundamental difference that orbit control maneuvers are autonomously planned and commanded by a guidance and control software which adopts the algorithms described in the previous chapter. The deterministic feedback control law makes use of the input absolute *Main* and *Target* orbit states generated by the GPS-based navigation process at 1 Hz rate. The maneuver commands are fed to the propulsion system model and to the accelerometer model described in the previous subsections. Consequently maneuver execution errors are introduced in the numerical orbit propagation and realistic accelerometers measurements are provided to the navigation filter for the incorporation of maneuvers.

**Table 3.10:** Settings of the EKF used during the 48-hours closed-loop scenario.

Parameter	Value	Parameter	Value
<i>A-priori standard deviation</i>		<i>Process noise</i>	
$\sigma_r$ [m]	1000.0	$\sigma_{a_r}$ [nm/s <sup>2</sup> ]	75.0
$\sigma_v$ [m/s]	1.0	$\sigma_{a_t}$ [nm/s <sup>2</sup> ]	150.0
$\sigma_{C_D}$	1.0	$\sigma_{a_n}$ [nm/s <sup>2</sup> ]	100.0
$\sigma_{a_r}$ [nm/s <sup>2</sup> ]	750.0	$\sigma_{c\delta t}$ [m]	500.0
$\sigma_{a_t}$ [nm/s <sup>2</sup> ]	1500.0	<i>Measurements standard deviation</i>	
$\sigma_{a_n}$ [nm/s <sup>2</sup> ]	1000.0	$\sigma_{PR}$ [m]	0.2
$\sigma_{c\delta t}$ [m]	500.0	$\sigma_{CP}$ [mm]	2
$\sigma_N$ [m]	0.1	<i>Maneuver parameters</i>	
<i>Auto-correlation time scale</i>		$\sigma_{\delta v}$ [%]	10.0
$\tau_a$ [s]	900.0		
$\tau_{c\delta t}$ [s]	100.0		

The formation maintenance control law applied to the constellation is based on along-track and cross-track pulses only, cf. Section 2.4.4. The control windows for the relative eccentricity and inclination vectors are kept constant during the complete simulation and are given by  $a\delta e^{\max} = 2$  m and  $a\delta i^{\max} = 1$  m. The resulting maneuver cycle for in-plane and out-of-plane formation maintenance is given by about 12 h and 7 h, respectively with correspondent individual along-track and cross-track maneuvers of  $\delta v_t \approx 1.2$  mm/s and  $\delta v_n \approx 2.5$  mm/s.

The settings applied to the EKF for absolute and relative navigation during the closed-loop simulation are collated in Table 3.10 and are again identical for *Main* and *Target*. Compared to the open-loop settings of Table 3.9, the empirical accelerations a-priori and steady state variances are selected 5.0 times larger, while the pseudorange and carrier phase measurements noise is set to 0.2 m and 2 mm, respectively. The a-priori standard deviation of the maneuver delta-v parameters is set to 10 % of the a-priori value provided by the accelerometer model.

In the closed-loop scenario the dominating force is given by the propulsion thrust with accelerations of the order of  $6500000$  nm/s<sup>2</sup> (cf. Table 3.7), obvi-

ously the uncertainties associated to the simple orbit maneuver dynamic model implemented in the navigation filter (cf. Eq. (3.14)) are huge and have to be compensated through the empirical accelerations. The selected standard deviations (still three orders of magnitude smaller than the thrust acceleration) reflect the attempt to give more kinematic properties to the filter, which, compared to the open-loop case, should trust the GPS measurements more than its dynamic model. Considering that the velocity increments produced by an orbit control maneuver (i.e., order of mm/s) are hard to separate from the spacecraft absolute velocity (i.e., about 7.5 km/s), we expect the maneuver effects to be absorbed by other state parameters like e.g. the aerodynamic drag coefficient  $C_D$  and the GRAPHIC carrier phase ambiguities, and not only by the estimated maneuver itself and the empirical accelerations. Furthermore it has been found that the overall accuracy of the absolute navigation is increased if more weight is given to the GRAPHIC data types relative to the single difference carrier phase measurements. This is due to the fact that the absolute orbit determination of *Main* and *Target* is highly coupled through the processing of high accurate SDCP observables. If the carrier phase measurements are over-weighted with respect to the pseudoranges, the SDCP data types play the role of a rigid arm between the spacecraft which can produce a detrimental offset of the estimated spacecraft absolute positions.

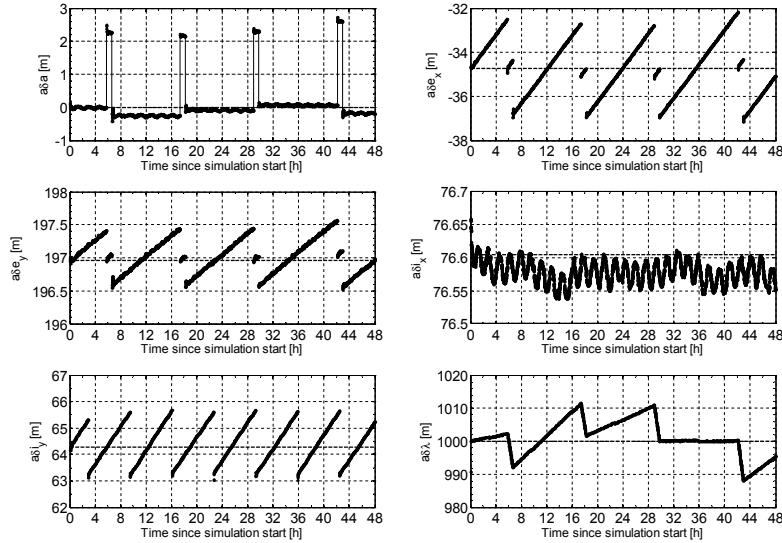


**Fig. 3.10:** Actual (dotted line) and nominal (dashed line) relative orbital elements during the 48-hours closed-loop simulation.

Fig. 3.10 depicts the relative orbital elements computed by the guidance and control software during the 48 hours closed-loop simulation arc. As expected the relative eccentricity and inclination vectors are confined within the prescribed control window. The relative semi-major axis is affected by offsets caused by the execution of orbit control maneuvers in (anti-)along-track direction, and, after each pair of maneuvers, is set to a desired target value to control the mean along-track separation. As a consequence the relative mean argument

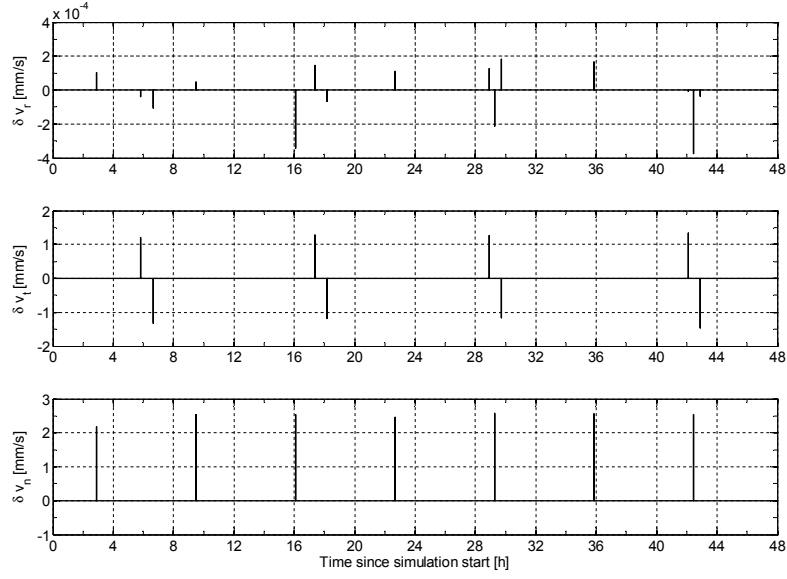


**Fig.3.11:** Orbit control maneuvers actually executed by *Main* mapped into the orbital frame aligned with the radial (top), along-track (middle) and cross-track (bottom) directions.

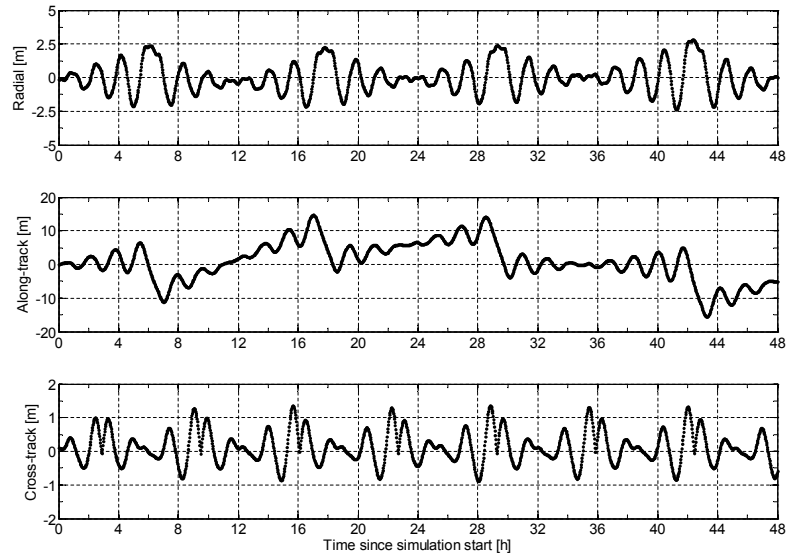


**Fig.3.12:** Control tracking error mapped into the orbital frame aligned with the radial (top), along-track (middle) and cross-track (bottom) directions. Refer to the body of text for a definition of these errors. Statistics computed excluding the convergence phase of the EKF provide a control accuracy of 6.1 m (3D, RMS).

of latitude is steered within about 10 m from its nominal value. The maneuvers actually executed by the propulsion system on *Main* are illustrated in Fig. 3.11. The velocity increments are planned and executed as expected in along-track and cross-track directions at regular intervals, the cross-coupling caused by the attitude determination errors produces velocity variations in radial direction as well.

For completeness the relative orbit control errors, or control tracking errors, are computed by subtracting the actual relative motion of *Main* with respect to *Target* from the desired relative motion as described by the selected nominal relative orbital elements (cf. Table 3.4 and Eq. (2.18)). As shown in Fig. 3.12 the relative position control errors stay below 2.5/15.0/1.5 m in radial, along-track and cross-track directions, respectively, for an overall control accuracy of 6.1 m (3D, RMS).

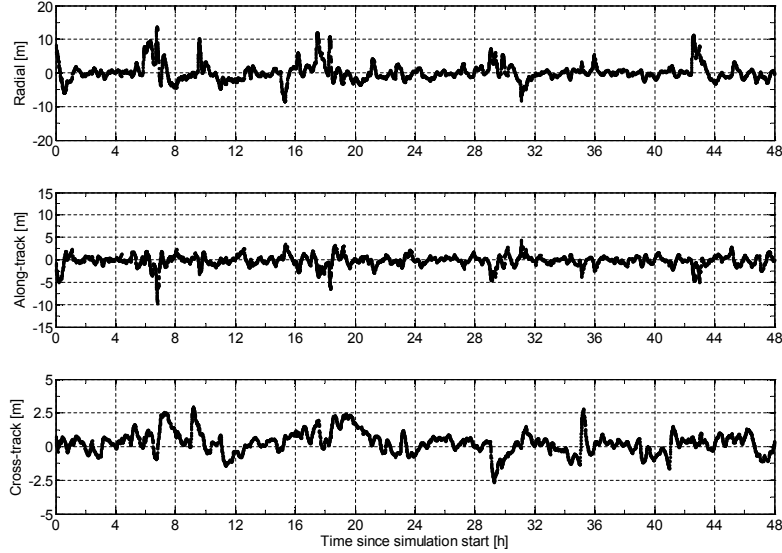


**Fig. 3.13:** Absolute *Main* position error mapped into the orbital frame aligned with the radial (top), along-track (middle) and cross-track (bottom) directions. Statistics computed excluding the convergence phase of the EKF provide an absolute navigation accuracy of 2.9 m (3D, RMS).

The accuracy of the navigation filter is evaluated as already done for the open-loop scenario, the navigation errors are computed by subtracting the estimated position and velocity of the *Main* and *Target* spacecraft from the true reference trajectory in the ECEF reference frame at 10 s samples. The absolute and relative navigation errors are then mapped in the orbital frame and plotted in Figs. 3.13-3.16. Upon filter convergence, the obtained absolute and relative navigation accuracy for the position is 2.9 m and 4.1 mm (3D, RMS), respectively (cf. Figs. 3.13 and 3.14). Compared to the open-loop test case, the typical absolute position errors are increased by about 1 m and show peaks correlated with the execution of maneuvers. Note that the coupling between radial and along-track errors is even more pronounced in the presence of maneuvers. Apart from isolated spikes in cross-track direction, the relative position errors are only slightly affected by the execution of orbit control maneuvers with an accuracy degradation of only half a millimeter.

The impact of the orbit maintenance maneuvers is higher on the absolute and relative velocity which are affected by errors of 9.2 mm/s and 0.01 mm/s (3D, RMS), respectively (cf. Figs. 3.15 and 3.16). At the instance of an orbit control maneuver the absolute velocity errors increase to values of several tens of mm/s which are then quickly re-absorbed by the EKF thanks to the collection of



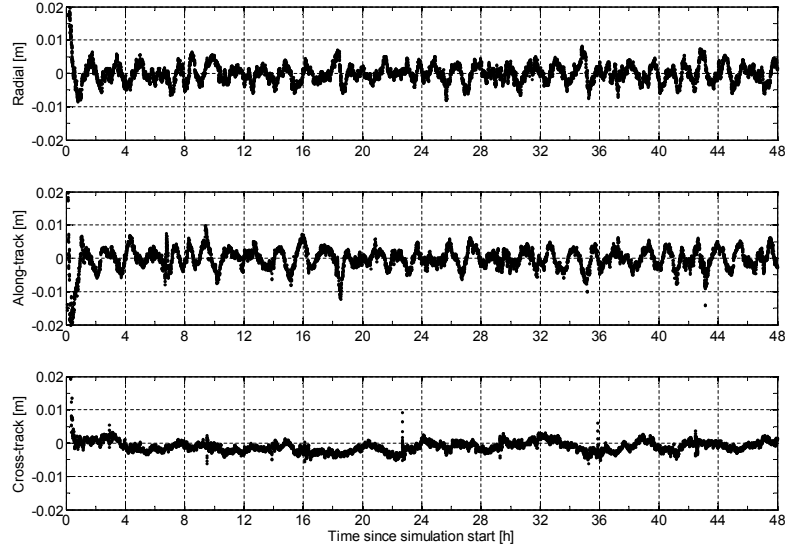


**Fig.3.14:** Relative position error (i.e., *Main* with respect to *Target*) mapped into the orbital frame aligned with the radial (top), along-track (middle) and cross-track (bottom) directions. Statistics computed excluding the convergence phase of the EKF provide a relative navigation accuracy of 4.1 mm (3D, RMS).

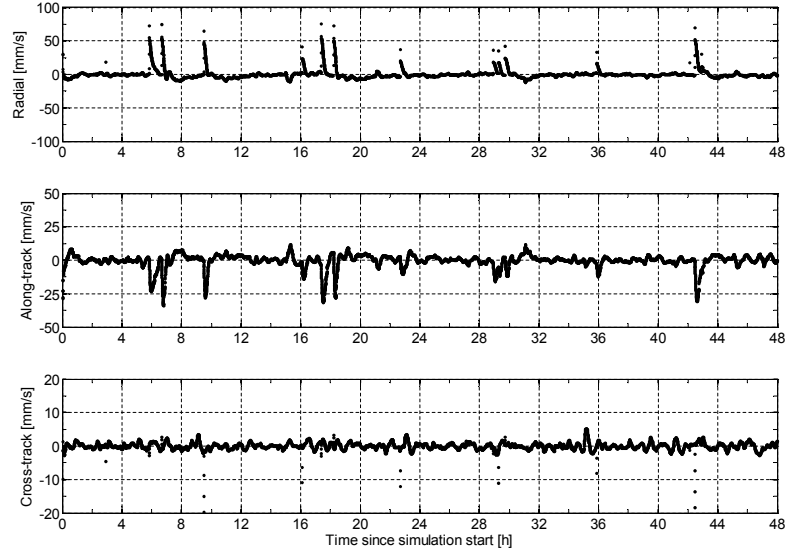


**Fig.3.15:** Absolute *Main* velocity error mapped into the orbital frame aligned with the radial (top), along-track (middle) and cross-track (bottom) directions. Statistics computed excluding the convergence phase of the EKF provide an accuracy of 9.2 mm/s (3D, RMS).

new GPS measurements. The compensation of the velocity error in cross-track direction is obtained immediately within the next EKF call, while the effects in the orbital plane are present for several minutes due to the high dynamic coupling and to lower sensitivity in the radial direction. The absolute empirical accelerations estimated during the closed-loop simulation (cf. Fig. 3.9) are also strictly correlated to the maneuver executions and to the discussed velocity er-

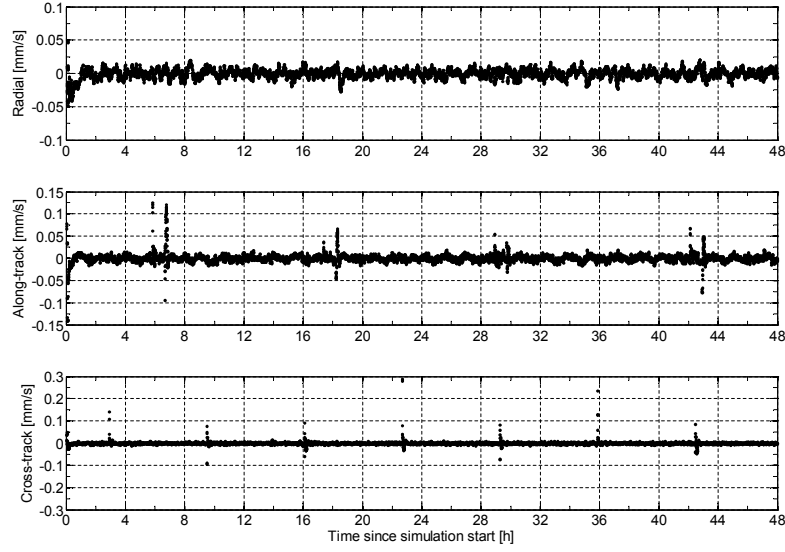


**Fig.3.16:** Relative velocity error (i.e., *Main* with respect to *Target*) mapped into the orbital frame aligned with the radial (top), along-track (middle) and cross-track (bottom) directions. Statistics computed excluding the convergence phase of the EKF provide an accuracy of 0.01 mm/s (3D, RMS).

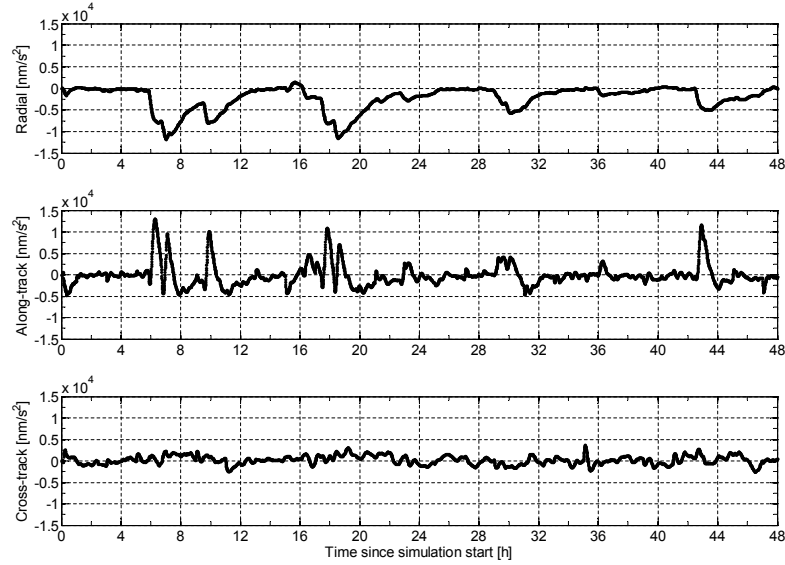


**Fig.3.17:** Empirical accelerations of *Main* mapped into the orbital frame aligned with the radial (top), along-track (middle) and cross-track (bottom) directions.

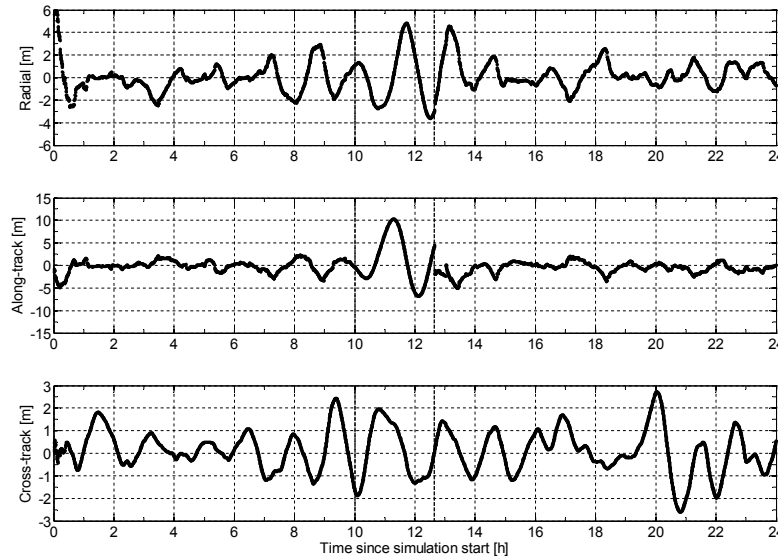
rors. In particular the radial and along-track components reach values of about  $10000 \text{ nm/s}^2$ , while the cross-track component stays below  $5000 \text{ nm/s}^2$  and is less affected by maneuver executions.

According to this preliminary verification the filter design is compliant to the assigned orbit determination requirements in representative open-loop and closed-loop test cases. So far only nominal operations scenarios have been considered, thus additional tests are discussed in the following to address the be-

havior of the navigation system during contingency operations where GPS data gaps have to be handled.

### GPS Data Gaps

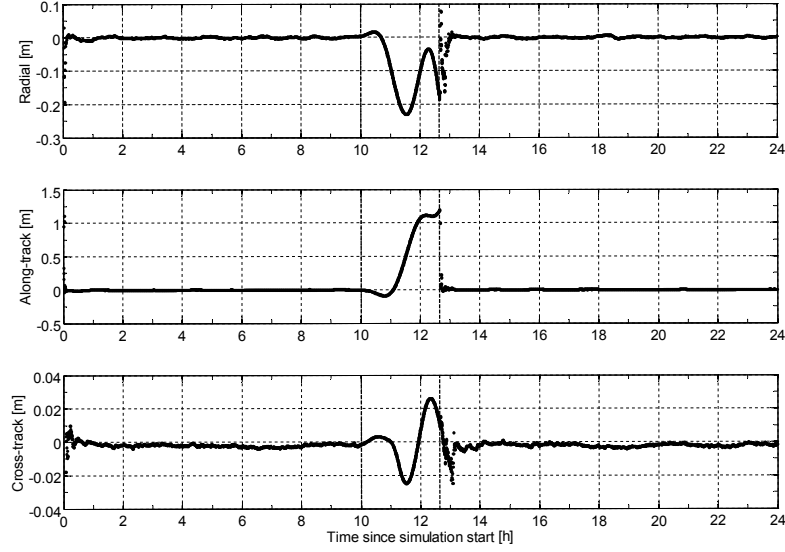
During nominal GPS operations, the navigation system performs only short arc orbit predictions over time intervals of 92 seconds between subsequent measurement updates of the EKF (cf. Section 3.3.2). In practice longer prediction arcs may be encountered during mission operations when invalid GPS measurements are provided to the navigation system. In these occasions only the time update of the EKF is performed and the orbit propagation accuracy is mainly driven by the force model implemented in the navigation filter. The third and fourth test cases are intended to assess the orbit prediction accuracy of the navigation software through the introduction of long outages of GPS measurements. Such events can occur during mission operations due to e.g. GPS receiver track losses, bus communication problems or inter-satellite-link malfunctions.



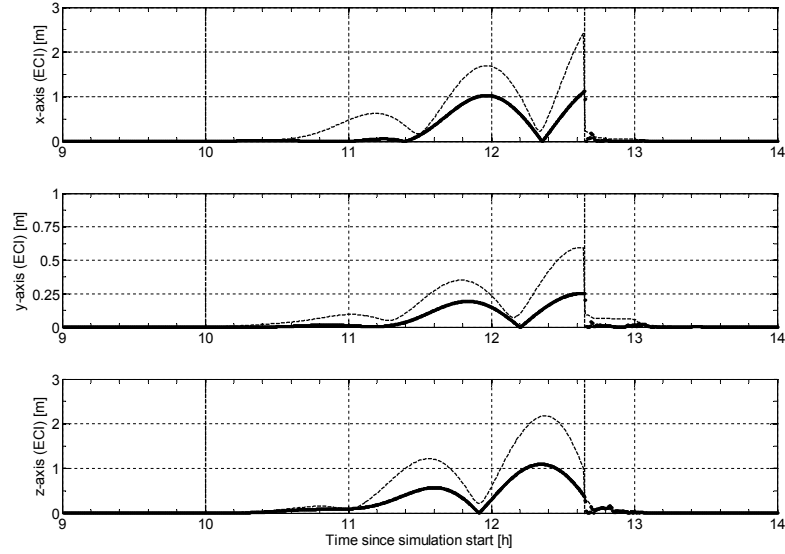
**Fig. 3.18:** Absolute *Main* position error mapped into the orbital frame aligned with the radial (top), along-track (middle) and cross-track (bottom) directions. Vertical dashed lines indicate start and end of the orbit prediction arc where no GPS measurements are available.

First we decide to interrupt the provision of GPS measurements from both spacecraft during the open-loop simulation presented earlier for a time span of 2.5 h starting at 10 h from the initial epoch. The resulting absolute and relative position errors, during both the orbit determination and prediction arcs, are illustrated in Figs. 3.18-3.20.

Fig. 3.18 depicts the absolute position error mapped into the orbital frame. The maximum orbit prediction error over the data outage arc amounts to about 5/10/2 m in radial, along-track and cross-track directions, respectively. It is characterized by an oscillating pattern of growing amplitude which is difficult to distinguish from the typical orbit determination error pattern.



**Fig.3.19:** Relative position error (i.e., *Main* with respect to *Target*) mapped into the orbital frame aligned with the radial (top), along-track (middle) and cross-track (bottom) directions. Vertical dashed lines indicate start and end of the orbit prediction arc where no GPS measurements are available.



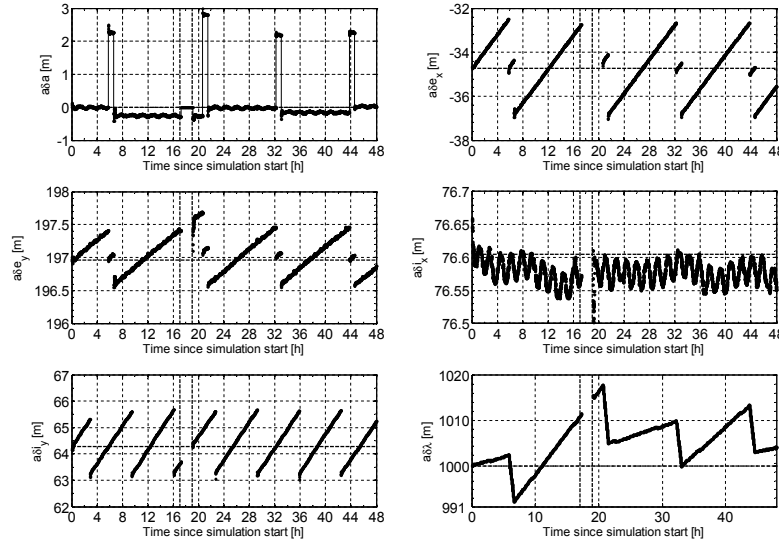
**Fig.3.20:** Relative position error (dotted thin line) and associated formal standard deviation (bold line) expressed in the ECI frame during the orbit prediction arc where no GPS measurements are available.

Fig. 3.19 depicts the relative position error mapped into the orbital frame. The maximum relative orbit prediction error over the data outage arc amounts to about 0.25/1.3/0.03 m in radial, along-track and cross-track directions, respectively. In contrast to the absolute orbit prediction, the relative prediction errors are much higher than the steady state relative orbit determination accuracy and are clearly distinguishable in the plot.

An important functionality of the navigation filter is to provide a mean-

ingful measure of the navigation accuracy on-board PRISMA. This is of special interest when designing Fault Detection and Isolation Recovery (FDIR) functionalities or collision avoidance algorithms which rely on the GPS-based navigation. Provided that the navigation filter is properly tuned, the formal covariance of the EKF can be used as an indicator of the navigation error.

As an example Fig. 3.20 shows the relative position error and the associated formal standard deviation during the orbit prediction arc where no GPS measurements are available. In this case the computed standard deviation provides a conservative assessment of the relative prediction accuracy following a pattern which recalls the actual prediction error. In general the formal covariance is highly influenced by the EKF a-priori and process noise settings and care has to be taken when interpreting it as a measure of the navigation error.



**Fig. 3.21:** Actual (dotted line) and nominal (dashed line) relative orbital elements during the 48-hours closed-loop simulation with GPS data gaps. Vertical dashed lines indicate start and end of the orbit prediction arc where no GPS measurements are available.

Finally we decide to introduce a 2 h GPS data gap in the more challenging closed-loop scenario. Here the difficulties are manifold, first of all the expected orbit prediction errors are larger because the velocity accuracy is inherently lower in closed-loop operations, second the guidance and control software has to be able to detect the anomaly of the GPS-based navigation system and avoid the execution of maneuvers during the prediction arc. In order to verify these aspects we place the GPS data gap at 17 h from simulation start, in such a way the orbit prediction arc overlaps exactly with the execution of two along-track maneuvers as shown by the previous closed-loop nominal test case in Fig. 3.11.

Fig. 3.21 depicts the relative orbital elements computed by the guidance and control software during the 48 hours closed-loop simulation arc. The start and end of the GPS data outage is indicated by vertical dashed lines. As expected the control software interrupts its guidance computations in correspondence of the two hours data gap. Even if the relative eccentricity vector control window

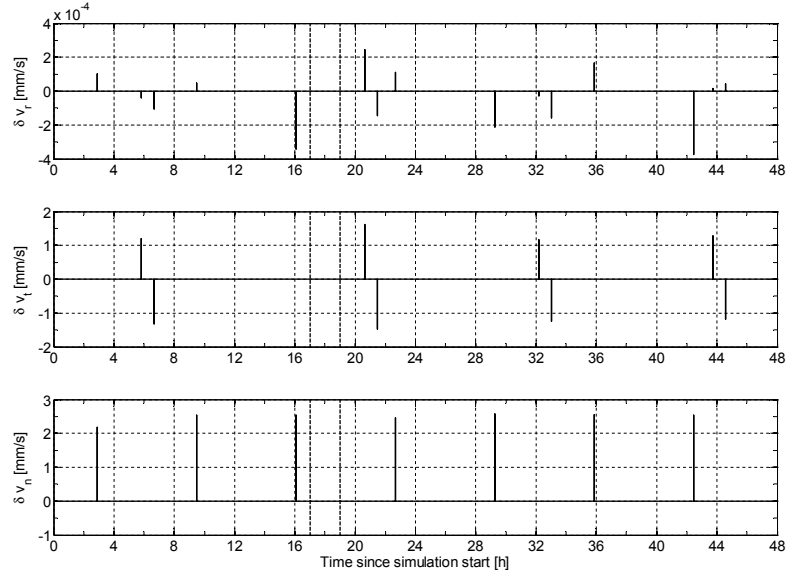


**Fig. 3.22:** Orbit control maneuvers actually executed by *Main* mapped into the orbital frame aligned with the radial (top), along-track (middle) and cross-track (bottom) directions. Vertical dashed lines indicate start and end of the orbit prediction arc where no GPS measurements are available.

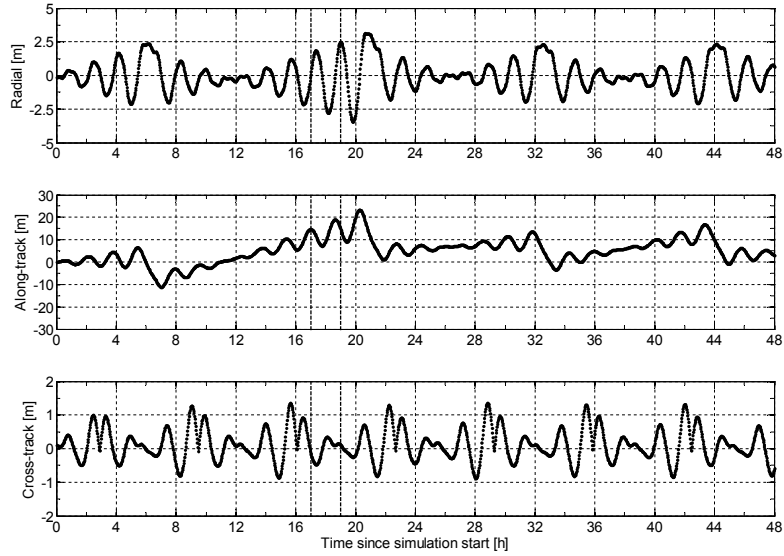


**Fig. 3.23:** Control tracking error mapped into the orbital frame aligned with the radial (top), along-track (middle) and cross-track (bottom) directions. Vertical dashed lines indicate start and end of the orbit prediction arc where no GPS measurements are available.

is hardly violated, the along-track maneuvers are not executed and delayed after the end of the contingency. As clearly shown by Fig. 3.22, shortly after the end of the data outage a pair of larger maneuvers is executed to recover the nominal configuration (cf. Fig. 3.11 for comparison with the nominal case). The main impact on the relative orbital elements is given by a longer drift of the relative mean argument of latitude which affects the control tracking error in

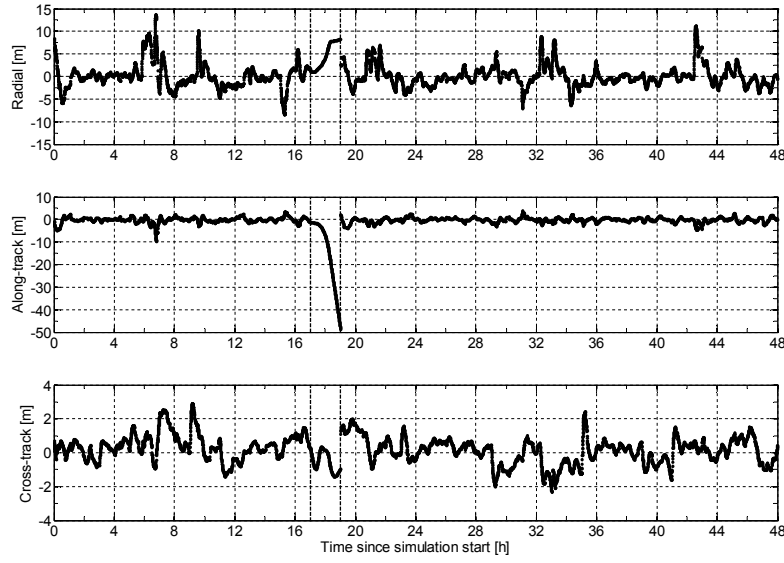


**Fig. 3.24:** Absolute *Main* position error mapped into the orbital frame aligned with the radial (top), along-track (middle) and cross-track (bottom) directions. Vertical dashed lines indicate start and end of the orbit prediction arc where no GPS measurements are available.

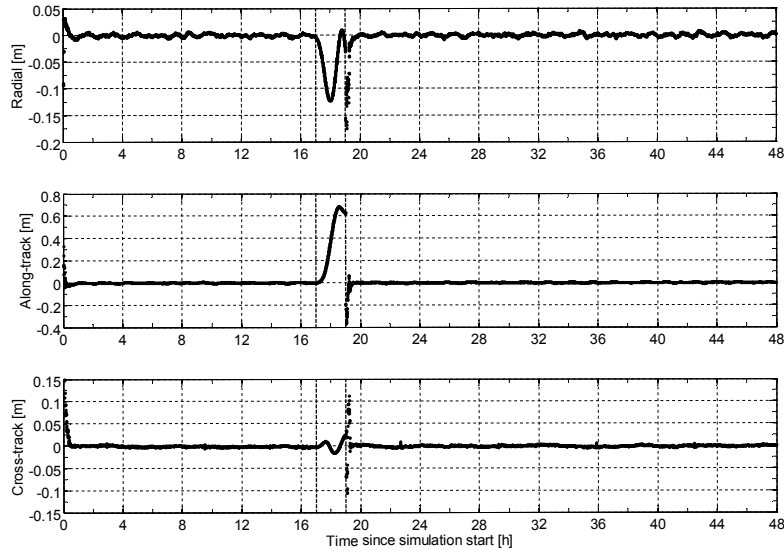


**Fig. 3.25:** Relative position error (i.e., *Main* with respect to *Target*) mapped into the orbital frame aligned with the radial (top), along-track (middle) and cross-track (bottom) directions. Vertical dashed lines indicate start and end of the orbit prediction arc where no GPS measurements are available.

along-track direction by a few meters (cf. Fig. 3.23).

The accuracy of the navigation filter is evaluated as usual, Fig. 3.24 depicts the absolute position error mapped into the orbital frame. The maximum orbit prediction error over the data outage arc amounts to about 8/50/1.5 m in radial, along-track and cross-track directions, respectively. Compared with the open-loop case, the prediction performance in radial and especially along-track

directions is reduced mainly because of the degraded velocity accuracy. Fig. 3.25 depicts the relative position error mapped into the orbital frame. The maximum relative orbit prediction error over the data outage arc amounts to about 0.2/0.7/0.1 m in radial, along-track and cross-track directions, respectively. In contrast to the absolute orbit prediction, the relative prediction error is comparable with the open-loop case.

### 3.4.3 Validation using GRACE Flight Data

The Gravity Recovery And Climate Experiment (GRACE) mission [Tapley and Reigber, 1999] is a joint project of the National Aeronautics and Space Administration (NASA) and the German Aerospace Center (DLR). Its primary objective is the generation of Earth gravity field models with high spatial and temporal resolution. It consists of two identical formation flying spacecraft, namely GRACE-A and GRACE-B, which were launched on March 17, 2002 with a Rockot launcher from Plesetsk, Russia. Following the injection into a near-polar, near-circular orbit of 490 km altitude, the two spacecraft have been separated by roughly two degrees in orbital longitude. Since then, regular formation keeping maneuvers have been executed to maintain a relative along-track separation of  $220 \pm 50$  km, which provides optimum working conditions for measuring high-order harmonic components in the Earth's gravity field. Key mission's instruments are the Ka-Band Ranging System (KBR) and on-board accelerometers. The KBR instrument measures the change in distance between both spacecraft, which is a measure for the change in gravity, within a precision of  $10 \mu\text{m}$  at 1 Hz samples. Both spacecraft are equipped with the JPL BlackJack GPS receivers and offer an ideal setup to validate the accuracy of GPS-based absolute and relative navigation.

As previously explained the PRISMA and TerraSAR-X/TanDEM-X formations will be characterized by baselines of a few kilometers, thus differential ionospheric effects are expected to be very small [van Barneveld et al., 2008] and have been neglected in the design of the navigation filter. GRACE offers a unique opportunity to verify this assumption thanks to the so-called switch maneuver which was executed in December 2005 to exchange the order of the GRACE satellites. The exchange of position was required to limit the surface erosion of the on-board KBR horn by atomic oxygen and to avoid the risk of spurious K-Band range signals caused by lacking thermal control of the horn. The GRACE switch maneuver was initiated by a series of three slight velocity changes of GRACE-B, starting on December 3, 2005. As time went by, GRACE-B drifted slowly from a trailing position to a leading position, passing GRACE-A at a closest distance of a mere 431.2 m on December 10, 2005 [Montenbruck et al., 2006]. As a fundamental consequence, for about one day, the GRACE formation geometry assumed characteristics very similar to the envisioned PRISMA and TerraSAR-X/TanDEM-X missions.

The goal of this section is to verify the navigation software design and assess the absolute and relative navigation accuracy using real GPS data obtained from this unique testbed. Raw single frequency GPS data from the JPL Black-



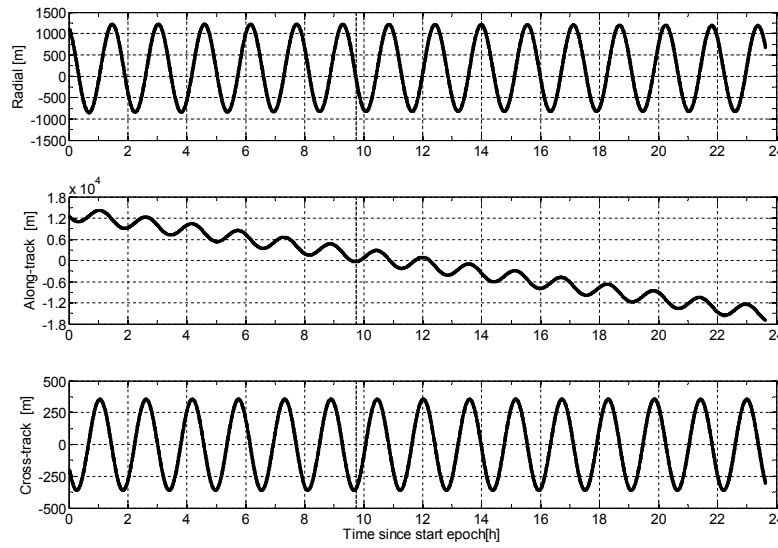


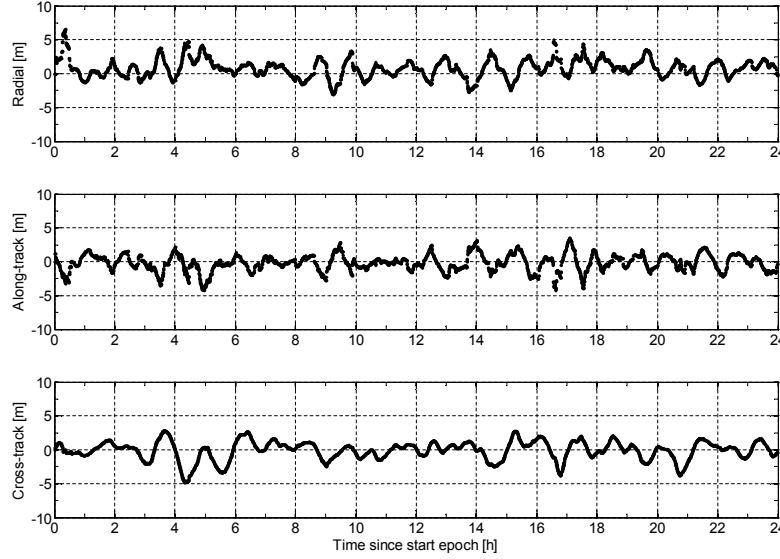
**Fig. 3.26:** Actual relative position of GRACE-A with respect to GRACE-B mapped into the orbital frame aligned with the radial (top), along-track (middle) and cross-track (bottom) directions. The vertical dashed line indicates the point of closest approach at a minimum separation of 431.2 m.

Jack receivers are employed during the swap phase on December 9–10, 2005 or Day of Year (DOY) 243–244. During this period, both satellites are flying in close formation with inter-satellite separations below 20 km. The PEM software, used so far to emulate the Phoenix-S receivers, is simply replaced by a function which reads the raw GPS data of GRACE-A and GRACE-B provided in RINEX format and feeds the navigation software with Mitel messages (i.e., Phoenix receiver output data format) every 10 s. The handling of GPS ephemeris normally provided by the Phoenix-S receivers is replaced by the usage of the real broadcast ephemerides for DOY 243–244. The correction of the GPS antenna offsets with respect to the center of mass makes use of the GRACE star camera quaternions available as part of the telemetry stream. Fig. 3.26 illustrates the relative motion of GRACE-A with respect to GRACE-B during the selected GPS data arc. The along-track separation drifts from about 12 km at the initial epoch (9. December 2005, 20:00:00.0 GPS Time) to approximately –16 km after 24 h. The radial and cross-track components of the relative motion oscillates periodically with typical amplitudes of 2 km and 700 m, respectively and are phased according to parallel relative eccentricity and inclination vectors.

The key settings applied to the EKF for absolute and relative navigation during the processing of GRACE flight data are listed in Table 3.11 and are identical for GRACE-A and GRACE-B. The a-priori and steady state variances applied to the state variables are similar to the open-loop test case. A larger standard deviation for the empirical acceleration in radial direction has been selected to absorb the stronger Earth's gravity field effects present at the GRACE lower altitude (i.e., 300 km lower than PRISMA). The pseudorange and carrier phase measurement noise level is set to 0.1 m and 0.1 mm, respectively and re-

**Table 3.11:** Settings of the EKF used to process GRACE flight data.

Parameter	Value	Parameter	Value
<i>A-priori standard deviation</i>		<i>Process noise</i>	
$\sigma_r$ [m]	1000.0	$\sigma_{a_r}$ [nm/s <sup>2</sup> ]	30.0
$\sigma_v$ [m/s]	1.0	$\sigma_{a_t}$ [nm/s <sup>2</sup> ]	20.0
$\sigma_{C_D}$	1.0	$\sigma_{a_n}$ [nm/s <sup>2</sup> ]	20.0
$\sigma_{a_r}$ [nm/s <sup>2</sup> ]	300.0	$\sigma_{c\delta t}$ [m]	500.0
$\sigma_{a_t}$ [nm/s <sup>2</sup> ]	200.0	<i>Measurements standard deviation</i>	
$\sigma_{a_n}$ [nm/s <sup>2</sup> ]	200.0	$\sigma_{PR}$ [m]	0.1
$\sigma_{c\delta t}$ [m]	500.0	$\sigma_{CP}$ [mm]	0.1
$\sigma_N$ [m]	0.05		
<i>Auto-correlation time scale</i>			
$\tau_a$ [s]	900.0		
$\tau_{c\delta t}$ [s]	100.0		

**Fig. 3.27:** Absolute GRACE-A position error mapped into the orbital frame aligned with the radial (top), along-track (middle) and cross-track (bottom) directions. Statistics computed excluding the convergence phase of the EKF provide an absolute navigation accuracy of 2.5 m (3D, RMS).

flects the accuracy of the JPL Blackjack receiver measurements.

The accuracy of the navigation process is evaluated by comparing the navigation output in the ECEF reference frame with a DLR's precise reference trajectory whose absolute and relative position accuracy is better than 4 cm and 0.1 cm (3D, RMS) [Kroes, 2006]. Absolute and relative navigation errors are then mapped into the orbital frame and plotted in Fig. 3.27 and 3.28, respectively. Upon filter convergence, the obtained absolute navigation accuracy for the position is 2.5 m (3D, RMS). This result is close to what we have obtained in the previous test cases and gives good confidence on the realism of the adopted simulation environment. The relative navigation accuracy is given by 3.2 cm

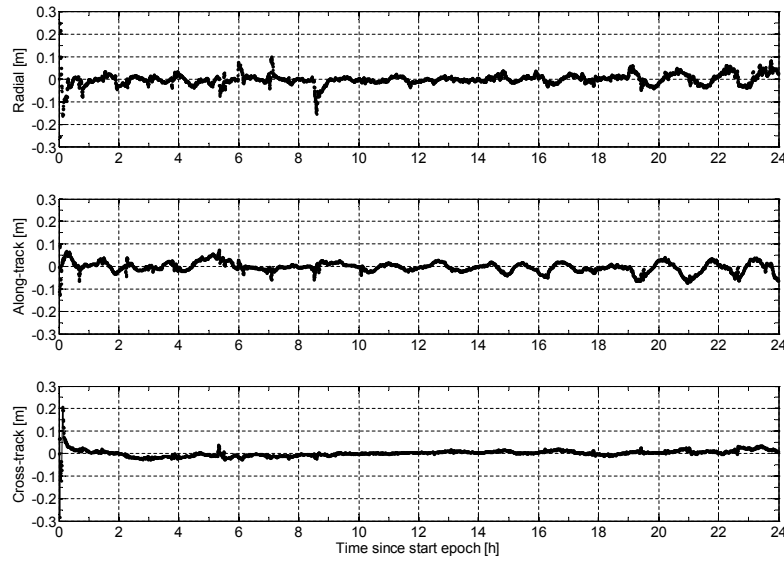


**Fig. 3.28:** Relative position error (i.e., GRACE-A with respect to GRACE-B) mapped into the orbital frame aligned with the radial (top), along-track (middle) and cross-track (bottom) directions. Statistics computed excluding the convergence phase of the EKF provide a relative navigation accuracy of 3.2 cm (3D, RMS).

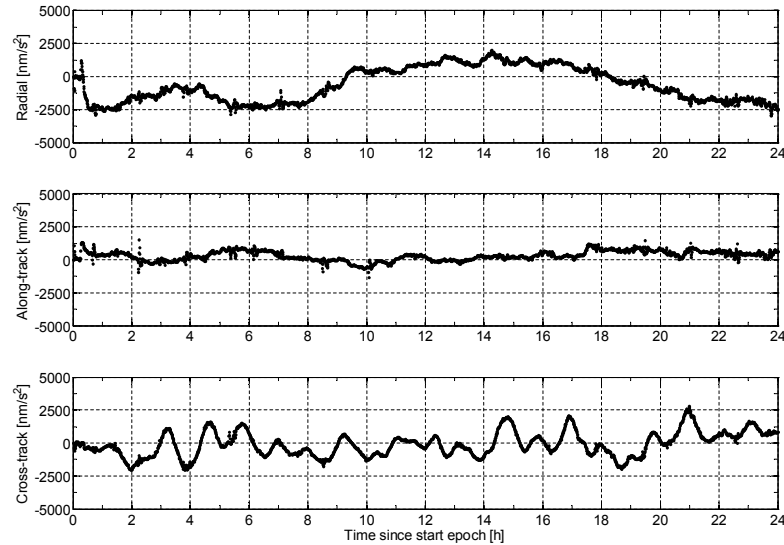


**Fig. 3.29:** Empirical accelerations of GRACE-A mapped into the orbital frame aligned with the radial (top), along-track (middle) and cross-track (bottom) directions.

(3D, RMS) and is nearly one order of magnitude larger than what obtained in the open-loop and closed-loop test cases.

The increased relative navigation error results are mainly caused by the ionospheric path delays. This is confirmed by simulations which make use of GPS data provided by the GRACE BlackJack receivers on the second transmitting frequency (L2). The usage of the ionosphere-free pseudorange and carrier-phase L1/L2 combinations, instead of the usual single frequency counterparts,

provides a relative navigation accuracy of 1 cm over the same data arc and confirms again that ionospheric effects can be safely neglected when dealing with closely flying spacecraft. Overall the GRACE formation testbed provides results which are well comparable with the previous test cases. For completeness the absolute and relative velocity accuracy obtained with GRACE flight data is around 4.7 mm/s and 0.095 mm/s (3D, RMS), respectively. Table 3.12 collates the real-time absolute and relative navigation accuracy evaluated in the three considered tests (i.e., open-loop, closed-loop and GRACE) for an easier cross comparison.

**Table 3.12:** Summary of real-time absolute and relative navigation accuracy (3D, RMS) evaluated in the open-loop, closed-loop and GRACE test cases.

Test cases	Absolute		Relative	
	Position [m]	Velocity [mm/s]	Position [mm]	Velocity [mm/s]
Open-loop	1.9	2.7	3.6	0.006
Closed-loop	2.9	9.2	4.1	0.01
GRACE	2.5	4.7	32.0	0.095

## 4. GNC System Architecture

### 4.1 Model-Based Software Design

#### 4.1.1 General Concept

Embedded software development is traditionally performed on a programming level with a focus on software engineering aspects. In most traditional cases, software validation is addressed very late in the development process, and often on hardware prototypes only. Errors found in hardware or software at this stage are very costly. It can be time consuming to trace problems back to their cause and errors related to incomplete, incorrect, or conflicting requirements may even necessitate a fundamental redesign.

It is only recently that model-based approaches are emerging where emphasis is given to system engineering methods. This approach raises the abstraction level for the development in order to allow an efficient handling of ever more complex systems. Engineers can continuously test the design as it evolves, checking it against requirements and finding mistakes earlier in development when they are easier and less costly to correct. In addition, model-based design automates code generation for the embedded system by eliminating the need to hand-code the guidance, navigation and control algorithms.

Benefits of a model-based over a traditional development strategy are expected in the field of robustness, predictability, scalability, efficiency and faster development schedules [Edfords, 2005]. For PRISMA, a model-based design method is used for the complete on-board application software. To this end, the on-board software is implemented in Matlab/Simulink blocks which are then auto-coded with Real Time Workshop and executed under the operating system Real-Time Executive for Multiprocessor Systems (RTEMS) on the on-board LEON3 processor [Gaisler, 2001].

#### 4.1.2 System Structure

The on-board software (OBS) architecture consists of a layered structure with a Basic Software (BSW) level and an Application Software (ASW) level communicating with each other through dedicated message queues. While the BSW includes basic applications, device drivers and I/O-utilities, the ASW encapsulates all top-level applications like spacecraft control and telecommand and telemetry.

The ASW consists of a number of application components with each application component encapsulating a logically-grouped functionality. Each application component has a uniform interface and internal structure and is executed via a Asynchronous Monotonic Scheduler (AMS) scheduler with a specified sample time and priority. While external data stores provide access to the

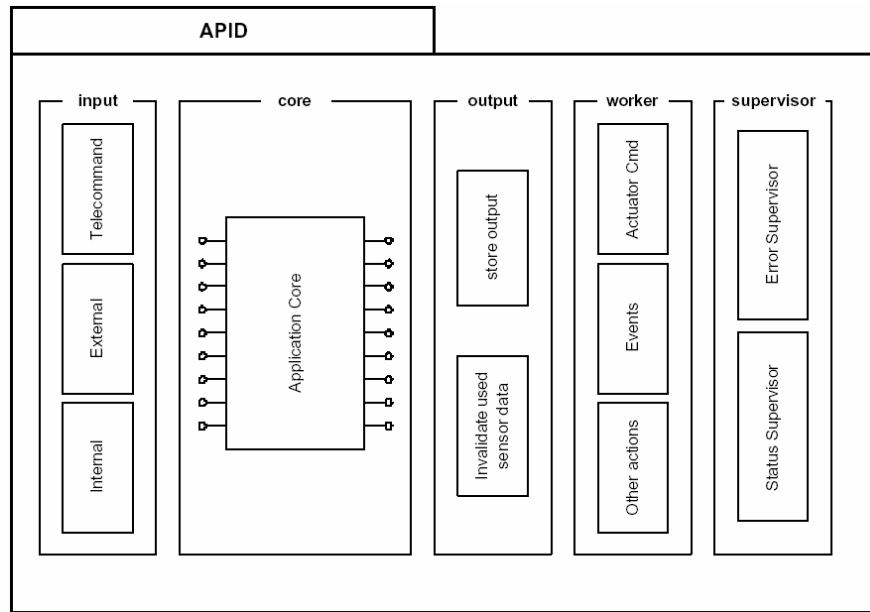


**Fig. 4.1:** Internal structure of an application component [Edwards, 2005].

Remote Terminal Unit (RTU) components, the internal data store is used for communication between application components.

The internal structure of an application core is shown in Fig. 4.1. Here, the input section comprises the processing of incoming telecommands as well as external data, e.g. from sensors and internal data from other application components. The application core holds most of the application component algorithms. The output section stores the external output vector and holds a component which invalidates used sensor data. The worker sends actuator commands, housekeeping and provides other services subsequent to the application core. Finally, the supervisor basically implements the FDIR functions.

### 4.1.3 Specific Application Cores

The application core implements specific functionally-grouped algorithms. It is implemented as an input/output function, i.e. the function retrieves the input vector, executes its algorithms and delivers its output vector. The algorithms in the application core are executed at the basic sample time of the application component or multiples thereof with the restriction that their execution time must be smaller than the basic sample time. Thus, algorithms with excessive computational demands may not be treated in application cores with small sample times.

Most of the GNC algorithms involve sensor data processing and filtering with limited computational requirements and can therefore be grouped into a GNC application component which runs at a 1 Hz rate. However, the navigational task of absolute and relative orbit determination based on GPS data is computationally very demanding and may thus not be integrated in a straight-

forward manner into the GNC application component. Therefore, the ORB application component has been defined which is executed at a sample time of 30 s and allows a proper separation of computational intensive GNC algorithms from less demanding ones. The functions which interface directly the GPS hardware are located in the BSW application component.

As a consequence, the software architecture for navigation, guidance and control must take into account the specific application components for PRISMA and associate functional tasks with the appropriate application components. The characteristics of application components for the GPS-based flight software are summarized in 4.1.

**Table 4.1:** Summary of application components applied for GPS-based flight software.

Component Name	Sample Time [s]	Characteristics
BSW	1.0	Holds the direct interface with the GPS hardware
GNC	1.0	Holds the majority of GNC algorithms which can be executed within the sample time
ORB	30.0	Holds the time-consuming dynamical algorithms which may not be executed in a 1 s sample time

## 4.2 Architectural Design

### 4.2.1 Physical System

#### Space Segment

Following launch, the *Main* and *Target* spacecraft will stay in a clamped configuration (Fig. 1.2) for system check-out, initial performance tests and first experiments. Upon separation of the two spacecraft, *Main* acts as communications relay between the ground control center and *Target*. In particular, the communication between *Main* and *Target* relies on an ISL which forwards commands to *Target* and provides telemetry to *Main*. Part of the provided *Target* telemetry is processed on-board *Main*, e.g. GPS messages from *Target*, while other telemetry is routed through *Main* back to the ground control center. A top-level architecture of this configuration is provided in Fig. 3.1.

#### GPS System

The Phoenix-S GPS system on *Main* and *Target* will provide pseudorange and carrier phase measurements for the PRISMA navigation system on *Main*. GPS measurements collected on *Target* are transferred to *Main* via the ISL. The navigation system provides absolute position and velocity of the participating spacecraft to be used by the *Main* GNC system as well as the other PRISMA experiments. The GPS system will also provide timing information.

The physical architecture of the GPS system is identical on *Main* and *Target*. For redundancy, two Phoenix-S GPS receivers are available, which are con-

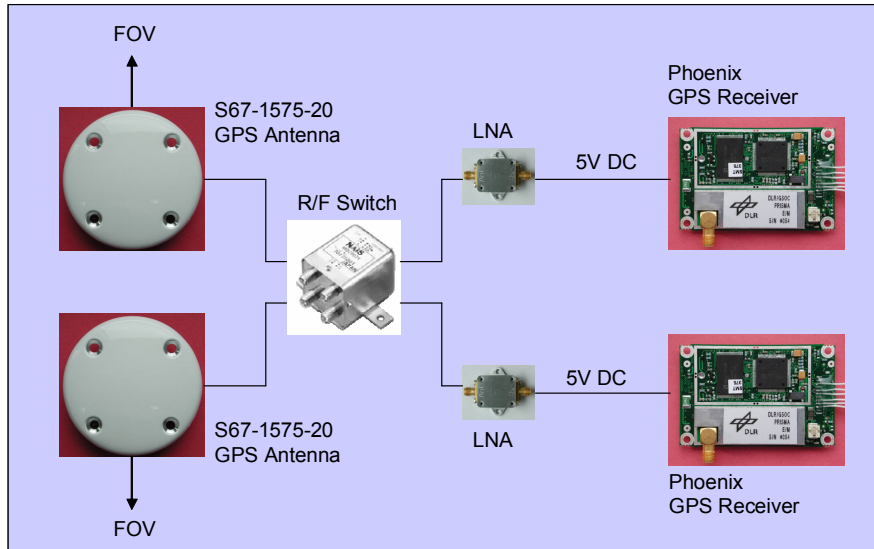


**Fig. 4.2:** PRISMA Phoenix-S GPS system on *Main* and *Target*.

nected to two GPS antennas via a coaxial switch. The dual antenna system provides increased flexibility for handling non-zenith pointing attitudes and antennas may be selected by ground command. Only one receiver will be active at any time. The overall physical architecture of the PRISMA GPS system on *Main* and *Target* is shown in Fig. 4.2.

Each GPS receiver is connected to its own low-noise amplifier (LNA) and provides 5 V DC for its operation via the RF input. Compared to a single LNA placed between the antenna and the coaxial switch, this configuration avoids the need for an external LNA power supply and DC blocks. Furthermore, the adopted design reduces the risk of single-point failures. The use of a passive antenna, finally, allows the insertion of a band-pass or notch-filter prior to the coaxial switch and LNAs, if adverse out-of-band RF signals should be encountered during interference tests.

#### 4.2.2 Software Architecture

##### Building Blocks

The overall architectural design of the GPS-based flight software on the *Main* spacecraft is depicted in Fig. 4.3. Here, gray boxes indicate the BSW, GNC and ORB application cores of their respective application components. The software is structured into subsystems, according to their functional objectives, which are indicated as green boxes. The depicted architectural design emphasizes the flow of information which is directed from left to right and shows exclusively software modules developed in the frame of this research. Sensors and actuators involved in the GPS-based GNC functionalities are represented by white shadowed boxes. Straight lines indicate data variables which are directly exchanged between application components, while dashed lines repre-



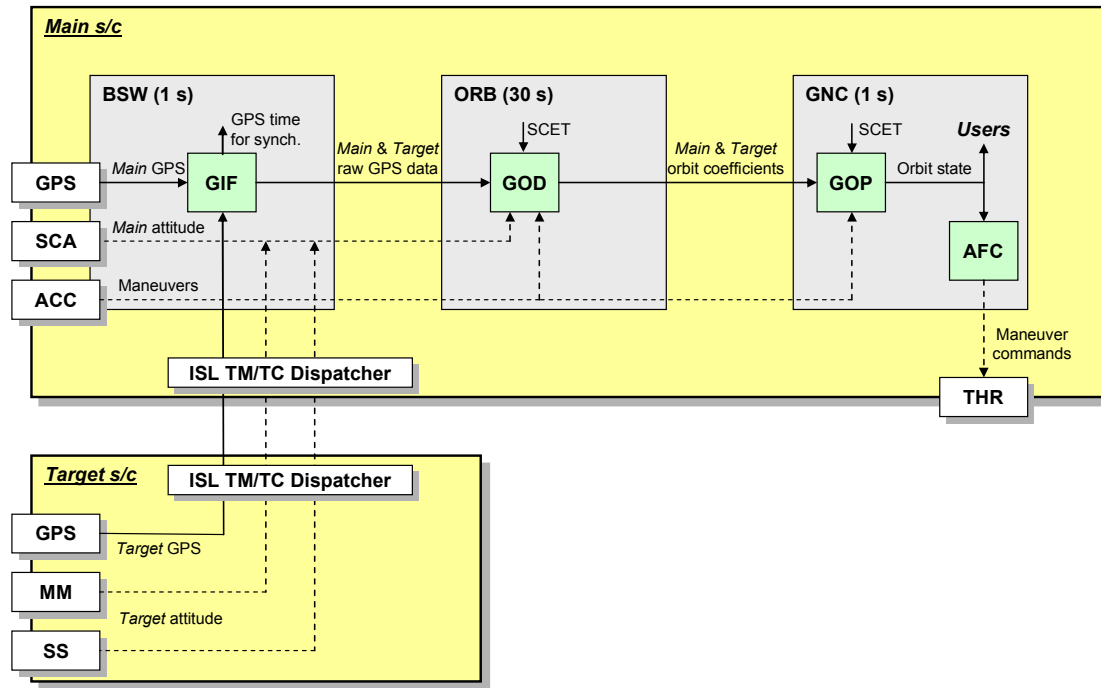


**Fig. 4.3:** Top-level architecture of GPS-based application software on *Main* highlighting the data flow (from left to right).

sent variables which are conditioned and filtered by auxiliary OBS modules (not indicated).

The GPS interface (GIF) is located within the BSW application core and receives the messages from the operational Phoenix-S receiver on *Main* and on *Target*. GIF performs message validation, editing, and extraction and stores the extracted raw GPS data for access by the orbit determination function. GIF provides to the OBS the GPS time for on-board time synchronization and writes GPS data and internal status parameters to a data buffer for further download as house-keeping data.

GPS raw measurements are read as internal data by the GPS-based Orbit Determination (GOD) which is part of the ORB application core. GOD comprises the complete orbit determination task which provides the absolute trajectories of *Main* and *Target*. To this end, both time and measurement updates of the Extended Kalman filter are executed. In the case that no valid GPS data for the past processing interval are available only a time update is performed. GOD requires as input antenna, attitude and maneuver data to compute the GPS antenna offset with respect to the center of mass and account for past thruster impulses. As a result, GOD outputs *Main* and *Target* orbit parameters which are also stored internally. These parameters are then accessed by GOD in the next execution step to compute position/velocity at the successive measurement times and by the orbit prediction function located in the GNC core.

The GPS-based Orbit Prediction (GOP) subsystem retrieves the on-board

time, or Spacecraft Elapsed Time (SCET), and the orbit coefficients which have been generated by GOD. These parameters are used to compute 1 Hz updates of the *Main* and *Target* position and velocity at the SCET. In the case that orbit maneuvers have been executed in the past interval, GOP generates a new set of orbit coefficients which is used internally until a new set is provided by GOD. Auxiliary information provided by GOD is applied by GOP to derive accuracy-related information on the *Main* and *Target* state.

The Autonomous Formation Control (AFC) subsystem reads the current *Main* and *Target* state vectors as computed by GOP and performs the guidance calculations based on the nominal relative orbital elements and predefined control windows. As a result, the required velocity increments are computed and provided to the OBS for maneuver execution.

### Model-based Design

The basic building blocks described above have been detailed and implemented in a Matlab/Simulink environment. To that end, top-level subsystems have been created describing interfaces within the BSW, ORB and GNC application cores. The subsystems are depicted in Fig. 4.4.

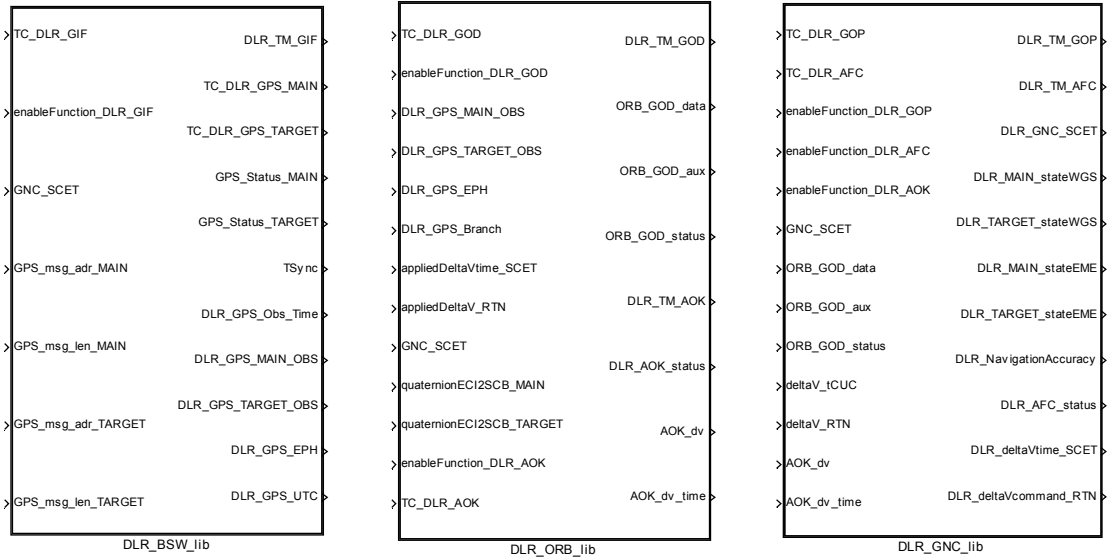


**Fig. 4.4:** Top-level Simulink subsystems implementing the GPS-based GNC application software.

The BSW and ORB subsystems are not composed of further subsystems on a Matlab/Simulink level. In contrast, the GNC subsystem has an internal more detailed structure on the Matlab/Simulink level which reflects the different functional tasks described above. This inner structure is depicted in Fig. 4.5. At the lowest level, the developed subsystems (GIF, GOD, GOP and AFC) consist of S-functions providing a C/C++ interface to the application software [MathWorks, 2002]. These S-functions are hand-coded in C/C++ and are based on the libraries of Montenbruck and Gill [2001a]. Purpose, tasks, interfaces and timeline of each S-function are described in the next section.

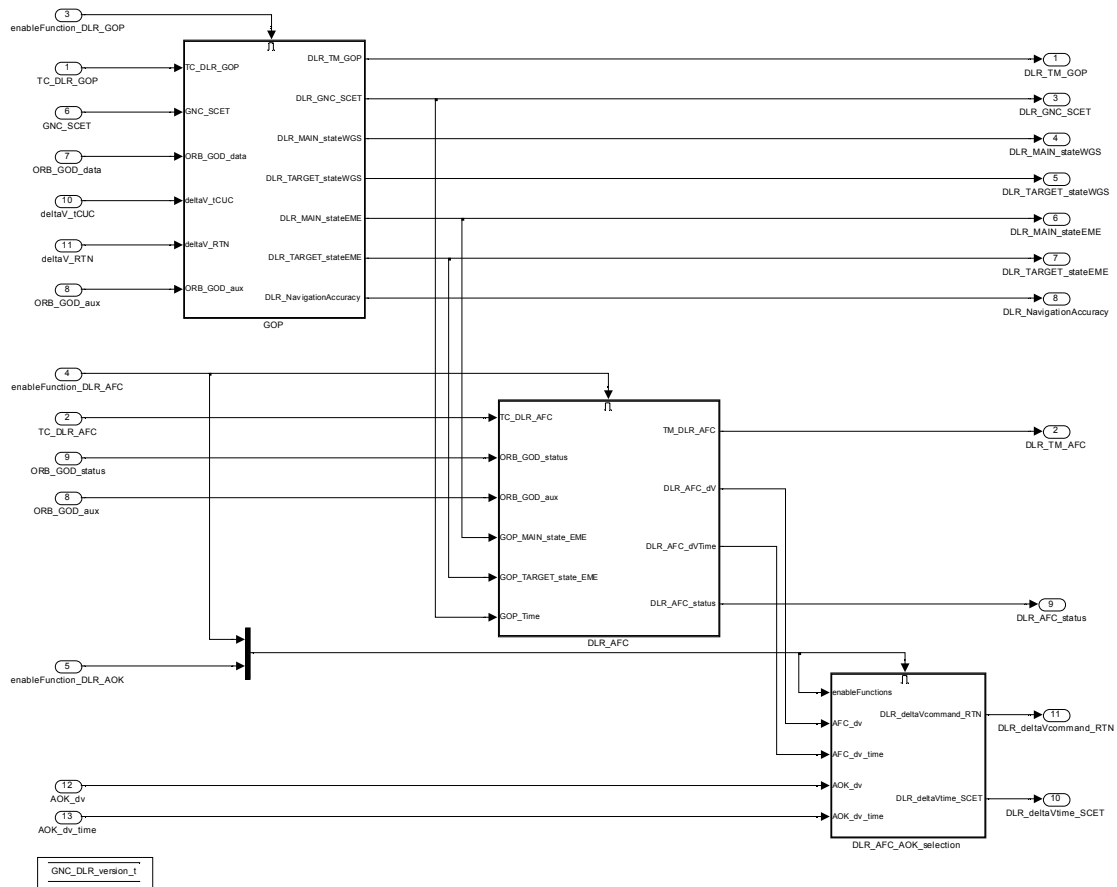


**Fig. 4.5:** Architecture of GPS-based application software within the GNC application core.

## 4.3 Software Modules

### 4.3.1 GPS Interface

The GPS Interface (GIF) represents the link between the Phoenix-S GPS receivers (on-board *Main* and *Target*) and the GPS-based Orbit Determination (GOD) on-board *Main*. Specifically, all Phoenix-S messages are forwarded to GIF that performs message validation, data verification, and extraction. GIF receives Mitel messages from the operational Phoenix-S receivers and store their raw data for access by GOD. GIF extracts the GPS time from the receiver messages and provides it to the OBS for on-board time synchronization. Furthermore GIF handles the GPS broadcast ephemeris and, if necessary, sends request ephemeris commands to the receivers. Finally, GIF outputs GPS data and internal status parameters as telemetry data. In particular, the main functions of the GPS interface are to

1. retrieve and execute commands for control of the GIF task
2. read *Main* and *Target* Phoenix-S receiver messages from the GPS buffer

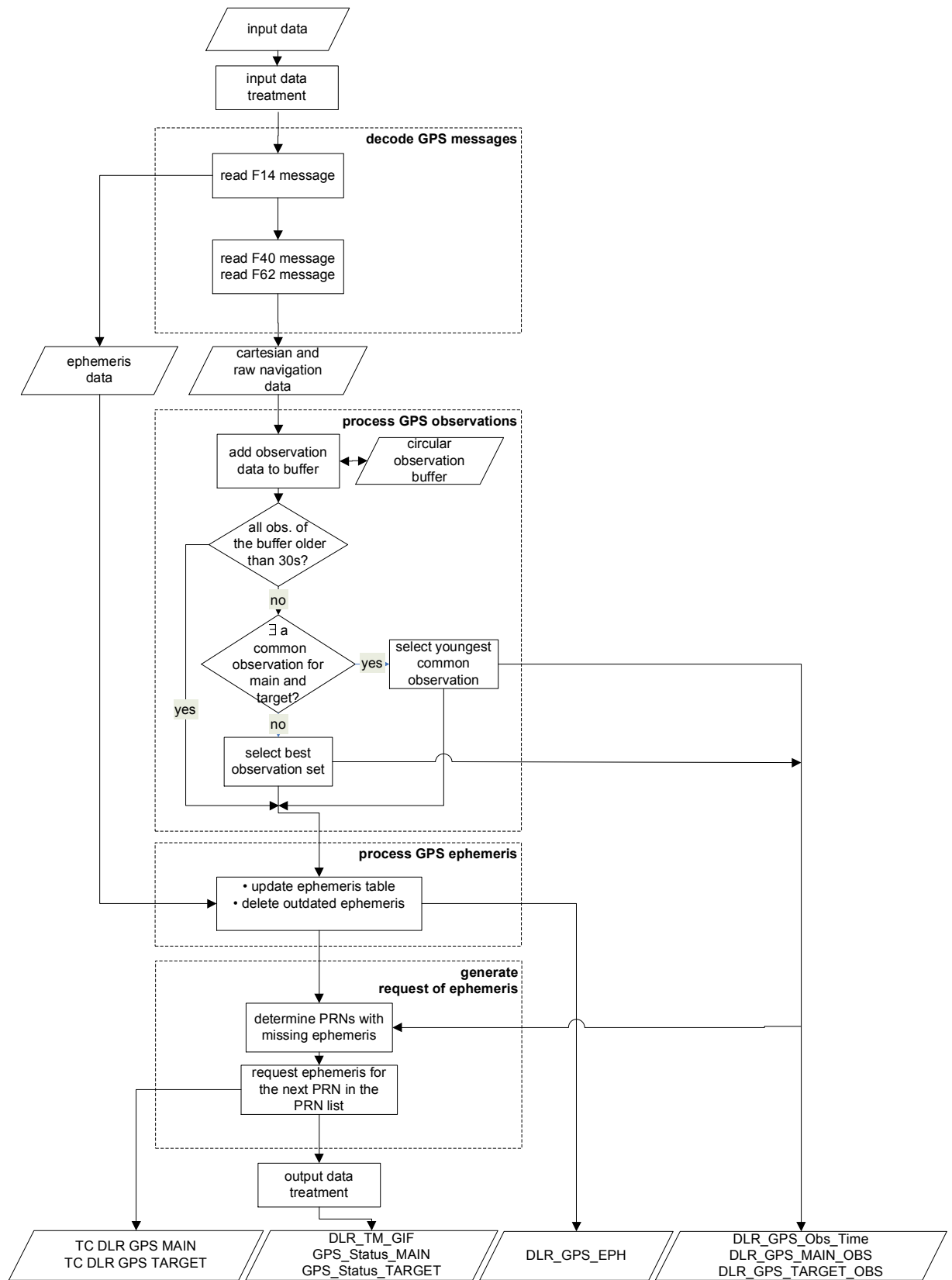


**Fig. 4.6:** Top level processing scheme and logic of GIF.

**Table 4.2:** List of GIF inputs.

Input variable name	Type(Size)	Description
TC.DLR.GIF	double(8)	Telecommand parameters for GIF control (e.g., task activation parameters and editing criteria)
enableFunction.DLR.GIF	boolean(1)	Flag for GIF activation
GNC.SCET	uint32(2)	On-board time (synchronized to GPS time)
GPS_msg_adr_MAIN	uint32(1)	Address of <i>Main</i> Phoenix-S receiver output data
GPS_msg_len_MAIN	uint32(1)	Length of <i>Main</i> Phoenix-S receiver output data
GPS_msg_adr_TARGET	uint32(1)	Address of <i>Target</i> Phoenix-S receiver output data
GPS_msg_len_TARGET	uint32(1)	Length of <i>Target</i> Phoenix-S receiver output data

**Table 4.3:** List of GIF outputs.

Output variable name	Type(Size)	Description
DLR.TM.GIF	uint8(5)	Telemetry parameters for GIF monitoring (e.g., status parameters, number of satellites tracked)
TC.DLR.GPS.MAIN	uint8(8)	Request of broadcast ephemeris from <i>Main</i>
TC.DLR.GPS.TARGET	uint8(8)	Request of broadcast ephemeris from <i>Target</i>
GPS.Status.MAIN	uint8(1)	<i>Main</i> GPS system status byte (e.g., navigation validity, Mitel messages arrival)
GPS.Status.TARGET	uint8(1)	<i>Target</i> GPS system status byte (e.g., navigation validity, Mitel messages arrival)
TSync	uint32(2)	GPS time for on-board synchronization
DLR.GPS.Obs.Time	uint32(2)	GPS time of measurements provided to GOD
DLR.GPS.MAIN.OBS	double(69)	<i>Main</i> navigation sol. and raw GPS measurements (e.g., pseudorange, carrier phase, range-rate)
DLR.GPS.TARGET.OBS	double(69)	<i>Target</i> navigation sol. and raw GPS measurements (e.g., pseudorange, carrier phase, range-rate)
DLR.GPS.EPH	double(992)	GPS broadcast ephemeris
DLR.GPS.UTC	uint8(1)	GPS-UTC time difference

3. perform a validation of Phoenix-S receiver messages
4. retrieve, sample and store the GPS data from the *Main* and *Target* Phoenix-S receivers messages for a 30 s interval

5. output time, C/A pseudoranges, L1 integrated carrier phase, range-rate (Doppler), Carrier-to-noise ratio, channel status and broadcast ephemeris data for GPS-based Orbit Determination (GOD)
6. send requests of broadcast ephemeris data to the Phoenix-S receivers on *Main* and *Target* if not available
7. output GIF status and GPS raw data as telemetry data.

Upon the first activation, GIF stays in an end-less loop and is executed every 1 s as a low priority task within the BSW application core. Inputs and outputs of the GIF module are listed in Table 4.2 and 4.3, respectively. Order and variable names correspond to the subsystem illustration in Fig. 4.4. Variable data types and number of vector elements are listed in the second column. The top level processing scheme and logic of GIF is depicted in Fig. 4.6.

#### 4.3.2 GPS-based Orbit Determination

The GPS-based orbit determination (GOD) applies GPS pseudorange and carrier phase data from the *Main* and *Target* Phoenix-S receivers to determine the current position and velocity of the *Main* and *Target* spacecraft. For initialization exclusively navigation solutions are used. GOD is based upon a real-time reduced-dynamic orbit determination. For absolute navigation a linear combination of Coarse/Acquisition (C/A) pseudorange and L1 carrier phase measurements is employed, termed the GRAPHIC data type.

GRAPHIC data are free from ionospheric errors since the ionospheric group delay in pseudorange measurements is equal in size but opposite in sign to the ionospheric phase change in carrier phase measurements. For relative navigation, a single difference processing of carrier phase measurements fully exploits the accuracy potential of this data type. In fact differencing across receivers reduces broadcast ephemeris and ionospheric errors. Still, the measurements equation requires the estimation of the float biases. Absolute and relative navigation are combined in a unique filter which estimates directly the absolute orbit states of *Main* and *Target*, and indirectly the relative motion within the formation. In particular, the main functions of the GPS-based orbit determination are to

1. retrieve and execute commands for control of the GOD task
2. read GPS data from the GIF buffer
3. retrieve attitude and maneuver-related data
4. perform the Extended Kalman filter initialization
5. perform a GPS data editing
6. perform GPS measurements combination (i.e., GRAPHIC and SD carrier phase data types)

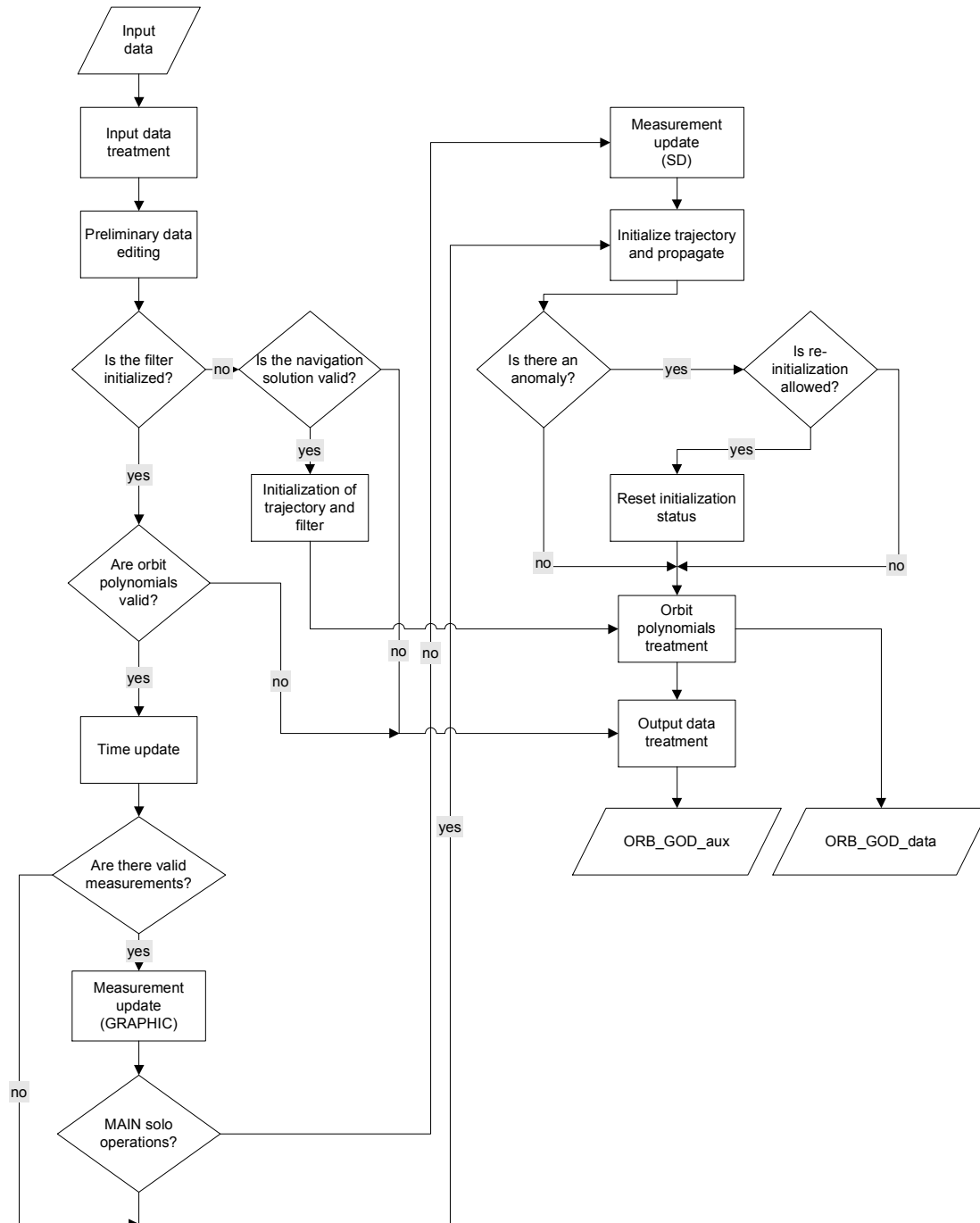


**Fig. 4.7:** Top level processing scheme and logic of GOD.

**Table 4.4:** List of GOD inputs.

Input variable name	Type(Size)	Description
TC.DLR.GOD	double(97)	Telecommand parameters for GOD control (e.g., EKF settings, editing criteria, modes)
enableFunction.DLR.GOD	boolean(1)	Flag for GOD activation
DLR.GPS.MAIN.OBS	double(69)	<i>Main</i> nav. sol. and raw GPS measurements (e.g., pseudorange, carrier phase, range-rate)
DLR.GPS.TARGET.OBS	double(69)	<i>Target</i> nav. sol. and raw GPS measurements (e.g., pseudorange, carrier phase, range-rate)
DLR.GPS.EPH	double(992)	GPS broadcast ephemeris
DLR.GPS.Branch	uint8(4)	Flags for GPS antenna and receiver in use
appliedDeltaVtime.SCET	uint32(124)	History of past maneuvers times (last 62 applied maneuvers)
appliedDeltaV_RTN	double(186)	History of past maneuvers sizes (last 62 applied maneuvers)
GNC.SCET	uint32(2)	On-board time (synchronized to GPS time)
quaternionECI2SCB.MAIN	double(4)	<i>Main</i> attitude at GPS measurement time (cf. GIF output DLR.GPS.Obs.Time)
quaternionECI2SCB.TARGET	double(4)	<i>Target</i> attitude at GPS measurement time

**Table 4.5:** List of GOD outputs.

Output variable name	Type(Size)	Description
DLR.TM.GOD	double(171)	Telemetry parameters for GOD monitoring (e.g., EKF state, formal covariance)
ORB.GOD.data	double(112)	Quintic Hermite coeff. of <i>Main</i> and <i>Target</i> (pos., vel. and acc. at RK4R micro-steps)
ORB.GOD.aux	double(20)	Estimated ballistic coeff. and navigation accuracy (i.e., abs./rel. pos./vel. standard deviations)
ORB.GOD.status	uint8(1)	GOD status byte (e.g., status, orbit polynomials validity, error flags)

7. account for orbit maneuvers in propagation and estimation
8. perform a time update of the Extended Kalman filter
9. decide on, and if positive, perform a measurement update of the Extended Kalman filter
10. compute associated standard deviations
11. provide interpolating polynomials to a buffer for orbit prediction
12. output GOD status data and orbit determination results as telemetry.



GOD is a complex and time-consuming task which is executed every 30 s as a low priority task within the ORB application core. A more frequent execution would not add significant information from GPS measurements as compared to an orbital period of about 6000 s. The provision of position and velocity data at every second is provided within the GPS-based orbit prediction (GOP), which is part of the GNC application core. Thus, a clear separation of time-consuming and rapid turn-around times is achieved through execution in different application cores with different sample times. Inputs and outputs of the GOD module are listed in Table 4.4 and 4.5, respectively. Order and variable names correspond to the subsystem illustration in Fig. 4.4. Variable data types and number of vector elements are listed in the second column. The top level processing scheme and logic of GOD is depicted in Fig. 4.7.

### 4.3.3 GPS-based Orbit Prediction

The GPS-based orbit prediction (GOP) module interpolates and outputs the current *Main* and *Target* absolute state vectors (i.e., position and velocity) based on the trajectory coefficients determined by GOD. These state vectors are the major output of the overall GPS navigation system and constitute the primary orbit interface for the subsequent GNC tasks.

**Table 4.6:** List of GOP inputs.

Input variable name	Type(Size)	Description
enableFunction_DLR_GOP	boolean(1)	Flag for GOP activation
TC_DLR_GOP	double(4)	Telecommand parameters for GOP control (e.g., task activation and editing criteria)
GNC_SCET	uint32(2)	On-board time (synchronized to GPS time)
ORB_GOD_data	double(112)	Quintic Hermite coeff. of <i>Main</i> and <i>Target</i> (pos., vel. and acc. at RK4R micro-steps)
deltaV_tCUC	uint32(124)	History of past maneuvers times (last 62 applied maneuvers)
deltaV_RTN	double(186)	History of past maneuvers sizes (last 62 applied maneuvers)
ORB_GOD_aux	double(20)	Estimated ballistic coeff. and navigation accuracy (i.e., abs./rel. pos./vel. standard deviations)

Furthermore, GOP adjusts the trajectory coefficients of *Main* and *Target* in the presence of maneuvers executed by the *Main* spacecraft. In addition, GOP outputs auxiliary orbit related information for access by the GNC system and in particular AFC. The main GOP functions are to

1. retrieve and execute commands for control of the GOP task
2. retrieve maneuver data

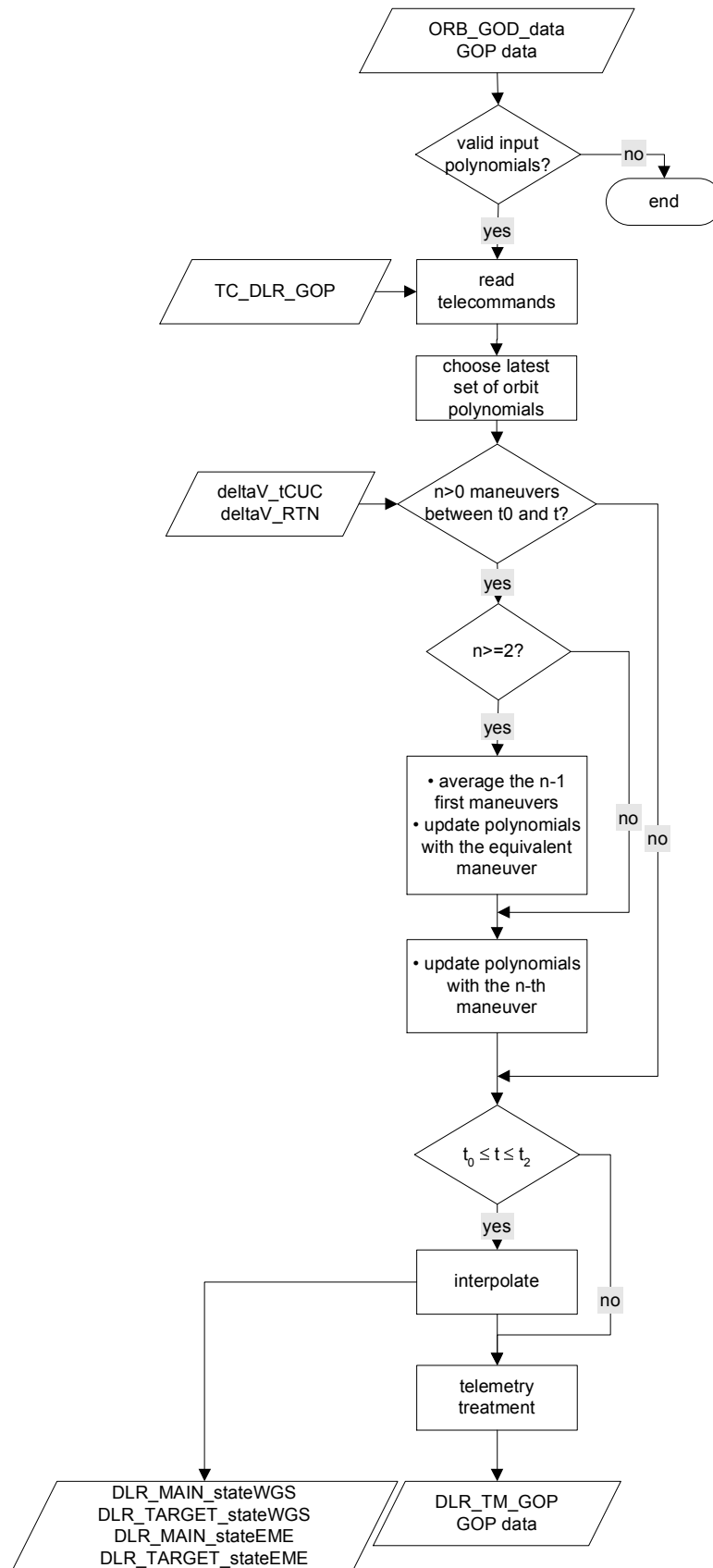


**Fig. 4.8:** Top level processing scheme and logic of GOP.

**Table 4.7:** List of GOP outputs.

Input variable name	Type(Size)	Description
DLR_TM_GOP	uint8(1)	Telemetry parameters for GOP monitoring (e.g., status byte)
DLR_GNC_SCET	uint32(2)	Time of delivered orbit state (equals input on-board time)
DLR_MAIN_stateWGS	double(6)	<i>Main</i> position and velocity in ECEF frame
DLR_TARGET_stateWGS	double(6)	<i>Target</i> position and velocity in ECEF frame
DLR_MAIN_stateEME	double(6)	<i>Main</i> position and velocity in ECI frame
DLR_TARGET_stateEME	double(6)	<i>Target</i> position and velocity in ECI frame
DLR_NavigationAccuracy	double(18)	Abs. and rel. navigation accuracy from EKF (i.e., position/velocity standard deviations)

3. retrieve trajectory coefficients delivered by GOD and stored by GOP at the previous call
4. update the *Main* trajectory coefficients in the orbit buffer in case of maneuvers
5. compute the *Main* and *Target* state vectors in ECEF and ECI coordinates
6. output auxiliary data like e.g. *Main* and *Target* accuracy indicators
7. output GOP data to telemetry (e.g., status, results, auxiliary data).

Upon the first activation, GOP stays in an end-less loop, triggered once per second like all standard GNC tasks. Inputs and outputs of the GOP module are listed in Table 4.6 and 4.7, respectively. Order and variable names correspond to the subsystem illustration in Fig. 4.5. Variable data types and number of vector elements are listed in the second column. The top level processing scheme and logic of GOP is depicted in Fig. 4.8.

#### 4.3.4 Autonomous Formation Control

The Autonomous Formation Control (AFC) module realizes an autonomous on-board orbit control of the *Main* spacecraft with respect to the *Target* spacecraft. To this end, the concept of relative eccentricity/inclination vector separation of the formation is applied together with an active control of the relative semi-major axis and mean argument of latitude.

AFC receives current navigation data from the GPS-based orbit prediction (GOP) and computes the deviation of the current relative state from the reference relative state in order to generate velocity increments for autonomous maneuver execution. The relative states are based upon a relative orbital elements

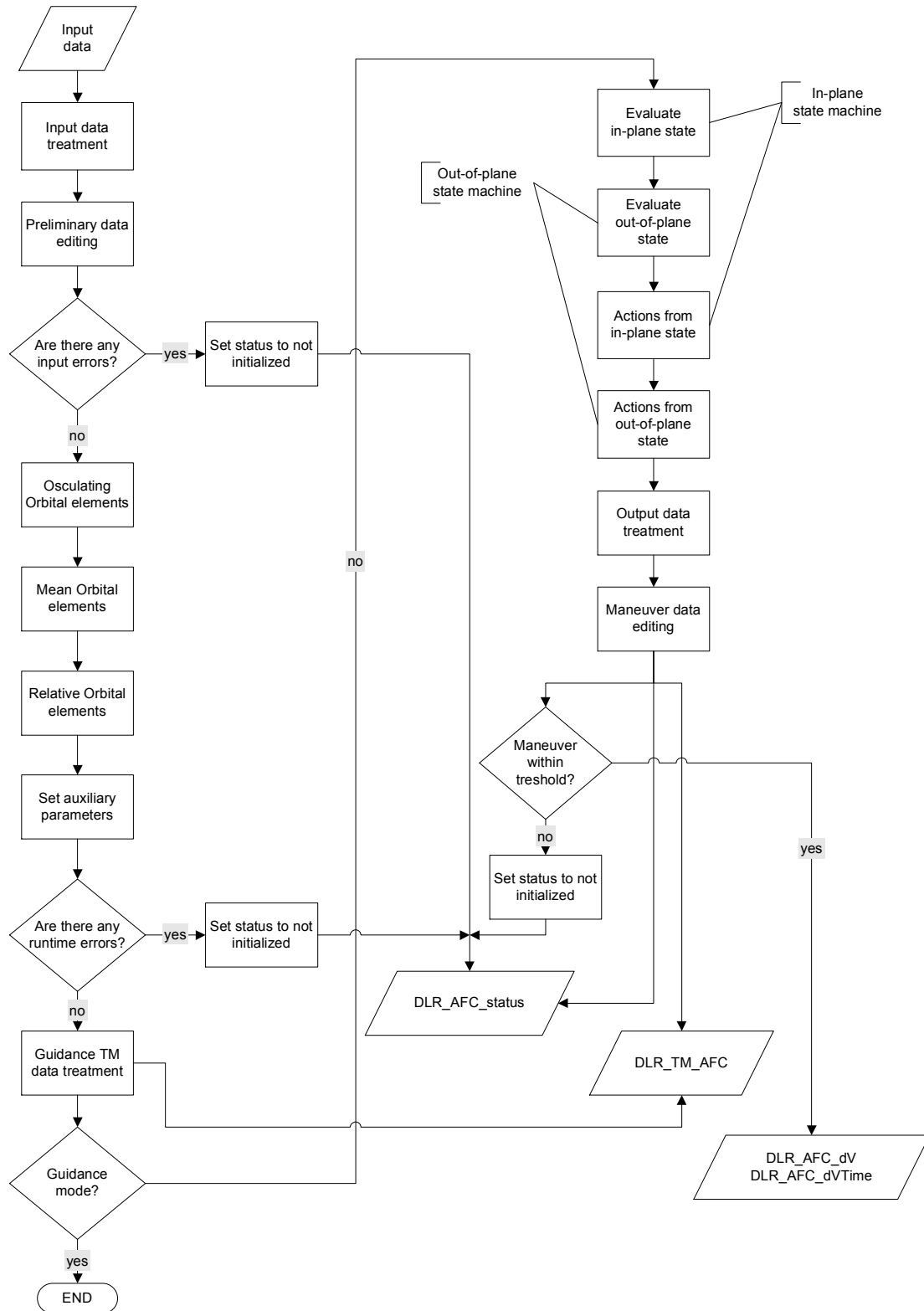


**Fig.4.9:** Top level processing scheme and logic of AFC.

**Table 4.8:** List of AFC inputs.

Input variable name	Type(Size)	Description
enableFunction_DLR_AFC	boolean(1)	Flag for AFC activation
TC_DLR_AFC	double(29)	Telecommand parameters for AFC control (e.g., task activation and editing criteria)
ORB_GOD_status	uint8(1)	GOD status byte (e.g., status, polynomials validity, error flags)
ORB_GOD_aux	double(20)	Estimated ballistic coeff. and navigation accuracy (i.e., abs./rel. pos./vel. standard deviations)
GOP_MAIN_state_EME	double(6)	<i>Main</i> position and velocity in ECI frame
GOP_TARGET_state_EME	double(6)	<i>Target</i> position and velocity in ECI frame
GOP_Time	uint32(2)	Time-tag of input orbit state delivered by GOP (equals on-board time)

**Table 4.9:** List of AFC outputs.

Input variable name	Type(Size)	Description
DLR_TM_AFC	double(64)	Telemetry parameters for AFC monitoring (e.g., guidance parameters, machine states, maneuvers)
DLR_AFC_dV	double(3)	Size of commanded maneuver in Hill's orbital frame
DLR_AFC_dVTime	uint32(2)	Time of commanded maneuver (start of thrust pulse)
DLR_AFC_status	uint8(1)	AFC status byte (e.g., initialization status, error flags)

representation. The control concept applies a simple and robust deterministic maneuver planning to achieve the desired formation configuration. In particular, the functions of AFC are to

1. retrieve command parameters to control and configure AFC operations
2. compute the absolute mean orbital elements of *Main* and *Target* from GOP output
3. compute the relative orbital elements of *Main* with respect to *Target*
4. evaluate the deviation of the current relative state from the reference relative state
5. implement a state machine for in-plane maneuver planning
6. implement a state machine for out-of-plane maneuver planning

7. evaluate the necessity of in-plane or out-of-plane maneuvers
8. computes and outputs the execution time(s) and velocity increment(s) for *Main*
9. provide telemetry information on internal status and guidance and control parameters.

Upon activation, AFC is triggered once per second like all standard GNC tasks. Inputs and outputs of the AFC module are listed in Table 4.8 and 4.9, respectively. Order and variable names correspond to the subsystem illustration in Fig. 4.5. Variable data types and number of vector elements are listed in the second column. The top level processing scheme and logic of AFC is depicted in Fig. 4.9.

#### 4.3.5 Error Diagnostics within the Flight Software

On top of the main functionalities outlined in the previous subsections, each flight software module outputs status bytes indicating anomalies or deficiencies detected during execution. This secondary functionality provides valuable input to specific Fault Detection Isolation and Recovery (FDIR) algorithms implemented into the on-board software. The objective of this measure is to improve robustness and continuity of the system operations, independent from ground contacts.

The error diagnostics are output at each execution step of the software module. The diagnostics are based on the setting of specific bit flags as part of a single byte value. A detailed description of the status bytes issued by GIF (for *Main* and *Target* separately), GOD, GOP and AFC is given in Table 4.10. If the described situation is identified, the bit is set to one otherwise it remains zero.

GIF computes the status bytes GPS\_Status\_MAIN and GPS\_Status\_TARGET (cf. Tables 4.3 and 4.10). While bits 0 and 1 characterize the communication chain between the receiver and GIF in general, bits 2 and 3 require the decoding of messages within GIF and the computation of the message checksum for validation. Bit 4 is set when at least one GPS satellite is tracked. Bit 5 indicates whether each of the tracked satellites has valid ephemerides in the GIF buffer. Finally, bit 6 indicates whether the F40 message has a valid status flag.

GOD computes the status byte ORB\_GOD.Status (cf. Tables 4.5 and 4.10). The first five bits are used to identify the tasks which have been performed by GOD (e.g., initialization, time and measurement updates, maneuver estimation). While the last three bits indicate faulty or anomalous operations of GOD. In particular bit 5 is set when the age of the measurement update is older than a threshold provided via TC. Bit 6 indicates if a persistent measurement error is detected. This error is computed by comparing each observation with the modeled one. If the difference is persistently larger than a TC-defined threshold for longer than a TC-defined time then bit 6 is set. Finally bit 8 indicates a run-time failure typically due to illegal operations (e.g., divisions by zero or square roots

**Table 4.10:** Structure of status bytes issued by GPS-based flight software modules.

GPS.Status.MAIN		
GPS.Status.TARGET		
Position in byte	Value (hex)	Description
0	0x01	Bytes arrived in last 30 s
1	0x02	Mitel msg arrived in last 30 s
2	0x04	F62 with valid checksum in last 15 s
3	0x08	F40 with valid checksum in last 15 s
4	0x10	At least one satellite tracked
5	0x20	F14 messages complete
6	0x40	Valid navigation from F40
ORB.GOD.Status		
Position in byte	Value (hex)	Description
0	0x01	Filter initialized
1	0x02	Valid orbit polynomials at call time (before EKF)
2	0x04	Valid <i>Main</i> and <i>Target</i> navigation solutions
3	0x08	Flag for measurement update
4	0x10	Flag for maneuver estimation
5	0x20	Flag for old measurement update
6	0x40	Flag for persistent measurement error
7	0x80	Flag for run-time failure
DLR.TM.GOP		
Position in byte	Value (hex)	Description
0	0x01	GNC SCET inside interpolation interval
1	0x02	Replacement of internal orbit coeff. by GOD
2	0x04	Maneuver time prior to end of interpolation interval
3	0x08	Maneuver applied
4	0x10	Navigation accuracy overwriting enforced by TC
5	0x20	Absolute <i>Main</i> nav. accuracy below threshold
6	0x40	Absolute <i>Target</i> nav. accuracy below threshold
7	0x80	Relative nav. accuracy below threshold
DLR.AFC.status		
Position in byte	Value (hex)	Description
0	0x01	Input telecommands are not valid
1	0x02	Input navigation is not valid
2	0x04	AFC controller is initialized
3	0x08	Planned maneuver violates editing thresholds
4	0x10	Overlap between in-plane and out-of-plane maneuvers
5	0x20	Run-time failure in AFC initialization
6	0x40	Run-time failure in in-plane maneuver planning
7	0x80	Run-time failure in out-of-plane maneuver planning

of negative numbers). Note that GOD has the capability to re-initialize itself either via TC from ground or autonomously. The latter functionality is normally enabled via TC and is triggered internally by the setting of bits 5, 6 or 7.

GOP computes the status byte DLR\_TM\_GOP (cf. Tables 4.7 and 4.10). Bit 0 indicates if the input GNC SCET time (which is the on-board time at which the GOP output state is requested) lies inside the internally stored orbit polynomial coefficients. If bit 0 is set, then no interpolation is performed by GOP and a default zero output is provided. Bit 2 indicates if new orbit coefficients have

been delivered by GOD and have replaced the old internally stored ones (i.e., the end time of the GOD polynomials is larger than the end time of the currently stored GOP polynomials). Bits 3 and 4 indicates if a maneuver has been used to update the internal orbit coefficients. Finally bits 4 to 7 give information on the navigation accuracy estimates based on the formal covariance of the EKF implemented in GOD.

AFC computes the status byte `DLR_AFC_status` (cf. Tables 4.9 and 4.10). Bits 0 and 1 characterize the validity of the input TCs and the navigation solution provided by GOP. Bit 2 indicates if the AFC controller has been initialized. Bit 3 is set when the planned maneuver size is larger than a predefined threshold. Due to the deterministic nature of the maneuver planning process, it is possible to detect non-nominal maneuvers which have been wrongly planned and block their execution in advance. Bit 4 indicates if close in-plane and out-of-plane maneuvers have been merged into one single thrust. Finally bits 5, 6 and 7 are set when illegal operations (e.g., divisions by zero or square roots of negative numbers) have been detected in various phases of the AFC state machine process. Detected illegal operations are not performed and cause the automatic re-initialization of the controller.

The overall FDIR concept for GNC operations based on GPS could apply valuable information provided by the issued status bytes. Since additional information is expected to be available at a FDIR level, e.g. power consumption of the units, AOCS modes, such a concept is out of the scope of this thesis.

## 4.4 Maneuver Handling within the Navigation System

### 4.4.1 Maneuver Related Interfaces

The GOP module interpolates the orbit coefficients provided by GOD and finally supplies the various GNC core functions as well as the PRISMA payload with continuous position and velocity data of *Main* and *Target*. Due to the different data rates of the GPS-based navigation modules, orbit maneuver data have to be taken into account in both GOD and GOP. In particular at each GNC step, the GOP task accounts for maneuvers which have not been considered by GOD in the last orbit determination/prediction process.

To this end, a maneuver data history is necessary at the GOD and GOP input ports which covers a time interval  $\Delta t_M$  starting from the current epoch  $t_{curr}$  backwards in time (cf. Fig. 4.10). In general,  $t_{curr}$  refers to the time of the last accelerometers measurements being processed in the GNC core. Due to the time latencies of the data communication chain from the BSW to the ASW layer and to the delay induced by the further processing in the GNC core,  $t_{curr}$  will differ from the on-board time  $t_{GNC}$ , input to GOP, by a maximum of 1.5 s.

The choice of  $\Delta t_M$  is strictly related to the time properties of the numerical orbit propagation performed in GOD. After each call, GOD generates a set of orbit polynomials for *Main* and *Target* that covers a total orbit prediction interval of length  $\Delta t_P$ . The validity interval of the polynomial coefficients starts



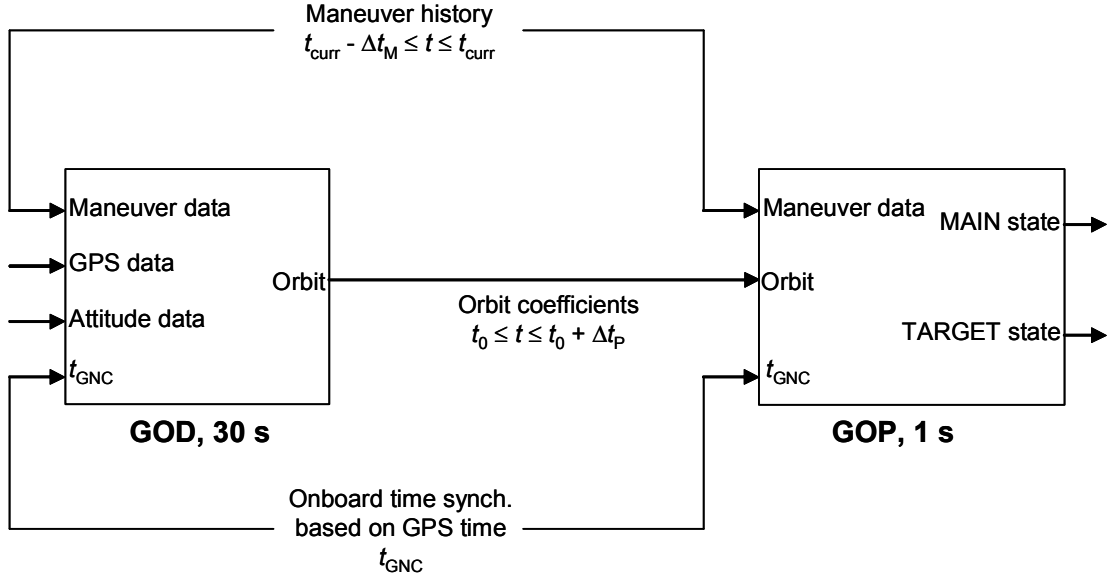


**Fig. 4.10:** Schematic view of maneuver-related interfaces.

at the characteristic time  $t_0$ . In case of valid GPS measurements for a measurement update,  $t_0$  equals the time tag of the observations at measurement update. In case that no GPS measurements are available for a measurement update,  $t_0$  equals the actual on-board time  $t_{\text{GNC}}$  provided by the GNC core. GOD must be able to take into account in the orbit determination process all maneuvers which occurred in the time interval between the newly computed  $t_0$  and its previous value. In a conservative scenario the last valid GPS measurements processed in GOD could be almost 60 s old and an arbitrary number of maneuvers could have been executed up to the time  $t_{\text{GNC}}$  of the present GOD execution. In contrast to the time tag  $t_{\text{GPS}}$  of the GPS messages delivered by the Phoenix-S receivers,  $t_{\text{GNC}}$  is not aligned to GPS integer seconds. Thus, a safety margin of 2 s is considered in the computation of  $\Delta t_{\text{M}}$  for a total value of 62 s.

Similar considerations apply for the choice of  $\Delta t_{\text{P}}$ . The orbit prediction has to cover the time interval between the previously determined  $t_0$  and its new value. A conservative assessment suggests this time span not to be smaller than 90 s. Considering in addition the asynchronous triggering of the GOD and GOP functions with respect to  $t_{\text{GPS}}$ , a safety value of 92 s is chosen for  $\Delta t_{\text{P}}$ . This avoids situations in which  $t_{\text{GNC}}$  is outside the orbit polynomials validity interval.

The maneuver history data comprise execution time and size of the maneuver executed by *Main* on a 1 Hz rate. In particular, for each second of accelerometer measurements an equivalent impulsive maneuver is computed with its total velocity variation mapped in the orbital frame and its center of burn time as GPS time. Accordingly, the maneuver interface consists of two input vectors. A vector of velocity increments containing  $3 \times 62 = 186$  doubles and a vector of center of burn times containing  $2 \times 62 = 124$  integer time parameters. The maneuver history vectors are organized in such a way that the maneuver data are positioned in chronological order with the latest maneuver located at the first

array index and the most recent maneuver located at the last free array index. The maneuver vector is updated every second.

#### 4.4.2 GPS-based Orbit Prediction

The main objective of GOP is to output the orbit state  $\mathbf{x} = (\mathbf{r}, \mathbf{v})$  in the ECEF and ECI reference systems. To this end, GOP evaluates a set of orbit coefficients  $\mathbf{C}$  at SCET time at a 1 Hz rate. The coefficient set  $\mathbf{C}$  is given by  $(\mathbf{x}, \dot{\mathbf{x}})|_{t_0, t_0+1h, t_0+2h}$ , a total of 27 values (for each spacecraft and reference frame, respectively) which allow for a quintic Hermite interpolation of the spacecraft position within the interval  $[t_0, t_2 = t_0 + 2h]$  (cf. Section 3.3.2).

To provide a continuous output of the current position and velocity, GOP has to store its coefficient set  $\mathbf{C}$  between subsequent calls. GOP updates its coefficient set in two cases:

1. In case of a new polynomial set, issued by GOD
2. In case of maneuvers with maneuver times within the coefficient set interval.

The logic for updates of the coefficient set is depicted in Fig. 4.11.

Any new coefficient set  $\mathbf{C}^{\text{GOD}}$  from GOD is detected by an end time  $t_2$  ( $\mathbf{C}^{\text{GOD}}$ ) which extends the currently stored end time  $t_2$  ( $\mathbf{C}^{\text{GOP}}$ ). Upon detection, the new coefficient set replaces the internally stored set.

Input to GOP are furthermore vectors which store executed maneuver times and velocity increments over the past 62 seconds. The need to change the coefficient set due to a maneuver is detected by a maneuver time  $t_M$  which is within the current coefficient interval and has a magnitude within configurable lower and upper threshold values. In this case, the coefficients are updated to reflect that maneuver and the new validity interval is  $[t_M, t_2]$ . This shortens the interval while keeping the same end time  $t_2$ . Note that in order to limit the computational effort of GOP a maximum of two equivalent maneuvers is incorporated in the orbit coefficients when the total number of maneuvers  $n$  is larger than two. In particular the first equivalent maneuver is computed as the weighted average of the first  $n - 1$  velocity increments, while the second maneuver corresponds to the  $n$ -th velocity increment in the input buffer. The algorithms used to update the orbit coefficients with maneuver data are described in Section 3.3.3.

#### 4.4.3 GPS-based Orbit Determination

The maneuver handling within GOD is based on a simple logic. At each call the maneuver history data are processed. All valid maneuvers that lie in the time interval comprised between the old  $t_0$  (i.e., the last measurement epoch processed by GOD or  $t_{\text{GNC}}$  at last GOD call) and the newly computed  $t_0$  (i.e., the new measurement epoch processed by GOD or the present  $t_{\text{GNC}}$ ) enter the

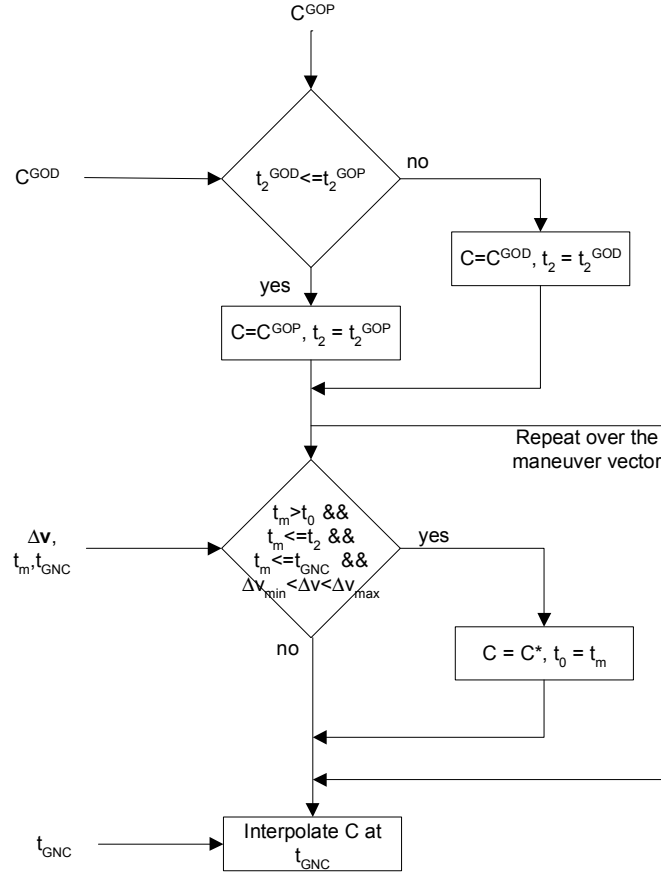


**Fig. 4.11:** Processing scheme of maneuvers within GOP.

estimation scheme described in Section 3.2.3. If no valid GPS measurements are available, the maneuvers are considered for an update of the orbit polynomials and for the subsequent numerical propagation.

All maneuvers with  $t_M > t_0$  are not considered in the current GOD call but will be considered by GOP. However, these maneuvers will be properly estimated at the next GOD call, if valid GPS measurements are available. Fig. 4.12 depicts a potential timeline for four consecutive GOD calls, highlighting the maneuver-related processes.

GOD call #1 shows a nominal scenario with one impulsive maneuver (cf. triangle) followed by valid GPS measurements (cf. circle). First, GOD updates the available orbit polynomials (cf. first horizontal line with arrow ends from top) with the maneuver information to generate new coefficients (cf. second horizontal line from top). Next, GOD interpolates the state at the time of the GPS measurement using the newly computed set of orbit coefficients (cf. vertical arrow). Now, time and measurement update of the EKF can be performed with the direct estimation of a single maneuver via the extension of the filter state. Finally, the numerical orbit propagation is performed covering a total time interval of 92 s (cf. third horizontal line from top).

Call #2 shows the case of a maneuver executed after the GPS measurements.

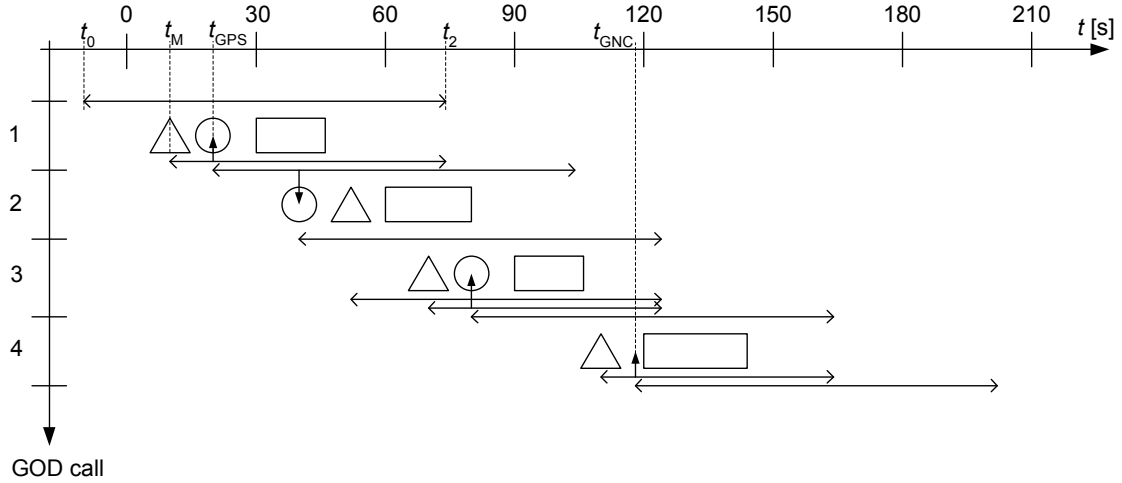


**Fig. 4.12:** Schematic view of GOD timeline with respect to maneuvers. Four GOD calls (top to bottom) are illustrated vs. time (left to right). Rectangles indicate GOD execution (computational activity). Triangles indicate maneuvers. Circles indicate GPS measurements provided by GIF to GOD. Horizontal lines with arrow ends indicate the time validity of the orbit coefficients  $C$ . Vertical arrows indicate the interpolation task performed by GOD before the time update. The vertical arrows start from the orbit coefficients which are used for interpolation. Representative time variables are only shown for the first GOD call.

Here, only the interpolation of the old orbit coefficients is performed, followed by the EKF steps and by the numerical orbit propagation. The occurrence of the maneuver is not considered in the current GOD call, but in the successive GOP and GOD runs.

Call #3 shows how the previously neglected maneuver is re-considered, together with a subsequent maneuver, via proper update of the polynomials (performed one time for each maneuver) and EKF steps. Note that the last considered maneuver was executed during the previous GOD call.

GOD call #4 illustrates the case of no valid measurements available but maneuvers performed. Here, the orbit polynomials are updated, the trajectory is interpolated at the input on-board time  $t_{GNC}$  and the usual numerical integration is performed.

## 4.5 Max-Path Unit Tests of GPS-based Flight Software

A max-path is defined as a unit test that reproduces the conditions of maximum computational load of a software module via the provision of a minimum quantity of constant inputs. The advantage of using a max-path unit test is given by the fact that the maximum CPU load can be assessed or reproduced through one or few calls of the software module under consideration. This section describes the definition and implementation of the max-path unit tests of the developed GPS-based flight software for the PRISMA mission. First a description of the software development environment is provided. Next a description of the defined max-path tests is given. Finally the results obtained from the exe-

cution of the max-path tests on a representative LEON3 board at DLR are presented. These are realistic estimates of the computational load expected on the PRISMA on-board computer and will be confirmed by hardware-in-the-loop system level tests conducted on the actual on-board computer in the next chapter.

#### 4.5.1 Software Development and Testing Environment

As mentioned earlier, the development of the PRISMA GPS-based GNC software discussed in this research is based on Matlab/Simulink and C++. While Matlab/Simulink offers powerful tools for high level model-based design and real time applications, C++ is a lower level language and is therefore suitable for programming tasks that require high computational load. The processing layer of the software system is implemented in C++, including, for example, numerical orbit integration and data filtering. On the other hand the communication layer is implemented in Matlab/Simulink, including for example input/output interfaces, time synchronization and callback methods. The interface between the two programming layers is given by S-Function pre-build blocks in Matlab/Simulink.

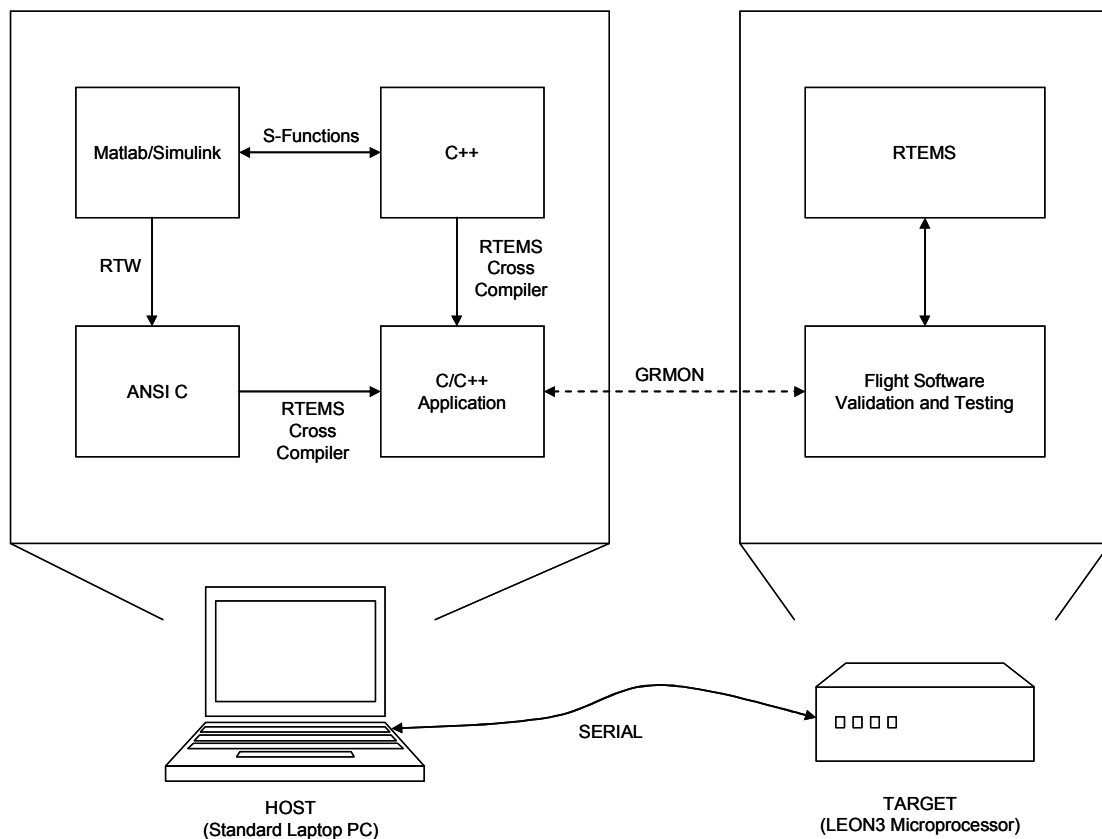


**Fig. 4.13:** Schematic of the GPS-based software development environment.

As illustrated in Fig. 4.13, the flight software is generated using Real Time

Workshop (RTW) Embedded Coder for an automatic translation of the Matlab/Simulink blocks into ANSI C-code. The automatically generated C-code is then compiled and linked together with the handwritten C++ sources using the Real-Time Executive for Multiprocessor Systems (RTEMS) cross-compiler system (RCC). Finally, the flight application is downloaded from the development host computer, a standard laptop PC (cf. Table 4.11 for details), into the target microprocessor, a LEON3 board (cf. 4.12 for details), for validation and testing.

**Table 4.11:** Host hardware (standard laptop PC) features for software development and testing environment at DLR.

Component	Description
Laptop model	Dell Latitude D610
CPU	Intel(R) Pentium(R) M processor 1.86 GHz ACPI GenuineINTEL x86 Family 6 Model 13
Memory controller	1.0 GB of RAM with Physical Address Extension

The FPGA configuration described in Table 4.12 for the target board is the one used at DLR for preliminary testing of the flight software prior to its full integration into the spacecraft on-board computer. The LEON3 FPGA-based microprocessor implements a 32-bit processor compliant with the SPARC V8 architecture which is particularly suited for embedded applications [Gaisler, 2001]. It is clocked at 24 MHz, it recognizes bit flips and is fault tolerant. Compared to the actual flight computer, the major difference is represented by the adopted memory configuration. In particular a proprietary FT PROM/SRAM controller (ver 3) from [Gaisler, 2001] is implemented on-board with a capacity of 8x2048 kbyte static ram. In addition, dedicated interface hardware proprietary of Gaisler Research (e.g., Parallel Packet interface, Multi-processor Interrupt Controller), Astrium (e.g., SpaceWire link) and Bosch (e.g., CAN Controller) are supported by the PRISMA LEON3 processor. These aspects are, however, not considered as limiting factors for the portability of the GPS-based software from the test environment at DLR to the PRISMA *Main* on-board computer.

Tables 4.13 and 4.14 show the list of software items used for the test and validation of the flight software at DLR. More specifically Table 4.13 lists software tools required on the host laptop PC, while Tables 4.14 lists the tools required on the target LEON3 board.

Most of the listed software items are available as part of RCC. RCC is a cross-compilation system for both ERC32 and LEON processors. The following components are included:

1. GNU C/C++ compiler
2. Linker, assembler, archiver etc.

**Table 4.12:** Target hardware (LEON3 microprocessor) features for software development and testing environment at DLR.

Component	Description
Board model	LEON FPGA GR-PCI-XC2V
CPU	LEON3FT SPARC V8 Processor (ver 0x0) 24 MHz, win8, hwbp 4, itrace 128, lddel 1
FPU	GRFPU-lite icache 1x8 kbyte, 32 byte/line, dcache 1x4 kbyte, 16 byte/line
Memory controller	FT memory controller (ver 0x1) 32-bit prom, 32-bit sdram: 1x64 Mbyte, col 9, cas 2, ref 7.7 us

**Table 4.13:** Tools required on the host system for software development and testing at DLR.

Item	Name/Identifier	Version/Release
Operating system	Windows XP	Professional Edition (2002)
Linux emulator	Cygwin	Release 1.5.18-1
C/C++ compiler (host)	Microsoft Visual C++ .NET	Version 7.1 (2003)
C/C++ compiler (target)	gcc	Version 3.2.3
Standard C++ library	libstdc++.a	Version 3
Matlab/Simulink	Matlab Simulink RTW	Version 7.1 R14Sp3 Version 6.3 R14Sp3 Version 6.3 R14Sp3
Debug monitor	RTW Embedded Coder GRMON Professional	Version 6.3 R14Sp3 Version 1.1.6

3. Newlib standalone C-library
4. RTEMS real-time kernel with network support
5. Boot-prom utility
6. GDB cross-debugger for sparc and graphical user interface.

Using the GDB debugger, it is possible to perform source-level symbolic debugging on the real target hardware [Gaisler, Last accessed: 2006].

#### 4.5.2 Max-Path Tests Definition

The maximum execution time of a software module is obtained through the stimulation of as many sections of the code as possible. The definition of the

**Table 4.14:** Tools required on the target system for software development and testing at DLR.

Item	Name/Identifier	Version/Release
Real-time kernel	RTEMS	Version 4.6.5

proper inputs in order to obtain a max-path unit test is mainly based on a good knowledge of the code. Nevertheless a careful analysis of the maximum peaks in the execution times of the software during several long-term runs represents a valuable crosscheck to verify the assumptions made in the definition of the test. In practice an accurate analysis of the long-term simulations executed on the LEON3 board enables the definition of reliable max-path unit tests. These tests reproduce the conditions of maximum computational load for each flight software module. In particular GIF, GOD, GOP and AFC are stimulated with specific constant inputs that provide the maximum computational effort on the LEON3 board. Dedicated RTEMS functions (e.g., `rtems_clock_get`) are used to estimate the execution time of each software module. The dynamic memory allocation is closely monitored to determine if memory leaks exist in the heap region of the LEON3 board RAM. The RTEMS function `malloc_info(index)`, which is a modified version of the function `malloc_dump(void)`, is used to obtain information about the heap usage during run-time for each software module.

The max-path tests have been defined in a Matlab/Simulink environment as basic Simulink models retrieving the necessary inputs from the Matlab workspace. In a second step, the unit test models have been translated automatically in RTEMS applications using RTW and RCC. As an example Fig. 4.14 shows the Simulink model of the max-path unit test for GOD.

The maximum computational load of GIF is obtained if the following conditions are valid:

1. The input buffers containing Mitel messages are completely filled with data coming from the *Main* and *Target* GPS receivers.
2. All the incoming messages are valid.

The max-path unit test consists of one simulation step.

The maximum computational load of GOD is obtained if the following conditions are valid:

1. All the twelve channels of the GPS receivers on-board *Main* and *Target* are allocated and raw GPS data are provided for all the tracked satellites.
2. All the incoming measurements are considered valid by GIF and GOD.
3. The maximum possible number of impulsive orbit control maneuvers (i.e., 62) is included in the navigation process.



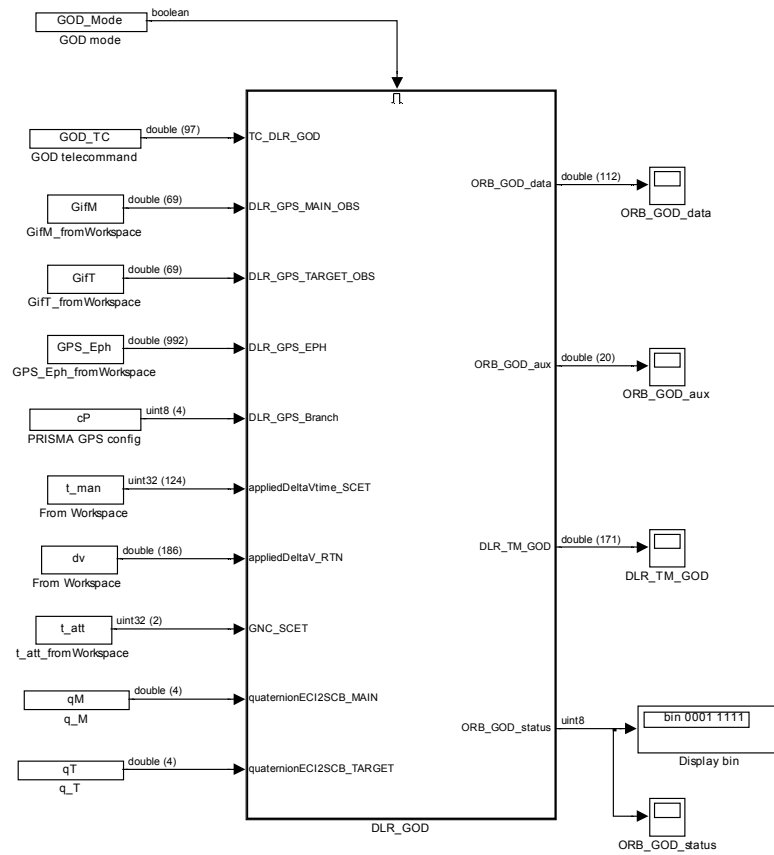


**Fig. 4.14:** Simulink model of max-path unit test for GOD.

The max-path unit test consists of three simulation steps.

The maximum computational load of GOP is obtained if the following condition is valid:

1. The orbit polynomial coefficients have to be updated by GOP including the maximum possible number of impulsive orbit control maneuvers (i.e., 62).

The max-path unit test consists of two simulation steps.

The maximum computational load of AFC is obtained if the following conditions are valid:

1. The AFC state machine triggers the simultaneous computation of an in-plane and out-of-plane orbit control maneuver.
2. The computation of atmospheric drag is activated and AFC has already executed one maneuver pair.

The max-path unit test consists of 27 simulation steps.

### 4.5.3 Results from Max-Path Tests

Table 4.15 lists the measured maximum execution times obtained from the max-path unit tests on the LEON3 board at DLR. Similar figures are obtained when executing the tests on the *Main* engineering model board at the Swedish Space Corporation (SSC) [Florio and D'Amico, 2007]. The CPU loads are computed by dividing the maximum execution time of each software module by its sample time (i.e., 1 s for the BSW and GNC cores, 30 s for the ORB core).

**Table 4.15:** Maximum execution times and correspondent net CPU load of GPS-based flight software modules.

Application Core	Software Module	Task	Time [ms]	CPU load [%]
BSW (1 s)	GIF	Proc. Inputs	2	11.1
		Proc. Messages	104	
		Proc. Observations	1	
		Proc. Ephemeris	2	
		Proc. Outputs	2	
		<b>Total</b>	<b>111</b>	
ORB (30 s)	GOD	Proc. Inputs	9	26.8
		Initialization	(3379)	
		Time update	864	
		Measurement update	6694	
		Proc. Outputs	464	
		<b>Total</b>	<b>8031</b>	
GNC (1 s)	GOP	<b>Total</b>	<b>68</b>	6.8
	AFC	Proc. Inputs	3	
		Guidance	10	
		In-plane State	1	
		Out-of-plane State	1	
		In-plane Actions	5	
		Out-of-plane Actions	1	
		Proc. Outputs	1	
		<b>Total</b>	<b>22</b>	

As expected GOD and GIF generate the maximum peaks of the CPU load with 11.1% and 26.8%, respectively. Because of this, the BSW and ORB application cores are implemented as low priority tasks on the *Main* onboard computer. A net CPU load below 30%, as prescribed by the requirements, ensures that the GIF and GOD functions can be executed within the sample time of the respective cores.

The most computational intensive task of GIF is shown to be the processing of Mitel messages provided by the Phoenix-S GPS receivers (i.e., mainly message buffering and strings handling). The computational load of GOD is proportional to the number of measurements to be processed by the measurement update (cf. Section 3.2.4). When the EKF filter initialization is necessary, no time

and measurement updates are performed and the total GOD execution time reduces to  $9 + 3379 + 464 = 3852$  ms. The maximum load of GOP is dominated by the incorporation of maneuvers within the orbit coefficients. While most of the AFC computations are performed by the guidance task (i.e., basically mean orbital elements computation).



## 5. Formation Flying Testbed

### 5.1 System Testing and Validation Concept

The PRISMA system development and testing at the Swedish Space Corporation (SSC) is based on the SATellite LABoratory (SATLAB) facility [Bodin, 2005]. SATLAB is a software/hardware laboratory providing a unified configurable simulation environment for use in several applications within the PRISMA project. The supported system level simulations can typically consist of:

1. Software system tests to verify the required functionality of the on-board software (OBS)
2. Closed-loop tests involving the integrated Flight Model (FM) spacecraft
3. Closed-loop tests involving different levels of Engineering Model (EM) or FM hardware-in-the-loop
4. Test development on a system level simulator
5. Development of operational procedures in a system level simulator
6. Operator training by means of system level simulations
7. Test results and flight results analysis

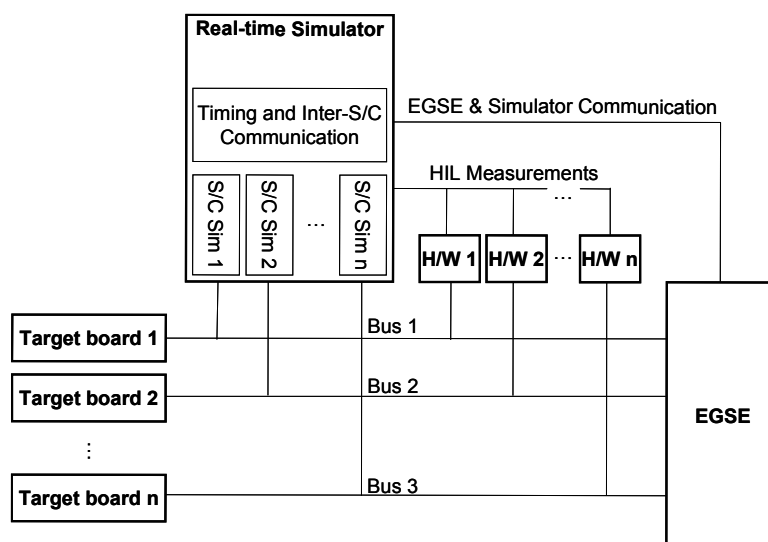


**Fig. 5.1:** General SATLAB configuration at SSC [Bodin, 2005].

The simulation environment runs the OBS on flight representative target hardware (i.e., EM or FM on-board computers), and includes different levels of hardware-in-the-loop (HIL). SATLAB supports simultaneous simulations of several spacecraft in formation flying. Fig. 5.1 illustrates the most general configuration of SATLAB. The figure shows how several spacecraft can be simulated, each with its own target computer and communication bus. The figure also shows how hardware is included in the loop for each of the simulated spacecraft and how these can be commanded or read from the simulator. The communication link between the Electrical Ground Support Equipment (EGSE) and the simulator is also indicated in the figure. The real-time environment implemented in SATLAB resides in the simulator and the target computers. In particular the simulator is a standard desktop PC, treated as a Matlab/Simulink xPC target, while the target platforms are LEON3 Fault Tolerant (FT) processors. The backbone of the software system is the Real Time Workshop (RTW) Embedded Coder by which the real time applications are auto-coded and launched on the target units.

In the sequel two configurations of the SATLAB facility are used to perform a step wise validation of the system functionality and performance. A first setup includes only EM on-board computers. Apart from the xPC target and the Telemetry/Telecommand (TM/TC) network, no additional hardware is in the loop. The GPS receivers are modeled through a software emulator integrated in the real-time simulator (cf. Section 5.2). The second adopted configuration of SATLAB includes the fully integrated PRISMA spacecraft in a controlled environment (clean room). The GPS flight hardware is installed on the *Main* and *Target* satellites and connected through asynchronous serial interfaces to the on-board computers. The Phoenix-S GPS receivers on the two spacecraft are stimulated through Radio Frequency (RF) signals produced by a 2x12 channels Spirent GSS7700 GPS Signal Simulator (GSS) [SPIRENT, 2006]. The GSS is steered in closed-loop by the SATLAB real-time simulator and, as a consequence, can reflect the execution of orbit and attitude maneuvers to the GPS measurements collected by the Phoenix-S receivers (cf. Section 5.3).

## 5.2 Formation Control Experiment Rehearsal

Within the GPS-based GNC system development discussed in this research, a series of real-time HIL tests have been conducted at various stages to verify the proper integration of the flight software within the on-board software and computer. Through these tests, it has been possible to verify communication, telemetry and telecommand, interface and functionalities of the integrated flight software. A representative HIL test conducted in the SATLAB facility in the time frame March 17 to 24, 2008 is presented in the sequel [D'Amico and Florio, 2008]. The scope of the test is to verify the performance of the GPS-based GNC software integrated in the PRISMA on-board computer. The test strategy tries to stimulate the software modules in order to enable the execution of most of the available functionalities and execution paths. As described

in the following, the Autonomous Formation Control (AFC) module is operated in all the available modes (i.e., guidance only, open-loop and closed-loop) and is asked to maintain and reconfigure autonomously several formation flying configurations. Here the first SATLAB setup discussed in the previous section is adopted, where GPS measurements are emulated through a software model of the Phoenix-S receiver.

### 5.2.1 Test Specification

The start time of the real-time HIL scenario corresponds to 2 July 2006, 00:00:00.0 GPS Time in calendar date format or (835833600s, 0 $\mu$ s) in CUC format. Here, CUC stands for CCSDS Unsegmented Time Code and depicts the epoch in GPS seconds past the origin of GPS time scale, i.e. 6. January 1980, 00:00:00.0 UTC (cf. Appendix for details). The second element of the CUC denotes the fractional seconds in units of microseconds. The following relations

$$\begin{aligned} \text{GPS} - \text{UTC} &= 14 \text{ s} \\ \text{UT1} - \text{UTC} &= 0.1931340 \text{ s} \end{aligned} \quad (5.1)$$

have been assumed for the GPS and UTC time differences and the UT1 and UTC time differences respectively. The simulation scenario covers a time interval of 96 hours that corresponds to approximately 64 orbital revolutions.

The true trajectories for the *Main* and *Target* spacecraft are propagated within the SATLAB real-time simulator and are available in the telemetry stream in the ECEF and in the ECI reference frames. The trajectories are obtained via numerical orbit propagation including the aspherical Earth gravity field through an expansion in spherical harmonics up to degree and order 16 and the Sun and Moon third body forces. Among the non-gravitational accelerations atmospheric drag and solar radiation pressure are modeled as attitude dependent forces. The spacecraft parameters for the simulation scenario are collated in Table 3.5. The transformation between the ECEF and the ECI reference systems is accomplished by applying Earth's rotation, nutation and precession according to the International Earth Rotation Service (IERS) conventions [IERS, Last accessed: October 2010]. Nutation and precession rotation matrices are computed once at start time and kept constants throughout the reference scenario.

**Table 5.1:** Phoenix-S Emulator (PEM) settings for SATLAB test.

Parameter	Value
DLL Bandwidth [Hz]	0.08
PLL Bandwidth [Hz]	9.0
Elevation mask [°]	5.0
Vertical TEC [TECU]	10.0
Ephemeris error [m]	2.0

It shall be noted that the reference frames, the force model and the numerical integration scheme applied within the SATLAB facility are substantially

different from the implementations in the GPS-based GNC software and in the test environment adopted in Chapter 3 (cf. Appendix for details on the reference systems). The adoption of different and not well known models in the validation of the flight software is considered a conservative aspect of the test campaign, especially in view of the numerical validation performed on the prototype software as a standalone unit at DLR (cf. Section 5.3). Furthermore, apart from the Phoenix-S GPS receivers, more accurate models for sensors and actuators are implemented by the manufacturers in the SATLAB facility. The GPS receivers are modeled through the PEM software described in Section 3.4.1. Thanks to the model-based software development approach, PEM is ported easily from the Matlab/Simulink environment at DLR to the SATLAB facility at SSC. The applied GPS-related specifications are summarized in Table 5.1. Compared to the settings applied in previous tests described in Section 3.4.1, here the broadcast ephemeris errors are characterized by a standard deviation of 2.0 m. As a consequence we expect larger absolute positioning errors in radial direction with respect to the tests conducted in Section 3.4 at the decimeter level.

**Table 5.2:** Initial *Target* orbital elements and relative orbital elements for SATLAB test.

Initial time		Value	
Epoch (GPS time in CUC) [s]		835833600	
GPS-UTC [s]		14.0	
UT1-UTC [s]		0.193134	
Orbit elements	Value	Relative orbit elements	Value
$a$ [m]	7078135.0	$a\delta a$ [m]	0
$u$ [°]	0.0	$a\delta\lambda$ [m]	9.3
$e_x$ [-]	0.001	$a\delta e_x$ [m]	-34.7296
$e_y$ [-]	0.0	$a\delta e_y$ [m]	196.9616
$i$ [°]	98.19	$a\delta i_x$ [m]	76.6044
$\Omega$ [°]	189.89086	$a\delta i_y$ [m]	64.2788

Based on the epoch selected above, the orbital elements of *Main* and *Target* have been defined. The spacecraft will be injected into a sun-synchronous orbit with 700 km altitude and about 98.2° inclination. A dusk-dawn orbit with 18 h nominal local time at the ascending node (LTAN) is considered in the scenario. Table 5.2 lists the selected absolute and relative orbital elements which correspond to a bounded, centered formation configuration with zero mean along-track separation.

For the considered simulation scenario the nominal *Main* spacecraft body axes are aligned with the orbital frame, thus providing a default nadir/zenith spacecraft pointing. While the *Target* desired attitude is set to a Sun-pointing mode throughout the simulation with a coarse zenith pointing direction of the GPS antenna in use. Compared to previous simulations documented in this thesis, here the integrated test includes the full OBS comprising, among others, the Attitude and Orbit Control Subsystem (AOCS). The *Main* spacecraft AOCS makes use of Star Cameras (SCA) for attitude determination and mainly Re-



action Wheels (RW) for attitude control (cf. Table 1.3). This enables a typical three-axes attitude control accuracy at  $10^{-2}$  degrees. On the other hand the *Target* spacecraft AOCS makes use of Sun Sensors (SS) and Magnetometers (MM) for attitude determination and only Magnetic Torque rods (MT) for attitude control (cf. Table 1.3). This allows a three-axes attitude control accuracy of several degrees only. Of particular relevance here are the *Target* attitude estimation errors which are characterized by oscillations with amplitudes of about  $2^\circ$  around all axes. Considering that the GPS antenna offset with respect to the center of mass is about 0.36 m, such an on-board attitude uncertainty affects directly the GPS-based navigation accuracy by approximately 1 cm.

Furthermore the *Main* spacecraft makes use of a dedicated attitude guidance function during the execution of orbit control maneuvers. This attitude mode tries to align one dedicated thruster with the desired thrust direction (the chosen thruster is the one which is closest to the desired firing direction). Compared to a standard approach where the maneuver thrust is distributed among the available thrusters without re-orientation of the spacecraft, this method should reduce the maneuver execution errors and the total propellant consumption. In particular the typically small delta-v maneuvers commanded by AFC for relative orbit control are not split into even shorter burns on multiple thrusters which may easily lie below the minimum impulse bit. Anyhow attitude control errors during the re-orientation phase cause a spurious distribution of the thrust among more thrusters.

### 5.2.2 Flight Software Settings

In order to control the execution of the flight software modules (i.e., GIF, GOD, GOP and AFC) during the SATLAB test, dedicated time-tagged TC procedures are sent by the EGSE to the on-board computer.

**Table 5.3:** Nominal relative orbital elements and phases of the relative eccentricity/inclination vectors characterizing the four formation flying configurations to be maintained and acquired autonomously by AFC.

Nominal relative elements Time frame (hours)	Config. 1 0–24	Config. 2 24–48	Config. 3 48–72	Config. 4 72–96
$a\delta a^{\text{nom}}$ [m]	0	0	0	0
$a\delta \lambda^{\text{nom}}$ [m]	0	0	0	300
$a\delta e_x^{\text{nom}}$ [m]	-34.7296	0	0	0
$a\delta e_y^{\text{nom}}$ [m]	196.9616	200	300	300
$\varphi^{\text{nom}}$ [°]	100	90	90	90
$a\delta i_x^{\text{nom}}$ [m]	76.6044	50	0	0
$a\delta i_y^{\text{nom}}$ [m]	64.2788	86.6025	100	100
$\vartheta^{\text{nom}}$ [°]	40	60	90	90

In view of the real mission operations needs, AFC is operated in three modalities in a step-wise approach: guidance only, open-loop and closed-loop. The

guidance mode lasts 1 hour. In this mode AFC computes the absolute and relative orbital elements, in addition to status bytes and auxiliary telemetry parameters. The open-loop mode is then activated and lasts 4 hours. In this mode AFC executes the complete in-plane and out-of-plane state machines and computes maneuver parameters which are not sent for execution to the thruster command distribution chain. Finally AFC enters the closed-loop mode in which maneuver commands are sent to the propulsion system. Two sub-modes are stimulated in closed-loop which differ by the used in-plane orbit control algorithm. The along-track sub-mode lasts for 24 hours and implements maneuvers in flight and anti-flight direction only (cf. Section 2.4.4). The radial sub-mode covers the remaining 72 hours and makes use of radial maneuvers as described in Section 2.4.6.

**Table 5.4:** Settings of the EKF used by GOD during the 96-hours real-time SATLAB scenario.

Parameter	Value	Parameter	Value
<i>A-priori standard deviation</i>		<i>Process noise</i>	
$\sigma_r$ [m]	1000.0	$\sigma_{a_r}$ [nm/s <sup>2</sup> ]	50.0
$\sigma_v$ [m/s]	1.0	$\sigma_{a_t}$ [nm/s <sup>2</sup> ]	30.0
$\sigma_{C_D}$	1.0	$\sigma_{a_n}$ [nm/s <sup>2</sup> ]	10.0
$\sigma_{a_r}$ [nm/s <sup>2</sup> ]	500.0	$\sigma_{c\delta t}$ [m]	500.0
$\sigma_{a_t}$ [nm/s <sup>2</sup> ]	300.0	<i>Measurements standard deviation</i>	
$\sigma_{a_n}$ [nm/s <sup>2</sup> ]	100.0	$\sigma_{PR}$ [m]	0.05
$\sigma_{c\delta t}$ [m]	500.0	$\sigma_{CP}$ [mm]	2.0
$\sigma_N$ [m]	0.025	<i>Maneuver parameters</i>	
<i>Auto-correlation time scale</i>		$\sigma_{\delta v}$ [%]	30.0
$\tau_a$ [s]	900.0		
$\tau_{c\delta t}$ [s]	100.0		

The AFC closed-loop activities foresee four formation flying configurations. Each constellation covers a time arc of 24 hours. AFC has to autonomously acquire and maintain the desired configurations for the prescribed period of time. Table 5.3 lists the desired formation geometries in terms of relative orbital elements as provided to AFC via TC. The commanded control windows for the relative eccentricity and inclination vectors are kept constant during the complete test and are given by  $a\delta e^{\max} = a\delta i^{\max} = 2$  m. The initial relative geometry corresponds to non-parallel relative eccentricity/inclination vectors with relative perigee and relative ascending node at 100° and 40° respectively. These angles are modified in the second formation flying configuration which is characterized by a relative eccentricity vector aligned with the y-axis and a relative inclination vector at 60° phase. Parallel relative eccentricity/inclination vectors are applied in the third and fourth configurations which differ by a mean along-track separation of 300 m.

The settings applied to the EKF in GOD for absolute and relative navigation during the SATLAB test are collated in Table 5.4 and are identical for *Main* and *Target*. The selected empirical accelerations a-priori and steady state variances

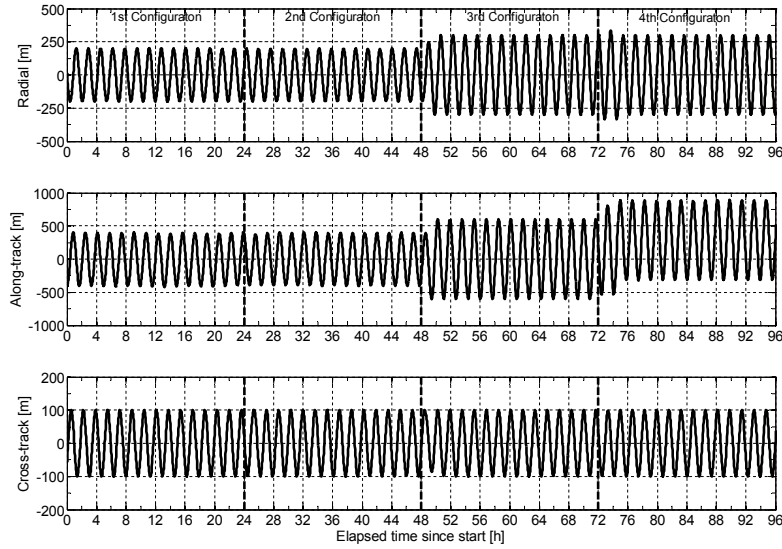


**Fig. 5.2:** Actual relative motion of *Main* w.r.t. *Target* mapped into the radial (top), along-track (middle) and cross-track (bottom) directions. Vertical dashed lines indicate reconfigurations of the formation triggered by TC.

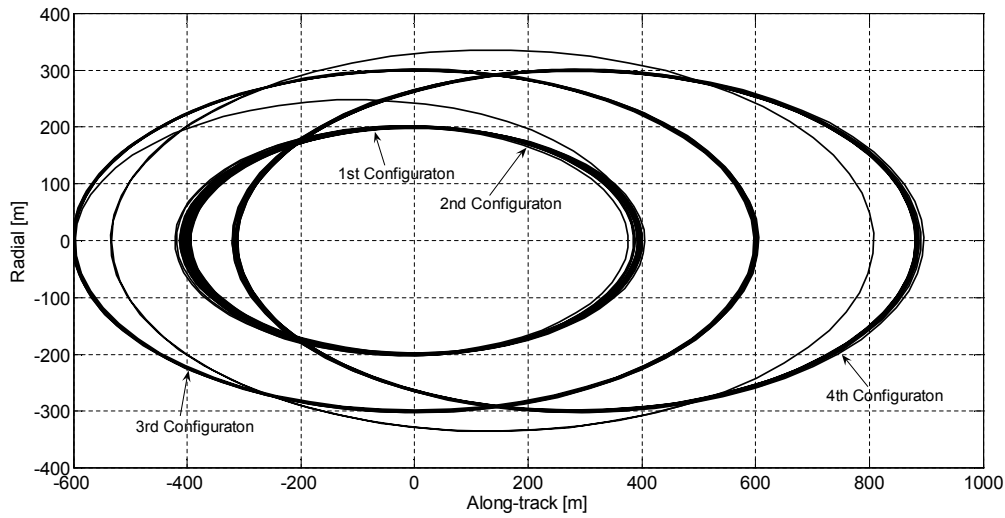


**Fig. 5.3:** Actual relative motion of *Main* w.r.t. *Target* mapped into the along-track/radial plane. Arrows and associated text indicate the different formation flying configurations which are maintained and reconfigured autonomously.

are smaller than the settings of Table 3.10 applied in the standalone simulation environment at DLR. This is mainly due to the truncated Earth's gravity field model implemented in the SATLAB real-time simulator. Pseudorange and carrier phase measurements noise are set to 0.05 m and 2 mm respectively. The a-priori standard deviation of the maneuver delta-v parameters is set to 30 % of the a-priori value provided by the accelerometer filtering chain. It shall be noted that no tuning of the EKF was conducted on the SATLAB facility and a-priori settings have only been selected based on previous simulations conducted in

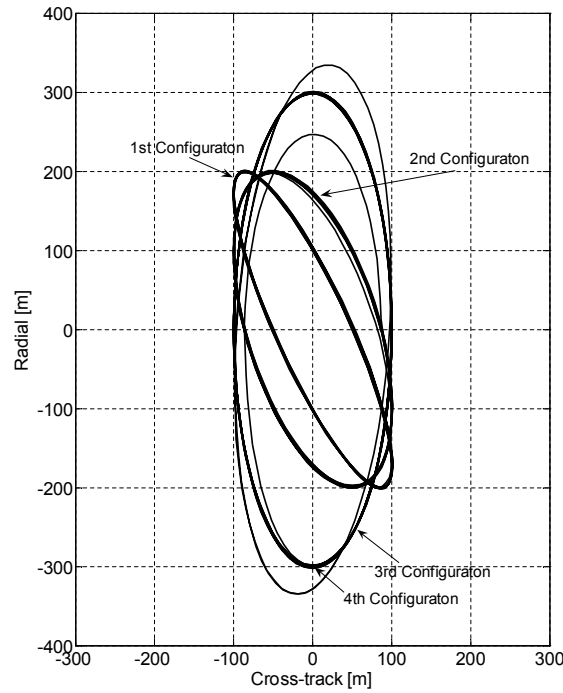


**Fig. 5.4:** Actual relative motion of *Main* w.r.t. *Target* mapped into the cross-track/radial plane. Arrows and associated text indicate the different formation flying configurations which are maintained and reconfigured autonomously.

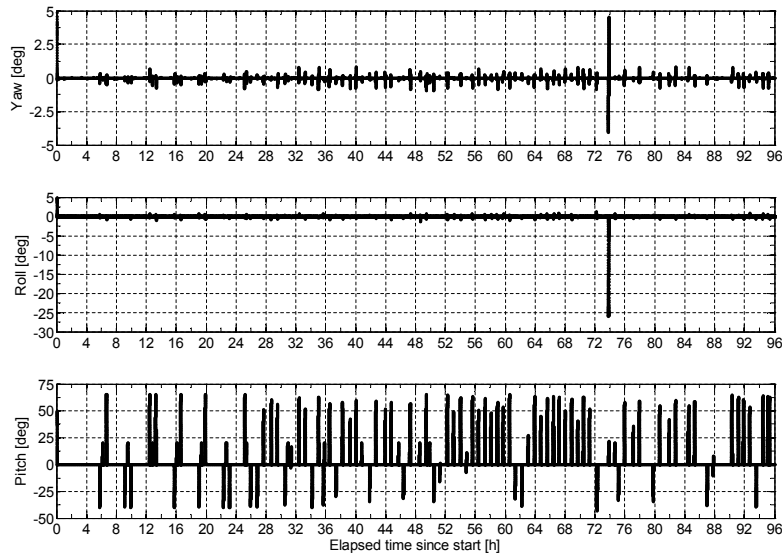
the standalone environment at DLR (cf. Section 3.4.2).

### 5.2.3 True Motion from Real-time Simulator

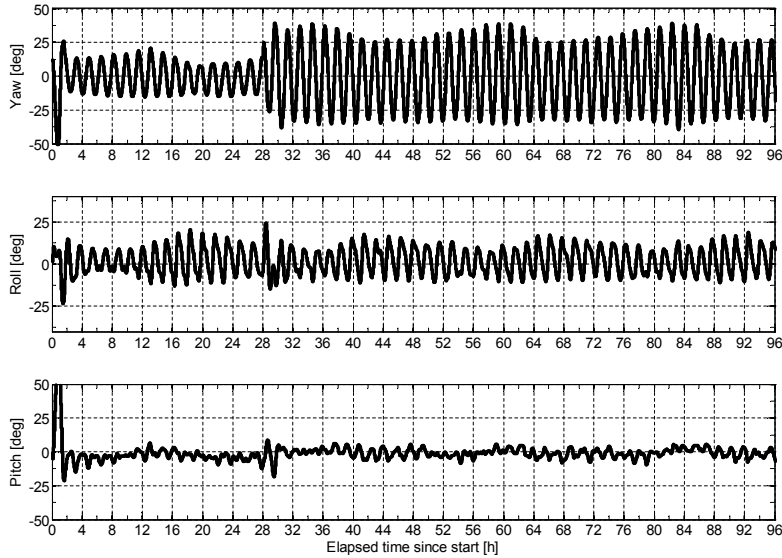
The SATLAB facility provides telemetry logging for the *Main* and *Target* on-board computers as well as the real-time simulator. In particular the actual orbit and attitude motion propagated within the simulator are logged as part of the telemetry stream during the real-time SATLAB test. Fig. 5.2 depicts the actual relative motion of *Main* with respect to the *Target* in the local orbital frame aligned with the radial, along-track and cross-track axes. For clarity the reference relative motion is also projected onto the along-track/radial and cross-track/radial planes in Fig. 5.3 and 5.4. The different formation flying configurations are also indicated in the plots.

Fig. 5.5 depicts the actual orientation of the *Main* body frame with respect to the orbital frame. The adopted attitude parameterization corresponds to the Euler rotation angles sequence 3-1-2 [Wertz, 1997]. These parameters are named in the sequel yaw, roll and pitch angles and correspond to rotations around radial, along-track and cross-track directions respectively. Positive yaw, roll and pitch rotations are clockwise around the respective axes.

During thrust free phases, the *Main* body axes are closely matching the orbital frame with maximum angular errors of  $0.03^\circ$ . During the execution of orbit control maneuvers the attitude guidance function re-orient the spacecraft as mentioned above. The main resulting effect is a sudden variation of the pitch



**Fig. 5.5:** Actual attitude motion of *Main* with respect to the orbital frame. The adopted 3-1-2 Euler angles parameterization corresponds to rotations about the radial (yaw, top), along-track (roll, middle) and cross-track (pitch, bottom) directions respectively. Positive yaw, roll and pitch angles are clockwise around the respective axes.



**Fig. 5.6:** Actual attitude motion of *Target* with respect to the orbital frame. The adopted 3-1-2 Euler angles parameterization corresponds to rotations about the radial (yaw, top), along-track (roll, middle) and cross-track (pitch, bottom) directions respectively. Positive yaw, roll and pitch angles are clockwise around the respective axes.

angle (cf. Fig. 5.5, bottom) which settles at the desired value for the duration of the in-plane maneuver. Out-of-plane maneuvers do not normally require a re-orientation of the spacecraft because the used thruster is nominally aligned with the normal to the orbit plane.

Fig. 5.6 depicts the *Target* attitude in terms of yaw, pitch and roll angles as

done for *Main*. In this case the attitude control, in Sun/zenith pointing mode, is characterized by yaw and roll oscillations of about  $20^\circ$  amplitude. It is noted that an attitude event occurs around 27 hours from simulation start. In particular the amplitude of the yaw attitude oscillations increases by roughly  $10^\circ$ . A closer inspection of the AOCS TM/TC shows that an unintentional attitude reference quaternion change was set due to a wrong telecommand.

### 5.2.4 Flight Software Status

Each flight software module produces as output a status byte containing flags for telemetry monitoring and FDIR support (cf. Table 4.10). Fig. 5.7 illustrates the most relevant flags delivered by the OBS during the 96 hours real-time SATLAB test. Each row of subplots refers to a different software module, in order from top: GIF, GOD, GOP and AFC.

The GIF status is shown to be nominal. The Mitel messages from the Phoenix-S receivers on *Main* and *Target* are never older than 30 s during the simulation (top left and top middle subplots). The number of tracked GPS satellites is always larger/equal than one (top right subplot).

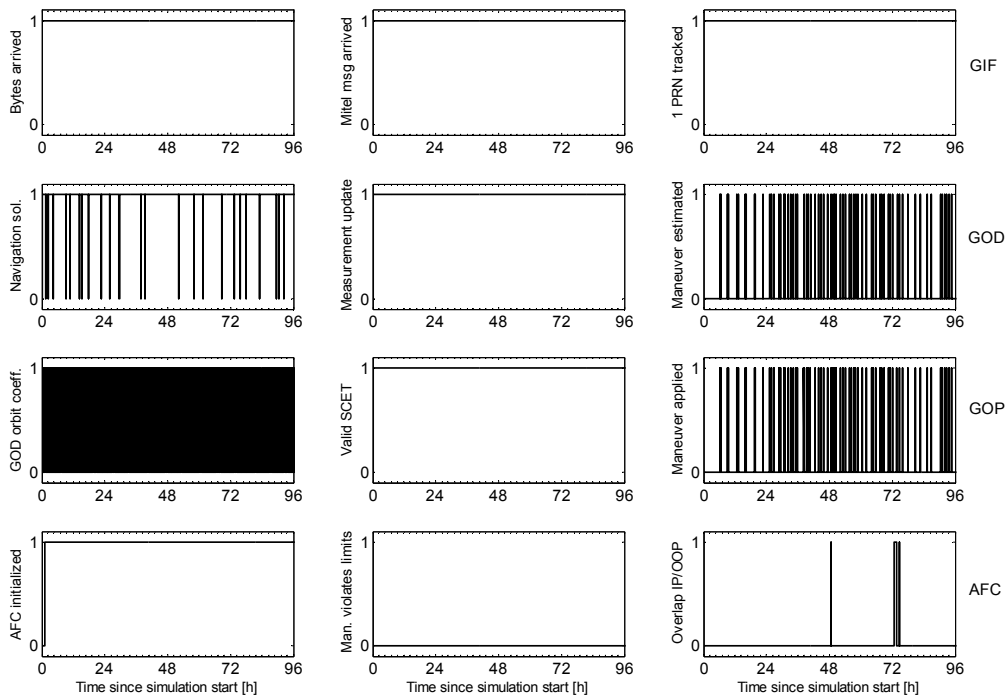


**Fig. 5.7:** Relevant flight software status flags during the SATLAB test. Each row of subplots refers to a different software module, in order from top: GIF, GOD, GOP and AFC (see text for details).

The GOD status flags show that GPS navigation solutions for *Main* and *Target* are flagged as invalid several times (GOD left subplot). This is due to the fact that in these occasions GOD has no input navigation solutions from GIF. An analysis of the GPS messages, available in the telemetry stream, shows that

actually in several occasions GIF receives valid *Target* raw data (i.e., F62 messages) but no navigation solutions (i.e., F40 messages). This is due to the loss of single telemetry packets sent through the ISL from *Target* to *Main*. The navigation solutions are only used for initialization of the EKF within GOD, thus the measurement update is performed at each call of GOD during the test (GOD middle subplot). The last status bit of GOD shows the occurrence of several maneuver estimation events.

The GOP status byte shows that new orbit coefficients are regularly provided by GOD at 30 s intervals and replaced internally by GOP. The input SCET time is always within the validity interval of the orbit polynomials (GOP middle subplot), and the maneuver delta- $v$ 's are applied by GOP in parallel with the GOD processing (cf. GOP and GOD right subplots).

Finally nominal operations of AFC are illustrated by the last status flags (bottom subplots). AFC is first initialized upon convergence of the EKF (after about one orbital revolution). The commanded maneuver sizes are always within the thresholds prescribed via TC. It is interesting to note that during the second and third constellation reconfigurations (at 48 and 72 hours respectively), an overlap of in-plane and out-of-plane orbit control maneuvers occur (indicated by the flag Overlap IP/OOP in bottom right subplot). In these occasions simultaneous corrections of the relative eccentricity and inclination vectors are applied through combined thrusts with in-plane and out-of-plane components.

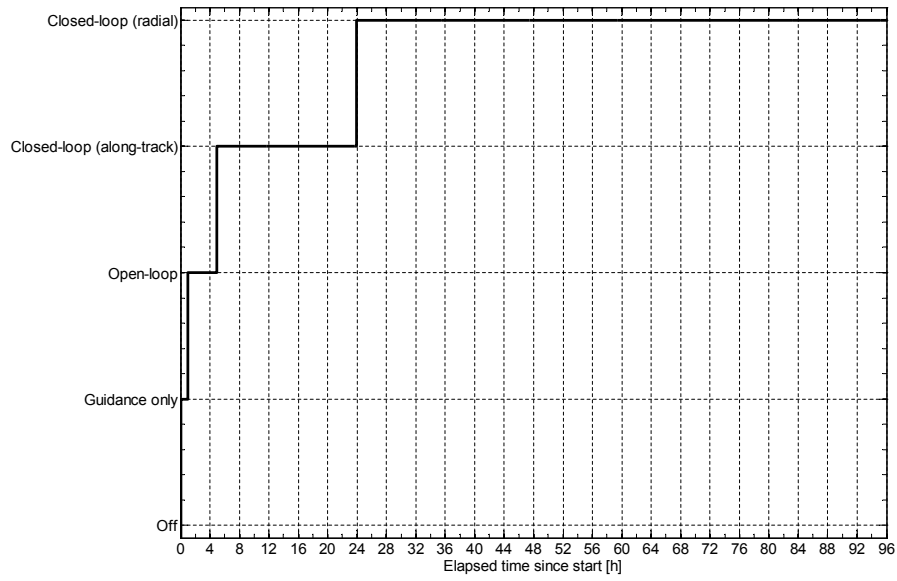
### 5.2.5 Guidance and Control Results

Fig. 5.8 depicts the AFC controller mode during the SATLAB test. As prescribed via time-tagged commands, AFC is first operated in guidance only and open-loop modes for 1 and 4 hours respectively. Next the closed-loop activities are triggered with along-track and radial submodes starting at 24 and 48 hours from start respectively. The relative orbital elements are computed as part of the guidance process and illustrated in Fig. 5.9.

The match between desired (cf. Table 5.3) and actual relative orbital elements is within the control windows during formation keeping phases. Formation reconfiguration phases are clearly visible at 24, 48 and 72 hours with large changes of the relative orbital elements. A total of 43 pairs of in-plane maneuvers and 17 out-of-plane maneuvers are issued by AFC to maintain the formation geometry and reconfigure it when required from ground. The in-plane and out-of-plane maneuver counters are shown in fig. 5.10.

The maneuver counter is reset at each re-configuration of AFC. The number of in-plane formation keeping maneuvers refers to the number of maneuver pairs. As expected the number of out-of-plane formation keeping maneuvers is reduced to zero for configurations with  $\Delta i = 0$  (identical spacecraft inclination).

Finally the relative orbit control errors, or control tracking error, are computed by subtracting the actual relative motion of *Main* with respect to *Target* from the desired relative motion as described by the selected nominal relative orbital elements (cf. Table 5.3). As shown in Fig. 5.11, during formation keeping



**Fig. 5.8:** AFC controller mode during the SATLAB test. The mode is identified by an integer number contained in the AFC TM stream. AFC is first operated in guidance only and open-loop modes for 1 and 4 hours respectively. Next the closed-loop activities are triggered with along-track and radial submodes starting at 24 and 48 hours from start respectively.

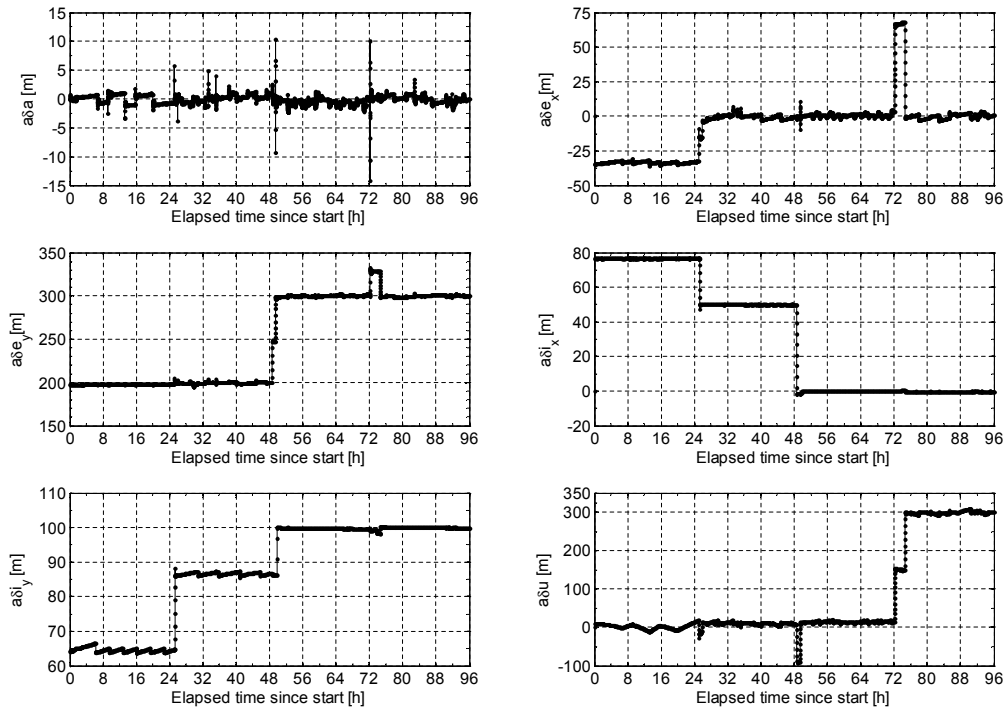


**Fig. 5.9:** Estimated relative orbital elements computed by AFC during the guidance process. The relative orbital elements are maintained close to the commanded nominal values listed in Table 5.3. Formation reconfiguration phases are clearly visible at 24, 48 and 72 hours with large changes of the relative orbital elements.



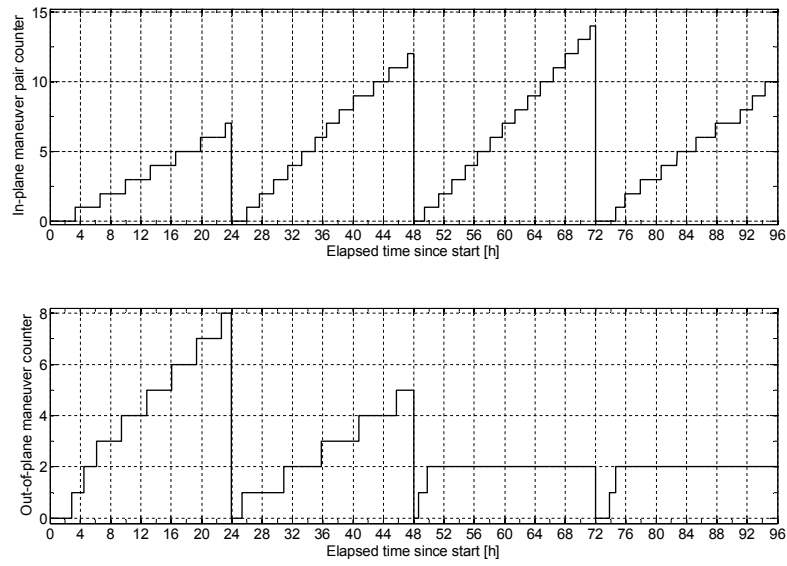


**Fig. 5.10:** In-plane (top) and out-of-plane (bottom) maneuver counter computed by AFC during the SATLAB test. The maneuver counter is reset at each re-configuration of AFC. The number of in-plane formation keeping maneuvers refers to the number of maneuver pairs. The number of out-of-plane formation keeping maneuvers is zero for configurations with  $\Delta i = 0$  (identical spacecraft inclination).

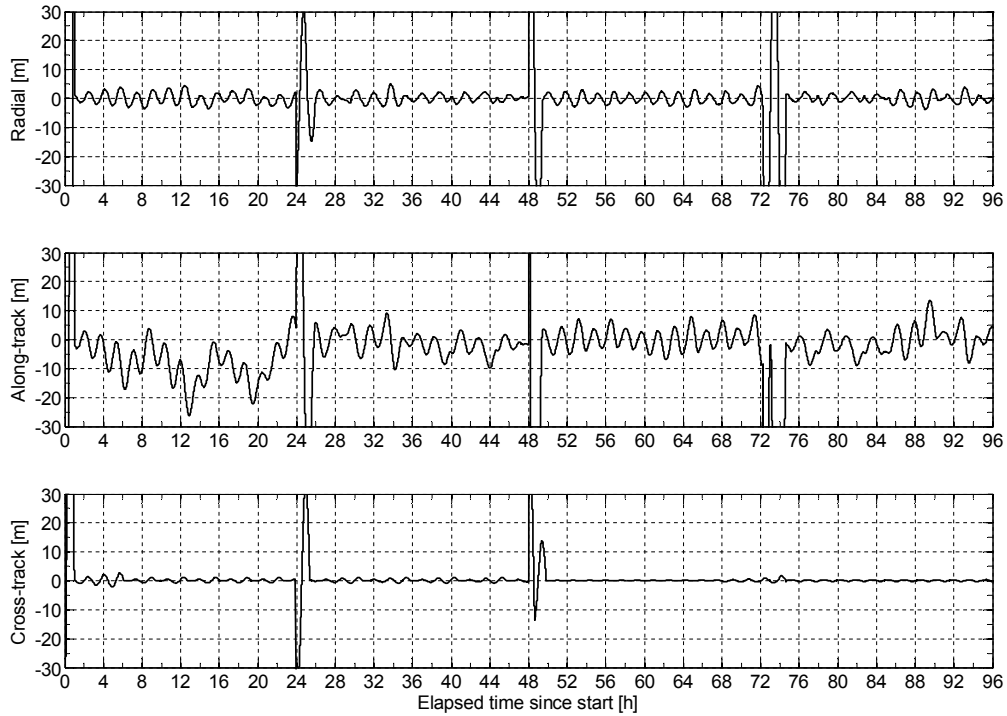


**Fig. 5.11:** Control tracking error mapped into the orbital frame aligned with the radial (top), along-track (middle) and cross-track (bottom) directions.

phases, the relative position control errors stay below 5.0/25.0/2.5 m in radial, along-track and cross-track directions respectively. The formation reconfigura-

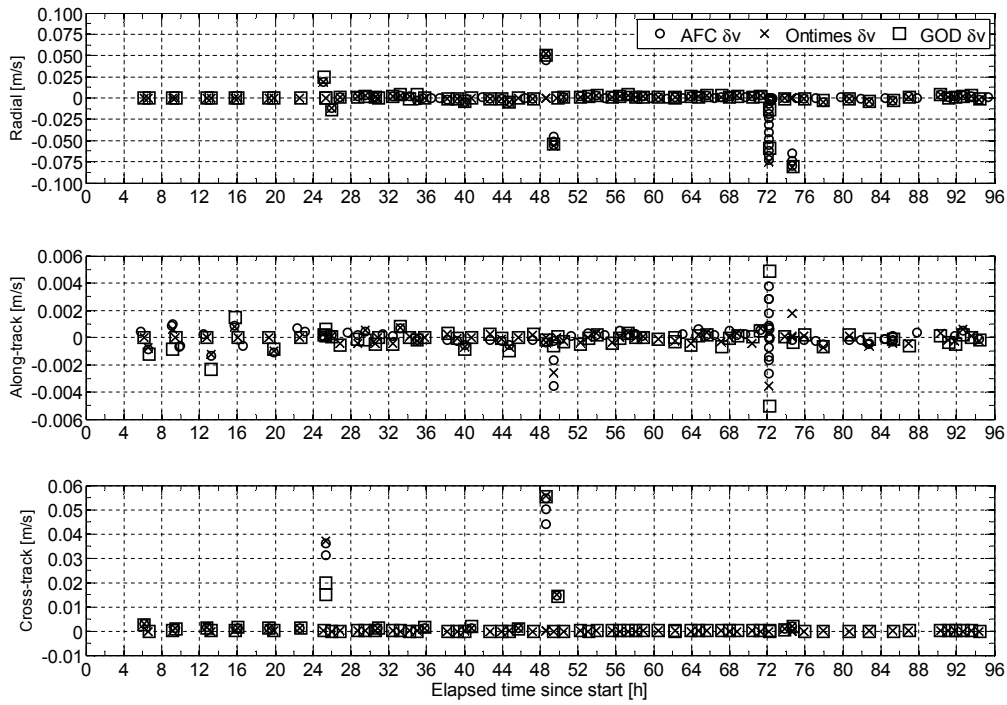


**Fig. 5.12:** Radial (top), along-track (middle) and cross-track (bottom) maneuvers requested by AFC (circles), realized by the hydrazine thrusters (crosses) and estimated by GOD (squares) during the SATLAB test.

tions are obtained through the same analytical feedback control law used for formation keeping (cf. Section 2.4.6). This approach simplifies enormously the flight code development, testing and operations, in fact the same TM/TC interfaces are applied. The drawback of this strategy resides in the responsiveness of the control system or, more simply, on the re-convergence time which is limited to a minimum of one orbital revolution (about 1.5 h).

A net improvement of the control performance can be observed when switching from the first to the next formation flying configurations. This effect is especially visible in along-track direction (cf. relative mean argument of latitude in Fig. 5.9) and is due to the radial closed-loop mode which implements maneuvers in radial direction. This avoids offsets of the relative semi-major axis and unintentional drifts of the relative mean argument of latitude at a higher fuel consumption cost (cf. Section 2.4.6).

A critical aspect of the integrated GNC system is the verification of the closed-loop activities. Relative orbit control maneuvers are requested by AFC in the form of impulsive velocity variations in the orbital frame centered on *Main*. The time and delta-v size information is used by auxiliary functions in the GNC core to send commands to the thrusters in terms of burn start time and duration for each thruster to be used. The AOCS performs a re-orientation of the spacecraft in order to align only one thruster with the maneuver direction. The maneuver induced accelerations are measured by the accelerometers on-board *Main*. These measurements are conditioned, filtered and used to com-

pute equivalent impulsive velocity variations for each second of thrust. The a-priori measured delta-v information and time are provided to GOD and GOP for incorporation in the navigation process. Fig. 5.12 shows the AFC maneuver requests (circles), the actual thruster on-times (crosses) and the GOD maneuver estimates (squares).

The maneuver on-times are converted to delta-v's (nominal thrust of 1 N is applied) and mapped to the orbital frame by taking into account the true *Main* attitude and the thruster orientation. The mismatch between AFC requests and realized thruster activations is typically confined below 5% but in some cases is 21% of the actually applied delta-v. It can be noticed that the largest values of the maneuver execution errors correspond to the largest maneuvers (i.e., cm/s size). These errors are mainly due to the fact that the AFC maneuver time commands are interpreted as pulse-centers instead of pulse-start times, thus inducing a mismatch between -applied- thrusts and -final- requests by AFC. The error introduced by the accelerometers is usually better than 3% but can be up to about 50% for large maneuvers. Accordingly, the correspondence between GOD estimates and thrusters activations varies a lot but it is in most cases better than 30%. It is noted that the flight software is only required to incorporate maneuvers in the navigation process in order to ensure a smooth and accurate state estimate during operations. Thus no functional or performance requirements are defined for the real-time estimation of the executed delta-v's.

### 5.2.6 Navigation Results

The accuracy of the navigation filter is evaluated as usual. The navigation errors are computed by subtracting the position and velocity of the *Main* and *Target* spacecraft provided by GOP from the true reference trajectory logged from the SATLAB real-time simulator in the ECEF reference frame at 10 s samples.

The absolute and relative navigation errors are then mapped in the orbital frame and plotted in Figs. 5.13-5.16. Upon filter convergence, and excluding the formation reconfiguration phases, the obtained absolute and relative navigation accuracy for the position is 3.2 m and 7.8 cm (3D, RMS) respectively (cf. Figs. 5.13 and 5.14). The convergence time is shown to be always below one orbital revolution ( $< 1.5$  h). Compared to the closed-loop test case addressed in Section 3.4.2, the relative position errors are more than ten times larger due to the different attitude motion of the two spacecraft and the high attitude estimation errors which affect mainly the *Target* spacecraft. Note that the relative position errors increase after about 24 hours of real-time SATLAB simulation. This is due to the change of *Target* attitude (cf. Fig. 5.6) and to the change of AFC mode. In fact, starting with the second formation flying configuration, AFC adopts maneuvers in radial direction which are more difficult to absorb in the navigation process. Despite the degradation in navigation accuracy, the control performance is improved by the usage of the AFC radial closed-loop mode. The absolute position errors are only slightly increased due to the higher broadcast ephemeris errors and the more intense maneuver activity.

The absolute and relative velocity are affected by errors of 1.27 cm/s and

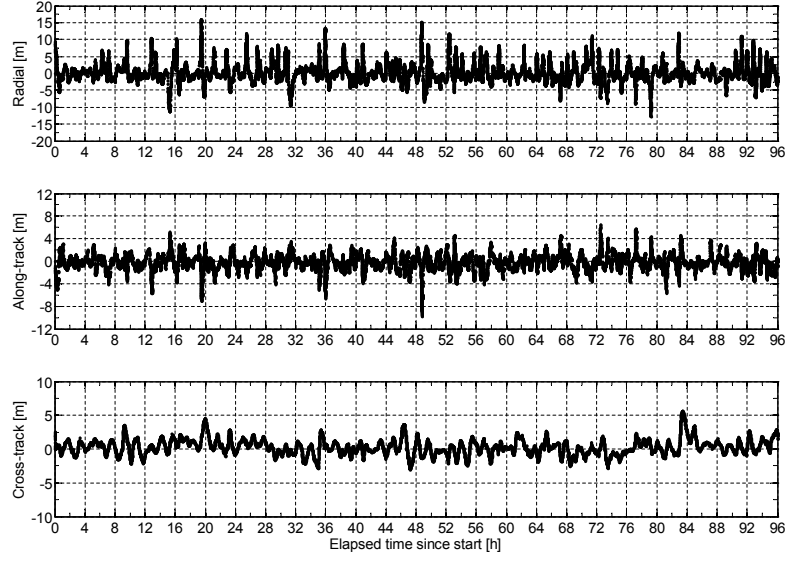


**Fig.5.13:** Absolute *Main* position error mapped into the orbital frame aligned with the radial (top), along-track (middle) and cross-track (bottom) directions. Statistics computed excluding the convergence phase of the EKF provides an absolute navigation accuracy of 3.2 m (3D, RMS).

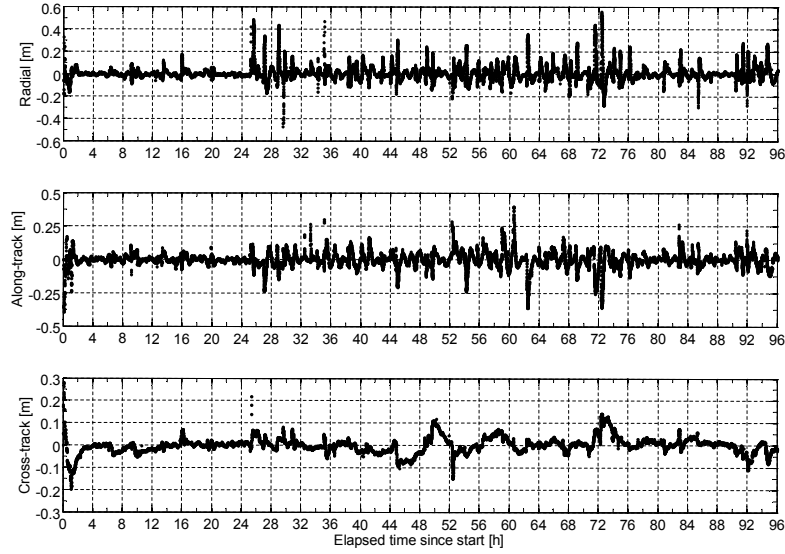


**Fig.5.14:** Relative position error (i.e., *Main* with respect to *Target*) mapped into the orbital frame aligned with the radial (top), along-track (middle) and cross-track (bottom) directions. Statistics computed excluding the convergence phase of the EKF provides a relative navigation accuracy of 7.8 cm (3D, RMS).

0.36 mm/s (3D, RMS) respectively (cf. Figs. 5.15 and 5.16). The error trend is similar to the results obtained in Section 3.4.2. At the instance of an orbit control maneuver the absolute velocity errors increase to values of several tens of mm/s which are then slowly re-absorbed by the EKF thanks to the collection of new GPS measurements. Similar to the relative position errors, the relative velocity shows a degraded accuracy due to the high angular velocity and attitude

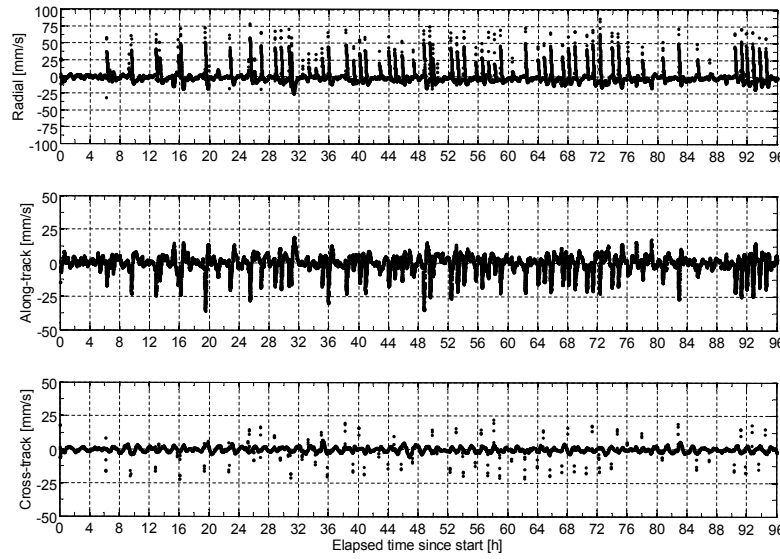


**Fig. 5.15:** Absolute *Main* velocity error mapped into the orbital frame aligned with the radial (top), along-track (middle) and cross-track (bottom) directions. Statistics computed excluding the convergence phase of the EKF provides an accuracy of 1.27 cm/s (3D, RMS).

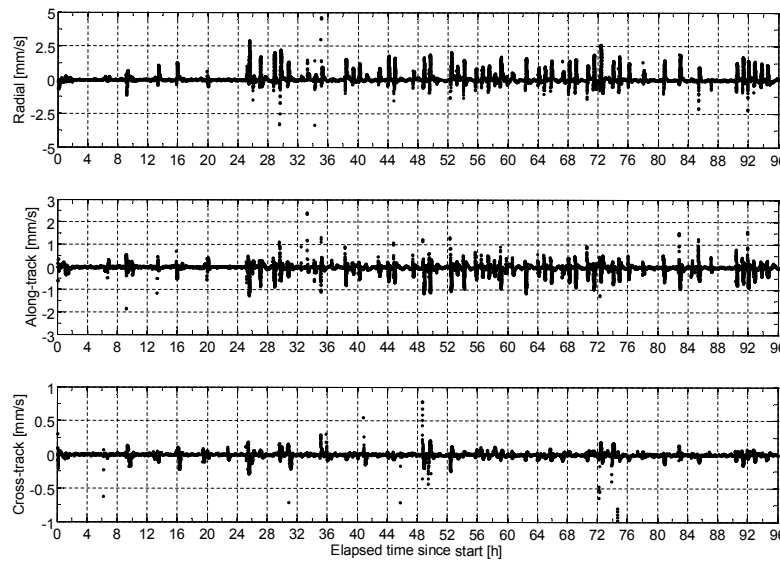


**Fig. 5.16:** Relative velocity error (i.e., *Main* with respect to *Target*) mapped into the orbital frame aligned with the radial (top), along-track (middle) and cross-track (bottom) directions. Statistics computed excluding the convergence phase of the EKF provides an accuracy of 0.36 mm/s (3D, RMS).

estimation errors affecting the *Target* spacecraft. The absolute empirical accelerations estimated during the SATLAB simulation (cf. Fig. 5.17) are also strictly correlated to the maneuver executions and to the discussed velocity errors. In particular the radial component reaches values of about  $20000 \text{ nm/s}^2$ , while the along-track and cross-track components stay below  $5000 \text{ nm/s}^2$  and are less affected by maneuver executions. These figures are similar to the ones obtained

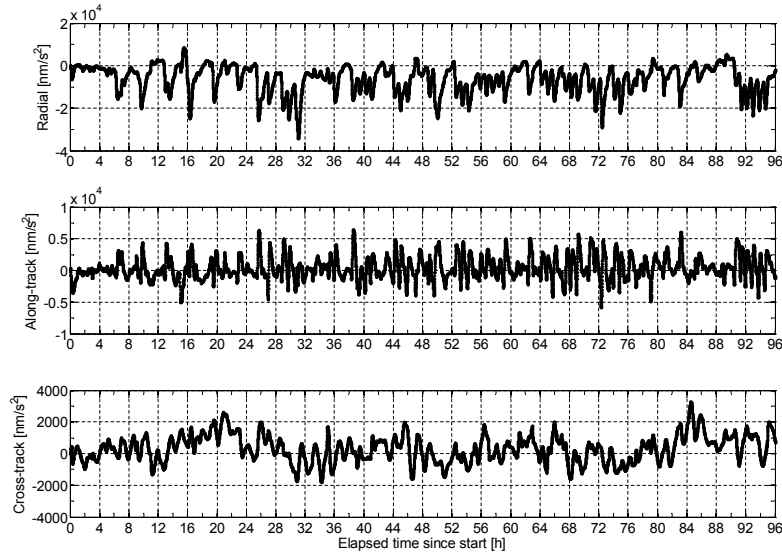


**Fig. 5.17:** Empirical accelerations of *Main* mapped into the orbital frame aligned with the radial (top), along-track (middle) and cross-track (bottom) directions.

in the standalone validation of the prototype algorithms presented in Section 3.4.2 (cf. Fig. 3.17) and are smaller than 0.3 % of the applied thrust acceleration (order of  $6500000 \text{ nm/s}^2$ ).

### 5.2.7 Flight Software Timeliness

A major add-on of the SATLAB test, compared to the standalone validation at DLR discussed in Chapter 3, is the analysis of the flight software execution times. Time measurements could be performed during the execution of the specific application components and have been logged as part of the OBS telemetry. Fig. 5.18 shows such measurements during the complete 96 hours SATLAB test arc.

More specifically the figure illustrates the time elapsed between -task entering running state- and -task finished-, i.e. the duration of the application component scheduled in that task. This also includes the accumulated time for higher-priority tasks that are preempting the lower-priority tasks during the execution (which is estimated around  $100 \text{ ms/s}$ ). GIF and GOD are contained in low-priority application cores (BSW and ORB respectively), while GOP and AFC are part of the GNC core, which includes e.g. GNC, AOCS and Power/Thermal functionalities.

Normally the BSW total execution times, driven by GIF, lie between about 20 and 60 ms. Only when broadcast ephemeris messages (i.e., F14 messages) are issued by the Phoenix-S receivers the total execution time of the BSW core can reach 112 ms. The GNC task has an average execution time of about 200 ms. Peaks up to 268 ms are visible in correspondence of the maneuver executions and are mainly due to GOP and to the AOCS attitude guidance functions. Finally the most demanding ORB task has an average total execution time of

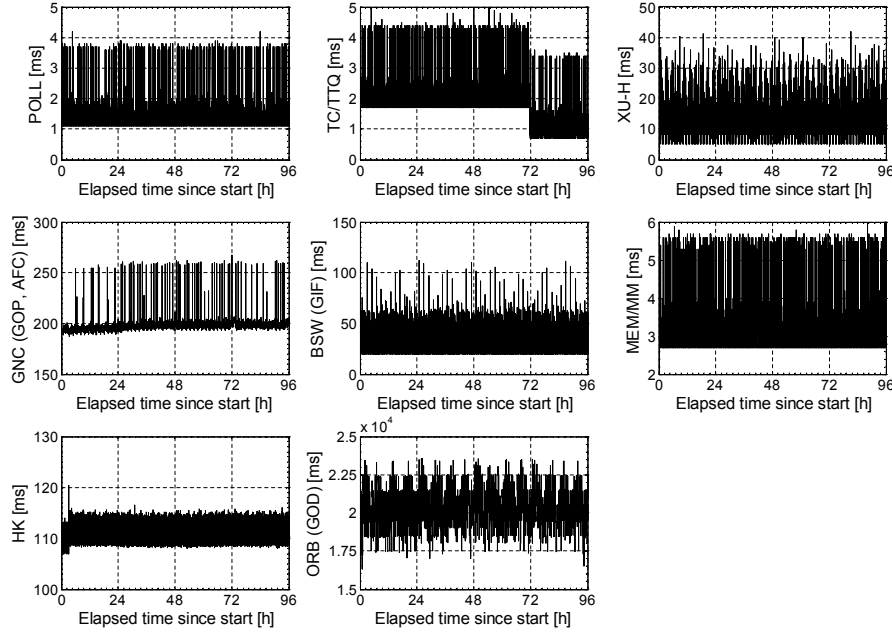


**Fig. 5.18:** Time measurements from the *Main* on-board computer during the SATLAB test. The subplots show the duration of the I/O and busy-wait polling (POLL, up-left), TC and time-tagged TC Queue (TC/TTQ, up-mid), BSW high priority (XUH, up-right), GNC/AOCS core (GNC, mid-left), BSW low priority (BSW, mid-mid), Memory management and mass memory (MEM/MM, mid-right), House Keeping TM (HK, bottom-left) and ORB core (ORB, bottom-right) tasks.

about 20 s with peaks of approximately 24 s. Considering the given measures and the accumulated time for higher-priority tasks, the average CPU time available for the ORB core is about 500 ms/s, but only a fraction of it is actually required. Thus the average CPU load during the SATLAB test is approximately 30%. This figure is in accordance with the max-path unit tests described in Section 4.5.2. It is noteworthy that the execution time of GIF and GOD is always below its sample time (i.e., 1 s and 30 s respectively), and consequently ensures a proper execution of the navigation process.

Finally Fig. 5.19 shows the GOD telemetry parameter which indicates the time elapsed since the last *Main* and *Target* measurement updates. The age of the measurement update is typically between 30 s and 40 s but reaches peaks of 50 s in certain cases. Note that a periodic pattern is clearly visible in Fig. 5.19, in fact dense phases of 20–40 s age appear approximately every 24 hours. A closer inspection shows that this is a result of the clock drift between the SATLAB real-time computer and the *Main* on-board computer. The drift is about 10 s per day and in addition the actual start time of GOD and GIF (triggered by the OBS pulse per second) also varies with the current CPU load. The asynchronous execution of these tasks, in combination with the 10 s sample time of the GPS messages, results in periods where we see 40 s updates and shortly after 20 s updates, or alternatively 20 s updates and shortly after 40 s updates. Later, when the clocks have drifted more, the GPS messages arrive at times which are not

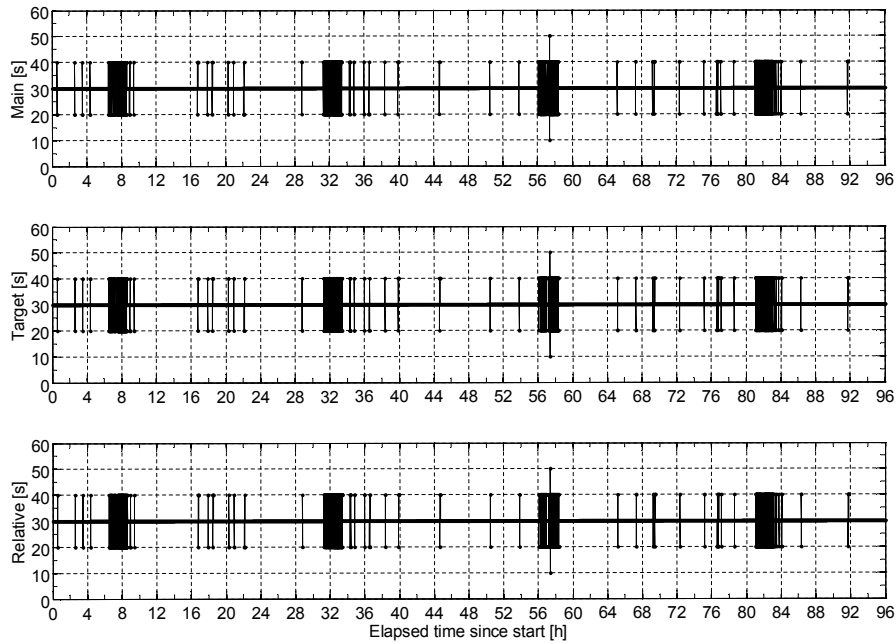


**Fig. 5.19:** Time elapsed since the last *Main* measurement update (top), *Target* measurement update (middle) and single difference carrier phase measurement update (bottom) performed by GOD during the SATLAB test. Maximum peaks up to 50 s are visible and are caused by the latency of the GPS/GIF HW/SW chain output in combination with the total execution time of GOD. Dense peaks of 40 s old measurement updates occur approximately every 24 hours.

close to the start of GOD and we see a rather steady 30 s measurement update. The actual length of one dense phase of 20 – 40 s age is about 2 hours, about 10% of a day, which means that during the peak the clock drift is about 1 s. As a consequence the peaks of the measurement update age occur when the GOD execution is synchronized to the GPS message arrival time within about 0.5 s.

### 5.3 Integrated Tests with GPS Hardware in the Loop

The most representative system functional and performance tests have been conducted in the spacecraft integration hall at the Swedish Space Corporation premises in the time frame March 23 to March 31, 2009. An overview of the test configuration and the key hardware elements is given in Fig. 5.20. Artificial GPS signals for *Main* and *Target* are generated by a Spirent GSS7700 signal simulator providing L1 signals for up to 12 satellites. Each of the two outputs is split by a M/A-COM Power Divider and fed to the four available RF flight cables (two on each spacecraft) which normally connect the GPS antennas with the RF switch (cf. Fig. 4.2). In other words, the GPS antennas (mounted at the edges of the solar panels on *Main* and on the sides of the *Target* spacecraft body) are disconnected from the cables and bypassed to allow the delivery of GPS signals to the rest of the GPS hardware chain (cf. Fig. 4.2 for an overview of the GPS architecture).



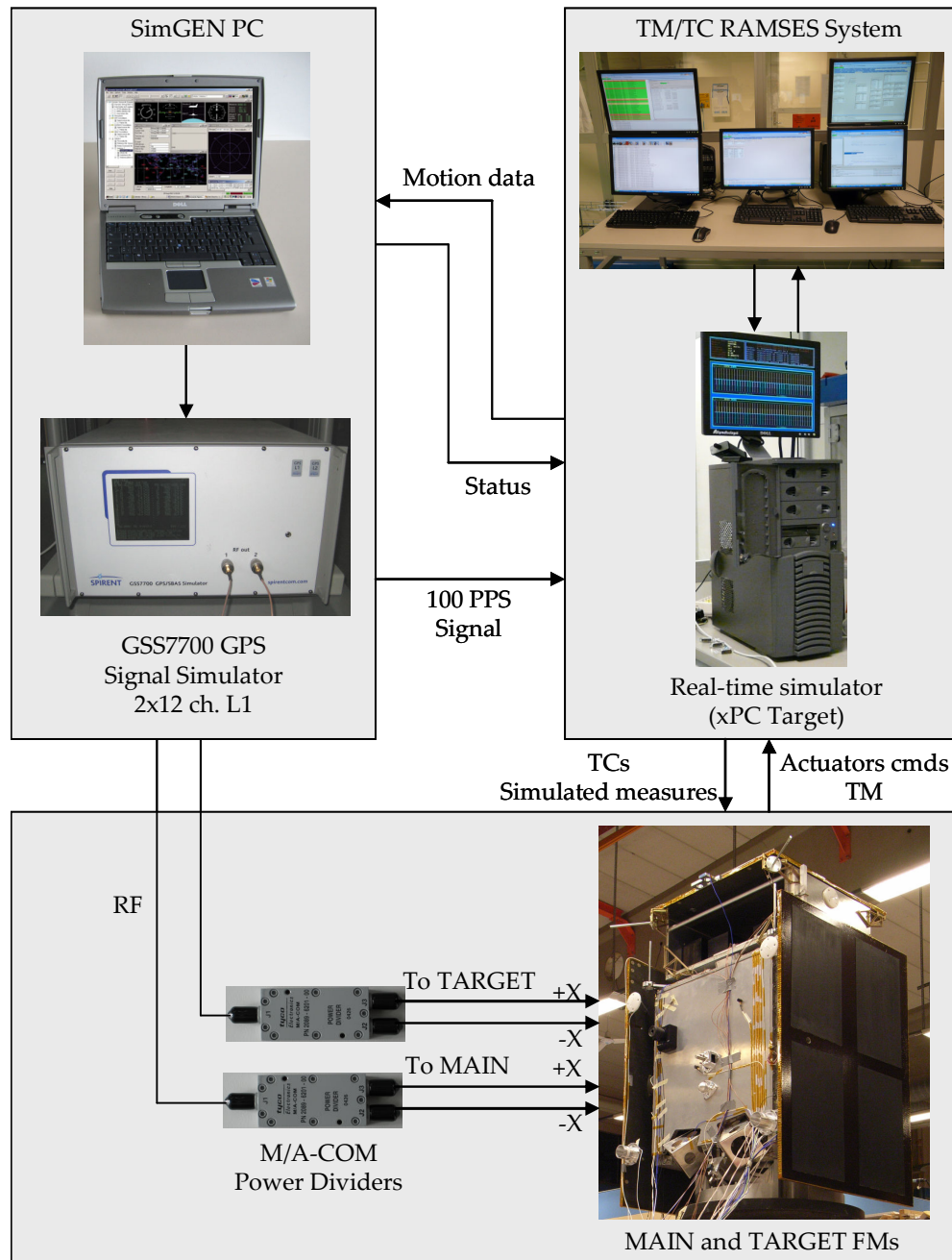


**Fig. 5.20:** Hardware setup for GPS integrated tests on spacecraft flight models.

The GSS is steered in a remote mode by the SATLAB real-time simulator (xPC target) which can model translational and rotational motion (i.e., orbit and attitude), sensors and actuators, as well as other parts of a multiple spacecraft system. The absolute time reference of the system is the oscillator of GSS. Therefore it is required that all other participants of the closed-loop system are synchronized with the clock of GSS. The GSS provides TTL level 100 Pulse-Per-Sec (PPS) signal which is used as the timing reference. The key feature of

the simulator is its capability to perform 10 ms step work of simulation at the timing continuously synchronized with GSS. Overall the simulator provides real-time motion data to GSS via TCP/IP interface. Motion data includes orbit/attitude information of each spacecraft and epoch time. The adopted force model for orbit and attitude propagation has already been described in Section 5.2.1.

As a central element of the complete HIL setup, the xPC target simulator handles the direct interfaces with the spacecraft and the TM/TC RAMSES ground system [SSC, Last accessed: 2009]. In particular, simulated measurements are provided to the spacecraft on-board computer for missing sensors (e.g., attitude sensors and accelerometers). Actuator commands are sent by the AOCS/GNC systems on *Main* and *Target* to the xPC target, which emulates their effects and update accordingly the motion data sent to the GSS. Furthermore spacecraft telemetry and operator procedures (telecommands) are handled in a flight-like manner through the RAMSES ground system. The Inter Satellite Link (ISL) is also modeled within the xPC target, thus TM/TC and exchange of data (e.g., estimated attitude quaternions and GPS data) are first provided to the ISL model in the SATLAB real-time simulator and then routed to their final destination on *Main* or *Target*.

Note that the same RF signal is fed to the two inputs of the on-board RF switch. Through the proper coordination of commands to the RF switch and motion data delivered by the SATLAB real-time simulator, it is possible to handle GPS antenna switches and select the desired GPS branch in a consistent manner. This enables the realistic emulation, at a system level, of mission phases where the spacecraft are tumbling and automatic antenna switches are commanded by the on-board software.

The following subsections give a detailed description of two relevant integrated system tests conducted with spacecraft flight hardware in the loop. The first test is dedicated to the verification of the overall closed-loop GNC activities during a representative formation keeping experiment. The second test is a highly realistic emulation of the PRISMA spacecraft separation sequence, probably the most challenging mission phase from a GPS subsystem point of view. Compared to the simulations documented in the previous sections, both tests are only a few hours long due to the limited accessibility of the integrated flight spacecraft at the Swedish Space Corporation.

### 5.3.1 GPS Signal Simulator Scenario Definition

A dedicated GSS scenario is designed as a framework for the integrated tests with GPS hardware in the loop conducted on PRISMA. The simulation is based on orbit and attitude motion data provided remotely by the SATLAB real-time simulator, thus no use of the GSS internal propagator and attitude handling is made. The GPS constellation is modeled based on the actual GPS almanac for the week 1381 (2 July 2006), which is propagated to the scenario time within the signal simulator. The influence of ionospheric path delays and broadcast ephemeris errors is properly taken into account through configuration files with

realistic error sources as described in the following. The antenna diagram corresponds to a Sensor Systems S67-1575-141 antenna without ground plane as used on PRISMA.

The GPS constellation definition is based on a YUMA almanac describing the true constellation for GPS week 1381. It comprises a total of 29 satellites (all PRNs except 12, 31 and 32). It may be noted that PRN 3 and 6 are simulated but have a non-nominal health code (063 in the almanac file).

To assess the impact of broadcast ephemeris and clock errors on the navigation solution computed by the receiver and on the real-time navigation system, intentional position offsets have been added as part of the GPS constellation configuration file. These offsets affect the simulated trajectory but are not applied to the broadcast ephemeris message issued by the simulator. For simplicity, the offsets are constant in time and applied only to the radial satellite position. No tangential and normal offsets have been configured since this would not provide added realism to the simulation. In an effort to mimic a realistic User Equivalent Range Error, the applied offsets are based on uniformly distributed random numbers with zero mean and a standard deviation of 1.5 m (cf. Table 5.5). It is noted that the activation of broadcast ephemeris errors affects only the estimated receiver position but has virtually no impact on the velocity component of the navigation solution.

**Table 5.5:** Intentional broadcast ephemeris errors in downward direction ( $\Delta Z$ ) as applied in the GPS constellation definition file.

PRN	$\Delta Z$ [m]	PRN	$\Delta Z$ [m]
1	-1.98	17	1.87
2	0.87	18	1.26
3	-0.77	19	-0.46
4	0.07	20	1.67
5	-1.51	21	0.90
6	0.03	22	-0.88
7	-3.95	23	1.41
8	1.07	24	0.03
9	0.03	25	-0.38
10	-2.28	26	0.61
11	0.36	27	-0.53
12	n.a.	28	-2.65
13	1.38	29	-0.14
14	-2.65	30	0.36
15	1.80	31	n.a.
16	1.06	32	n.a.

The simulator is configured to generate GPS signals for all satellites above a  $5^\circ$  elevation cut-off angle measured from the Earth tangent. Satellites are selected based on a power level criterion using sequential replacement and 30 s sampling. The actual elevation at which a specific satellite is selected or discarded depends on the total number of channels supported by the simulator as well as the number of satellites visible at a specific time. Compared to a Posi-

tional Dilution Of Precision (PDOP) based channel allocation, the power level based selection ensures continuous and uninterrupted signals throughout the visibility period of each satellite.

By default, the simulator generates a GPS signal strength compatible with the minimum signal level specified for the GPS system (approx.  $-130$  dBm for satellites at a mean distance from the observer) and a  $0$  dB vertical antenna gain. The overall signal level may, however, be adjusted to account for the actual antenna gain (about  $3 - 5$  dB in the boresight direction) as well as the actual GPS signal strength (approx.  $< 3$  dB above specification). In addition, a higher than normal signal level is required to compensate for the higher noise temperature experienced in simulator testing compared to the usual antenna sky temperature [Montenbruck and Holt, 2002]. Considering finally the power losses caused by the power dividers (about  $3$  dB, cf. Fig. 5.20), a software signal amplification of  $+10$  dB has been found appropriate to reproduce the signal strengths observed in open-air receiver tests for various single-frequency GPS receivers.

The application of ionospheric path delays (and a corresponding carrier phase advance) within the GSS scenario is based on the Lear mapping function [Lear, 1989] with a constant Total Electron Content (TEC) of  $10$  TECU, i.e.  $10 \cdot 10^{16}$  electrons/m<sup>2</sup>.

### 5.3.2 Short-term GPS-based Closed-Loop Test

#### Test Specification

The fundamental difference between the following HIL closed-loop test and the formation control rehearsal presented in Section 5.2 lies in the SATLAB setup configuration. Apart from the usage of the *Main* and *Target* spacecraft flight models, the Phoenix-S software emulator PEM is now replaced by actual flight GPS hardware. The specification of this first integrated closed-loop test with GPS hardware in the loop is thus nearly identical to the one presented in Section 5.2. For clarity Table 5.6 specifies once more the initial conditions in terms of start time, GPS-UTC and UT1-UTC time differences, *Main* and *Target* state vectors in ECI coordinates. The rest of the test description focuses then on the differences with respect to the previous SATLAB long-term test.

**Table 5.6:** Initial *Main* and *Target* spacecraft orbits.

Initial time		Value	
Epoch (GPS time in CUC) [s]		835833600	
GPS-UTC [s]		14.0	
UT1-UTC [s]		0.193134	
State vector (EME2000)		Target value	Main value
Position [m]	$x$	6952528.480	6952540.221
	$y$	1321236.001	1321360.018
	$z$	0.000	-380.737
Velocity [m/s]	$v_x$	199.61648	199.83605
	$v_y$	-1050.40982	-1050.44461
	$v_z$	7433.88732	7433.83929

The execution of the flight software modules (i.e., GIF, GOD, GOP and AFC) during the integrated test is triggered by dedicated time-tagged TC procedures which are sent through the RAMSES ground system to the on-board computer. Practical constraints are the limited availability of operators and access to flight spacecraft models, thus the test duration shall not exceed 8 hours. In order to shorten the length of the test, compared to the long-term rehearsal presented in Section 5.2, AFC is now only operated in two modalities: open-loop and closed-loop (radial sub-mode). In open-loop mode, maneuvers are normally planned by AFC but commands are not sent to the GNC system for execution. The closed-loop mode is enabled at around 1.5 hours from start, here maneuvers are actually commanded in radial, along-track and cross-track directions as described in Section 2.4.6.

AFC has to autonomously maintain the initial formation geometry for a time period of about 6.5 hours. The desired nominal relative orbital elements correspond to the first configuration listed in Table 5.3 (i.e., Config. 1). The commanded control windows for the relative eccentricity and inclination vectors are kept constant during the complete test and are given by  $a\delta e^{\max} = a\delta i^{\max} = 2\text{ m}$ . The initial relative geometry corresponds to non-parallel relative eccentricity/inclination vectors with relative perigee and relative ascending node at  $100^\circ$  and  $40^\circ$  respectively. As a consequence both in-plane and out-of-plane maneuvers are required to counteract the drifts of relative eccentricity and inclination vectors mainly caused by the Earth oblateness. In contrast to the previous test, here the delta-v attitude guidance function is enabled after 5 hours from start in order to verify the behavior of the system with and without this feature in the limited available time frame.

The settings applied to the EKF in GOD for absolute and relative navigation during the integrated system test are collated in Table 5.4 and are identical to the ones previously applied in Section 5.2.

#### Estimated Attitude

Figures 5.21 and 5.22 show the on-board estimated attitude during the HIL integrated system test on *Main* and *Target*. The attitude is parameterized in terms of the Euler angles yaw, roll and pitch with respect to the local orbital frame (sequence 3-1-2). As expected the *Main* spacecraft is aligned with the local orbital frame. Small randomly distributed spikes affect the estimated attitude of *Main* (about  $< 0.05^\circ$ ), but are not visible in the provided axes scale. After the activation of the delta-v attitude guidance function on *Main* at approximately 5 hours, larger rotations around all axes are executed in concurrence with orbit maneuvers. The *Target* attitude is also roughly aligned with the orbital frame with periodic oscillations of  $\pm 20^\circ$  in yaw and  $\pm 5^\circ$  in pitch/roll.

The GPS antennas on *Main* and *Target* are not located at the spacecraft center of mass, thus attitude estimation errors translate directly to relative navigation errors of the EKF in GOD. Here the attitude errors are comparable with the ones obtained in previous tests (Section 5.2). Of particular relevance are the *Target* attitude estimation errors which are characterized by oscillations with amplitudes of about  $2^\circ$  around all axes. This uncertainty affects the GPS-based

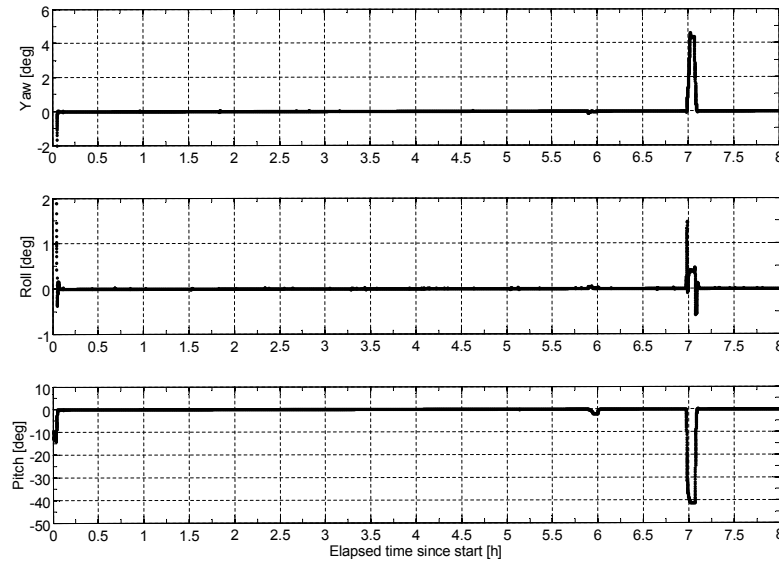


**Fig. 5.21:** Estimated attitude motion of *Main* with respect to the orbital frame. The adopted 3-1-2 Euler angles parameterization corresponds to rotations about the radial (yaw, top), along-track (roll, middle) and cross-track (pitch, bottom) directions respectively. Positive yaw, roll and pitch angles are clockwise around the respective axes.

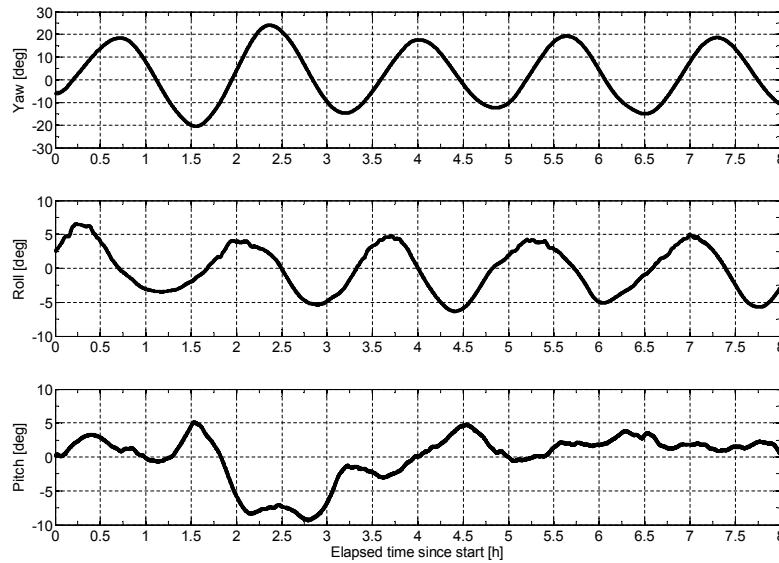


**Fig. 5.22:** Estimated attitude motion of *Target* with respect to the orbital frame. The adopted 3-1-2 Euler angles parameterization corresponds to rotations about the radial (yaw, top), along-track (roll, middle) and cross-track (pitch, bottom) directions respectively. Positive yaw, roll and pitch angles are clockwise around the respective axes.

navigation accuracy by approximately 1 cm.

### Flight Software Status

Each flight software module produces as output a status byte containing flags for telemetry monitoring and FDIR support (cf. Table 4.10). Fig. 5.23 il-

illustrates the most relevant flags delivered by the OBS during the 8 hours HIL system test. Each row of subplots refers to a different software module, from top to bottom: GIF for *Main*, GIF for *Target*, GOD, GOP and AFC.

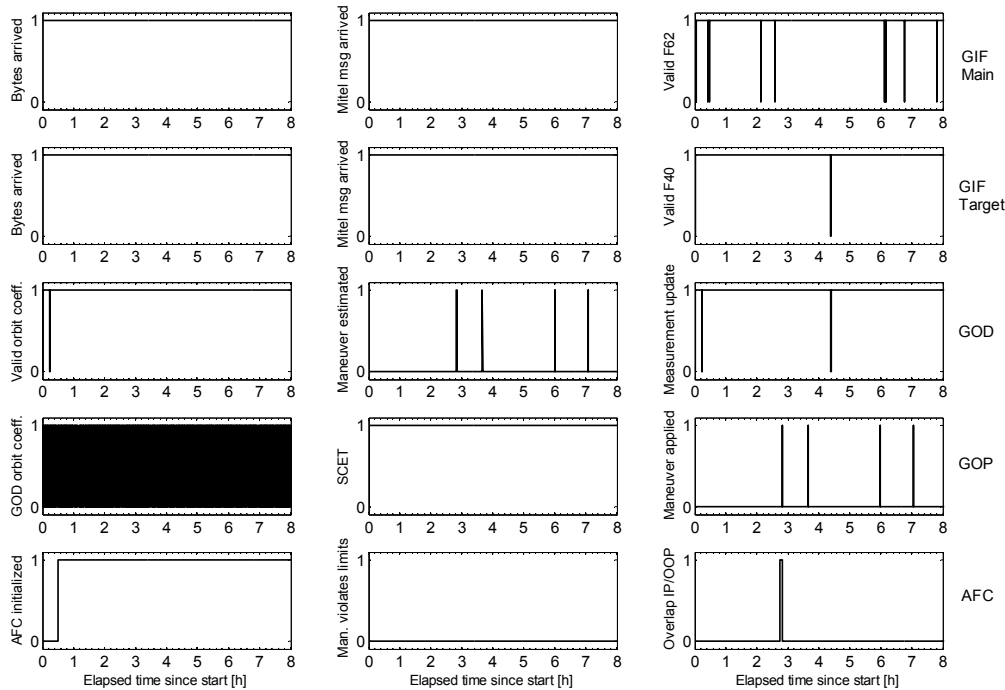


**Fig. 5.23:** Relevant flight software status flags during the HIL integrated system test. Each row of subplots refers to a different software module, in order from top: GIF for *Main*, GIF for *Target*, GOD, GOP and AFC (see text for details).

The GIF status is nominal, bytes and Mitel messages from the Phoenix-S receivers on *Main* and *Target* are never older than 30s during the simulation (top left and top middle subplots). In several occasions the F62 messages (GPS raw data) are flagged as invalid by GIF (top right subplot) while, at the same time, valid F40 messages (navigation solutions) are received. This phenomenon affects only *Main* data and is caused by spurious communication delays ( $> 15$  s) in the delivery of *Main* F62 data. In one occasion the *Target* navigation solution is flagged as not valid by GIF (GIF for *Target*, right subplot).

According to the design of GOD, the navigation filter is initialized as soon as valid navigation solutions from *Main* and *Target* are received simultaneously. In this specific operational case, GOD is initialized in a relatively early stage during the convergence phase of the attitude estimation filter on *Main* (cf. first minutes in Fig. 5.21). In order to reduce the consequent sub-optimal convergence time (about 1 hour vs. typically 10 minutes), the GOD filter is re-initialized via TC from ground. This is indicated by the GOD status flag 'Valid orbit coeff' which is always set to invalid before a GOD re-initialization (GOD left subplot). Maneuvers are incorporated by GOD four times, in accordance with the commands issued by AFC (GOD middle subplot). No measurement update is performed by GOD in two occasions. First when GOD is re-initialized

at about 15 minutes from start (cf. GOD logic in Fig. 4.7). Later at 4.4 hours from start when no valid navigation solution is available from *Target* (GOD right subplot). In particular GOD performs a measurement update only if synchronous measurements from *Main* and *Target* are available. This pass criterion for the execution of the measurement update is quite conservative and is equivalent to a request of navigation fix on both spacecraft. In fact as soon as less than four GPS satellites are tracked, the receiver time drifts and is not aligned anymore to integer seconds.

The GOP status byte shows that new orbit coefficients are regularly provided by GOD at 30 s intervals and replaced internally by GOP. The input SCET time is always within the validity interval of the orbit polynomials (GOP middle subplot), and the maneuver delta- $v$ 's are applied by GOP in parallel with the GOD processing (cf. GOP right subplot).

Finally nominal operations of AFC are illustrated by the last status flags (bottom subplots). AFC is first initialized around 0.5 hours from start. The commanded maneuver sizes are always within the thresholds prescribed via TC. Note that the first in-plane and out-of-plane orbit control maneuvers overlap (indicated by the flag 'Overlap IP/OOP' in bottom right subplot). In this occasion, simultaneous corrections of the relative eccentricity and inclination vectors are applied through combined thrusts with in-plane and out-of-plane components.

### Guidance and Control Results

Fig. 5.24 depicts the AFC controller mode during the HIL integrated system test. As prescribed via time-tagged commands, AFC is first operated in open-loop mode until 1.5 hours from start. Next the closed-loop activities are triggered with radial submode for the rest of the real-time simulation. The relative orbital elements are computed as part of the guidance process and illustrated in Fig. 5.25.

The match between desired (cf. Config. 1 in Table 5.3) and actual relative orbital elements is within the prescribed control windows. A total of 2 pairs of in-plane maneuvers and 2 out-of-plane maneuvers are issued by AFC to maintain the nominal formation geometry as required from ground. The in-plane and out-of-plane maneuver counters are shown in fig. 5.26.

Finally the relative orbit control errors, or control tracking error, are computed by subtracting the actual relative motion of *Main* with respect to *Target* from the desired relative motion as described by the selected nominal relative orbital elements. As shown in Fig. 5.27, the relative position control errors stay below 2.5/10.0/1.5 m in radial, along-track and cross-track directions respectively.

A critical aspect of the integrated system test is the verification of the closed-loop activities with GPS hardware in the loop. Relative orbit control maneuvers are requested by AFC in the form of impulsive velocity variations in the orbital frame centered on *Main*. The time and delta- $v$  size information is used by auxiliary functions in the GNC core to send commands to the thrusters in terms of burn start time and duration for each thruster to be used. The delta- $v$  atti-



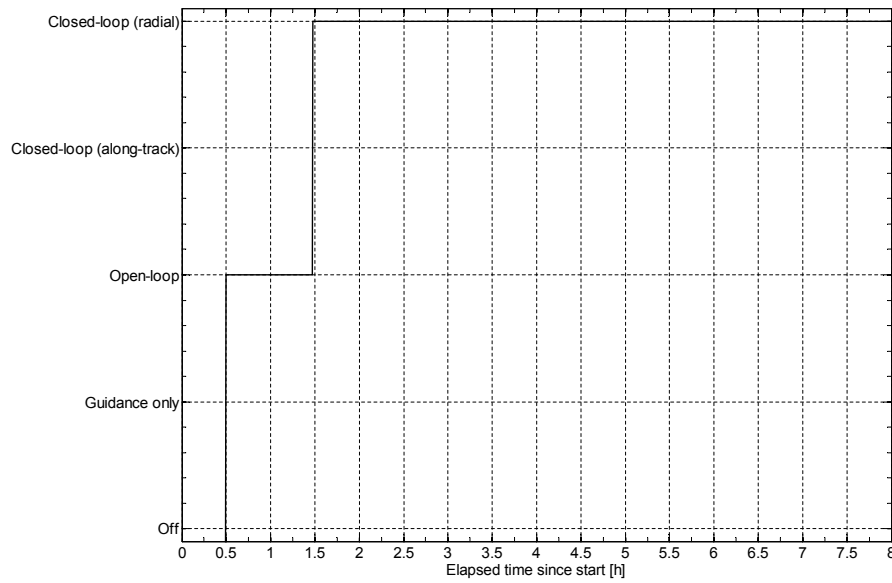


**Fig. 5.24:** AFC controller mode during the SATLAB test. AFC is first operated in open-loop mode until 1.5 hours from start. Next the closed-loop activities are triggered with radial sub-mode for approximately 6.5 hours.

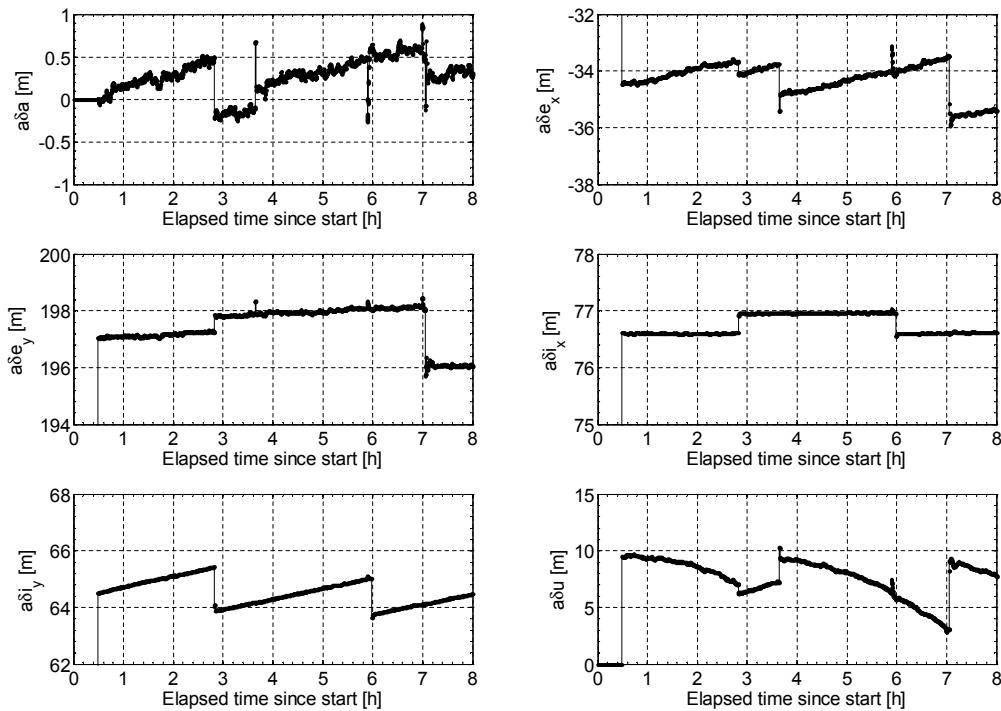


**Fig. 5.25:** Estimated relative orbital elements computed by AFC during the guidance process. The relative orbital elements are maintained close to the commanded nominal values listed in Table 5.3 (Config. 1).

tude guidance is only enabled at 5 hours from start. Thus the AOCS performs a re-orientation of the spacecraft at the occurrence of the last two maneuvers

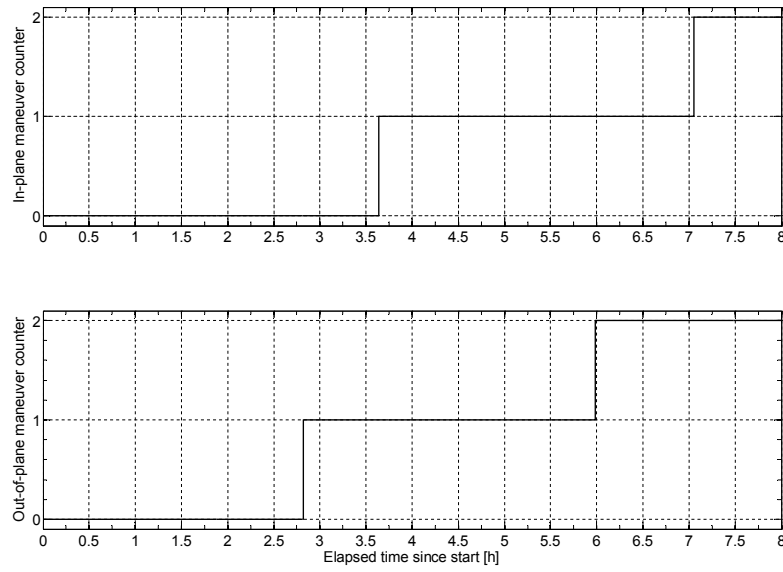


**Fig. 5.26:** In-plane (top) and out-of-plane (bottom) maneuver counter computed by AFC during the integrated HIL system test. The number of in-plane formation keeping maneuvers indicates a total of two maneuver pairs. The total number of out-of-plane formation keeping maneuvers is two.

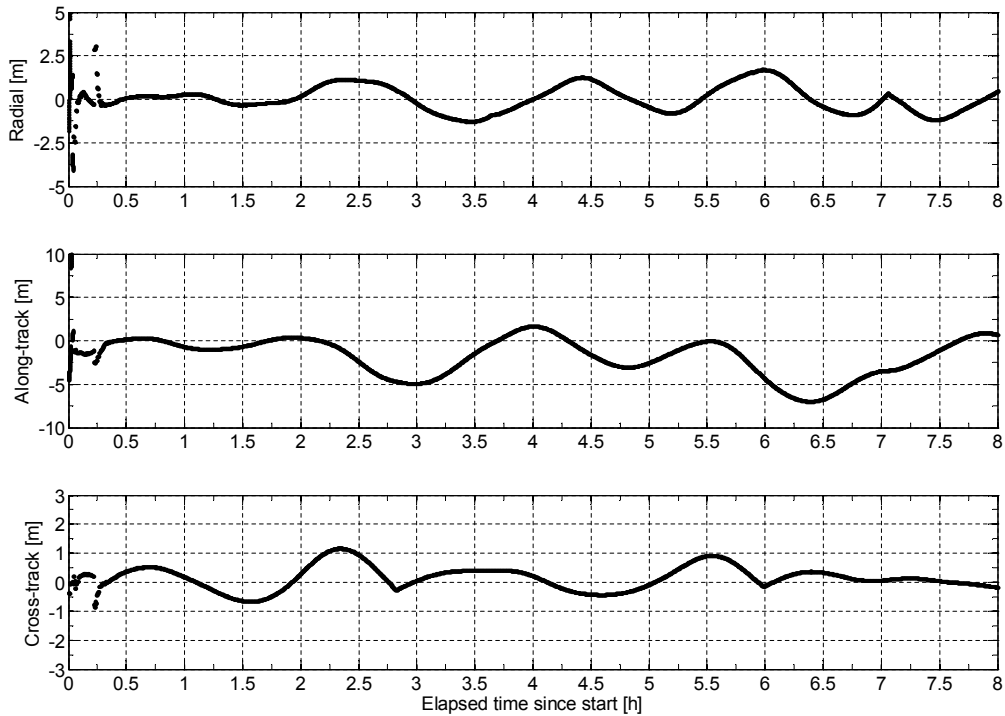


**Fig. 5.27:** Control tracking error mapped into the orbital frame aligned with the radial (top), along-track (middle) and cross-track (bottom) directions.

only. The maneuver induced accelerations are measured by the accelerometers on-board *Main*. These measurements are conditioned, filtered and used to compute equivalent impulsive velocity variations for each second of thrust. The

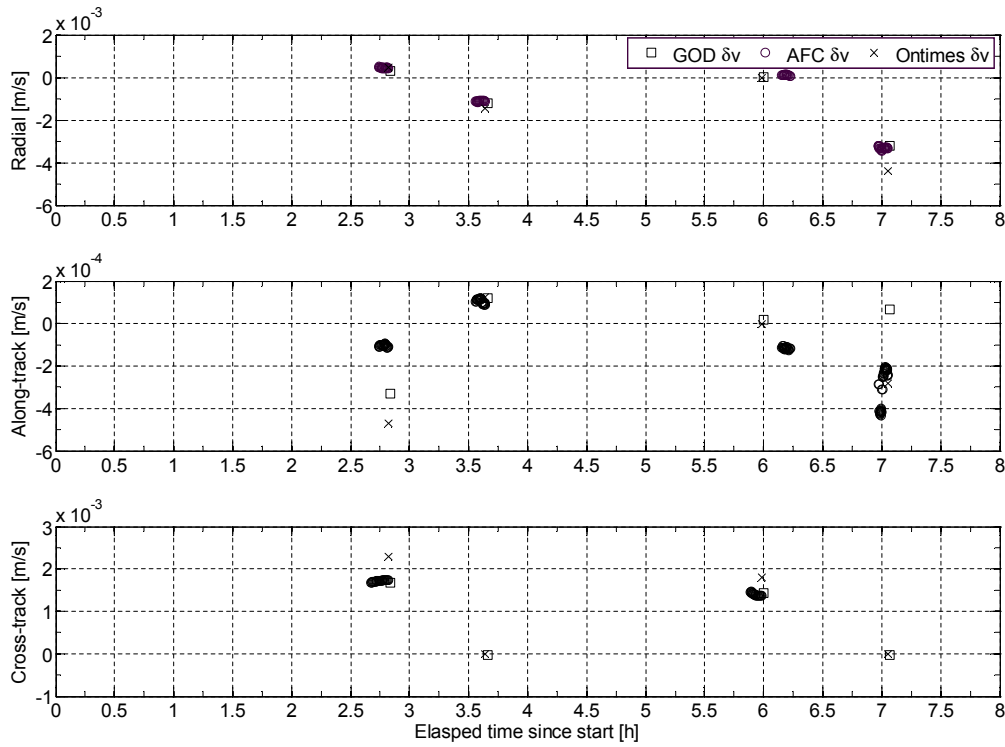


**Fig. 5.28:** Radial (top), along-track (middle) and cross-track (bottom) maneuvers requested by AFC (circles), realized by the hydrazine thrusters (crosses) and estimated by GOD (squares) during the HIL integrated system test.

a-priori measured delta-v information and time are provided to GOD and GOP for incorporation in the navigation process. Fig. 5.28 shows the AFC maneuver requests (circles), the actual thruster on-times converted to delta-v's (crosses) and the GOD maneuver estimates (squares).

The maneuver on-times are converted to delta-v's (nominal thrust of 1 N is applied) and mapped to the orbital frame by taking into account the true *Main* attitude and the thruster orientation. The mismatch between AFC requests and realized thruster activations is typically confined below 5% of the actually applied delta-v. The error introduced by the accelerometers is usually better than 3% for the small maneuvers executed in this test. The correspondence between GOD estimates and thrusters activations is better than 30%. It can be noticed that the delta-v attitude guidance has a detrimental effect on the performance of the GOD maneuver estimation. In particular the re-orientations of the *Main* spacecraft induce a reduction of commonly visible satellites and a degradation of PDOP. Furthermore the larger absolute position errors affect the AFC maneuver planning process in the computation of the maneuver location and size. This is especially visible in the large variations of the a-priori along-track delta-v computed by AFC in the last maneuver depicted in Fig. 5.28.

### Navigation Results

The accuracy of the navigation filter is evaluated as usual. The navigation

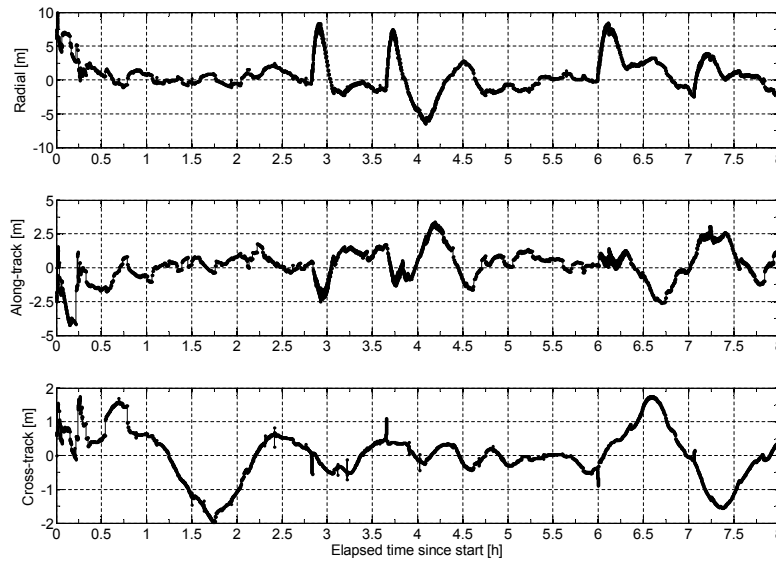


**Fig. 5.29:** Absolute *Main* position error mapped into the orbital frame aligned with the radial (top), along-track (middle) and cross-track (bottom) directions. Statistics computed excluding the convergence phase of the EKF provides an absolute navigation accuracy of 2.68 m (3D, RMS).

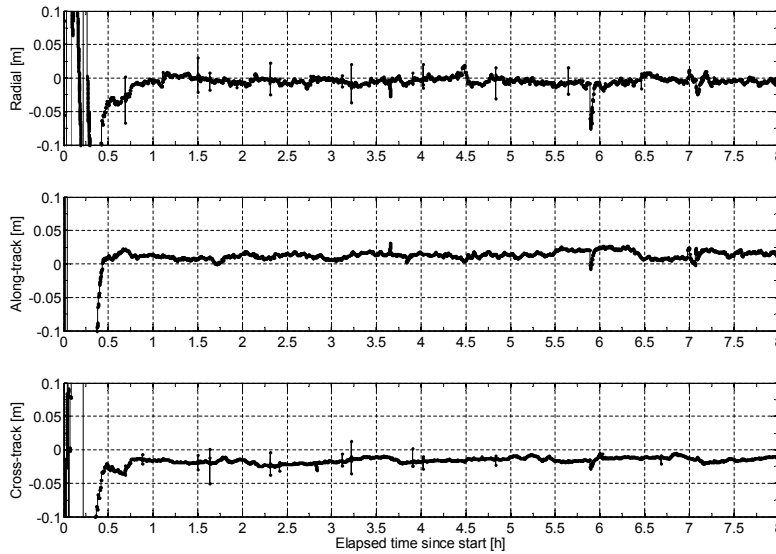


**Fig. 5.30:** Relative position error (i.e., *Main* with respect to *Target*) mapped into the orbital frame aligned with the radial (top), along-track (middle) and cross-track (bottom) directions. Statistics computed excluding the convergence phase of the EKF provides a relative navigation accuracy of 2.25 cm (3D, RMS).

errors are computed by subtracting the position and velocity of the *Main* and *Target* spacecraft provided by GOP from the true reference trajectory logged from the GPS signal simulator in the ECEF reference frame at 1 s samples.

The absolute and relative navigation errors are then mapped in the orbital frame and plotted in Figs. 5.29-5.32. Upon filter convergence, the obtained abso-

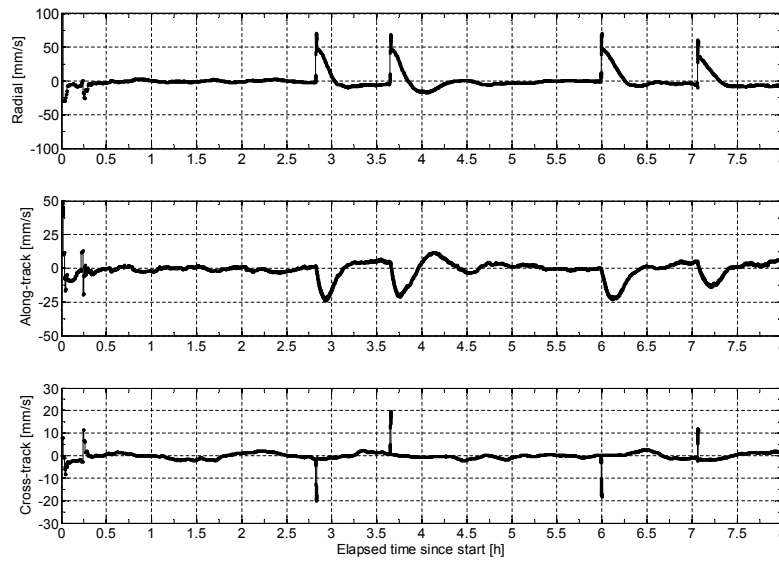


**Fig. 5.31:** Absolute *Main* velocity error mapped into the orbital frame aligned with the radial (top), along-track (middle) and cross-track (bottom) directions. Statistics computed excluding the convergence phase of the EKF provides an accuracy of 1.35 cm/s (3D, RMS).

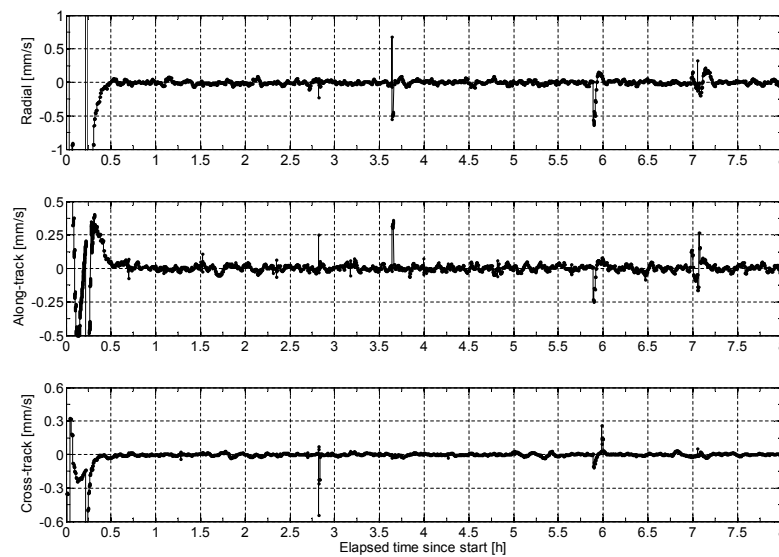


**Fig. 5.32:** Relative velocity error (i.e., *Main* with respect to *Target*) mapped into the orbital frame aligned with the radial (top), along-track (middle) and cross-track (bottom) directions. Statistics computed excluding the convergence phase of the EKF provides an accuracy of 0.06 mm/s (3D, RMS).

lute and relative navigation accuracy for the position is 2.68 m and 2.25 cm (3D, RMS) respectively (cf. Figs. 5.29 and 5.30). Compared to the closed-loop test case addressed in Section 5.2, the absolute and relative position errors show a better performance. The absolute navigation is affected by lower broadcast ephemeris errors, while the relative navigation profits from the temporarily disabled delta-v attitude guidance function.

The absolute and relative velocity are affected by errors of 1.35 cm/s and 0.06 mm/s (3D, RMS) respectively (cf. Figs. 5.31 and 5.32). The error trend is similar to what was obtained in the previous tests. At the instance of an orbit control maneuver the absolute velocity errors increase to values of several tens of mm/s which are then slowly re-absorbed by the EKF thanks to the collection of new GPS measurements.

### Flight Software Timeliness

As for the previous SATLAB test, time measurements are performed on-board during the OBS execution and logged as part of the telemetry stream. Fig. 5.33 shows such measurements during the complete 8 hours HIL integrated system test.

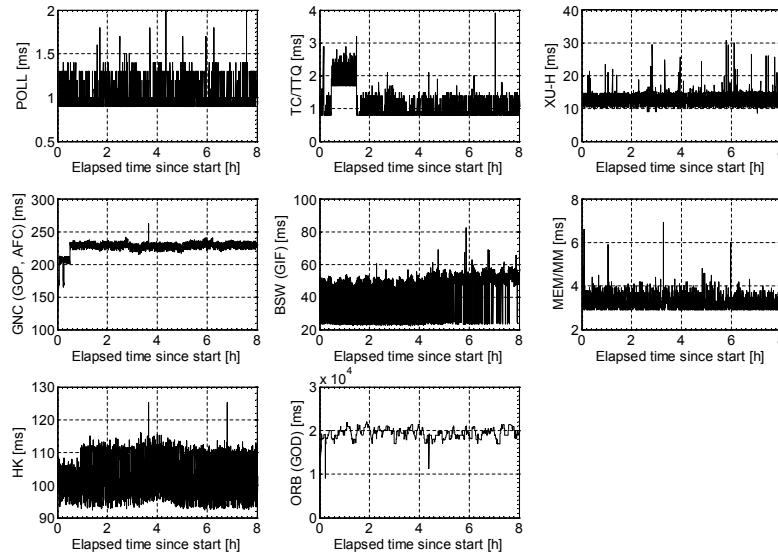


**Fig. 5.33:** Time measurements from the *Main* on-board computer during the SATLAB test. The subplots show the duration of the I/O and busy-wait polling (POLL, up-left), TC and time-tagged TC Queue (TC/TTQ, up-mid), BSW high priority (XUH, up-right), GNC/AOCS core (GNC, mid-left), BSW low priority (BSW, mid-mid), Memory management and mass memory (MEM/MM, mid-right), House Keeping TM (HK, bottom-left) and ORB core (ORB, bottom-right) tasks.

Normally the BSW total execution times, driven by GIF, lie between about 20 and 60 ms. The GNC task has an average execution time of about 230 ms. The most demanding ORB task has an average total execution time of about 20 s. The total execution time of GOD drops to about 10 s in two occasions when no measurement update is performed. Considering the given measures and the accumulated time for higher-priority tasks, the average ORB core CPU load during the test is approximately 30%. This figure is in accordance with the max-path unit tests described in Section 4.5.2. It is noteworthy that the execution time of GIF and GOD is always below its sample time and consequently ensures a proper execution of the navigation process.

### 5.3.3 PRISMA Spacecraft Separation Sequence

The *Main* and *Target* spacecraft are clamped in a single combined unit (cf. Fig. 1.2) after the separation from the launcher. This configuration is held for a time frame of approximately 25 days during which early operations are performed aiming at the activation and health check of the various spacecraft units. The GPS hardware on both spacecraft will be switched on and verified during this phase. Furthermore the ISL will be activated and will allow the transmission of GPS measurements from *Target* to *Main* for a zero-baseline verification of the GPS-based navigation system. Only afterward *Target* will be released from *Main* on ground command by firing one of the two redundant wire cutters of the separation mechanism. The challenge of the subsequent early proximity operations phase is to maintain the formation safety and in particular minimize the risk of collision by making use of a reduced subset of the overall guidance, navigation and control functionalities available on the two spacecraft. Although the GPS system has not been designed specifically to support safe mode activities, it is considered the best candidate to support fault detection, isolation and recovery tasks during this formation flying configuration due to its inherent versatility and robustness. This section provides an overview of the simulation scenario and addresses the verification of the on-board navigation software during the separation sequence of the PRISMA formation. The following HIL integrated test demonstrates the robust operation of the GPS navigation system under the adverse conditions of the separation event and the subsequent non-nominal spacecraft attitude.

#### Test Specification

In the frame of the GNC system functional and performance validation campaign, a dedicated HIL scenario has been defined to assess the behavior of the GPS-based navigation system during the separation sequence of the PRISMA formation. The scenario defines a specific timeline for the separation sequence and emulates the realistic orbital and attitude motion of the spacecraft. After the separation from the launcher, *Main* and *Target* are clamped to each other forming the so-called COMBINE configuration. This configuration is held for a time frame of approximately 25 days after which *Target* will be released from *Main* via a time-tagged command. Because of practical constraints, the real-time simulation covers a time interval of about 8.5 hours and starts approximately 30 minutes before the separation event.

The true *Main* and *Target* translational and rotational motion is obtained through the numerical integration of the equations of motions in the SATLAB real-time simulator (xPC Target) as already described in Section 5.2.1. Table 5.7 lists the initial ECI state for the *Main* spacecraft. It represents a Sun-synchronous polar orbit with an ascending node near 6 PM (dusk-dawn orbit). In the COMBINE configuration *Target* is modeled with half a meter *Main* attitude dependent offset. Thus the initial orbits of *Main* and *Target* are almost identical at start time. Before separation, *Main* is turned from having *Target* ahead in along-track, to a separation attitude almost perpendicular to the orbital plane. As *Main* is

**Table 5.7:** Initial *Main* and *Target* spacecraft orbits.

Initial time		Value
Epoch (GPS time in CUC) [s]		933163200
GPS-UTC [s]		14.0
UT1-UTC [s]		0.193134
State vector (EME2000)		<i>Main</i> value
Position [m]	$x$	4920670.204
	$y$	3461284.366
	$z$	3715690.318
Velocity [m/s]	$v_x$	-2458.46373
	$v_y$	-3266.40702
	$v_z$	6300.52503

moving toward the sun, relative to *Target*, there will be good lighting condition to document the event with the Digital Video System on *Main*. The separation of *Target* from *Main* is performed through a ground command by firing one of two redundant wire cutters. The event is modeled as an instantaneous velocity variation for the *Main* and *Target* spacecraft. An additional impulsive maneuver is performed by *Main* 1.5 orbital revolutions after separation to cancel out the along-track drift and consequently stop the increase of along-track separation from *Target*.

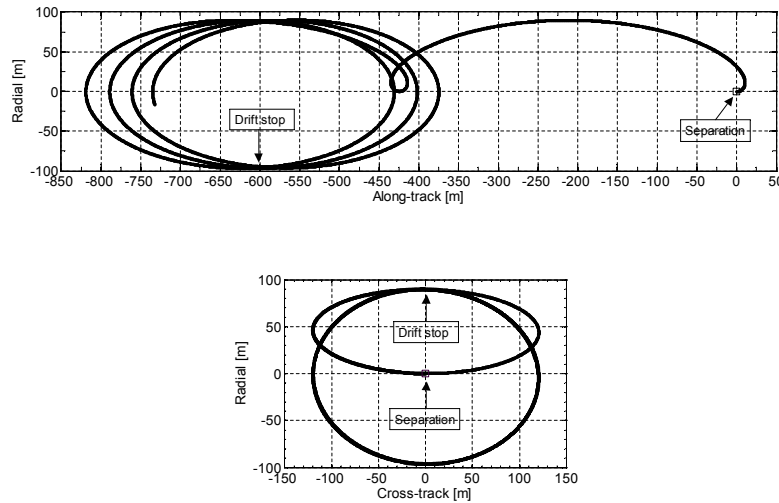


**Fig. 5.34:** Actual relative motion of *Main* w.r.t. *Target* projected onto the along-track/radial (top) and radial/cross-track (bottom) local planes. Separation and drift stop events are indicated in the plots.

The resulting relative motion of the *Main* spacecraft with respect to *Target* is depicted in Fig. 5.34. It may be recognized that the ejection of *Target* instantaneously changes the orbital planes of both spacecraft and results in a periodic cross-track separation of about 120 m amplitude. At the same time, the along-track velocity change modifies the relative semi-major axis by 41 m, which results in mean along-track drift of about 400 m per revolution. When the drift is



ultimately stopped by *Main* after 1.5 orbits, the spacecraft are sufficiently well separated in along-track distance. Furthermore, a high level of passive collision avoidance is achieved through the adopted phasing of the relative eccentricity and inclination vectors (cf. Section 2.2) after the drift stop maneuver. It results in an elliptic relative motion in cross-track and radial direction and ensures a minimum separation of about 90 m at all times. Potential uncertainties in the knowledge of the along-track separation that might be caused by thruster performance errors or differential drag will therefore have no impact on safety of the initial PRISMA formation.

### Navigation Software Settings

Table 5.8 lists the relevant TC parameters and the correspondening values used to control the execution of the GPS-based Orbit Determination (GOD) software during the separation sequence test. Compared to the settings applied in previous simulations, here the only differences are given by a larger measurement standard deviation for the pseudorange (i.e.,  $\sigma_{PR} = 2.0$  m) and a larger a-priori standard deviation for the GRAPHIC biases (i.e.,  $\sigma_N = 10.0$  m).

**Table 5.8:** Settings of the EKF used by GOD during the HIL integrated separation sequence test.

Parameter	Value	Parameter	Value
<i>A-priori standard deviation</i>		<i>Process noise</i>	
$\sigma_r$ [m]	1000.0	$\sigma_{ar}$ [nm/s <sup>2</sup> ]	50.0
$\sigma_v$ [m/s]	1.0	$\sigma_{at}$ [nm/s <sup>2</sup> ]	30.0
$\sigma_{C_D}$	1.0	$\sigma_{an}$ [nm/s <sup>2</sup> ]	10.0
$\sigma_{ar}$ [nm/s <sup>2</sup> ]	500.0	$\sigma_{c\delta t}$ [m]	500.0
$\sigma_{at}$ [nm/s <sup>2</sup> ]	300.0	<i>Measurements standard deviation</i>	
$\sigma_{an}$ [nm/s <sup>2</sup> ]	100.0		
$\sigma_{c\delta t}$ [m]	500.0		
$\sigma_N$ [m]	10.0	$\sigma_{PR}$ [m]	2.0
<i>Auto-correlation time scale</i>		$\sigma_{CP}$ [mm]	2.0
		<i>Maneuver parameters</i>	
$\tau_a$ [s]	900.0	$\sigma_{\delta v}$ [%]	30.0
$\tau_{c\delta t}$ [s]	100.0		

These values are the result of a dedicated tuning which has been performed to find the best trade-off between relative navigation accuracy and realistic formal covariance of the EKF during attitude tumbling phases. In general, it can be shown that the settings providing the minimum relative position errors do not correspond to the ones providing the most realistic covariance of the filter, especially during the execution of attitude and orbit maneuvers. This partial inconsistency is mainly due to the processing, in a single filter, of data types characterized by different systematic errors (i.e., GRAPHIC and single-difference carrier-phase measurements), but can be neglected during nominal and safe mission phases. On the contrary, this aspect has to be carefully taken into account when dealing with risky operational scenarios like the PRISMA spacecraft separation sequence. In particular the highest priority during this phase is

the provision of a reliable navigation information (i.e., consistent relative state and expected accuracy), rather than the availability of a true relative position with uncertain accuracy.

It has to be noted that, by design, GOD incorporates only maneuvers executed by the *Main* spacecraft in the navigation process. The inclusion and estimation of these maneuvers requires the a-priori knowledge of the equivalent impulsive velocity variations imparted to the *Main* spacecraft. The separation event of *Target* from *Main* represents the only occasion in the *Target* operational life after orbit injection where an impulsive maneuver is applied to the spacecraft. This information is not provided to the navigation modules during the test, which take into account only coarse a-priori information relative to the *Main* spacecraft. For completeness, the total delta-v imparted by the separation mechanism is given by  $\delta v_n \approx -8.4 \text{ cm/s}$  and  $\delta v_t \approx 1.8 \text{ cm/s}$ . While the drift stop maneuver amounts to  $\delta v_t \approx -2.1 \text{ cm/s}$ .

### Estimated Attitude

Prior to the *Target* separation, PRISMA maintains a Sun/Zenith orientation. Here, the solar panels face the Sun and the *Main* orientation is optimized to ensure a good GPS visibility. Due to the choice of a dusk-dawn orbit, the spacecraft body axes remain roughly aligned with the radial, along-track and cross-track direction at all times. The active GPS antennas on *Main* and *Target* deviate by less than  $30^\circ$  from the zenith direction in the COMBINE configuration before separation. This gives a good sky visibility during the initialization and check-out of the GPS system.

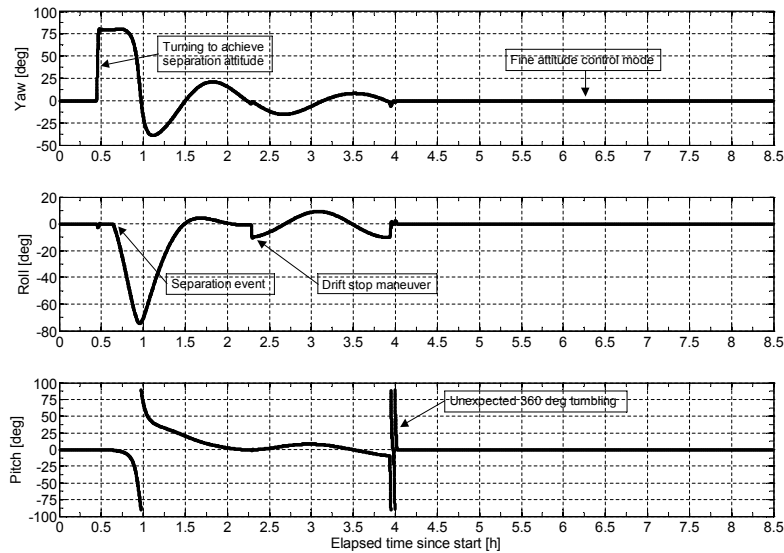


**Fig. 5.35:** Estimated attitude motion of *Main* with respect to the orbital frame. The adopted 3-1-2 Euler angles parameterization corresponds to rotations about the radial (yaw, top), along-track (roll, middle) and cross-track (pitch, bottom) directions respectively. Positive yaw, roll and pitch angles are clockwise around the respective axes. The main events during the separation sequence timeline are indicated in the plots.

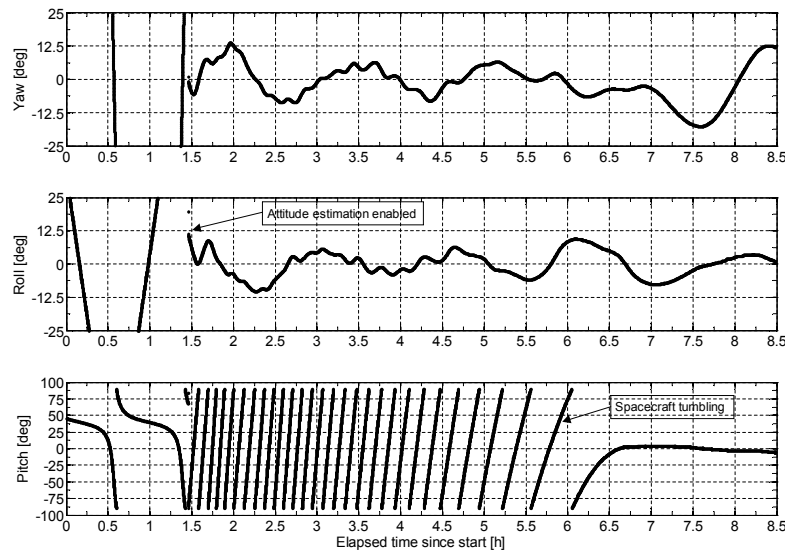


**Fig. 5.36:** Estimated attitude motion of *Target* with respect to the orbital frame. The adopted 3-1-2 Euler angles parameterization corresponds to rotations about the radial (yaw, top), along-track (roll, middle) and cross-track (pitch, bottom) directions respectively. Positive yaw, roll and pitch angles are clockwise around the respective axes. The main events during the separation sequence timeline are indicated in the plots.

Figures 5.35 and 5.36 show the attitude estimated on-board *Main* and *Target* during the separation sequence. After release from *Main*, the *Target* spacecraft starts tumbling with angular velocities up to 2 deg/s around an axis normal to the separation direction. *Target* then starts acquiring the desired Sun pointing orientation. Once it has been reached (within less than half an orbit), the attitude estimation function is enabled and *Target* keeps on tumbling around the Sun direction with a rate of about 7 rev/orbit. Indeed, the *Target* attitude control is only based on magnetic control, and this low tumbling motion provides a gyroscopic stiffness and ensures the spacecraft safety in Sun Acquisition and Safe Mode [Camille et al., 2007]. The spacecraft stays in this mode for a few orbits before it switches to a Sun/Zenith reference attitude.

The *Main* spacecraft attitude is *Target*/Sun pointing, and performs half a rotation around the orbit normal within one hour after separation. The fine attitude control mode, based on star tracker measurements, is entered at about 4 hours from start (cf. Fig. 5.35). Note that the *Main* transition from coarse to fine AOCS mode is affected by a contingency with an unexpected spacecraft tumbling (i.e., full 360° pitch rotation) due to the upload of wrong TCs to the spacecraft. Automatic switches of the GPS antennas are performed on *Main* and on *Target* during the separation sequence to use the unit with better GPS constellation visibility (i.e., unit antenna vector with positive radial coordinate). This functionality is always enabled on *Main*, but is only available after 1.5 hours from start on *Target*, as soon as the attitude estimation function is active.

### Flight Software Status

Figure 5.37 shows the status bytes (cf. Table 4.10) generated by the on-board

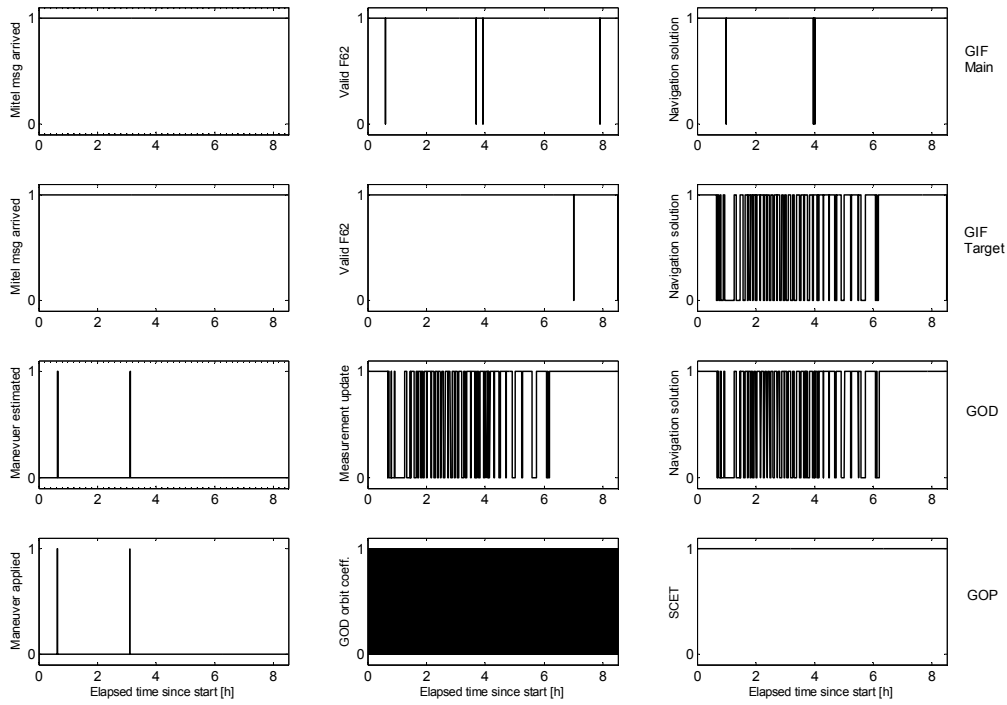


**Fig. 5.37:** Relevant flight software status flags during the HIL separation sequence test. Each row of subplots refers to a different software module, in order from top: GIF for *Main*, GIF for *Target*, GOD and GOP (see text for details).

navigation software during the HIL integrated separation sequence test (in order from top: GIF for *Main*, GIF for *Target*, GOD and GOP). Compared to previous tests, the key consideration here is that the GPS receiver on *Target* loses its navigation fix for a few minutes around pitch angles of  $\pm 90^\circ$  (i.e., when the GPS antennas are switched). As a consequence, no measurement update is performed by GOD at these occasions. Maneuvers are incorporated by GOD and GOP two times, in accordance with the delta-v's imparted by the separation mechanism and by the drift stop maneuver.

### Navigation Results

The behavior of the GPS navigation system during the separation sequence is strictly correlated with the attitude motion of the spacecraft (cf. Figs. 5.35 and 5.36). The orientation of the active GPS antennas on *Main* and *Target* drives the visibility condition of the GPS satellites. In particular Fig. 5.38 depicts the number of GPS satellites tracked by *Main* (top), by *Target* (middle) and by both spacecraft simultaneously (bottom) as computed by GIF. The visibility condition on *Main* is only degraded during two tumbling phases, namely after separation at 1 hour and 4 hours from simulation start. On the contrary, the number of satellites tracked by the Phoenix-S receiver on *Target*, and consequently the number of common visible satellites, drop to zero throughout the complete separation sequence (twice per spacecraft revolution).

As soon as no navigation fix is provided by one of the spacecraft, GOD does

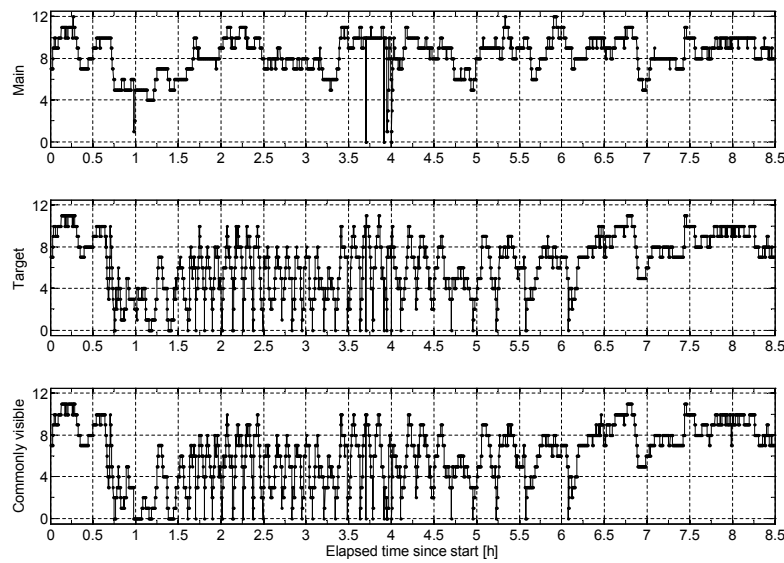


**Fig. 5.38:** Number of GPS satellites tracked by *Main* (top), by *Target* and commonly visible (bottom) as computed by GIF.

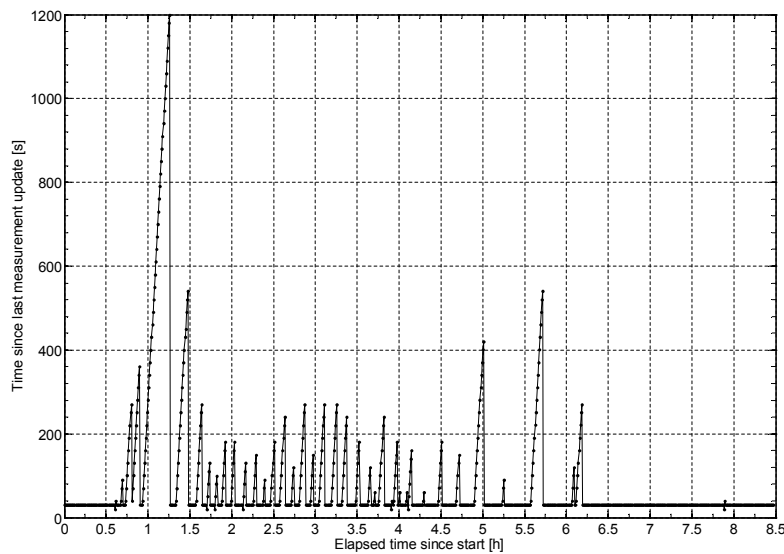


**Fig. 5.39:** Elapsed time since last EKF measurement update during the HIL separation sequence test.

not perform a measurement update. Consistently, the time elapsed since the last measurement update increases as illustrated in Fig. 5.39 at several occasions. The longest time-update only (or propagation only) phase of the EKF is shown to be 1200 s shortly after the separation of *Target* from *Main*. Here the *Target* spacecraft is tumbling and no attitude knowledge is available on-board, which is required to automatically switch the GPS antennas.

The relative position accuracy achieved during the complete separation sequence is shown in Fig. 5.40. The estimation errors are obtained by comparing the true trajectory logged from the GSS with the 1 Hz output of GOP. Overall the

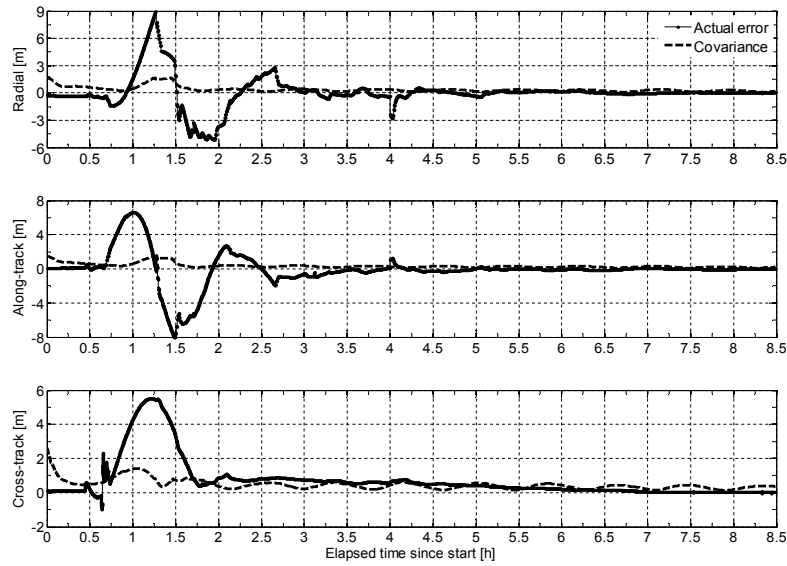


**Fig. 5.40:** Relative position error (i.e., *Main* with respect to *Target*) mapped into the orbital frame aligned with the radial (top), along-track (middle) and cross-track (bottom) directions. The maximum relative position error amounts to 10 m (3D, RMS).

navigation error behaves as expected. The relative position error before separation (not visible in the provided scale) is characterized by mean values which correspond to the *Target* GPS antenna offsets from the center of mass. Note that no *Target* attitude information is provided to GOD before separation. The relative position error has a peak of about 10 m after separation, which is due to the delta- $v$  at separation, to the spacecraft tumbling and to the missing attitude information on-board. It is then slowly re-absorbed and decreases to less than 0.5 m after 4 hours from start. The performance of the navigation system could be improved if GOD would perform a measurement update based on at least *Main* measurements, when no navigation solution is available from *Target*. The formal covariance of the EKF during the separation sequence is also depicted in Fig. 5.40. As expected the accuracy estimate is only able to reproduce the true error at steady state, while immediately after separation the uncertainty of the relative position can be a few meters off.

## 6. Conclusions

The main goal of this research was to design, implement and test an innovative GPS-based guidance, navigation and control system for dual-spacecraft formations in low Earth orbit. This dissertation has guided the reader through its key development and verification steps and, based on the results from the previous chapters, has demonstrated that this objective has been fulfilled. In particular, the direct outcome of the work documented here is a flight-ready spaceborne autonomous formation flying system which has been integrated into the PRISMA technology demonstration mission (SSC/SNSB) (Section 1.6.1). In order to put in evidence the underlying systems design approach, the research material has been presented in a step-wise way with a gradually increasing level of complexity and integration. A concise chapter-by-chapter summary of the main results obtained in the frame of this research is presented in the following.

### 6.1 Summary

The first chapter of this thesis addresses the demand of autonomous formation flying technology. An outlook at upcoming Earth's gravity field and synthetic aperture radar interferometry missions, or at even more advanced applications, like dual- and multi-spacecraft telescopes at high altitudes, demonstrates clearly the need for the deployment and on-orbit validation of such techniques which are nowadays characterized by a low level of technology readiness (Section 1.2). Section 1 identifies the main drivers and requirements for the design of a guidance, navigation and control system for remote sensing formations (Section 1.3). These are not only representative of PRISMA (Section 1.6.1) or, partially, of the TanDEM-X mission (Section 1.6.2), but find their applicability in a vast class of future formation-flying applications for Earth observation. The primary GNC goals are to provide a safe, collision-free guidance law, to implement a real-time navigation system capable of continuous absolute and relative position accuracies at 3 m and 0.2 m (3D, RMS) respectively, and to implement a robust control algorithm for formation keeping with an accuracy of 30 m (3D, RMS).

The second and third chapters addresses the preliminary design of the guidance, navigation and control algorithms through a detailed mathematical description and a preliminary numerical validation of the presented techniques. The resulting contributions to the body of knowledge are manifold and, as re-proposed in the sequel, influence mainly the areas of impulsive relative orbit control and combined GPS-based absolute/relative navigation. Section 2 investigates a formation-flying concept able to realize the demanding baselines for aperture synthesis, while minimizing the collision hazard associated with prox-

imity operations. An elegant formulation of the linearized equations of relative motion is derived, discussed and adopted for satellite formation design (Section 2.1). The concept of eccentricity/inclination-vector separation, originally developed for geostationary satellites, has been successfully extended to LEO formations. It provides immediate insight into key aspects of the relative motion and is particularly useful for orbit control purposes and proximity analysis (Section 2.2). The effects of the relevant differential perturbations acting on an initial nominal configuration have been presented (Section 2.3), and a fuel-efficient orbit control strategy has been designed to maintain and reconfigure the formation geometry (Section 2.4). In a preliminary validation effort, the method is applied to the PRISMA formation and basic software simulations show clearly the simplicity, effectiveness but also the envisioned accuracy limitations of the formation-flying concept (Section 2.4.7).

The determination of the relative motion between individual satellites in near real-time is fundamental to the proposed autonomous formation guidance and control. In particular differential GPS represents an ideal sensor in LEO, which can be used to directly measure the relative positions and velocities to a high level of accuracy at low costs. Section 3 presents the trade-off design of an accurate and robust GPS-based navigation system in terms of filter structure, adopted measurements, state parameters and dynamics modeling. In parallel with the navigation design, the adopted decision matrix approach offers a general review of possible techniques to absolute and relative navigation (Section 3.2.2). In particular, raw measurements of carrier phase and pseudorange from two or more user spacecraft made to common GPS satellites in the constellation can be subtracted from each other to reduce systematic errors. Compared to typical raw measurements, differenced GPS observation data have a high level of common error cancellation and, as a consequence, are less sensitive to GPS satellite clock offsets, GPS broadcast ephemeris errors, ionospheric refraction, and biases due to hardware delays. A fundamental characteristic of the adopted integrated filter design is the determination of the absolute states of the participating spacecraft through the processing of two different data types: un-differenced GRAPHIC measurements of the individual spacecraft as well as single-difference carrier-phase measurements. It has been shown that this approach has several advantages over classical navigation concepts available in literature. First of all, the full information content provided by the available measurements can be exploited to its largest extent. In fact no strict requirement on common GPS satellite visibility is necessary to provide relative state estimates. Secondly, the higher intrinsic accuracy of differenced carrier phase measurements provides an indirect advantage to the determination of the absolute states. Last but not least, initialization and maneuver handling of the combined filter design is much simplified if compared to split filters dedicated to the independent reconstruction of absolute and relative states. As done for the guidance and control tasks in the preceding chapter, Section 3.4 is devoted to a preliminary validation of the navigation process. In particular, dedicated open-loop and closed-loop tests show the basic compliance of the design to the



system functional and performance requirements in terms of navigation accuracy, incorporation of maneuvers and robustness to GPS data gaps. Pure numerical simulations are furthermore complemented by a real-world test using GPS and attitude flight data from the Gravity Recovery and Climate Experiment (GRACE) mission during the closest encounter of the twin satellites on December 10, 2005 (Section 3.4.3).

The GNC functions, separately addressed and unit tested in the first chapters, are merged into a comprehensive autonomous formation-flying system in Section 4. Here, an overview of the software and hardware architectural design has been provided with a focus on the novel model-based design approach. Each flight software module has been described in terms of functionalities, input/output interfaces, timeliness characteristics and internal processing schemes. Special attention has been given to two key aspects of the integrated system which are usually neglected in other studies: the support of on-board fault detection isolation and recovery functions and the maneuver incorporation within the navigation system. Error diagnostics are systematically generated by the GNC flight software in the form of status bytes which provide an overview of the current process status and eventual run-time errors. This valuable information can be used either on-board for automatic reactions to contingency situations or on-ground for an efficient and transparent monitoring of the GNC system during mission operations. A description of the maneuver incorporation process within the GPS-based Orbit Determination (GOD) and Prediction (GOP) functions has been provided in Section 4.4. Special attention has been given to a consistent assessment of the full maneuver handling chain. Thrust requests issued by the Autonomous Formation Control (AFC) software are executed by the propulsion system, in parallel dedicated accelerometer units measure the resulting velocity variations which are then conditioned, filtered and routed back to the GOP and GOD flight software modules for incorporation within the navigation system. The last part of Chapter 4 has been finally devoted to the verification of the real-time capability of the developed flight software prior to its full integration into the PRISMA on-board computer. In particular the GPS-based GNC modules have been embedded into a representative LEON-3 based on-board computer. Dedicated max-path unit tests have been conducted to assess the maximum computational effort of each software module and predict the expected on-board CPU load in worst case execution scenarios. The load estimates have been shown to be consistent with hardware-in-the-loop system level tests conducted on the actual on-board computer flight models at a later stage.

The ultimate functional and performance validation of the system once integrated into the PRISMA spacecraft in its flight configuration with hardware-in-the-loop (HIL) has been addressed in Section 5. A sophisticated formation flying testbed has been used to perform realistic closed-loop tests including the full uninterrupted end-to-end communication chain from the GPS sensors to the hydrazine thrusters (Section 5.3). To this end a 2x12 channels Spirent GPS signal simulator (GSS) has been used in-the-loop to generate single-frequency

GPS signals for two independent vehicles. The GSS provides the time reference for the complete SATellite LABoratory (SATLAB) facility at the Swedish Space Corporation (SSC) and is triggered in real-time by an xPC target simulator which models the translational and rotational motion of the participating spacecraft and all the satellite units which are not available in physical hardware (cf. Figure 5.20). Compared to the preliminary system validation discussed throughout the thesis, the final outcome of these integrated HIL tests is extremely valuable for various reasons. Most importantly, it has been possible to replace the Phoenix-S Emulation (PEM) software used so far with the space qualified flight model of the Phoenix-S based hardware. This has enabled the verification of functionalities which are not supported by PEM, and the simulation of the integrated GPS-based GNC system under conditions which can only be encountered on-orbit after the launch of the PRISMA mission. Among others, it has been possible to gain confidence with the data communication between GPS hardware and on-board computer, with the proper commanding of the GPS receiver either from ground or automatically on-board, with the proper GPS receiver operations through aided start-up procedures issued by the on-board software, with the robust operations of the navigation system during spacecraft tumbling through automatic switches of the GPS antennas in use, and with the overall response of the navigation system to orbit control maneuvers.

## 6.2 Navigation and Control Accuracy

Throughout the various sections of this thesis, special attention has been given to the assessment of the real-time navigation and control accuracy. Three important considerations can be done on this aspect.

First of all, the results obtained in numerous tests, conducted under different software development environments, on different computer platforms, and stimulated by various sources of input data (i.e., GPS and attitude estimation data) show a good overall consistency. In particular the level of realism of the test cases has been gradually increased. Initially, the GPS-based flight software was wrapped in Matlab S-Functions and embedded in Simulink models for software-only simulations. Here GPS data produced by a software emulator (PEM) or obtained from the GRACE mission have been used in a standalone environment at DLR on a standard Windows-based laptop PC (Section 3.4). Later, the overall application has been ported to a representative LEON-3 based platform under the RTEMS operating system to verify the reproducibility of the numerical results, the usage of memory and CPU resources (Section 4.5). In a final step, the GPS-based functions have been integrated into the PRISMA on-board software and tested in the spacecraft on-board computer as part of the SATLAB facility at SSC. Here, independently developed dynamic models, numerical integration algorithms, more realistic sensor and actuator emulators, as well as the actual AOCS software have been used. In a two stage process, the GPS measurements have been first generated like usual by PEM (Section 5.2),

and later replaced by the actual GPS hardware flight models (Section 5.3).

The second relevant consideration to be made is on the expected navigation accuracy and on the fulfillment of the prescribed requirements. As indicated by the numerous test campaigns, absolute real-time on-board positioning accuracies are expected to be around 3 m (3D, RMS) in the presence of thrust activities. The major difference in the evaluation of the absolute positioning errors has been observed when changing the settings for the broadcast ephemeris errors from a standard deviation of 1.5 m to 2.0 m. The latter value has been applied only in the formation flying rehearsal documented in Section 5.2, and has caused a consistent increase of the absolute navigation errors by about 0.5 m. Evidently, this result shows the main driver of the on-board absolute navigation accuracy. A possible mitigation strategy for this source of error is the provision to the spacecraft of GPS orbit and clock data which are more precise of the standard broadcast ephemeris available in the GPS data stream [IGSCB, Last accessed: June 2008]. Operational limitations related to the TM/TC data rate budget and to the visibility of the formation from ground have to be carefully considered in this case.

The relative navigation accuracy depends critically on the attitude profile during specific mission phases and may range from a worst case accuracy of around 0.5 m if the GPS antennas of *Main* and *Target* point in different directions (cf. steady state results in Section 5.3.3) down to a few cm if a sufficient number of common GPS satellites is tracked by the two spacecraft (cf. Section 5.3.2). In the latter case the accuracy is limited by the restricted attitude knowledge of the *Target* spacecraft and the lacking knowledge of GPS antenna phase pattern variations in the spacecraft environment. If ultimate real-time relative positioning accuracy (at the millimeter level) is required, then accurate attitude knowledge shall be available on both spacecraft (e.g., through the adoption of star trackers), so to enable real-time integer ambiguity resolution like demonstrated in [Leung, 2003]. In this case, special care shall be given to a robust and reliable resolution of the integer ambiguities and to its impact on the real-time capabilities of the navigation system, especially in terms of memory usage and CPU load.

The third aspect to be considered is the expected relative orbit control accuracy. As first identified during the numerical validation of the relative motion model developed in this thesis (Section 2.3.4), an impulsive analytical feedback orbit control law based on the proposed linear solution can not be more accurate than a few meters (cf. Figure 2.8). Rigorous numerical simulations under ideal conditions (i.e., excluding sensor and actuator errors) conducted in Section 2.4.7 confirms this finding and shows how the relative orbital elements can be confined within prescribed control windows of about 2 m for the relative eccentricity and inclination vectors and 20 m for the relative mean argument of latitude. These results are basically confirmed by more realistic test cases which include the GPS-based navigation system as well as models for the propulsion system and accelerometers. The most realistic assessment of the control tracking errors has been depicted in Figures 3.12 and 5.11. It shows full compliance

to the requirements with maximum errors during formation keeping phases of 5.0/25.0/2.5 m in radial, along-track and cross-track directions respectively. Overall the obtainable control accuracy is driven by the impulsive feedback algorithm itself, which relies on pairs of maneuvers separated by half an orbital revolution, rather than sensor and actuator errors. The relative motion in between these maneuvers is then mainly governed by the natural orbit perturbations (especially differential gravity and differential drag). The resulting control system design can be considered as an optimal choice in view of the prescribed objectives. In fact, it provides the desired control accuracy through a minimum number of thrust activations, a reduced propellant consumption, minimum collision risk, utmost simplicity and predictability. On the other hand, in contrast to the identified margins of improvement of the navigation system, the developed relative orbit control strategy is not able to exploit the full potential associated with the availability, in real-time, of an accurate estimate of the relative state.

A fundamental question that still remains unanswered after the presented system functional and performance tests is how to validate the precision of the relative position estimated on-board and, consequently, how to evaluate the actual control accuracy obtained in orbit. In general formation flying missions shall offer direct or indirect means to validate externally and independently the actual relative motion. Fortunately, PRISMA offers some ideal possibilities for self- and cross-comparison of relative navigation instruments. In fact, in addition to the GPS system contributed by DLR, it embarks, among its key instruments, the radio frequency formation flying (FFRF) sensor, developed by the French National Space Agency (CNES), and the visual based sensor (VBS) by the Danish Technical University (DTU). Both instruments represent a self-contained navigation system which does not rely on GNSS constellations and can therefore operate at arbitrary distances from the Earth. Furthermore, the Phoenix-S GPS receivers data will be sent to the ground as part of the telemetry data stream and used offline for routine post-facto Precise Orbit Determination (POD) at DLR. The resulting precise orbit solutions will represent the primary reference for absolute and relative position measurements and thus serve the characterization of the real-time GPS navigation system, of the FFRF and VBS sensors. Precise GPS-based orbits will also be generated by CNES and will contribute to the overall quality assessment of the DLR real-time and offline products [Montenbruck et al., 2008].

### 6.3 Outlook

The integration of the developed autonomous GNC system within a real spacecraft and the evaluation of its operational readiness conducted in the frame of this research can certainly be considered an important milestone in the roadmap to formation-flying. Many technical challenges have been faced and finally overcome in the development of the upcoming PRISMA and TanDEM-X missions, but I think that certain work areas which lie at the borders between

different disciplines need further reflections. This section tries to identify these work areas and give some recommendations for future study.

The first identified work area is formation Fault Detection Isolation and Recovery (FDIR). The method of relative eccentricity/inclination vector separation described in this thesis can not guarantee the safety of the formation and, at the same time, fulfill the science requirements for remote-sensing at all time and under all circumstances during the mission. A dedicated formation flying safe mode is necessary in order to respond to contingency situations where the mission is at risk. In particular a formation FDIR subsystem shall be designed in such a way to rely on a subset of sensors and actuators which are independent from the baseline used for GNC and AOCS purposes. Such FDIR functionalities, distributed among the participating spacecraft, shall not substitute but complement the FDIR functions of each spacecraft in a harmonic way. Some lessons learned can be inferred from the TanDEM-X and PRISMA formation flying missions. The collision avoidance strategy for the TanDEM-X mission relies fully on the method of relative eccentricity/inclination vector separation and on the capability of the ground to respond to contingencies. Unfortunately the original design of the AOCS safe mode on each spacecraft makes use of thrusters which affect the orbit motion and can potentially increase the collision risk. A collision risk factor is computed autonomously on-board, but can not be used by the spacecraft for a potential escape maneuver. In fact such an active collision avoidance strategy would rely on the same sensors and actuators which caused the contingency. On the contrary the PRISMA satellites are fully autonomous. Collision avoidance maneuvers are executed on-board in the case that the predicted relative position lies within a prescribed region defined around the client spacecraft. The uncertainty of the predicted relative position is taken into account through covariance analysis based on the output of the GPS-based navigation system (which is the baseline for formation navigation). Unfortunately the formal covariance of the EKF implemented in the GPS-based navigation system is not fully representative of the error associated to the estimated relative state, especially during phases where the spacecraft are subject to large attitude and/or orbit maneuvers. As mentioned above, the FDIR relies on the same subsystem which may have caused the contingency situation (e.g., GPS system or Hydrazine propulsion system in the PRISMA case). Furthermore no mechanism is implemented in PRISMA to abort or stop autonomously an experiment if an AOCS safe mode occurs on the passive satellite. Only ground intervention is foreseen in this case.

A second relevant work area is the trade-off between full spaceborne autonomy and ground-in-the-loop operations. The formation flying mission design shall be based on well defined requirements and aim at the best trade-off between ground-in-the-loop and autonomous functionalities. The main drivers for this choice are given by costs, system responsiveness, and control accuracy. A fully ground-based approach is characterized by high costs (driven mainly by personnel, development, operations and maintenance of ground-system, ground-stations usage) and relatively lower control accuracy (maneuvers com-

puted on-ground far before their implementation on-board on a more or less fixed time schedule), on the other hand the development of the space-segment follows a more traditional approach (e.g., no need for inter-satellite link, or control functionalities in AOCS software) and most of the extra burden is left to the mission control center. An autonomous GNC system can guarantee reduction of mission operations long-term costs, higher responsiveness to contingencies and higher control accuracy (especially due to the shorter control cycle). Obviously an autonomous orbit control system is normally not considered state-of-the-art by the manufacturer and need to be designed, implemented and tested.

A third subject of further study is the combination of absolute and relative orbit control for SAR formations. The typical requirements for a SAR formation aiming at both repeat and single pass interferometry (cf. TerraSAR-X and TanDEM-X missions respectively) prescribe the maintenance

1. of a predefined trajectory motion defined w.r.t. to an Earth-fixed Earth-centered reference frame to ensure ground-track repeatability to a certain accuracy (we refer to this problem as Absolute Orbit Control)
2. of a predefined geometry of the formation where the motion of the active spacecraft is defined w.r.t. to the orbital frame co-rotating and centered on the passive satellite (we refer to this problem as Relative Orbit Control)

The two problems are basically independent and can be addressed separately like done in PRISMA and TanDEM-X. This does not exclude that more efficient solutions exist which could combine absolute and relative orbit control in such a way to minimize propellant consumption and number of thruster activations.

Finally I would like to spend a few words on the synergies between formation flight in low Earth orbit as addressed in this research and future classes of distributed satellite systems like on-orbit servicing missions. Tight formation flight, as well as the transient phase to rendezvous and docking scenarios, typically requires fully autonomous GNC functions for formation control on-board the spacecraft. Such autonomy scenarios are not only relevant for future rendezvous and docking and formation flying applications, but are likewise mandatory for proximity operations, in-orbit servicing and robust collision avoidance procedures.

On-orbit servicing missions build a novel class of spacecraft missions. In such kind of missions a spacecraft (servicer) is launched into an orbit of another spacecraft (client). The servicer is navigated to the client with the intention to manipulate it in a predefined manner. Both approach and coupling of two spacecraft in orbit lead to various challenges in the area of space flight dynamics. Analysis of both rendezvous and formation flight is similar in the sense that both require the understanding of the dynamics of relative motion, and derivation of control laws that can be used for docking, or formation establishment and reconfiguration. Though in contrast to the highly cooperative precision formation flying technology which can rely on GNSS and on the exchange of data through inter-satellite links, on-orbit servicing missions are

non-cooperative and can only make use of self-contained instruments for relative navigation. The main obstacle is that such relative navigation sensors, like vision based cameras, or radars have little to no flight heritage. As a consequence, navigation systems are needed for sensor cross-validation and performance analysis, real-time proximity monitoring, and controlled co-operative mission phases which are characterized by a higher technology readiness. In this sense the research conducted in this thesis can be seen as precursor of more advanced applications which, although only during their first demonstrations in orbit, will need independent back-up guidance, navigation and control functionalities to ensure safety and avoid premature mission losses.

The Deutsche Orbitale Servicing Mission (DEOS) is a technology mission conducted by the German Aerospace Center (DLR). The mission objectives are in-orbit demonstrations of robotic rendezvous and docking technologies for advanced on-orbit servicing. In this framework, a variety of relative distances is considered ranging from baselines of several kilometres to tight proximity and combined operations. The former may conveniently be realized using ground-in-the-loop orbit control approaches. In contrast, tight proximity operations in the range of a few meters to hundreds of meters must be based on autonomous navigation functions implemented onboard the spacecraft. The key goal of DEOS is to demonstrate the technological capability of an active satellite servicer to rendezvous, closely approach and inspect autonomously a non-cooperative client spacecraft. This requires, on top of adequate actuators, relative sensors for vision based and radar navigation with little to no space flight heritage. In this context a GPS-based absolute and relative navigation system is desired on DEOS to enable real-time independent monitoring and verification of the relative motion between servicer and client, to guarantee the availability of a back-up relative navigation sensor in the case of failures and to perform post-flight analysis for mission performance evaluation and cross-validation of relative navigation sensors. The GPS-based navigation system developed in the frame of this thesis is currently considered the best candidate to serve these needs.





# Appendix

## A.1 Reference Frame Transformations

This appendix describes the transformation between reference frames employed in this research and in the PRISMA formation flying mission. The material is largely based on [Gill et al., 2006] and emphasis is given to a rigorous transformation chain relating GPS measurements and PRISMA star camera data. It is recommended to adopt the Earth-Mean Equator of J2000 (EME2000) system as the nominal Earth-centered Inertial (ECI) reference system for both the Guidance, Navigation and Control (GNC) system and for integrating the equations of motion within the GPS-based orbit determination system. Differences between the nominal reference frames and their actual realizations are discussed. Note that symbols and acronyms which are first encountered in this appendix are explained when they appear and are not listed in the dedicated List of Symbols and Acronyms sections.

### A.1.1 Standard Epochs and Time System

The GPS system time is adopted as time system for the applications on-board PRISMA. It differs from International Atomic Time (TAI) by a constant offset of 19 s and matched Universal Time Coordinated (UTC) when it was introduced in January 1980. The standard epoch is 6.0 January 1980 GPS Time (Julian Date JD(GPS) 2444244.5) which serves as origin for the GPS week count. The GPS week starts Sunday 0.00 GPS Time and the first week, starting at standard epoch, is assigned the week number (WN) 0 [Montenbruck and Gill, 2001a]. The WN for arbitrary dates is given by

$$WN = \frac{JD(GPS) - 2444244.5}{7} . \quad (A.1)$$

Within a GPS week, times are specified in seconds past the start of the week, yielding values between zero and 604800 s. Within PRISMA, time synchronization is nominally based upon a One-Pulse-per-Second (1PPS) signal and associated messages of the on-board Phoenix-S GPS receiver.

The representation of GPS time in the PRISMA on-board software (OBS) applies CCSDS Unsegmented Time Code (CUC) using a vector of two integers of four bytes each. The first integer represents the seconds elapsed since the origin of the GPS time scale, while the second integer accounts for the fractional part of the seconds and denotes the numbers of microseconds.

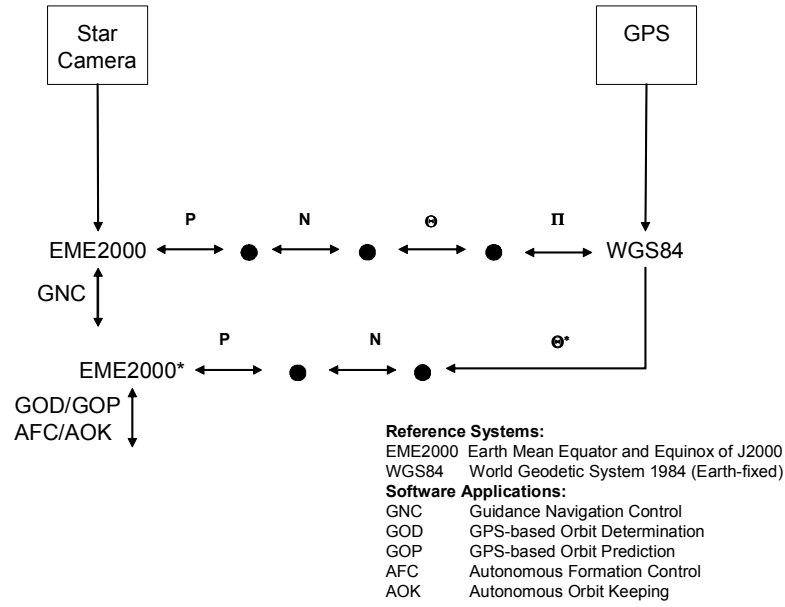


**Fig. A.1:** Reference system overview.

### A.1.2 Earth-Centered Reference Frames

The relevant Earth-centered reference frames are specified in the sequel with a focus to the well established systems like EME2000 and WGS84. Here the general expressions Earth-Centered Inertial (ECI) and Earth-Centered Earth-Fixed (ECEF) used throughout the thesis are finally characterized. An overview of the discussed reference systems is given in Fig. A.1.

#### A.1.2.1 Earth Mean Equator and Equinox of Date

The International Celestial Reference Frame (ICRF) provides a realization of the International Celestial Reference System (ICRS) using a catalog of distant VLBI radio sources [Arias et al., 1995]. In the optical regime, the realization is provided by the Hipparcos catalog, which is used as basis of the Danish Technical University (DTU) star camera.

The ICRF matches the Earth Mean Equator and Equinox of Date (EME2000) system, which has previously been employed in planetary ephemerides and star catalogs, on a level of some tens of milli-arcseconds. EME2000 is an inertial system which is aligned with the *mean* equator and equinox at the reference epoch J2000 (1.5 Jan. 2000). Its *z*-axis is parallel to the mean rotation axis of the Earth and the *x*-axis points into the direction of the mean vernal equinox, i.e. the ascending node of the Earth's mean orbital plane on the mean equator, at the fixed epoch J2000. Here, the term *mean* indicates that oscillations of the equator and ecliptic with periods of 2 weeks to 18.6 years (i.e. nutation) have been averaged.

### A.1.2.2 World Geodetic System 1984

The World Geodetic System 1984 (WGS84) system is a commonly adopted realization of an Earth-fixed reference system from a set of well-established ground station coordinates. Its axes are aligned with the adopted International Reference Pole and Meridian that are fixed with respect to the surface of the Earth. WGS84 can, at a level of a few centimeters, be considered as a particular implementation of an Inertial Terrestrial Reference Frame (ITRF).

#### Position Transformation

A position vector  $\mathbf{r}$  in the EME2000 frame is transformed by the matrix  $\mathbf{R}^{\text{eci}}$  to a position vector in the WGS84 frame  $\mathbf{r}_{\text{ecf}}$  according to [Montenbruck and Gill, 2001a]

$$\mathbf{r}_{\text{ecf}} = \mathbf{R}^{\text{eci}}(t)\mathbf{r} = \mathbf{\Pi}(t)\mathbf{\Theta}(t)\mathbf{N}(t)\mathbf{P}(t)\mathbf{r} \quad . \quad (\text{A.2})$$

The individual contributions of the reference frame transformation are described in the sequel.

#### *Polar Motion*

$$\mathbf{\Pi}(t) = \mathbf{R}_y(-x_p)\mathbf{R}_z(-y_p) \quad , \quad (\text{A.3})$$

where  $x_p$  and  $y_p$  denote the angular coordinates of the rotation axis with respect to the adopted reference pole.

#### *Sidereal Time*

$$\mathbf{\Theta}(t) = \mathbf{R}_z(\Theta(t)) \quad , \quad (\text{A.4})$$

where the true sidereal time  $\Theta(t) = \bar{\Theta}(t) + \Delta\psi \cos \epsilon$  is expressed as the sum of the mean sidereal time  $\bar{\Theta}$  and the equation of the equinoxes. The mean sidereal time is related to the UT1 time scale which differs from the Coordinated Universal Time (UTC) by up to 0.9 s.

#### *Nutation*

$$\mathbf{N}(t) = \mathbf{R}_x(-\epsilon - \Delta\epsilon)\mathbf{R}_z(-\Delta\psi)\mathbf{R}_x(\epsilon) \quad , \quad (\text{A.5})$$

where  $\epsilon$  denotes the mean obliquity of the ecliptic,  $\Delta\psi$  the nutation in longitude and  $\Delta\epsilon$  the nutation in obliquity.

#### *Precession*

$$\mathbf{P}(t) = \mathbf{R}_z(-z)\mathbf{R}_y(\vartheta)\mathbf{R}_z(-\zeta) \quad , \quad (\text{A.6})$$

with precession angles  $z$ ,  $\vartheta$  and  $-\zeta$ .

Characteristic values of angles related to the above described coordinate transformations are summarized in Table A.1

#### Velocity Transformation

**Table A.1:** Typical angles involved in the transformation from EME2000 to WGS84.

Type	Angle
Polar motion	0.3''
UTC-UT1 < 1 s	15''
Equation of Equinoxes	20''
Nutation	20''
Precession	50''/yr

Since the transformation matrix  $\mathbf{R}^{\text{eci}}$  is time dependent, a velocity vector  $\mathbf{v}$  in the inertial EME2000 system is transformed to the velocity vector  $\mathbf{v}_{\text{ecf}}$  in the rotating WGS84 system according to

$$\mathbf{v}_{\text{ecf}} = \mathbf{R}^{\text{eci}}(t)\mathbf{v} + \dot{\mathbf{R}}^{\text{eci}}(t)\mathbf{r} \quad . \quad (\text{A.7})$$

The time derivative of the transformation matrix may either be derived numerically from a differential quotient approximation or employing analytical approximations for the time derivative of the sidereal rotation matrix.

### A.1.3 Reference Frames in this Research

#### A.1.3.1 Co-moving Orbital Reference Frame

For the purpose of error analysis and in the framework of formation flying missions, an intuitive description of relative position and velocity is provided in an orbital frame, centered at and co-moving with the satellite. The reference frame, denoted generally as RTN (Radial,Tangential,Normal) or HCL (Height, Cross-track, Along-track), or Hill's orbital frame is defined by a triad of unit vectors  $(\mathbf{o}_r, \mathbf{o}_t, \mathbf{o}_n)$  which may be derived from the inertial position and velocity vectors of the satellite according to

$$\begin{aligned} \mathbf{o}_r &= \mathbf{r} / \|\mathbf{r}\| \\ \mathbf{o}_n &= (\mathbf{r} \times \mathbf{v}) / \|\mathbf{r} \times \mathbf{v}\| \\ \mathbf{o}_t &= \mathbf{o}_n \times \mathbf{o}_r \quad . \end{aligned} \quad (\text{A.8})$$

#### A.1.3.2 Star Camera and GNC system in PRISMA

The star camera employed for PRISMA is based on an input catalogue referred to the EME2000. Since no particular coordinate transformations are applied for the star camera within the GNC application, the dynamics of attitude motion within the GNC system are implicitly performed in the EME2000 system.

Using the star camera on *Main*, the attitude control accuracy will be about 50''. Since the *Target* spacecraft employs a simpler AOCS system, based on magnetometers and Sun sensors only, its attitude knowledge will be limited to 3–5°.

#### A.1.3.3 GPS-Based Navigation

The GPS-based navigation system on the *Main* spacecraft processes raw GPS measurements. The measurement modeling involves the computation of the

GPS satellite positions which is most easily performed in the WGS84 frame. Since the GPS navigation solutions also refer to the WGS84 system, this frame is, in general, a natural frame for GPS related computations.

On the other hand, the equations of motion can most easily be implemented in an inertial frame which avoids the need for Coriolis and centrifugal accelerations. Since the EME2000 is considered as a widely applied standard frame, it has been selected as reference frame for the numerical integration of the equations of motion within PRISMA. However, GPS-based navigation actually implements the EME2000\* system which differs from EME2000 by a neglect of the polar motion. Furthermore, the applied (UT1-UTC) correction is taken from a value uploaded via telecommand which might be off the true (UT1-UTC) value by  $\Delta t$ . Thus, the sidereal time transformation within GPS-based navigation employs a matrix  $\Theta^*$  and the transformation between EME2000 and EME2000\* is given by

$$\mathbf{r}^* = \mathbf{P}^t \mathbf{N}^t \mathbf{\Theta}^{*t} \mathbf{\Pi} \mathbf{\Theta} \mathbf{N} \mathbf{P} \mathbf{r} \approx \mathbf{R}_z(\omega_E \Delta t) \mathbf{r} \quad , \quad (\text{A.9})$$

which can be neglected for an on-board implementation. In the framework of PRISMA, the choice of the EME2000\* simplifies the interface to the GNC application, since the orbit determination output may directly be used within GNC without the need for further coordinate transformations.

It is noted that in addition to an output of the state vector in the EME2000 system, the state vector in the WGS84 system is also provided. This involves the back-transformation from the EME2000\* to the Earth-fixed system which leaves the provided output essentially unaffected by the particular choice of the inertial reference system.



# Bibliography

- Aguirre-Martinez M. and Sneeuw N. . Needs and tools for future gravity measuring missions. *Science Reviews*, 108(1-2):409–416, 2003.
- Alfriend K.T. , Schaub H. , and Gim D.W. . Gravitational perturbations, nonlinearity and circular orbit assumption effect on formation flying control strategies. Number AAS Paper 00-012. American Astronautical Society, February 2000.
- Alfriend K.T. , Vaddi S.S. , and Lovell T.A. . Formation maintenance for low Earth near-circular orbits. Number AAS Paper 03-652. AAS/AIAA Astrodynamics Specialist Conference, August 2003.
- Ardaens J.S. , D’Amico S. , Kazeminejad B. , Montenbruck O. , and Gill E. . Spaceborne autonomous and ground based relative orbit control for the TerraSAR-X/TanDEM-X formation. Number 03-652. 20th International Symposium on Space Flight Dynamics, Annapolis, USA, September 2007.
- Arias E.F. , Charlot P. , Feissel M. , and Lestrade J.-F. . The extragalactic reference system of the international earth rotation service, ICRS. *Astronomy and Astrophysics*, 303:604–608, 1995.
- Bainum P.M. . Breakwell memorial lecture: Review of astrodynamics, 1958 - 2001 - a personal perspective. *Acta Astronautica*, 51(1-9):517–526, 2002.
- Battin R.H. . *An Introduction to the Mathematics and Methods of Astrodynamics*. AIAA Education Series, New York, 1987.
- Bierman G.J. . *Factorization Methods for Discrete Sequential Estimation*. DOVER PUBLICATIONS, INC., Mineola, New York, 2006.
- Bodin P. . SATLAB Specification. Technical Report SPC31500-S25, Version 1.0, Swedish Space Corporation, Solna, 2005.
- Brouwer D. . Solution of the problem of artificial satellite theory without drag. *Astronomical Journal*, 64(1274):378–397, 1959.
- Brouwer D. and Clemence G.M. . *Methods of Celestial Mechanics*. Academic Press, New York, 1961.
- Bucy R.S. and Joseph P.D. . *Filtering for Stochastic Processes with Applications to Guidance*. Wiley, New York, 1968.
- Busse F.D. . *Precise Formation-State Estimation in Low Earth Orbit Using Carrier Differential GPS*. PhD thesis, Dept. of Aeronautics and Astronautics, Stanford Univ., Stanford, CA, March 2003.

- Camille C. , Berge S. , Bodin P. , and Jakobsson B. . 3-axis magnetic control with multiple attitude profile capabilities in the PRISMA mission. *Space Technology*, 26(3-4):137–154, 2007.
- Carpenter J.R. . Overview of decentralized control and formation flying testbed activities. Greenbelt Md., 2001.
- Carpenter J.R. and Schieeser E.R. . Semi major axis knowledge and GPS orbit determination. *Journal of the Institute of Navigation*, 48(1), 2001.
- Clohessy W.H. and Wiltshire R.S. . Terminal guidance system for satellite rendezvous. *Journal of the Aerospace Sciences*, 27:653–658, 1960.
- Creel T. , Dorsey A.J. , Mendickim P.J. , Little J. , Mach R.G. , and Renfro B.A. . The Legacy Accuracy Improvement Initiative. *GPS World*, 17/3:20, 2006.
- Cruickshank D.R. . *Genetic Model Compensation*. PhD thesis, The University of Colorado at Boulder, 1998.
- D’Amico S. and Florio S. De . Real-Time Satellite Laboratory Tests of DLR’s Flight Software: Second SATLAB campaign (v. 6.0.0). Technical Report PRISMA-DLR-TST-43, Deutsches Zentrum für Luft- und Raumfahrt, 2008.
- D’Amico S. and Montenbruck O. . Proximity operations of formation-flying spacecraft using an eccentricity/inclination vector separation. *Journal of Guidance, Control, and Dynamics*, 29(3), May–June 2006.
- D’Amico S. , Montenbruck O. , Arbinger Ch. , and Fiedler H. . Formation flying concept for close remote sensing satellites. Number AAS Paper 05-156. 15th AAS/AIAA Space Flight Mechanics Conference, Copper Mountain, Colorado, January 2005.
- D’Amico S. , Gill E. , Garcia M.F. , and Montenbruck O. . GPS-based real-time navigation for the PRISMA formation flying mission. ESA/ESTEC NAVITEC, Noordwijk, The Netherlands, December 2006a.
- D’Amico S. , Gill E. , and Montenbruck O. . Relative orbit control design for the PRISMA formation flying mission. AIAA Guidance, Navigation, and Control Conference, Keystone, Colorado, August 2006b.
- D’Amico S. , Florio S. De , Ardaens J.S. , and Yamamoto T. . Offline and hardware-in-the-loop validation of the GPS-based real-time navigation system for the PRISMA formation flying mission. 3rd International Symposium on Formation Flying, Missions and Technologies, Noordwijk, The Netherlands, April 2008.
- DeVries J.P. . Elliptic elements in terms of small increments of position and velocity components. *AIAA Journal*, 1(9):2626–2629, 1963.
- Ebinuma T. . *Precision Spacecraft Rendezvous Using Global Positioning System: an Integrated Hardware Approach*. PhD thesis, University of Texas, Austin, TX, 2001.
- Eckstein M.C. , Rajasingh C.K. , and Blumer P. . Colocation strategy and collision avoidance for the geostationary satellites at 19 degrees west. International Symposium on Space Flight Dynamics, 1989.



- Edfords A. . PRISMA ASW Subsystem Description. Technical Report PRISMA Phase B Study, Swedish Space Corporation, 2005.
- ESA . XMM-netwon. [sci.esa.int/xmm](http://sci.esa.int/xmm), Last accessed: 2007.
- Feucht U. , Nitsch A. , and Wagner O. . Attitude impact on the GRACE formation orbit. 3rd International Workshop on Satellite Constellations and Formations, Center of Studies and Activities for Space G. Colombo, Pisa, Italy, 2003.
- Florio S. D. and D'Amico S. . First Tests of the PRISMA Flight Software on LEON2 Board. Technical Report PRISMA-DLR-TN-14, Deutsches Zentrum für Luft- und Raumfahrt, 2007.
- Gaisler J. . *The LEON Processor User's Manual, Version 2.3.7*, 2001.
- Gaisler J. . RTEMS Cross-Compilation System, <http://www.gaisler.com/>, Last accessed: 2006.
- Gill E. and Montenbruck O. . The Onboard Navigation System for the BIRD Small Satellite. Technical Report ISRN DLR-FB-2002-2006, ISSN 1434-8454, Deutsches Zentrum für Luft- und Raumfahrt, April 2002.
- Gill E. and Runge H. . Tight formation flying for an along-track SAR interferometer. *Acta Astronautica*, 55(3-9):473–485, 2004.
- Gill E. , Montenbruck O. , and Bodin P. . Reference frames for the PRISMA formation flying mission. Technical Report DLR-GSOC TN 06-02, Deutsches Zentrum für Luft- und Raumfahrt, March 2006.
- Gill E. , D'Amico S. , and Montenbruck O. . Autonomous formation flying for the PRISMA mission. *AIAA Journal of Spacecraft and Rockets*, 44(3):671–681, 2007. DOI 10.2514/1.23015.
- Gim D. and Alfried K.T. . The state transition matrix of relative motion for the perturbed non-circular reference orbit. Number AAS Paper 01-222. In Proceedings of the AAS/AIAA Space Flight Mechanics Meeting, Santa Barbara, CA, February 2001.
- Hairer E. , Norsett S.P. , and Wanner G. . *Solving Ordinary Differential Equations I*. Springer-Verlag, Berlin-Heidelberg-New York, 1987.
- Harris I. and Priester W. . Time-dependent structure of the upper atmosphere. NASA, NASA TN D-1443, Goddard Space Flight Center, Maryland, 1962.
- Harting A. , Rajasingh C. K. , Eckstein M. C. , Leibold A. F. , and Srinivasamurthy K. N. . On the collision hazard of colocated geostationary satellites. Number AIAA 88-4239. AIAA/AAS Astrodynamics conference, Minneapolis, USA, 1988.
- Hartrampf M. , Gottzein E. , Mittnacht M. , and Miller C. . Relative navigation of satellites using GPS signals. Proceedings of Deutscher Luft- und Raumfahrt Kongress, 2002.
- Hill G. W. . Researches in the Lunar Theory. *American Journal of Mathematics*, 1:5–26, 1878.

- IERS . International Earth Rotation and Reference Systems Service. <http://www.iers.org/>, Last accessed: October 2010.
- IGSCB . IGS Products. <http://igsb.jpl.nasa.gov/components/prods.html>, Last accessed: June 2008.
- Inalhan G. , Tillerson M. , and How J.P. . Relative dynamics and control of spacecraft formations in eccentric orbits. *Journal of Guidance, Control and Dynamics*, 25(1):48–60, 2002.
- Jacchia L.G. . Revised static models of the thermosphere and exosphere with empirical temperature profiles. SAO Special Report 332, 1971.
- Jarnagin M.P. . Expansions in elliptic motion. *Astronomical Papers of the American Ephemeris*, 18, 1965.
- Jazwinski A.H. . *Stochastic Processes and Filtering Theory*. Academic Press, New York, 1970.
- Johannessen J.J. , Balmino G. , Provost C. Le , Rummel R. , Sabadini R. , Snkel H. , Tscherning C.C. , Visser P. , Woodworth P. , Hughes C. W. , LeGrand P. , Sneeuw N. , Perosanz F. , Aguirre-Martinez M. , Rebhan H. , and Drinkwater M. R. . The European gravity field and steady-state ocean circulation explorer satellite mission: Impact in geophysics. *Surveys in Geophysics*, 24(4):339–386, 2003.
- Kalman R.E. . A new approach to linear filtering and prediction problems. *ASME Trans.*, 82D(3545), 1960.
- Kasdin N.J. and Gurfil P. . Canonical modelling of relative spacecraft motion via epyclic orbital elements. Number AIAA 2003-5591. AIAA Guidance, Navigation and Control Conference and Exhibit, Austin, Texas, 2003.
- Kawano I. , Mokuno M. , Kasai M. , and Suzuki T. . First autonomous rendezvous using relative GPS navigation by ETS-VII. pages 393–400. in Proc. of the 12th International Technical Meeting of the Satellite Division of the Institute of Navigation, The Institute of Navigation, Nashville, TN, 1999.
- Kirschner M. . First results on the implementation of the GRACE formation. 3rd International Workshop on Satellite Constellations and Formations, Center of Studies and Activities for Space "G. Colombo", Pisa, Italy, February 2003.
- Krebs G. . Techsat-21 1, 2, 3. <http://space.skyrocket.de>, Last accessed: 2006.
- Kroes R. . *Precision Relative Positioning of Formation Flying Spacecraft using GPS*. PhD thesis, Delft University of Technology, The Netherlands, 2006.
- Kroes R. , Montenbruck O. , Bertiger W. , and Visser P. . Precise GRACE baseline determination using GPS. *GPS Solutions*, 9:21–31, 2005. DOI 10.1007/s10291-004-0123-5.
- Lear W.M. . GPS navigation for low-earth orbiting vehicles. (87-FM-2, Rev. 1), March 1989.

- Leung S. . *High Precision Real-Time Navigation for Spacecraft Formation Flying Using Spaceborne GPS Technology*. PhD thesis, School of Aerospace, Mechanical and Manufacturing Technology, Faculty of Engineering, RMIT University, 2003.
- Leung S. and Montenbruck O. . Real-time navigation of formation-flying spacecraft using global positioning system measurements. *Journal of Guidance, Control and Dynamics*, 28(2):226–235, 2005.
- Lyddane R.H. . Small eccentricities or inclinations in the Brouwer theory of the artificial satellite. *Astronomical Journal*, 68(8):555–558, 1963.
- MathWorks The . *Simulink manual, Writing S-Functions, Version 6*, 2002.
- Micheau P. . *Spaceflight Dynamics - Orbit Control Techniques for Low Earth Orbiting (LEO) Satellites*, chapter 13. Cepadues-Editions, edited by J.P. Carrou, 1995.
- Middour J.W. . Along track formation keeping for satellites with low eccentricity. AAS/AIAA Astrodynamics Specialist Conference, Durango, Colorado, USA, August 1991.
- Mohiuddin S. and Psiaki M.L. . Filtered dual-frequency carrier-phase differential GPS for relative navigation of high-altitude spacecraft. Number AIAA 2006-6797. AIAA Guidance, Navigation, and Control Conference and Exhibit, Keystone, Colorado, USA, 2006.
- Montenbruck O. and Gill E. . *Satellite Orbits—Models, Methods, and Applications*. Springer-Verlag, Heidelberg, Germany, 2001a.
- Montenbruck O. and Gill E. . State interpolation for on-board navigation systems. *Aerospace Science and Technology*, 5(3):209–220, 2001b.
- Montenbruck O. and Holt G. . *Spaceborne GPS Receiver Performance Testing, DLR/GSOC, TN 02-04, Issue 1.0*, 2002.
- Montenbruck O. and Markgraf M. . *User's Manual for the Phoenix GPS Receiver, DLR/GSOC, GTN-MAN-0120, Issue 1.7*, 2006.
- Montenbruck O. and Renaudie C. . *Phoenix-S/-XNS Performance Validation, DLR/GSOC, GTN-TST-0120, Issue 1.0*, 2007.
- Montenbruck O. , Kirschner M. , D'Amico S. , and Bettadpur S. . E/i-vector separation for safe switching of the GRACE formation. *Aerospace Science and Technology*, 10(7): 628–635, 2006. DOI 10.1016/j.ast.2006.04.001.
- Montenbruck O. , Delpech M. , Ardaens J.-S. , Delong N. , D'Amico S. , and Harr J. . Cross-Validation of GPS- and FFRF-based Relative Navigation for the PRISMA Mission. NAVITEC, Noordwijk, The Netherlands, 2008.
- Moreira A. , Krieger G. , Hajnsek I. , Hounam D. , Werner M. , Riegger S. , and Settelmeyer E. . TanDEM-X: A TerraSAR-X add-on satellite for single-pass SAR interferometry. Geoscience and Remote Sensing Society, International Geoscience and Remote Sensing Symposium, 2004.

- NASA . Overview of the DART mishap investigation results (for public release). [www.nasa.gov/pdf/148072main\\_DART\\_mishap\\_overview.pdf](http://www.nasa.gov/pdf/148072main_DART_mishap_overview.pdf), Last accessed: 2006.
- Ollivier M. , Duigou J.-M. Le , Mourard D. , O. Absil F. Cassaing , Herwats E. , Escarrat L. , Chazelas B. , Allard F. , Clédassou R. , du Foresto V. Coudé , Delpech M. , Duchon P. , Guidotti P.-Y. , Léger A. , Leyre X. , Malbet F. , Rouan D. , and Udry S. . PEGASE: a DARWIN/TPF pathfinder. pages 241–246. Proceedings of the International Astronomical Union, Cambridge University Press, 2005. DOI:10.1017/S1743921306009380.
- Persson S. , Jakobsson B. , and Gill E. . PRISMA demonstration mission for advanced rendezvous and formation flying technologies and sensors. Number 05-B56B07. 56th International Astronautical Congress, Fukuoka, Japan, International Astronautical Congress, 2005.
- Persson S. , Bodin P. , Gill E. , Harr J. , and Jörgensen J. . PRISMA—an autonomous formation flying mission. ESA Small Satellite Systems and Services Symposium (4S), Sardinia, Italy, September 2006.
- Reigber Ch. , Balmino G. , Schwintzer P. , Biancale R. , Bode A. , Lemoine J.M. , König R. , Loyer S. , Neumayer H. , Marty J.C. , Barthelmes F. , Perosanz F. , and Zhu S.Y. . A high quality global gravity field model from CHAMP GPS data tracking and accelerometry (EIGEN-1S). *Geophysical Research Letters*, 29(14), 2002. DOI: 10.1029/2002GL015064.
- Sabol C. , Burns R. , and McLaughlin C.A. . Formation flying design and evolution. *Journal of Spacecraft and Rockets*, 38(2):270–278, 2001.
- Sauer R. and Szabo I. . *Mathematische Hilfsmittel des Ingenieurs*, pages 248–250. Vol. 3, Springer-Verlag, Berlin, Germany, 1968.
- Scharf D.P. , Hadaegh F.Y. , and Kang B.H. . A survey of spacecraft formation flying guidance. International Symposium on Formation Flying, Missions and Technologies, November 2002.
- Schaub H. . Relative orbit geometry through classical orbit element differences. *Journal of Guidance, Control and Dynamics*, 27(5), September–October 2004.
- Schaub H. and Alfriend K.T. . Impulsive feedback control to establish specific mean orbit elements of spacecraft formations. *Journal of Guidance, Control and Dynamics*, 24(4):739–745, 2001.
- Schaub H. and Junkins J.L. . *Analytical Mechanics of Space Systems*. AIAA Education Series, Reston, VA, 2003.
- Schiff C. . Adapting covariance propagation to account for the presence of modeled and unmodeled maneuvers. Number AIAA Paper 2006-6294. AAS/AIAA Astrodynamics Specialist Conference, August 2006.
- Schweighart S. and Sedwick R. . High-fidelity linearized J2 model for satellite formation flight. *Journal of Guidance, Control and Dynamics*, 25(6):1073–1080, 2004.

- Shampine L. and Gordon M. . *Computer solution of Ordinary Differential Equations*. Freeman and Comp., San Francisco, 1975.
- Simon D. . *Optimal State Estimation, Kalman, H-infinity and non linear approaches*. Wiley, New York, 2006.
- SMO . The Chandra x-ray observatory—about Chandra. <http://chandra.harvard.edu/index.html>, Last accessed: 2007.
- Sneeuw N. and Schaub H. . Satellite clusters for future gravity field missions. *Gravity, Geoid and Space Missions*, pages 12–17, 2005. DOI: 10.1007/3-540-26932-0\_3.
- SPIRENT . *SimREMOTE USER MANUAL, DGP00792AAA, SPIRENT COMMUNICATION*, 2006.
- SSC . Ground System RAMSES, <http://www.prismasatellites.se/?id=9420>, Last accessed: 2009.
- Swerling P. . A proposed stagewise differential correction procedure for satellite tracking and prediction. (Report No. P-1292), January 1958.
- Tapley B.D. and Reigber C. . GRACE:a satellite-to-satellite tracking geopotential mapping mission. *Bollettino di Geofisica Teoretica ed Applicata*, 40(3-4), 1999.
- Tapley B.D. , Bettadpur S. , Ries J.C. , Thompson P.F. , and Watkins M. . GRACE measurements of mass variability in the earth system. *Science*, 3005(5683):503–505, 2004.
- UT/CSR . GRACE Gravity Field Model GGM01. <http://www.csr.utexas.edu/grace/gravity/ggm01/GGM01Notes.pdf>, University of Texas, Center for Space Research, 2003.
- Vadali S.R. , Schaub H. , and Alfriend K.T. . Initial conditions and fuel optimal control for formation flying of satellites. AIAA Guidance, Navigation, and Control Conf., July–August 1999.
- Vaddi S.S. , Alfriend K.T. , Vadali S.R. , and Sengupta P. . Formation establishment and reconfiguration using impulsive control. *Journal of Guidance, Control and Dynamics*, 28(2), March–April 2005.
- van Barneveld P.W.L. , Montenbruck O. , and Visser P.N.A.M. . Differential ionospheric effects in GPS based navigation of formation flying spacecraft. 3rd International Symposium on Formation Flying, Missions and Technologies, Noordwijk, The Netherlands, April 2008.
- Verhaegen M. H. . Improved understanding of the loss-of-symmetry phenomenon in the conventional kalman filter. NASA, NASA-TM-100041, December 1987.
- Ward P. . *Satellite Signal Acquisition and Tracking, in Understanding GPS, Principles and Applications*. E.D. Kaplan, Archtec House, Boston, 1996.
- Warren D.L.M. and Raquet J.F. . Broadcast vs precise GPS ephemerides: a historical perspective. *GPS Solutions*, 7:151–156, 2003.

Wertz J.R. . *Spacecraft Attitude Determination and Control*. Kluwer Academic Publishers, London, 1997.

Wiesel W.E. . Optimal impulse control of relative satellite motion. *Journal of Guidance, Control and Dynamics*, 26(1):74–78, 2003.

XEUS . X-ray observatory, study preparation activities, status report. (SCI-A/2006/054/NR), 2006.

Yunck T.P. . Coping with the atmosphere and ionosphere in precise satellite and ground positioning. *Environmental Effects on Spacecraft Positioning and Trajectories*, 73, 1993.

## Curriculum Vitae

Simone D'Amico was born in Novara, Italy, on July 16, 1976. He attended secondary school from 1989 until 1994 at the College Liceo Scientifico A. Antonelli in Novara. After that he studied Aerospace Engineering at the University Politecnico di Milano. During his studies he conducted a five months internship at Carlo Gavazzi Space SpA in Milan on the design of the Attitude Determination and Control System for the microsatellite Palamede. In 2002 he graduated with a Master's thesis in the frame of the flight dynamics operations for the Gravity Recovery and Climate Experiment (GRACE) formation flying mission, for which he spent nine months at the German Space Operations Center (GSOC) of DLR in Oberpfaffenhofen. He received the NASA Group Achievement Award as recognition of his achievements in the GRACE mission operations team.

After his graduation, in July 2003, he took on a position as young member of the scientific staff at the Flight Dynamics Division of the Space Flight Technology Department of DLR/GSOC. Until 2005 his main duties have been the design and implementation of the precise ground-in-the-loop control of the TerraSAR-X satellite and the flight dynamics lead of the Phase-A study for the TanDEM-X twin satellites formation. He received the DLR's Wissenschaft Preis 2006 in honor of scientific achievements related to the TanDEM-X mission design.

In 2006 he joined the GNSS Technology and Navigation division of the Space Flight Technology Department of DLR/GSOC and took on a position as research scientist in the frame of the PRISMA technology demonstration mission. His main duties have been the design, implementation and testing of the GPS-based guidance, navigation and control subsystem for PRISMA. At the end of 2006 he took over the project management of the DLR's contributions to PRISMA and, from 2007 on, he leads the Autonomous Formation Flying research team of the GNSS Technology and Navigation division at DLR/GSOC. His main research contributions are currently in the frame of the Spaceborne Autonomous Formation Flying Experiment (SAFE) on PRISMA and the TanDEM-X Autonomous Formation Flying (TAFF) system.

He has over 40 scientific publications including conference proceeding and peer-reviewed journal research articles. He is peer reviewer for various AIAA and IEEE journals and he has recently been nominated as Excellent Reviewer for the AIAA Journal of Guidance, Control, and Dynamics from October 1, 2007 through September 30, 2008. Furthermore he has been Programme Committee Member of the ESA 3<sup>rd</sup> International Symposium on Formation Flying Missions and Technologies, April 2008, in Noordwijk, The Netherlands.